



DEVELOPMENT OF INFRARED TECHNOLOGIES: ALL-OPTICAL MODULATION AND RANGEFINDING

By

JACK DONAL PETER COLLINS

A thesis submitted to
the University of Birmingham
for the degree of
DOCTOR OF PHILOSOPHY

Nanoscale Research Group
School of Physics and Astronomy
College of Engineering and Physical Sciences
University of Birmingham
April 2022

UNIVERSITY OF
BIRMINGHAM

University of Birmingham Research Archive

e-theses repository

This unpublished thesis/dissertation is copyright of the author and/or third parties. The intellectual property rights of the author or third parties in respect of this work are as defined by The Copyright Designs and Patents Act 1988 or as modified by any successor legislation.

Any use made of information contained in this thesis/dissertation must be in accordance with that legislation and must be properly acknowledged. Further distribution or reproduction in any format is prohibited without the permission of the copyright holder.

ABSTRACT

The longer wave infrared bands, including mid-wave infrared, spanning $3\text{ }\mu\text{m}$ to $8\text{ }\mu\text{m}$, and the long-wave infrared, spanning $8\text{ }\mu\text{m}$ to $14\text{ }\mu\text{m}$, remain a relatively unexplored field beyond thermal imaging. While their visible counterparts have found their way into a plethora of devices, mid-wave infrared and long-wave infrared see little to no use outside of defence and security, and laboratory settings. Due to these limited uses, thermal imaging and its accompanying technologies have not seen the same level of development as their visible counterparts. The effect of this limited development can be seen in the lack of choice of optical modulators for these wavelengths, and the lack of uses outside thermal imaging. However, the use of these longer wavelength infrared bands could be beneficial in areas where a high transmission in the atmosphere is required, due to their relative low attenuation compared to the visible range. Some of these use cases involve long distance rangefinding and optical wireless communication.

To enable these new applications, high speed modulators are required. One of the topics of this thesis involves the development and benchmarking of an all-optical shutter for the short-wave, mid-wave and long-wave infrared, for use in compact and rugged systems. This all-optical technology consists of a semiconductor optical window that on absorption of a high-energy optical pump in the near infrared, attenuates short-wave to long-wave infrared. The primary mechanism for the attenuation of the short-wave to long-wave infrared is intra-band absorption caused by excited free carriers in the semiconductor optical window. This shutter technology was used to improve the temporal accuracy of a slow mercury cadmium telluride detector in a femtosecond system, enabling observations on the order of picoseconds to be made. The shutter technology was then implemented in a smaller, breadboard sys-

tem, which was designed to test the shutter for real world applications such as time of flight rangefinding and active gated imaging in the long-wave infrared. With the system it was found that a microbolometer thermal camera could be externally gated using the all-optical shutter technology on the scale of microseconds.

An electronic solution for improving the temporal accuracy of mid-wave infrared and long-wave infrared was developed alongside the solid state shutter technology. As nothing similar exists on the market for mid-wave infrared rangefinding, custom electronics needed to be designed and made including a high-speed preamplifier, constant fraction discriminator and time-to-digital converter. Rather than externally gating a detector, a constant fraction discriminator was designed and custom built to provide high temporal accuracy. This constant fraction discriminator was able to negate the issues of amplitude walk and variation that would otherwise make the system unsuitable for measuring distances. To verify the performance of the system a visible wavelength benchmark was also built. The performance of the final implementation of the constant fraction discriminator system for the mid-wave infrared was compared to the threshold level triggering in the visible system. It was found that the performance of the mid-wave infrared rangefinder came close to the 633 nm benchmarking system, showing centimetre resolution, making the mid-wave infrared a viable option for rangefinding.

DEDICATION

Dedicated to my friends and family.

ACKNOWLEDGMENTS

I would like to start by thanking DSTL and the University of Birmingham for allowing me to carry out this research. I would like to especially thank Phil Soan from DSTL for your support and guidance during my research.

Thank you to the friends I've made along the way, especially my housemates during my research, Dr Dominic Phippen and Richard Barron. You guys really knew how to put a smile on my face. I'll never forget the 156 crew.

Thank you to all of the staff at NPRL, Dr Wolfgang Theis, Prof. Leigh Canham, Dr Quanmin Guo, for providing guidance and support during my research. I would also like to thank Dr William Terry for getting me going with Labview, and keeping an eye out for me when I first started out as a PhD researcher.

I would like to say a huge thank you to my supervisor, Dr Andrey Kaplan. Thank you for taking me on and believing that I could do this, I still can't believe I managed it. Thank you for guiding me, suggesting new ideas, and encouraging me to pursue different ideas. Thank you for your help in troubleshooting issues, connecting me with people, and explaining things to me that I should have already known!

I would like to thank the best lab partner I could have ever had, Dr Rihan Wu. Not only are you a master of optics and a laser whisperer (yes, I believe our laser had a personality), you are a great drinking partner, band mate, and most of all, best friend. My research would not have been what it is without your help and insight. Hopefully we will meet again to fix lasers and have a trip to the pub afterwards!

I would like to thank my family, especially my parents, Jane and Cliff, my sister Lizzie, and my partner Elli for being so supportive, the period during my research and write up has been a rollercoaster of exhilarating highs and deep lows. Not only did you all nod along while I was telling you about the excruciating detail of my research, but you also kept me going when things were going south. Without you guys I don't think I would have been able to do this. Thank you for being there for me and believing in me.

I could thank you all a million times over and it would never really be enough, but without a doubt, this would not have been possible without you.

Publications

Some of the work in this thesis originates from the publications listed below:

- Wu, R.; Collins, J.; Burgess, C. D.; Lamb, R. A.; Kaplan, A. "Demonstration of Time-of-Flight Technique with All-Optical Modulation and MCT Detection in SWIR/MWIR Range". In *Emerging Imaging and Sensing Technologies for Security and Defence III; and Unmanned Sensors, Systems, and Countermeasures*; Hollins, R. C., Buller, G. S., Lamb, R. A., Eds.; SPIE, 2018; Vol. 10799, p 2. <https://doi.org/10.1117/12.2500326>.
- Wu, R.; Collins, J.; Canham, L.; Kaplan, A. "The Influence of Quantum Confinement on Third-Order Nonlinearities in Porous Silicon Thin Films". *Applied Sciences* 2018, 8 (10), 1810. <https://doi.org/10.3390/app8101810>.
- Wu, R.; Collins, J.; Chekulaev, D.; Kaplan, A. "All-Optical Modulation and Ultrafast Switching in MWIR with Sub-Wavelength Structured Silicon". *Applied Sciences* 2019, 9 (9), 1808. <https://doi.org/10.3390/app9091808>.
- Collins, J.; Wu, R.; Davie, A.; Kaplan, A. "All-Optical Modulator for Gated Range Finding and Active Imaging in LWIR". In *Electro-Optical and Infrared Systems: Technology and Applications XVII*; Hickman, D. L., Bürsing, H., Eds.; SPIE: Online Only, United Kingdom, 2020; p 20. <https://doi.org/10.1117/12.2574006>.
- Wu, R.; Mathieu, T.; Storey, C. J.; Jin, Q.; Collins, J.; Canham, L. T.; Kaplan, A. "Localized Plasmon Field Effect of Gold Clusters Embedded in Nanoporous Silicon". *Adv. Optical Mater.* 2021, 9 (9), 2002119. <https://doi.org/10.1002/adom.202002119>.
- Wu, R.; Jin, Q.; Storey, C.; Collins, J.; Gomard, G.; Lemmer, U.; Canham, L.; Kling, R.; Kaplan, A. "Gold Nanoplasmonic Particles in Tunable Porous Silicon 3D Scaffolds

for Ultra-Low Concentration Detection by SERS". *Nanoscale Horiz.* 2021, 6 (10), 781–790. <https://doi.org/10.1039/D1NH00228G>.

- Wu, R.; Nekovic, E.; Collins, J.; Storey, C.; Canham, L.; Navarro-Cía, M.; Kaplan, A. "Taming non-radiative recombination in Si nanocrystals interlinked in a porous network". *Physical Chemistry Chemical Physics*. 2022 (Accepted)

Contents

	Page
1 Introduction	1
2 Assessment of Current Infrared Technologies - Literature Review	7
2.1 MWIR and LWIR	7
2.1.1 Rayleigh	8
2.1.2 Mie	10
2.1.3 Molecular Absorption	12
2.2 Infrared Modulators	14
2.3 Detection Technology	21
2.3.1 Thermopile	22
2.3.2 Pyroelectric Detectors	23
2.3.3 Micro Bolometer	24
2.3.4 Mercury Cadmium Telluride	27
2.3.5 Quantum Cascade Detector	28
2.3.6 Indium Arsenide Antimonide	29
2.4 Thermal Imaging	30
2.4.1 Non-uniformity Correction	30
2.4.2 Shutter Technology	32
2.5 Rangefinding	33
2.5.1 Phase Shift Method	33

2.5.2	Time of Flight Method	36
2.5.3	Infrared Ranging	39
2.6	Range Gated Active Imaging (RGAI)	40
3	System Operations	44
3.1	Femtosecond Laser System	45
3.1.1	Seed Laser	46
3.1.2	Regenerative Amplifier (RGA)	47
3.1.3	Chirped Pulse Amplification (CPA)	48
3.1.4	Optical Parametric Amplifier (OPA)	48
3.2	Breadboard System	50
3.2.1	Quantum Cascade Lasers (QCL)	51
3.2.2	Diode Laser	53
3.3	Electronics	54
3.3.1	Time to Digital Converter (TDC)	57
3.3.2	Microcontrollers	60
3.4	Experimental Setups	60
3.4.1	Pump Probe Spectroscopy	60
3.4.2	Breadboard Modulator Setup	61
3.4.3	Noise Reduction	61
3.5	Summary	69
4	Solid State Shutter	71
4.1	Operational Principles	73
4.2	Suitable Modulator Materials	77
4.2.1	Optical Silicon Window	77
4.2.2	Macro-Porous Silicon	77
4.2.3	Nano-Porous Silicon	81

4.2.4	Nano-Porous & Macro-Porous Modulator Spectra	81
4.3	Carrier Dynamics in Silicon	82
4.3.1	Free Carrier Excitation	82
4.3.2	Free Carrier Decay	84
4.4	Drude Model	86
4.5	Transmission simulation using the Transfer Matrix Method (TMM)	87
4.5.1	Refractive Index Calculation	88
4.5.2	Transfer Matrix Method Formation	89
4.5.3	Simulation Output	94
5	All-Optical Shutter	96
5.1	All-Optical Modulator for Picosecond Time of Flight in the SWIR and MWIR	98
5.2	Compact All-Optical Modulator for Gated Range Finding and Active Imaging in LWIR	103
5.2.1	Theory & Principle of Operation	104
5.2.2	Demonstration Setup	106
5.2.3	Results	110
5.2.4	Summary of Compact RGAI & ToF System	117
5.3	Porous Silicon Based Modulator	117
6	MWIR Time of Flight	121
6.1	Introduction	121
6.2	Optical system design	123
6.3	Electrical System	124
6.3.1	High Gain-Bandwidth Preamplifier	125
6.3.2	Constant Fraction Discriminator	129
6.3.3	Timing	139
6.4	Results and Discussion	140

6.4.1	TDC7200 Testing	140
6.4.2	633 nm Benchmarking	142
6.5	MWIR Rangefinder Testing	142
6.6	Summary and Outlook	149
7	Conclusion	152
A	Electrical Schematics	158
A.1	High Speed Preamplifier v2	158
A.2	CFDv4	158
A.3	CFDv6	163
A.4	TDC7200	165

List of Figures

2.1	Use of Short-Wave Infrared (SWIR) system for imaging through fog. Visible image (a) shown against a SWIR (b). The person in the fog is only visible with the SWIR system. From [2].	9
2.2	Relative scattered intensity against wavelength plotted from the relation $I_{sca} = 1/\lambda^4$	10
2.3	Calculated Mie-Lorentz scattering using the miepython package [33], with data from https://RefractiveIndex.Info [35, 36]. Extinction efficiency is plotted against photon wavelength for differing H ₂ O particle size to give an indication of performance in fog.	12
2.4	Calculated transmission for Mid-Wave Infrared (MWIR) atmospheric transmission window. This was calculated using the HAPI API for the HITRAN Database, data from [41].	15
2.5	Calculated transmission for Long-Wave Infrared (LWIR) atmospheric transmission window. This was calculated using the HAPI API for the HITRAN Database, data from [41].	16
2.6	Calculated transmission for 1.4µm to 12µm using the ATRAN model [43] with a zenith angle of 0° at altitudes of 100 m, 1 km and 10 km respectively. This model uses the HITRAN 2000/2001 database to calculate the absorption of each molecule.	17

2.7	Transmission spectrum calculated using MODTRAN for rural aerosols mid-latitude summer climate with a visual range of 1220 m shown in (a) (particle size $< 1 \mu\text{m}$), and midlatitude winter, foggy conditions, with a visual range of 610 m shown in (b). From [1, p. 571].	18
2.8	Detector technologies with their respective approximate optical bandwidths. Values gathered from what is available to purchase from a selection of vendors available at the time of writing (Thorlabs, Hamamatsu, Teldyne Judson, Laser Components as of 2022). Active cooling is required in some cases.	22
2.9	Illustration of a thermopile consisting of 2 thermocouples, represented by the grey and dark grey wires. The total voltage is proportional to the temperature $T + \Delta T$, and can be calculate by the number of thermocouples, N multiplied by each thermocouples voltage V_{out} . From [61].	23
2.10	Illustration of microbolometer pixel. The sensing membrane is fixed $\lambda/4$ above the reflector, typically $2.5 \mu\text{m}$, which forms the resonant cavity. This resonant cavity increases the efficiency of the absorber. The size of the absorber, including legs, dictates the pixel pitch. The Read Out Integrated Circuit (ROIC) in the substrate measures the resistance change of the microbolometer as it absorbs IR light.	25
2.11	Shown from a) to c) are images from an uncooled thermal camera without a Non-Uniform Calibration (NUC) applied, d) through f) shows the same images after using the minimizing the sum of the squares of errors (MSSE) algorithm. From [9].	31
2.12	SWIR passive (a) and SWIR gated imaging system (b) images at a range of 480m. This technology allows for isolating elements of a scene and the improvement in clarity due to reduction in backscattered photons. From [2].	40
3.1	Block diagram showing the primary components of the femtosecond system.	46

3.2	Schematic drawing of Chirped Pulse Amplification (CPA) optical setup. The beam enters the system as a short, low intensity, collimated pulse. The beam is then separated into its constituent wavelengths by a diffraction grating (<i>a</i>), otherwise known as the stretcher, before being collimated again at (<i>b</i>). At this point, the shorter wavelength light has travelled further than longer wavelengths, spreading out the pulse in time. The resulting pulse is then passed through the amplifier (<i>c</i>), increasing its intensity. Finally, the pulse is focussed onto the second diffraction grating, (<i>d</i>), the compressor. This compresses the pulse in time, as the longer wavelengths travel further than the shorter ones.	49
3.3	Simplified process showing the Difference Frequency Generation (DFG) and Sum Frequency Generation (SFG) processes.	49
3.4	Block diagram showing the infrared modulator breadboard setup. The Quantum Cascade Laser (QCL) provides the trigger signal to the system, meanwhile the Arbitrary Function Generator (AFG) provides the trigger for the Near Infrared (NIR) diode optical pump laser, and if required, a gate signal for the QCL for reducing the operating frequency. Red and black lines represent the optical and electrical paths, respectively.	51
3.5	Schematic diagram of QCL structure. Dashed lines represent the boundaries of each energy well. The step structure is caused by the applied voltage, V across the structure. Electrons tunnel through the barrier in between energy bands, in this case between E_2 and E_1 before relaxing, producing a photon, as represented by the oscillating line.	52
3.6	Simulation of bipolar generation for use with Constant Fraction Discriminator (CFD).	56

3.7	Simplified Transimpedance Amplifier (TIA) circuit topology. Gain of circuit goes as $V_{out} = i_D R_F$. Careful selection of capacitor C_F maintains stability of the amplifier.	57
3.8	59
3.9	Simplified schematic showing double modulation implementation into a pump probe experiment. Dotted box represents the delay line for the pump, while dashed lines represent electrical connections. The laser trigger operates at 1 kHz, and the chopper trigger operates at 500 Hz.	63
3.10	Results from a classic pump probe experiment compared to the double modulation implementation of pump probe.	65
3.11	Schematic diagram showing the key components of the pulse sampling method incorporated into the pump probe experiment. The pump optical path remains as the double modulation method, however a small fraction of the probe is split and guided to the reference detector so that the power can be monitored and used for noise reduction. The signals from both of the detectors are passed through stretching circuits before being sampled by a computer controlled, National Instruments PCI-6221 Data Acquisition (DAQ) device. .	66
3.12	All clocks are defined from the laser trigger 1 kHz signal. The highlighted area represents the gating of the PCI6221, and the red dashed lines represent the sampling time. The DAQ gate and sample trigger phase should be adjusted with respect to the laser trigger.	68
3.13	Noise reduction when using the pulse sampling method. The standard deviation of the signal before the transmission drop is 3×10^{-4} , suggesting that it would be possible to resolve changes on the order of 10^{-4} in signal variation.	69

4.1	Concept of the solid state shutter. Unshaded region represents the activation of the shutter. The grey highlighted region shows the off state, as free carriers recombine. All values are arbitrary in this case.	72
4.2	Equation 4.1 and 4.2 against temperature. Results valid between 0 K and 350 K for Equation 4.1.	74
4.3	Absorption coefficient plotted against incident wavelength. 800 nm proves to be a suitable wavelength for optical pumping due to the high absorption coefficient [147].	76
4.4	Scanning electron microscope images showing a top down view of macro-porous silicon on the left, and nano-porous silicon on the right. Taken from [149].	78
4.5	Transmission spectrum of nano-porous silicon (shown in (a)) and macro-porous silicon (shown in (b)) in the modulators off state. The transmission spectrum was measured using a Fourier-transform Infrared (FTIR) spectroscope. Interference fringes observed in both samples relate to multiple internal reflections within the porous silicon. Taken from [149].	79
4.6	Recorded transmission spectrum of MWIR signal after activation of the modulator, obtained using the pump-probe experiment. Macro-porous silicon (mpSi) displays a stronger change in transmission, compared to nano-porous silicon (npSi), around 4 μm . However, both materials tend to approximately 60% attenuation at wavelengths closer to 5 μm . Taken from [149].	80
4.7	Normalised photon absorption as a function of the modulator depth for 800 nm light. Value for absorption coefficient from [147].	83
4.8	Simple Transfer Matrix Method (TMM) set up. A substrate with refractive index n , sandwiched between two semi-infinite mediums of air. E field shown in black solid lines, H field in red.	88

4.9	Simulation of transmission of a 10 μm probe signal through a 500 μm thick sample as a function of optical pump power, provided by a 800 nm solid state diode.	95
5.1	Optical set up of the all optical gated shutter for Mercury Cadmium Tellurides (MCTs) detectors in the SWIR and MWIR, published in [155]. In this diagram, the probe pulse, in green, travels through the silica rod (1), then passes through the modulator (3) and silicon optical window (4), before being recorded by the MCT detector (5). The pump pulse, represented by the red line, travels along the computer controlled translational stage and retroreflector (2), before being directed onto the surface of the modulator (3). The silicon window (4) absorbs any remnant pump.	99
5.2	Time of Flight (ToF) results of air and silica rods, published in [155]. Shown above are the varying time of flights for the differing wavelengths while travelling through the silica rods.	102
5.3	Probe pulse broadening induced from passing through the silica rods, published in [155]. Shown above is the stretching of the falling edge of the change in transmission for the differing wavelengths while travelling through the silica rods.	103
5.4	Flow chart and pulse schematics of the synchronisation electronics.	107

5.5	ToF and RGAI feasibility demonstrator. The green and blue lines represent the short and long IR optical paths respectively. The red line represents the modulator laser beam. The signal laser is produced by a Hamamatsu QCL (<i>a</i>). The mirror (<i>b</i>) can be flipped down to switch between short and long optical paths. The activation laser for the modulator is provided by the 808 nm diode bar laser (<i>c</i>) The signal is then steered and focussed onto the modulator (<i>d</i>), and then either directed into the MCT (<i>e</i>), or into the uncooled thermal camera (<i>f</i>). For RGAI the mask is added between the final steering mirror and modulator window (<i>d</i>).	108
5.6	example	110
5.7	Normalised Time-of-flight data shown for the short optical path (SOP) in the left panel, and data for the long (LOP) and short optical paths in the right panel. The signals for the right panel have been normalised between 1 and 0. The intersections of linear fits were used to obtain the minima for both signals. The difference between minima on the abscissa determines the delay time introduced by travel along the longer optical path, corresponding to a distance of 30 m.	111
5.8	A selection of heatmaps of the π -symbol mask imaged by the thermal camera. The times correspond to difference between the modulation (gating) and signal lasers arrivals on the surface of the modulator.	113
5.9	Transmission of the modulator as a function of the gating time with respect to the signal arrival time. 0 μ s represents the two lasers overlapped in time on the modulator surface. The highlighted square area in (<i>a</i>) shows the group of pixels used to obtain the average value of the signal intensity. Three thermal images were averaged per data point.	115

5.10	The following heatmaps show that there is little to no effect of the modulator laser when the signal laser is not overlapped with the modulator laser; (a) modulator laser disabled, (b) modulator laser occurs 500 μ s after the signal laser, (c) modulator laser occurs 58 μ s after signal laser. The slight changes can be attributed to thermal lensing effects by the minor increase its temperature.	116
5.11	Transmission of the modulator as a function of the optical pumping power. Three thermal images were averaged per data point.	116
5.12	Fourier Transform Infrared (FTIR) spectrums (a-b) and pump-probe results (c-d) for low (a,c) and high porosity (b,d) samples. Higher porosity samples show a faster recombination, while across the board, hydrogenated samples show slower recombination. It is speculated that collapsing pores after re-hydrogenating the nano-porous silicon may have caused the difference between the hydrogenated and re-hydrogenated silicon for the FTIR spectrum and pump-probe results.	119
5.13	Recombination rate of hydrogenated and oxidised samples at varying porosities. Oxidised samples exhibit a much faster recombination rate, returning to normal levels of carriers significantly sooner than hydrogenated samples. . .	120

6.1	Schematic of optical and electrical setup for the MWIR rangefinder. The optical signal is provided by a laser diode, and is directed along a variable optical path (633 nm and 4.48 μm InAsSb) or fixed optical path (4.48 μm MCT), represented by the grey dashed line. The electrical signal path is represented by the black solid line. When benchmarking the system, the <i>CFD \mathcal{E} Delay</i> was omitted, represented by the black dashed line, as the rise time of the visible photodiode is on the nanosecond scale. The start signal is provided by the laser driver, and is first put through a level converter to ensure compatibility with the Time to Digital Converter (TDC). The TDC will measure the time between the start and stop signals.	124
6.2	TIA with included stray capacitances: capacitance due to circuit board layout and soldering C_{PCB} ; the common mode, C_{CM} , and differential mode, C_{DIFF} stray capacitances; and C_D , the diode capacitance. The photodiode has been separated into its constituent components.	126
6.3	Wide bandwidth non-inverting amplifier with a gain set by $V_{out} = V_{in}(1 + R_2/R_1)$. The greyed out section shows the simplified TIA schematic, the first stage of the preamplifier circuit.	128
6.4	Preamplifier response with the InAsSb photodiode. Rise time calculated to be 63 ns using the exponential fit.	130
6.5	Schematic highlighting primary components of the CFDv6 circuit. An input signal, V_{in} is first inverted, before then being split into three paths. Detail of the signal path is covered in text. V_{arm} is the arming threshold voltage, V_{zc} is the zero crossing voltage.	131

6.6	Progression of the signal throughout the CFD. Firstly a signal is supplied to the CFD (CFD V_{in}), the grey line is to guide the eye. This signal is buffered, inverted and amplified (Buffer Output). This is then split into three paths, the arming comparator outputs a low signal when a strong input is detected (Threshold Output), which is then stored in the storage flip flop, which outputs a high signal (Armed Flip Flop), which enables the output of the CFD. The attenuated, and the delayed and inverted pulses are mixed by a second OPA657 configured in a differential amplifier configuration, applying a small level of gain to generate the amplitude difference between the two signal. The zero crossing is then found in the mixed signal, represented by the dashed line. When the zero crossing (ZC) point is detected, the (ZC) comparator output goes high, triggering the output of the monostable vibrator. To buffer the signal, another comparator is used (CFD V_{out}). Finally the system is reset by the inverted out of the monostable vibrator, which resets the flip flop. . .	132
6.7	Dependence of capacitance and inductance on delay and impedance of a signal path.	135
6.8	Transmission line circuit, designed to achieve the maximum power transmission, and avoid reflection. The source and sink resistance R should be matched to the transmission line impedance. A unit of the transmission line is an inductor followed by a capacitor.	136
6.9	Delay induced by the delay board. Dashed lines cross the signal at 50% of amplitude of the pulse and are spaced 76 ns apart. Attenuation of the pulse can be attributed to the Direct Current (DC) resistance of the inductors. . .	137

6.10	Simulation showing how the delayed signal is mixed with the signal from the buffer. The top and middle right waveforms have been calculated from the theoretical gain applied by the mixer Operational Amplifier (opamp), with the bottom waveform being summed from the two mixed signals.	138
6.11	Boxplot showing the measured deviation for different stop-start delays produced by a two channel AFG. The boxes contain the 25th to 75th quartile, and the whiskers containing the $1.5 * IQR$, where IQR is the interquartile range. Outliers are shown in light grey, and the median shown in orange. The AFG produced two trigger signals separated by a set delay, 9999 samples were collected for each delay interval. In general, the stop signal arrives approximately 0.2 ns to 0.4 ns later than it should, settling at around 0.2 ns after 500 ns where mode 2 is enabled on the TDC (used for measuring times greater than 500 ns where the coarse counter is enabled). This added 0.2 ns could be induced from a differential in Printed Circuit Board (PCB) track lengths. . .	141
6.12	Comparison of the real added path length, shown by the theoretical line (1:1 ratio) against the measured path length by the 633 nm benchmarking system.	143
6.13	Positional and temporal error for the 633 nm benchmarking system.	144
6.14	Positional and temporal error for the MWIR rangefinder for threshold level triggering and the CFD system. A total of 9999 samples were taken and averaged for each translational stage position.	145
6.15	Positional and temporal error for the CFD benchmarking system.	146
6.16	Standard deviation of each position after 9999 samples for threshold level triggering shown in orange, and the CFD system, shown in blue. Both methods have a similar standard deviation, although threshold level triggering is more erratic.	147

6.17	Histograms showing the distribution of stop times for two different TDCs and signal conditioning. 2000 counts have been plotted, with the standard deviation for each histogram shown in the corner.	148
6.18	Range of amplitudes of signal input into CFDv6, measured after the mixing opamp. Inset shows the zero crossing in point in detail. All waveforms cross within 5 ns. Each waveform is an average of eight samples. Input amplitude to the CFD varied between 2 mV peak-to-peak to 55 mV peak-to-peak. . . .	149

Acronyms

a-Si Amorphous Silicon.

ADC Analogue to Digital Converter.

AFG Arbitrary Function Generator.

AOM Acousto-Optic Modulator.

APD Avalanche Photodiode.

CFD Constant Fraction Discriminator.

CPA Chirped Pulse Amplification.

CW Continuous Wave.

DAQ Data Acquisition.

DC Direct Current.

DFB Distributed Feedback.

DFG Difference Frequency Generation.

DMD Digital Micromirror Device.

DSP Digital Signal Processing.

e-APD Electron Injection Avalanche Photodiode.

EMI Electromagnetic Interference.

FPA Focal Plane Array.

FPGA Field Programmable Gate Array.

GaN Gallium Nitride.

GVD Group Velocity Dispersion.

IC Integrated Circuit.

IR Infrared.

LCD Liquid Crystal Display.

LIA Lock-in Amplifier.

LIDAR Laser Detection and Ranging.

LWIR Long-Wave Infrared.

MCT Mercury Cadmium Telluride.

MCU Microcontroller Unit.

MEMS Microelectromechanical system.

MQW Multiple Quantum Well.

MWIR Mid-Wave Infrared.

ND Neutral Density.

Nd:YLF Neodymium-doped Yttrium Lithium Fluoride.

NIR Near Infrared.

NUC Non-Uniform Calibration.

OPA Optical Parametric Amplifier.

opamp Operational Amplifier.

OWC Optical Wireless Communication.

PCB Printed Circuit Board.

PCI Peripheral Component Interconnect.

PEM Photoelastic Modulator.

PPKTP Periodically-Poled Potassium Titanyl Phosphate.

QCD Quantum Cascade Detector.

QCL Quantum Cascade Laser.

QWIP Quantum Well Infrared Detector.

RF Radio Frequency.

RG Regenerative Amplifier.

RGAI Range Gated Active Imaging.

ROIC Read Out Integrated Circuit.

SDG Synchronization & Delay Generator.

SFG Sum Frequency Generation.

SHG Second Order Harmonic Generation.

SLM Spatial Light Modulator.

SPAD Single Pixel Avalanche Diode.

SPD Single Pixel Detector.

SPI Serial Peripheral Interface.

SRH Shockley-Read-Hall.

SWIR Short-Wave Infrared.

TDC Time to Digital Converter.

TEC Thermoelectric Cooler.

Ti:Sapphire Titanium Sapphire.

TIA Transimpedance Amplifier.

TMM Transfer Matrix Method.

ToF Time of Flight.

TTL Transistor-Transistor Logic.

UV Ultra Violet.

VCO Voltage Controlled Oscillator.

VIS Visible.

VOx Vanadium Oxide.

WLC White Light Continuum.

Chapter One

Introduction

Infrared light is a slice of the electromagnetic spectrum that occupies the region between microwave and Visible (VIS). It provides an extra dimension for examining the world around us, allowing us to observe things that are invisible to the naked eye. The infrared region contains several sub-bands, namely Near Infrared (NIR), Short-Wave Infrared (SWIR), Mid-Wave Infrared (MWIR), and Long-Wave Infrared (LWIR), which cover 780 nm to 15 μm [1]. While infrared imaging, ranging from the SWIR, through MWIR to the LWIR, is commonly used in defence and security, it also offers numerous benefits for civilian uses. Common areas for defence usage are active night vision in the SWIR, where a burst of light illuminates the scene, and a SWIR camera recovers the scene [2]; thermal cameras used for food quality assessment, firefighting, structural and building analysis, to name a few [3, 4, 5, 6, 7]. Infrared sensing is also commonly used in applications that involve gas sensing, as many of the vibrational modes, such as O-H and C=C, lie in this wavelength range [8]. Given the potential industries that infrared imaging could be used in one may find it surprising that the development of technologies for infrared imaging has not kept pace with those in the visible spectrum.

One focus of the work covered in this thesis revolves around thermal cameras. To

give a brief overview: thermal cameras allow one to assess scenes from another perspective, highlighting areas that are hard or sometimes impossible to see when limited to the visible spectrum, and offer a faster, non-contact method for measuring temperatures of objects compared to using a temperature probe [1]. Compared to their visible counterparts, thermal cameras have not been developed to the same extent. The lack of development in thermal cameras is predominantly due to consumer demand; most modern electronic devices will have a visible silicon-based detector in it due to economies of scale and miniaturization. Like VIS cameras, thermal cameras are made up of four main parts, which consist of a lens group, aperture, shutter and sensor. There are the lens elements, which are responsible for gathering and focussing the light from the scene onto the sensor; the aperture, which controls the throughput of light to the sensor, the shutter, which provides a known temperature for calibration of the thermal sensor; and the sensor, which records the light from the scene.

Like a conventional VIS camera, thermal cameras require either a mechanical shutter or an electronic shutter [9]. In contrast to a conventional VIS camera, the role of the mechanical shutter in a thermal camera is to provide a uniform scene of known temperature. This mechanical shutter physically blocks the light from the scene. The uniform scene observed by the sensor is then used for calibration of the output of the sensor's pixels. Commonly known as a Non-Uniform Calibration (NUC), this process is used to adjust for thermal drift in the sensor and camera housing. However, the mechanical shutter is a delicate, moving, mechanical part which is susceptible to damage from rough treatment, and wear and tear. Due to the shutter also having to move, the system has a reasonably low maximum operation speed, with periodic periods while the sensor is 'blind' due to the shutter blocking light. In contrast, an electronic shutter does not involve any mechanical parts; instead, it quickly samples the intensity of each pixel in the sensor, usually a row at a time. This process is adequate, provided the scene is static, or at the very least, moves slower than the time it takes to read out all the pixel values. Issues occur when the subject of the image moves

faster than the time it takes for each row of the sensor is sampled, which can lead to the rolling shutter effect [10]. This effect is commonly observed when recording a fast moving object, like a propellor of a plane, where distortion of the blades is visible. It is important to note that this is different to blur incurred from long exposure times, where in the previous aeroplane example, a disk would be observed. When an electronic shutter is employed, the sensor itself needs to respond quickly. As well as an increased chance of tearing, a shutterless camera is more susceptible to damage from overexposure compared to a shuttered camera, as there is no physical barrier between the environment and sensor [11]. Nevertheless, both shuttered and shutterless thermal cameras are in use today, with either one, or both of the technologies implemented for a *‘best of both worlds’*.

For these reasons, an improvement on thermal cameras could be realised by introducing a faster modulator in place of the conventional mechanical shutter. For the VIS spectrum, high-speed optical modulators are abundant and one is spoilt for choice. From electro-optical devices to all-optical solutions there is a device for almost every requirement and situation [12, 13, 14]. However, as the wavelength of light increases typically the options for optical modulators diminish while cost increases. This increase is especially true beyond the telecommunication wavelengths, which start around 1550 nm. Not only is there less choice, usually the offerings are less mature than their visible counterparts.

A faster Infrared (IR) modulator would be a welcome addition to an optics laboratory. Thermal sensors, compared to their VIS and NIR silicon counterparts, while sensitive, are generally slower to respond [15]. These sensors also often require active cooling in the form of liquid nitrogen, or Thermoelectric Coolers (TECs), to achieve a good signal to noise ratio when recording a signal at longer wavelengths. While a modulator will not help with the cooling, it has the ability to improve the temporal resolution of the sensor through active gating. Due to its all-optical nature, the response time of the modulator proposed would be orders of magnitude faster than that of any mechanical system.

Another topic of this thesis is rangefinding; in particular, how a longer wavelength IR source could be combined with the solid state shutter technology to produce a Range Gated Active Imaging (RGAI) device. Early rangefinding devices, termed coincidence rangefinders, used a pair of mirrors separated by a long tube, with a prism in the centre to combine and generate the split image. By adjusting the angles of the two mirrors to correct the split image, and using trigonometry, it was possible to get an approximate range of object of interest [16]. This device was quickly replaced with laser rangefinders, commonly termed Laser Detection and Ranging (LIDAR). Laser rangefinding has numerous advantages over older optical rangefinders, including accuracy, robustness and speed of measurement [17, 18, 19]. There are two primary methods for laser rangefinding. The first of these is the phase shift method, where the phase of an outgoing and incoming wave of a amplitude modulated Continuous Wave (CW) laser is compared; and the second is the Time of Flight (ToF) method, where the roundtrip of a pulsed laser is measured.

A pioneering example of the phase shift method was conducted in 1849 by Armand Fizeau [20]. Fizeau used a rotating disk with cutouts, a light source, and a mirror 8 km away to measure the speed of light [20]. The light was shone through the disk, travelled the 8 km to the mirror, returning along the same path until it was met by the rotating disk, before being viewed by an observer. The rotating disk would create a binary, square wave pulse train at the rotational frequency of the disk. When half of the rotational period of the disk is the same as the distance to the mirror over the speed of light, the reflected light will disappear. Since the distance to the mirror and rotational frequency of the disk is known, the speed of light can be calculated. Armand Fizeau was able to measure the speed of light to be 310.000 km/s, this was later improved by Jean Léon Foucault, using a rotating mirror rather than a rotating disk, measuring the speed of light to be 298.000 km/s.

Most laser rangefinders used today rely on shorter wavelength sources [21], as discussed in relation to the fast optical technologies above. However, when trying to range

a distance using optical methods atmospheric conditions must be considered. Generally, shorter wavelengths in the VIS and NIR are more affected by absorption and scattering than longer wavelengths [22]. This absorption and scattering occurs due to aerosols, debris and molecules in the atmosphere. Theoretically the use of longer wavelengths would lead to increasing the maximum possible distance a rangefinder could achieve.

This thesis and included research, aims to correct the issues discussed above by developing an all-optical modulator for the MWIR and LWIR which can be used on a Focal Plane Array (FPA) or a Single Pixel Detector (SPD). The second chapter will give an overview of previous research and the current, state-of-the-art hardware for IR modulation, detection and rangefinding. The third chapter will discuss the equipment used to carry out this research. The fourth chapter will cover the operating principles of the all-optical shutter, material choices for the modulator, and the required power to generate a change in transmission. The fifth chapter will cover the experiments carried out to test the feasibility of the all-optical shutter in both a FPA camera and a SPD. The technology developed in this work aims to offer a replacement for mechanical shutters, through combining all of the benefits of a mechanical shutter while still operating in an all-optical fashion. The sixth chapter will look at the possibilities of using MWIR for rangefinding using the ToF method with custom timing electronics, circuit design and benchmarking will be covered here. The final part of this thesis will review the findings of this research and suggest possible areas of future directions.

Chapter Two

Assessment of Current Infrared Technologies - Literature Review

The following chapter investigates and presents the current technology and research available with regards to Infrared (IR) technology. The first section considers advantages of using longer wavelengths in applications which require high transmission in the atmosphere. The second section covers IR modulators, both current and devices in development, as well as IR detectors, Focal Plane Arrays (FPAs) and cameras. Finally, rangefinding for long distances, and active imaging is discussed.

2.1 MWIR and LWIR

The Ultra Violet (UV) to Short-Wave Infrared (SWIR) is a well-developed, mature market; there is plenty of choice for detectors and sources available for a wide range of applications ranging from everyday uses to military purposes. SWIR is a perfect option for covert operations since it is invisible and eye-safe. There are options for fast rise time, high bandwidth detectors that make it suitable for active imaging. Near Infrared (NIR) and SWIR have also

found a home in fibre optics, wavelengths around the 1550 nm mark are commonly referred to as the telecommunication wavelengths.

However, Mid-Wave Infrared (MWIR) and Long-Wave Infrared (LWIR) could offer advantages over the shorter wavelengths with regards to applications where atmospheric transmission is vital, with the added benefit of being eye-safe [23]. These band edges vary in the literature [1, 24, 25]; for example, according to Vollmer and Möllman, the IR range covers 780 nm up to 1 mm [1]. In this thesis, the range of IR that is of interest spans from the NIR, starting at 780 nm, to the LWIR, ending at 14 μm . Contained within this is the SWIR, that spans 780 nm (which also contains the NIR) to 1.7 μm , the MWIR that goes from 1.7 μm to 5 μm , to the LWIR which spans 8 μm to 14 μm [1, p. 10].

The atmospheric scattering and absorption of photons reduces the throughput, maximum transmission range and clarity of an image or can make it impossible to observe a scene. These issues can be caused by weather conditions, from turbulence to fog (see Figure 2.1), or from particulates in the air [22]. The main mechanisms for scattering will be discussed next, including Rayleigh scattering, Mie scattering, and absorption due to vibrational modes of molecules in the atmosphere. Since this work focusses on thermal imaging and investigates the possibility of long distance rangefinding, it is important to consider how these scattering effects could affect MWIR and LWIR wavelengths.

2.1.1 Rayleigh

Rayleigh scattering, proposed in the 19th Century by Strutt, is a scattering theory most famously known for giving the sky its blue colour[26]. The scattering originates from molecules in the atmosphere, which has a far stronger effect on shorter wavelengths compared to longer wavelengths. The intensity of the scattering can be described using the following scattering

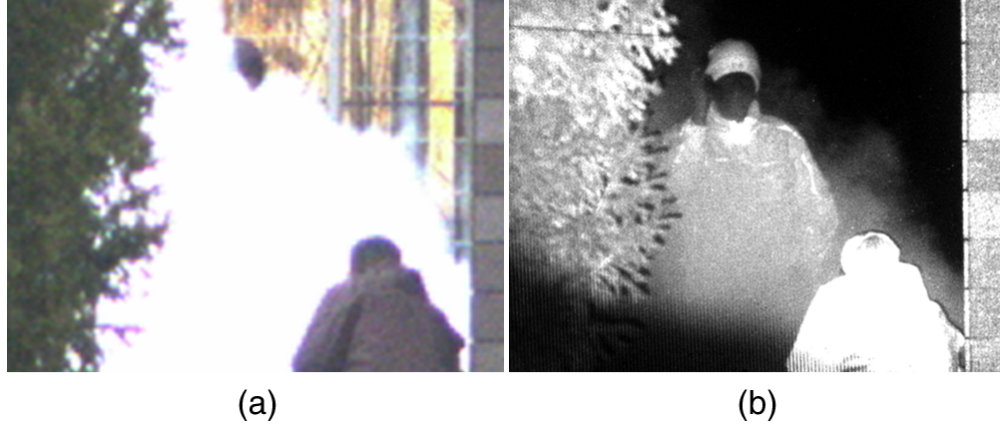


Figure 2.1: Use of SWIR system for imaging through fog. Visible image (a) shown against a SWIR (b). The person in the fog is only visible with the SWIR system. From [2].

phase function [27, p. 1120]:

$$P(\theta) = \frac{\lambda^2}{8\pi^2} \left(\frac{\pi D_p}{\lambda} \right)^6 \left| \frac{m^2 - 1}{m^2 + 2} \right|^2 (1 + \cos^2 \theta) F_0 \quad (2.1)$$

where λ is the wavelength, D_p is the diameter of the particle, m is the normalised refractive index $m = N/N_0$, where N is the refractive index of the particle, and N_0 is the refractive index of the surroundings, θ is the scattered angle and F_0 is the incident flux. If all but the wavelength is changed, a simple relationship can be devised: $I_{sca} \propto 1/\lambda^4$. This relative scattering intensity is plotted in Figure 2.2. When considering Rayleigh scattering, using a longer wavelength over Visible (VIS), and even SWIR, could show a significant improvement with regards to scattered intensity.

2.1.2 Mie

In contrast to Rayleigh scattering, Mie scattering is caused by larger particles in the air. These sorts of particles, otherwise known as aerosols, include dust, fog and debris, are on a much larger scale, typically $1\text{ }\mu\text{m}$ to $100\text{ }\mu\text{m}$. Mie scattering affects all wavelengths to some

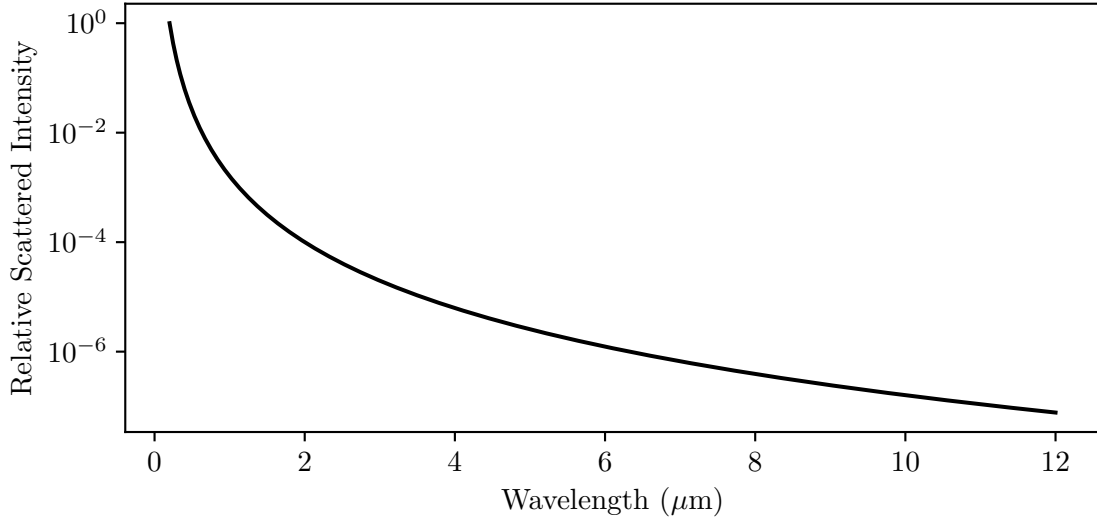


Figure 2.2: Relative scattered intensity against wavelength plotted from the relation $I_{sca} = 1/\lambda^4$.

degree and is the cause for the clouds appearing white. Mie scattering has been used in particle size analysis [28, 29]. To assess the potential implications of Mie scattering on MWIR and LWIR, there has been a significant investment in developing algorithms to determine the intensity of the scattering of different wavelengths. The effect of this can be significant, and is the primary reason SWIR is used over shorter wavelengths when conditions are poor. SWIR is commonly used for night vision and Range Gated Active Imaging (RGAI) covertly since it is invisible to the human eye [1, p. 500]. SWIR to LWIR also has a greater optical depth compared to shorter wavelengths when travelling through adverse weather conditions, such as fog and smoke, however these longer wavelengths will still struggle when it comes to imaging through rain and very dense fog [30, 31, 32].

While SWIR imaging does already offer an advantage over its shorter wave counterparts, it could be further improved by using longer wave radiation. Figure 2.3 shows the strength of absorption against the wavelength range for different H₂O particle sizes to mimic fog, and was calculated using the MiePython package [33]. It can be seen that the extinction

efficiency drastically falls away for particles with a radius less than 1 μm . However this is not the case for longer wavelengths around 3 μm . It should be kept in mind that this is for single particles only, particles clustered together are not considered in this case. The extinction efficiency, Q_{ext} , is defined with the following equation [34, p. 14]:

$$Q_{ext} = Q_{sca} + Q_{abs} \quad (2.2)$$

where Q_{sca} is the scattered efficiency and Q_{abs} is the absorbed efficiency. These efficiency factors are dimensionless, and follow the general equation:

$$Q_{sca} = \frac{C_{sca}}{\pi a^2} \quad Q_{abs} = \frac{C_{abs}}{\pi a^2}$$

where C_{sca} and C_{abs} is the scattering and absorption cross section, respectively, of the particle, and a is the radius of the particle [34, pp. 12, 14].

2.1.3 Molecular Absorption

When a photon passes through a gas, it could be absorbed, dependent on the energy levels of the molecules contained in the gas. This molecular absorption is commonly exploited in sensing for volatile and dangerous gases, where typically MWIR and LWIR sources are used. Some examples of gases that are sensed in this fashion include methane, carbon dioxide, ethane and carbon monoxide, however this is not an exhaustive list [37, 38, 39]. The use of gas sensing is an important safety tool in the gas processing industry, as it provides an early warning of gas leaks that could cause serious harm, as well as impacting on the environ-

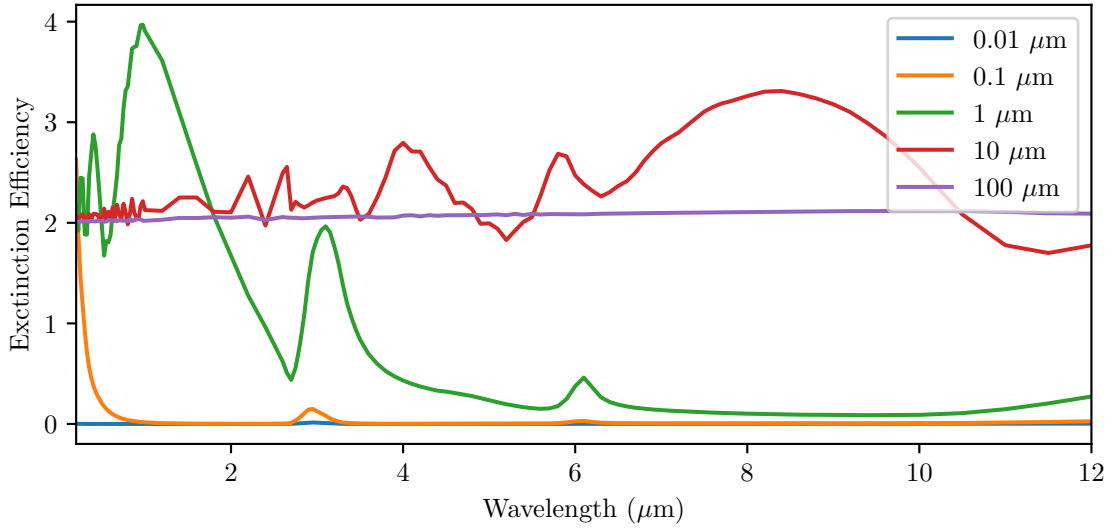


Figure 2.3: Calculated Mie-Lorentz scattering using the miepython package [33], with data from <https://RefractiveIndex.Info> [35, 36]. Extinction efficiency is plotted against photon wavelength for differing H₂O particle size to give an indication of performance in fog.

ment [1, p. 465][40]. There are numerous tools for computing the absorption of various gas molecules, however the one which will be focussed on in this work is the HITRAN database, coupled with version 1.2.2.0 of the HAPI API [41]. HITRAN is a database which includes absorption lines for gases found in the atmosphere, as well as numerous other parameters related to said molecules. The origin of the IR atmospheric transmission windows are predominately defined by the H₂O and CO₂ absorption lines. However, CO, CH₄, N₂O, O₃ and HDO also have a significant effect on IR[42, p. 40]. These molecules have strong absorption lines in the IR due to their molecular structure and chemical bonds between the atoms. The only real way to circumvent this issue, when maximum transmission is required, is to choose a source in the transmission window that is not significantly affected by the other molecules. If a suitable transmission window cannot be chosen, it is better to choose higher absorption in a less abundant gas. Figures 2.4 and 2.5 show the calculated absorption in the IR transmission windows for different molecules. From these figures you can clearly see the IR atmospheric windows produced by H₂O and CO₂. While there is significant absorption

from other molecules, in general their concentration in the atmosphere is much lower. From this data, any wavelengths in the H_2O atmospheric window will suffice, giving good atmospheric penetration, provided the particle size of water molecules stays on the micron scale as discussed in Section 2.1.2.

The effective atmospheric transmission window, combining the previously mentioned molecules, has been computed using the ATRAN model web interface [43] for SWIR to the LWIR, and can be seen in Figure 2.6. The transmission window has been calculated at altitudes of 100 m, 1 km and 10 km. It can be seen from this that as altitude increases, the absorption of IR reduces due to the decrease in the density of the air. Further to this, plots of the atmospheric transmission at varying horizontal path length and atmospheric conditions can be seen in Figure 2.7. Figure 2.7 (a) shows the transmission of SWIR to LWIR for horizontal path lengths of 1 km to 10 km in a midlatitude summer climate with a 1220 m visual range, with rural aerosols (particles size smaller than $1\text{ }\mu\text{m}$). Figure 2.7 (b) shows the transmission of SWIR to LWIR for horizontal path lengths of 0.1 km to 2 km in foggy conditions, where the visible range is 610 m. Both Figure 2.7 (a) and (b) were calculated using the MODTRAN model [1, p. 571]. From Figures 2.7 (a) and (b) it can be seen that longer wavelengths, apart from the absorption around $5\text{ }\mu\text{m}$ to $8\text{ }\mu\text{m}$, have good atmospheric penetration compared to the visible. It is worth noting however that the transmission of MWIR and LWIR in foggy conditions is highly dependent on the type of fog [1, p. 571].

2.2 Infrared Modulators

Optical modulators are a useful tool in the world of optics, both inside and outside of the laboratory. Optical modulators are used in numerous digital optical devices with commercial, medical and defence applications. Modulators are available in both electro-optical and

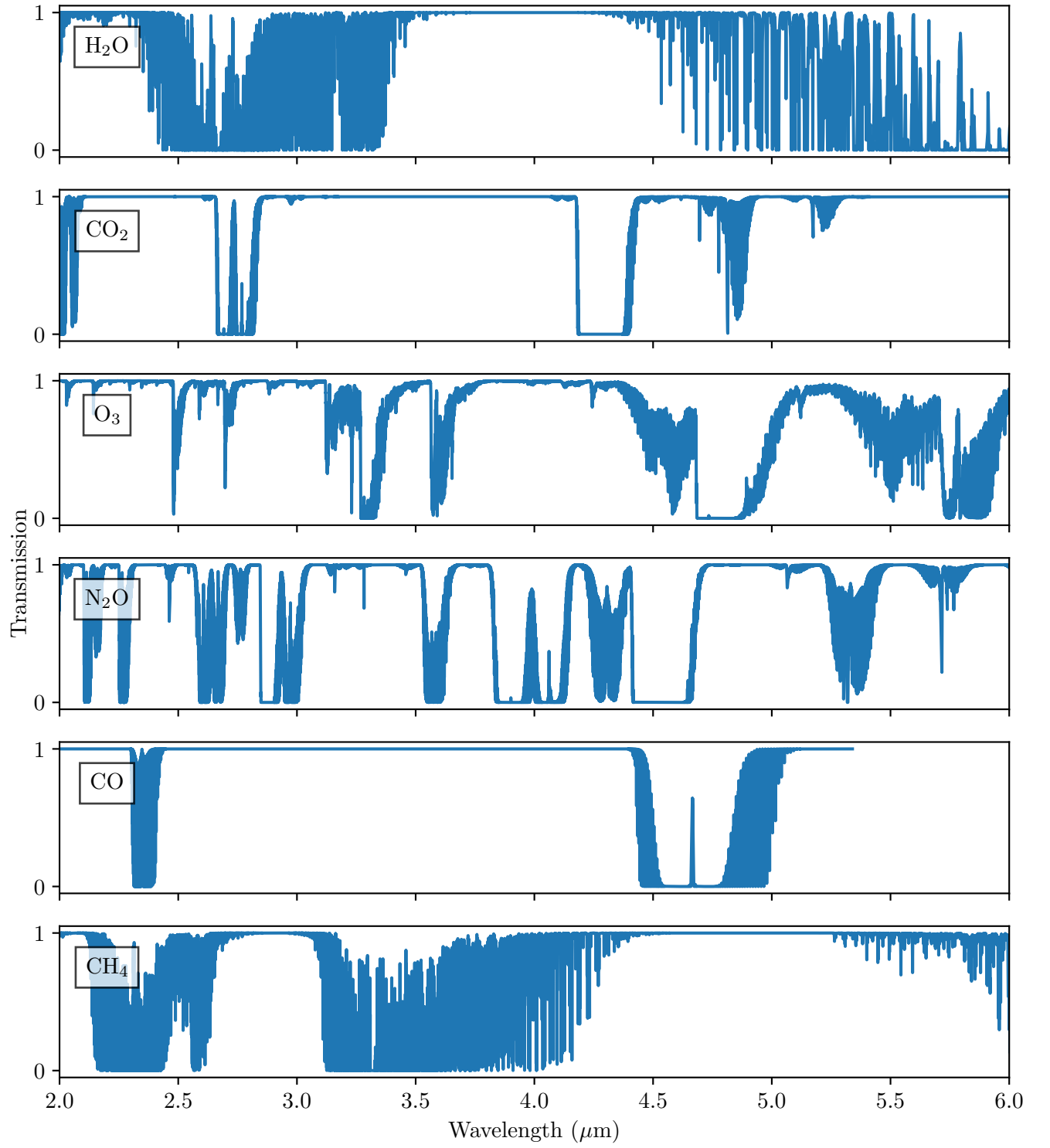


Figure 2.4: Calculated transmission for MWIR atmospheric transmission window. This was calculated using the HAPI API for the HITRAN Database, data from [41].

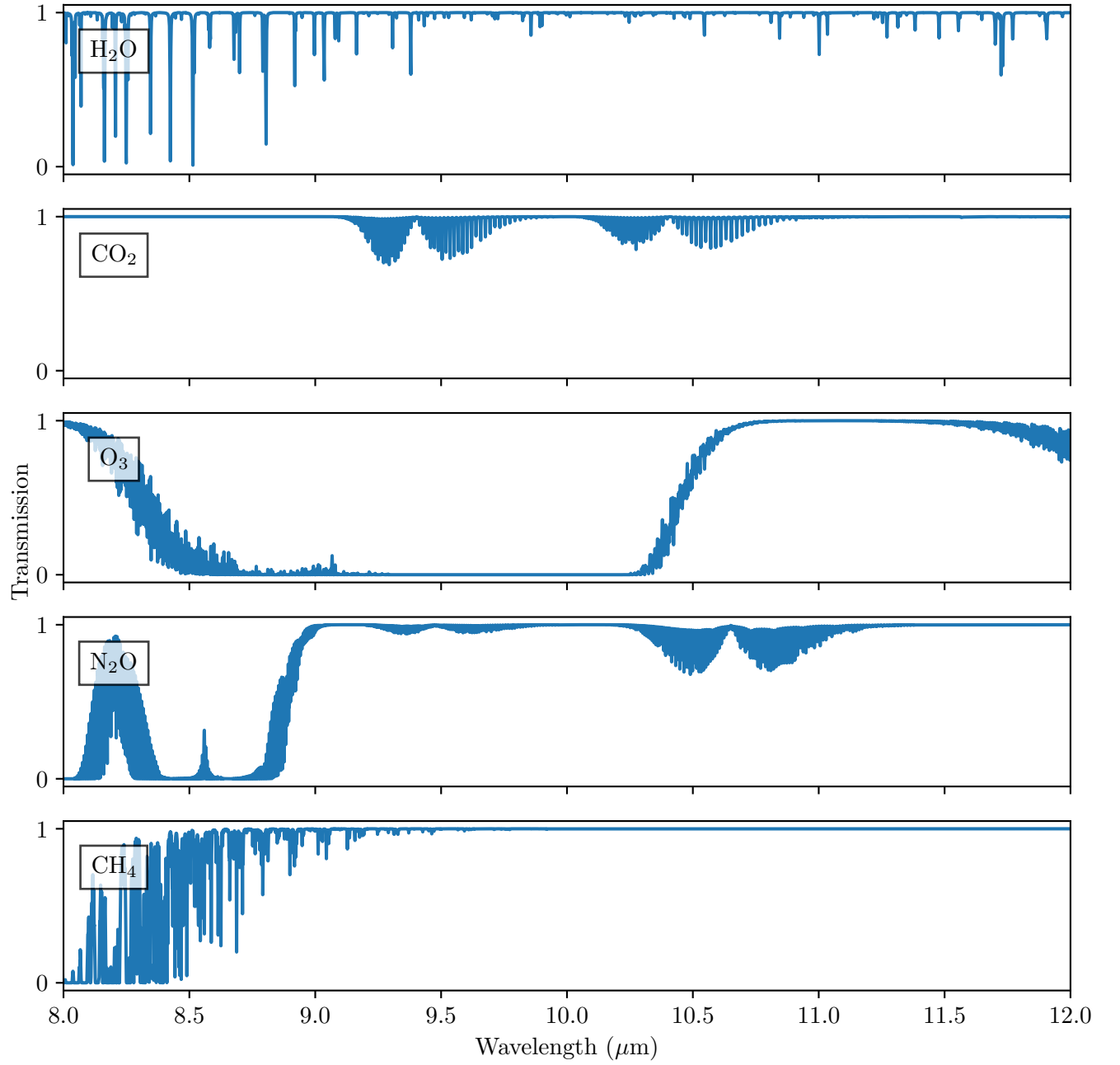


Figure 2.5: Calculated transmission for LWIR atmospheric transmission window. This was calculated using the HAPI API for the HITRAN Database, data from [41].

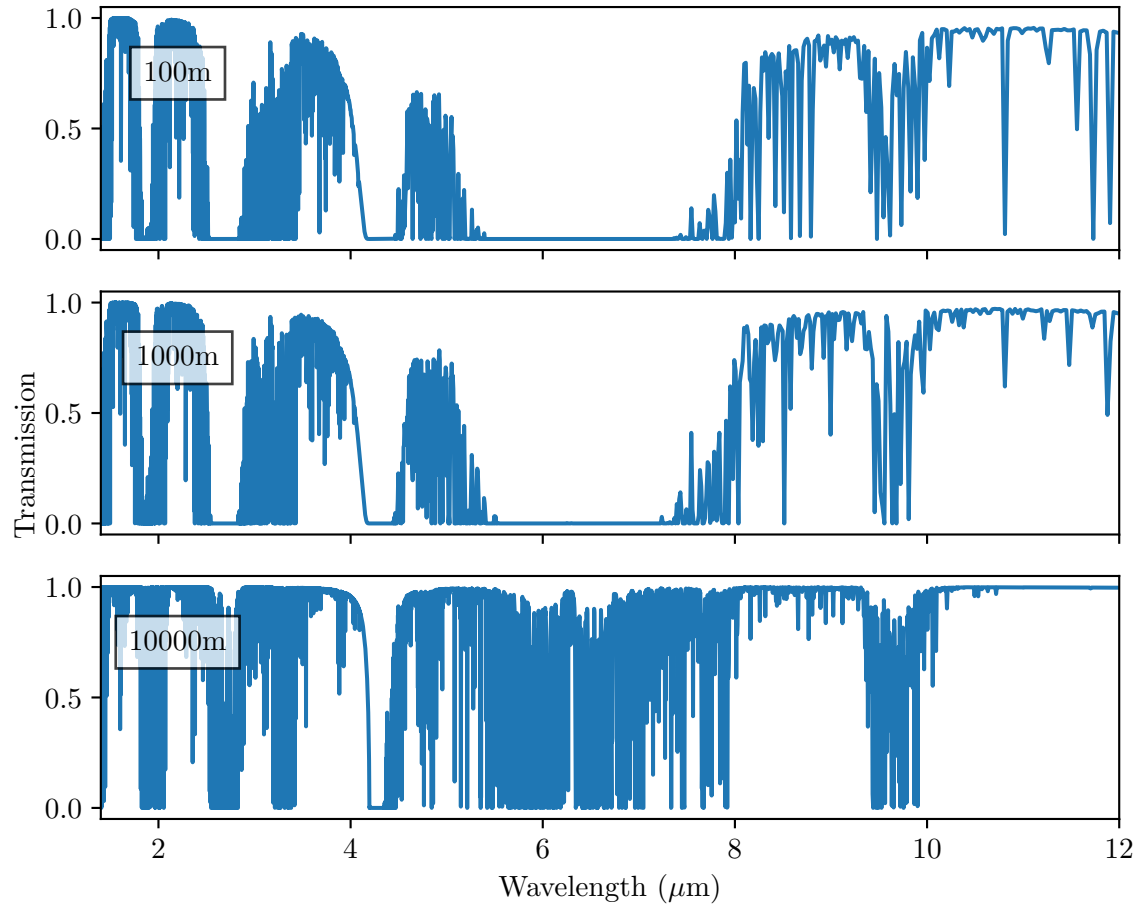


Figure 2.6: Calculated transmission for 1.4 μm to 12 μm using the ATRAN model [43] with a zenith angle of 0° at altitudes of 100 m, 1 km and 10 km respectively. This model uses the HITRAN 2000/2001 database to calculate the absorption of each molecule.

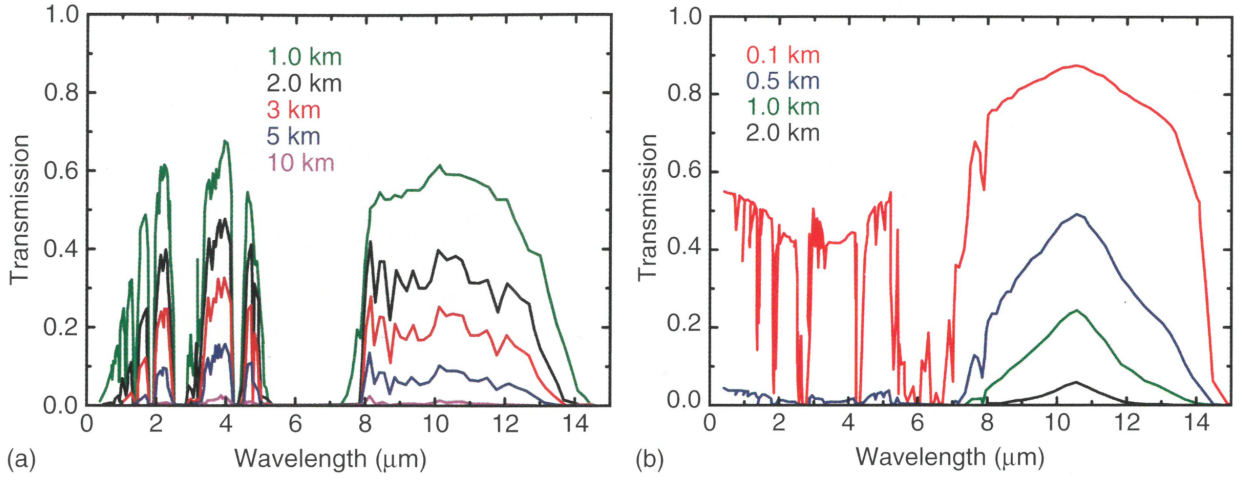


Figure 2.7: Transmission spectrum calculated using MODTRAN for rural aerosols midlatitude summer climate with a visual range of 1220 m shown in (a) (particle size $< 1 \mu\text{m}$), and midlatitude winter, foggy conditions, with a visual range of 610 m shown in (b). From [1, p. 571].

mechanical styles. Mechanical devices are often chosen for their simplicity, relative low cost, high contrast and high damage threshold. In contrast, if a high operating temporal bandwidth is required, electro-optical modulators are a more appropriate choice due to their solid state nature.

Common electro-optical modulators are Spatial Light Modulators (SLMs), which have seen multiple use cases. This includes Liquid Crystal Displays (LCDs) where the output brightness of pixels are controlled by adjusting the polarisation of light. Another use of SLMs is adjusting the phase of coherent light to produce interference patterns for use in real time holography [44], with commercial products appearing on the market with potential use in medical environments [45]. Optical modulators are common in fibre optic technology for transmitting data at high rates. While it is possible to modulate light sources directly, it also an option to modulate the light sources externally. This external modulation can lead to a higher performance when very short, defined changes in optical intensity are required. An example of this could be when data needs to be encoded in a carrier wave, or if one

source is used for multiple outputs [46]. A real world application of this would be communication between servers in datacentres, where high speed and low latency communication is required [47]. Other options for external modulation of light include Acousto-Optic Modulators (AOMs), which are commonly used in Q-Switched lasers for creating high energy pulses [48]. AOMs are able to change the direction of light travelling through them due to Bragg diffraction caused by travelling acoustic waves, while also adding a frequency change to the light. Mach-Zehnder Modulators allow for optical switches to be created in integrated photonic devices. They are able to modulate the amplitude of the light by splitting the light, adjusting the phase of one with respect to the other through the use of an electro-optical crystal, and recombining the two arms at the output. The bandwidth of these devices has been reported up to 70 GHz [13, 49, 50]. External modulation provides the option of sources, where a certain source may not be capable of fast turn-on and turn-off times necessary for high bandwidth applications.

In research laboratories, optical modulators can be key components in many optical setups including the generation of high power, short pulse length pulses. Pockels cells adjust the polarisation of light, and are key optics in the generation of ultrashort, high power pulses, due to their ability for a high modulation ratio and switching speed [51, 52]. Photoelastic Modulators (PEMs) are also an example of solid state modulators that affect polarisation. These devices operate in a similar fashion to AOMs, where a crystal is vibrated at a resonant frequency [12]. Polarisation based modulators could be effective for data transmission, allowing for beam steering through polarisation control coupled with silicon beam steering metasurfaces [53], allowing for bidirectional fibres coupled with polarisation maintaining fibres [54], or combining with SLMs to encrypt optical communication systems [46]. However polarisation devices fall short when the source is unpolarised such as for use in a camera system.

Modulators are not limited to only electro-optic and acousto-optic, there also exist

mechanical options, optical choppers are an example of this. A common sight in optical laboratories, optical choppers operate by periodically blocking the light source by rotating a disk with slits. While they are wavelength independent and offer a good contrast ratio, they have relatively low modulation frequency due to its mechanical component, frequently topping out at around 10 kHz due to mechanical stresses [55]. Microelectromechanical systems (MEMSs) reflectors, often called Digital Micromirror Devices (DMDs) are another mechanical modulator in the form of an array of tip-tilt mirrors for reflection modulation. Offering a high contrast ratio, these micro mirror devices can be manufactured to accommodate different wavelengths of light through selection of the reflector material. DMDs are spatial light modulators, and are fabricated as a plane array, allowing for images and patterns to be created. Due to the small physical size and weight of the individual reflectors, a high modulation frequency is possible. These devices can be found in projectors outside of the laboratory, and are also found in compressed and single pixel sensing [56].

The commercial availability of optical modulators for infrared is low in comparison to VIS and NIR modulators. Their lacking availability is primarily due to their niche uses outside of the consumer marketplace, which mostly include scientific research, sensing [57] and defence applications [58]. However, there are numerous areas where the use of infrared could offer some advantages. One such application suited to everyday life includes Optical Wireless Communication (OWC), where data is transmitted using free space optics, rather than with a fibre optic or copper conductors [59]. OWC has obvious benefits over using fibre optics or copper conductors due to not having to lay conduits underground for wires or suspend them in the air. Rabinovich et al. devised a method for an OWC between a ground station and an unmanned aerial vehicle. This technique for communication required only one laser located at the ground station [60]. To accomplish this, a corner cube retroreflector was attached to the unmanned aerial vehicle, with a Multiple Quantum Well (MQW) modulator in front of it. In the case of [60], the MQW modulator consisted of a 75 period structure of

alternating barriers (AlGaAs) and wells (InGaAs), with each layer measuring approximately 10 nm thick. This was sandwiched between an n and p type semiconductor, forming a p-i-n structure. Under an applied voltage, the structure would change its absorption for NIR light, allowing the unmanned aerial vehicle to modulate the incoming Continuous Wave (CW) laser beam and send data back to the ground station. The use of the corner cube ensures that the beam travels back towards the ground station. The temporal bandwidth of this system is limited by the RC time constant of the structure [60], in the case of this system they were able to transmit data at a rate of 1 Mbps [60].

Wavelengths in the MWIR and LWIR could prove to be excellent candidates for this application over UV, VIS or NIR. This advantage is due to atmospheric windows which lie in the MWIR and LWIR bands. The long wavelengths would also reduce scattering effects in the atmosphere, as discussed in Section 2.1.

2.3 Detection Technology

Development of MWIR and LWIR detectors has trailed that of VIS and SWIR significantly, mostly due to the cost of components and their perceived usefulness. Only recently have devices, such as thermal cameras, become available to the mass market. For instance, not only are there dedicated thermal cameras available on the consumer market, there are also thermal camera accessories that can be attached to mobile devices, such as the FLIR One. The FLIR lepton 3 module, that is used in the FLIR One, utilises an uncooled Vanadium Oxide (VOx) FPA microbolometer. The following will cover the various detection technologies that are available for IR.

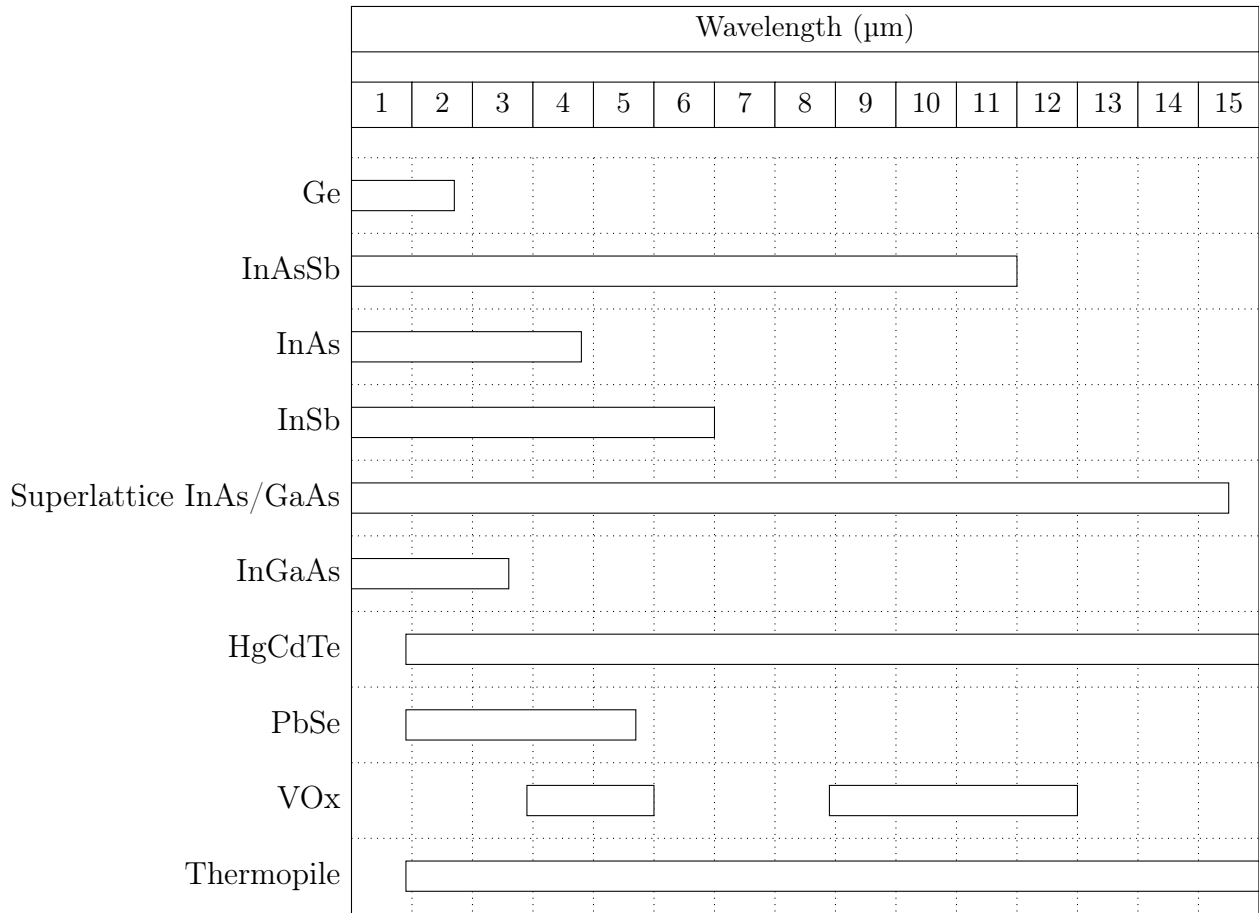


Figure 2.8: Detector technologies with their respective approximate optical bandwidths. Values gathered from what is available to purchase from a selection of vendors available at the time of writing (Thorlabs, Hamamatsu, Teldyne Judson, Laser Components as of 2022). Active cooling is required in some cases.

2.3.1 Thermopile

Thermopile detector technology exploits the Seebeck effect in two dissimilar metals to generate a varying voltage difference with temperature [61], as seen in Figure 2.9. A thermopile sensor can be visualised as multiple thermocouples joined in series, which provides a much higher voltage than a single thermocouple. Like microbolometers, these sensors tend to be slow, since they rely on the change in temperature of the sensor material itself, rather than

quantum effects that are seen in photodiodes. It is therefore of paramount importance to reduce the mass of these devices to reduce their response time. As thermopiles also rely on the absorption of photons to increase their temperature, it is important to select a material with a high absorption coefficient for the wavelengths required.

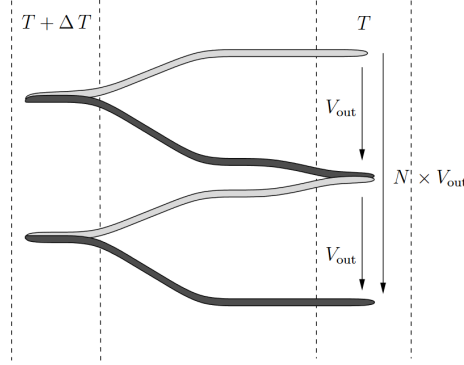


Figure 2.9: Illustration of a thermopile consisting of 2 thermocouples, represented by the grey and dark grey wires. The total voltage is proportional to the temperature $T + \Delta T$, and can be calculate by the number of thermocouples, N multiplied by each thermocouples voltage V_{out} . From [61].

Nevertheless, these slower technologies are commonly used in thermal cameras due to their lower cost and ease of fabrication. Common thermocouple materials used for thermopiles include bismuth-antimony and nickel-copper due to their high Seebeck coefficient [61].

2.3.2 Pyroelectric Detectors

Pyroelectric detectors differ greatly to thermopiles, rather than using the Seebeck effect, a pyroelectric detector uses a material that is heavily electrically polarised [62]. This material is usually ferroelectric with the electrical polarisation dependent on temperature change. When there is a change in temperature in the material, a change of voltage is induced across the device. This generated voltage fades with time, making it suitable only for pulsed light

applications. However, this has not stopped researchers developing cameras based on this technology [63, p. 1369]. This technology is commonly found in devices such as intruder alarms [63, p. 1367], where a person entering a static scene will generate a change in IR observed in the scene; optical fire alarms, where a fire will generate a sudden change in IR; gas sensing where a change in amplitude would signify the presence of a gas. This gas sensing method could be coupled with select wavelength lasers or a broadband source and bandpass filters to identify the gases detected [8].

Novel techniques for increasing the effectiveness of pyroelectric detector technology involve adding photonic structures to the surface of the detector to increase the coupling of radiation [64] for multigas sensing. Tan et al. [64] designed nanoantenna to help couple IR light into the detector, removing the need for bandpass filters. The nanoantenna are designed to efficiently couple certain wavelengths into the detector below, allowing to selectively measure wavelength intensities.

2.3.3 Micro Bolometer

Micro bolometers are a FPA device that, unlike conventional silicon FPA detectors you would find in common digital cameras, are able to photograph IR scenes. To accomplish this, the pixels of a micro bolometer are made of a material that readily absorbs IR light. These pixels must have a low heat capacity and show a strong thermoresistive dependence. Common materials include VOx and Amorphous Silicon (a-Si). At its core, the bolometer works by measuring a change in resistance induced from a change in temperature. This resistance change of the pixel can then be measured using Ohm's Law, before converting the resistance value to a temperature with use of a calibration curve. Invented in 1881 by Langley, the bolometer has seen rapid development since. The structure of a bolometer from top to bottom is outlined systematically and in detail next (see Figure 2.10 for a graphical

representation). At the top of the structure is a thin layer of conductive material. This layer should absorb the majority of the incident IR radiation to limit internal reflections. Not only would internal reflections limit the sensitivity of the device, reflections could also be detected on other pixels. This thin sensing layer is separated from the main substrate, with a reflector placed behind the sensing membrane. The distance between the sensing membrane and the reflective layer is approximately $\lambda/4$, where λ is the sensing wavelength, to form a resonant cavity. This resonant cavity increases absorption of the sensed wavelengths, increasing the sensitivity of the pixels. Separating the sensing membrane also reduces thermal conduction between the sensing membrane and the body of the camera. This suspension of the membrane is usually achieved with thin, stiff conductors. The sensing membrane can then be connected to a Read Out Integrated Circuit (ROIC) to measure the changes in resistance. Fabrication of these devices can be achieved by depositing layers of the photo-resistive material, and etching [66, 1].

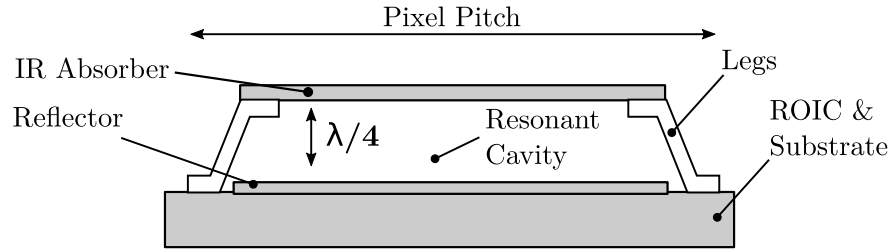


Figure 2.10: Illustration of microbolometer pixel. The sensing membrane is fixed $\lambda/4$ above the reflector, typically $2.5\ \mu\text{m}$, which forms the resonant cavity. This resonant cavity increases the efficiency of the absorber. The size of the absorber, including legs, dictates the pixel pitch. The ROIC in the substrate measures the resistance change of the microbolometer as it absorbs IR light.

To bring thermal sensors on par with their visible counterparts, there has been much focus on reduction in size of pixels [66]. The aim is to make the smallest possible sensor with the highest resolution, while at the same time maximising the active area of the pixel, otherwise known as the fill factor. Since the individual pixels need to be thermally isolated

from the main body of the camera, to ensure that only radiation from the scene affects the reading, there needs to be a structure that suspends the pixel above the substrate of the camera, and isolated both electrically and thermally, from neighbouring pixels. There have been numerous novel techniques for this, including umbrella structures. By supporting the structure underneath the active area, umbrella structures have been reported to achieve a fill factor above 92 % while maintaining a reasonable thermal time constant of 12 ms [67]. This is a challenging task for a number of reasons. To maintain a low thermal time constant the structure must be thin, yet not buckle under its own weight. In addition, to achieve a high fill factor and remain thermally isolated, most of the structure is unsupported [68].

Since bolometers essentially function by measuring an electrical change from their own change in temperature, there is a non-zero time constant for the material to reach the right temperature. For high speed application this is an important parameter to optimise. Recently there has been a push for introducing carbon nano-tubes into bolometers [69, 70]. Another direction for reducing the associated heating time constant is through the use of graphene sheets. Graphene is a tempting choice due to its atomic layer thickness which will aid in reducing the thermal constant of the bolometer. In a departure from conventional bolometry, one group was able to design and fabricate a bolometer that measured the resonant frequency of a graphene sheet. In this approach, the absorbed thermal radiation shifts the graphene sheet's resonant frequency away from its natural resonant frequency. This differs over traditional bolometry where the induced change in resistance of the graphene sheet would have been measured [71]. With this method, an operating bandwidth of up to 1 MHz was achieved, while also matching the sensitivity of other room temperature bolometer technologies. This method was implemented due to the lower thermosresistive effect of graphene.

Turning to a more conventional form of bolometry, one research group combined a graphene substrate with a photonic crystal. The photonic crystal was designed to efficiently

couple the incoming light, in this case SWIR, to the graphene substrate, increasing the induced electrical change. This provided a response time of 35 ps at cryogenic temperatures, although it was reported that the system could operate at room temperature with reduced sensitivity [72].

2.3.4 Mercury Cadmium Telluride

An early first generation photodiode infrared detection technology, HgCdTe, otherwise known as Mercury Cadmium Telluride (MCT), is a reliable, tested and widely used material for IR detection from the SWIR to LWIR [73, p. 296]. Commonly used at cryogenic temperatures with the use of liquid nitrogen, Thermoelectric Cooler (TEC) or a Stirling engine, it is a highly sensitive material, commonly with D^* rating in the high 1×10^9 Jones up to 1×10^{11} Jones [15]. The D^* rating is a figure of merit that quantifies the performance of thermal detectors, allowing for easier comparisons between different detector materials, areas and frequency bandwidths. The D^* rating can be related to the noise equivalent power by the following equation [1, p. 75]:

$$D_{\lambda}^* = \frac{\sqrt{A_D \Delta f}}{NEP_{\lambda}} \quad (2.3)$$

where A_D is the active area of the detector, Δf is the electrical bandwidth, and NEP_{λ} is the wavelength dependent noise equivalent power. Rise time for this detector technology ranges greatly from μ s to the low ns. Like other detector technologies, the rise time is highly dependent on the RC constant of the material, which is related to the detector area; reducing the active area of the detector will increase the bandwidth, at the expense of sensitivity. MCT detectors readily have a large optical bandwidth, and can be easily tuned during manufacture by adjusting the ratio of mercury to cadmium to achieve a peak

wavelength detectivity at a chosen wavelength.

2.3.4.1 Mercury Cadmium Telluride Avalanche Diodes

Currently, MCT avalanche photodiodes are under heavy development. As well as applications in high speed photonics, they are also being designed for use in astronomical imaging [74], Laser Detection and Ranging (LIDAR) [75, 76] and free space optical communications [77]. These detectors are generally lower noise than that of their visible counterparts, due to only electrons or holes initiating the multiplication, compared to holes and electrons in silicon and germanium Avalanche Photodiodes (APDs) [78].

2.3.5 Quantum Cascade Detector

An exciting detector technology on the horizon is Quantum Cascade Detector (QCD). First reported in 1987 by Levine et al. [79], researchers managed to design and fabricate a quantum cascade detector with an exceptionally high bandwidth, capable of rise time on the order of ps [79]. This detector technology works in a similar fashion to Quantum Cascade Lasers (QCLs), which are discussed in detail in Chapter 3. In brief, rather than relying on bandgaps of materials, the response of a QCD originates from the structure of the device itself. This structure consists of layers of alternating material; in the case of the work carried out by Levine et al., layers of GaAs/ $\text{Al}_x\text{Ga}_{1-x}\text{As}$. On absorption of a photon, electrons are excited via intersubband transitions to higher energy levels. The alternating layers of GaAs and $\text{Al}_x\text{Ga}_{1-x}$ form quantum wells, allowing electrons to tunnel from high energy levels in one well to lower ones in the second well. Usually in a period there are several quantum wells, however, these periods can be repeated to generate higher potential differences across the entire structure. These devices can be cryogenically cooled, with high D^* ratings of 7×10^9 Jones at a temperature of 50 K [80], although it is not a requirement. Hamamatsu have

reported on a room temperature QCD [81], at the expense of losing two orders of magnitude in its D^* value. The rise time of this detector was not explicitly mentioned in the article, but the recently released Hamamatsu P16309-01 was probably related to the QCD in this paper. This recently released detector offers a bandwidth of up to 20 GHz in the MWIR while operating at room temperature [82].

2.3.6 Indium Arsenide Antimonide

Suitable for the detection of MWIR and LWIR photons, InAsSb photovoltaic detectors offer an alternative to HgCdTe detectors. InAsSb detectors are available in cooled and uncooled versions. Uncooled detectors are an advantage for portable devices, but cooling will improve the D^* rating and extend the optical bandwidth. These devices have the added benefit of not including hazardous materials in the form of heavy metals, making them more suitable for consumer devices. InAsSb detectors have a high bandwidth, compared to that of HgCdTe when sensor size is similar, yet they lack the sensitivity provided by HgCdTe [83].

2.4 Thermal Imaging

Thermal cameras make use of the aforementioned detector technologies, in most cases, as FPAs to generate 2D images. Similar to conventional visible cameras, thermal cameras consist of a FPA with an optical system that focuses light onto the sensor. Shutters can be included for maintaining accurate readouts from the sensor through the application of Non-Uniform Calibration (NUC), as well as providing physical protection in cases of extreme thermal radiation, but are not necessary. ROIC and Digital Signal Processing (DSP) circuits are required for consolidating the information from the sensor to generate the images.

2.4.1 Non-uniformity Correction

The process of thermal imaging depends on the material used for the sensor, which come under the two categories of quantum devices and temperature change devices. Generally, quantum devices are used when a higher speed and sensitivity is required, while temperature change devices are more suitable for cheaper devices. The use of temperature change devices aids in keeping manufacturing costs down and decreases the need for exotic materials. Nevertheless, both systems rely on a NUC to generate accurate thermal images [84]. The importance of applying a NUC periodically is shown in Figure 2.11.

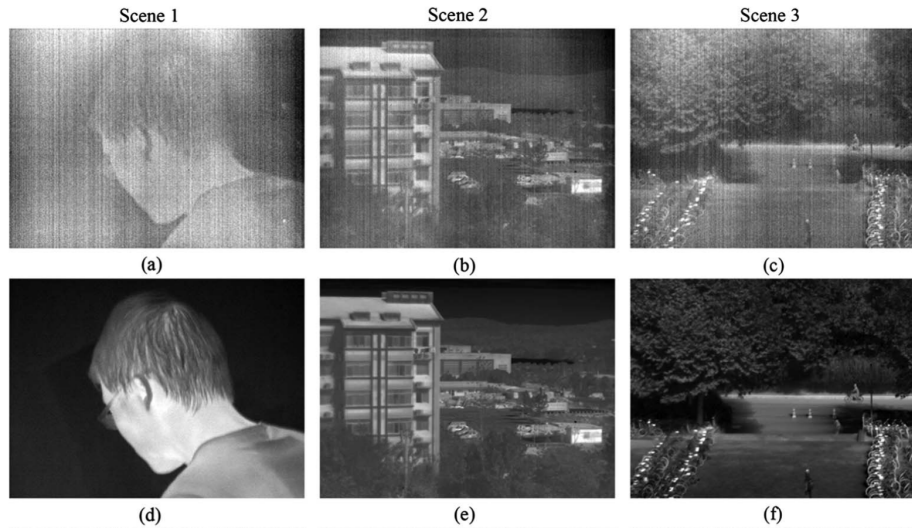


Figure 2.11: Shown from a) to c) are images from an uncooled thermal camera without a NUC applied, d) through f) shows the same images after using the minimizing the sum of the squares of errors (MSSE) algorithm. From [9].

During the operating cycle of a thermal camera, the camera body itself, including the sensor, will fluctuate. The increase in temperature is hard to avoid, and even when the sensor is actively cooled, the temperature of the camera housing (including lenses and mounts) can change. Left unchecked, this change in temperature is detrimental to the ability of the system to generate an image, either giving false values for measured temperatures in the scene, or a reduction in contrast, making it difficult to identify objects in the scene.

Due to manufacturing inconsistencies, all pixels will have a slightly different gain and report varying signals when illuminated with the same radiation. The process of a NUC aims to reduce the effect of self heating and gain inconsistencies by recalibrating the output of each pixel in the sensor. A correction for each pixel gain and offset is usually established when the camera is manufactured by placing a uniform grey blackbody source in front of the camera, and recording the value of each pixel at various temperatures. This calibration can then provide each pixel response, and how it differs between other pixels on the FPA [1, p. 108]. However, calibration does not always solve the issue entirely, as thermal cameras are mostly used for imaging non-uniform scenes.

For calibration, a uniform scene is required [84]. This uniform scene can be provided by a mechanical shutter to periodically block the sensor. This allows the camera to image a material of known temperature and uniformity. The camera can then calibrate the pixels output and correct for any drift, using the pre-calibrated values. The NUC is carried out periodically, with the time between each subsequent NUC dependent on the ambient and scene temperature. However, this process of periodically blocking the sensor is not ideal, even fast mechanical shutters will interrupt the imaging of the scene which is not acceptable in some use cases.

To solve the issues outlined above, shutterless NUC technology has been developed. This technology enables correction of the sensor while not interrupting the output of the sensor. A few manufacturers offer this including Thermoteknix and FLIR. The algorithms for NUC are commercially sensitive, however there is published research on the topic [85, 86, 9, 87]. There are several techniques that can be used to conduct a NUC including scene correction, where moving elements in the scene provide the required information to calibrate the sensor output; single-point to multi-point NUC correction, where a known reference, like a shutter or a known heat source [88], is used to perform a NUC.

2.4.2 Shutter Technology

As mentioned in the previous section, mechanical shutters are one of the potential solutions used for carrying out a NUC. In addition, mechanical shutters also provide other functions which include physical protection, and can also provide relief to over-exposure from intense radiation [11]. That is not to say they are without fault, as shutters are mechanical devices that are susceptible to damage, wear and tear, and have a limited speed, due to their mechanical nature. Shutterless technology has enabled cameras to carry out a NUC, however, it does not offer any protection to the sensor. Some research has been carried out into semi-transparent shutter technology, which allows for uninterrupted imaging while still maintaining a physical shutter [88]. However this technology does still require moving parts. In cases of security and defence, thermal imagers are sensitive to intense sources of infrared such as MWIR and LWIR lasers, and the current choice is between a mechanical shutter or a shutterless one. As outlined above, a mechanical shutter is able to provide protection to the sensor but lacks the responsivity required for a high repetition pulsed laser attack; whereas, the shutterless technology described above does not offer the sensor protection needed when using high powered sources in these applications. Therefore, one of the primary topics of this thesis is an investigation into a solid state shutter for infrared imaging, which could be used not only for protection and NUC, but also as a variable Neutral Density (ND) filter.

2.5 Rangefinding

There are two methods for measuring distance using lasers, the first being the phase shift method, the second being Time of Flight (ToF). While these methods both use photons to measure distance, and are both capable of achieving mm resolution, they operate in significantly different fashions. These two methods will be discussed in detail below, with

examples of what can be purchased today, and where the technology is heading. Generally, the ToF method has greater overall range, as it does not suffer a 2π phase ambiguity, however the phase shift method offers a higher precision. The detail of these two methods will be explored in the following sections. While they are two distinct methods, this has not stopped researchers attempting to combine the two methodologies.

2.5.1 Phase Shift Method

To measure distances using the phase shift method a CW laser is used. In its most basic form, this method uses a laser that is modulated so it has a sinusoidal amplitude at a set frequency. It is coupled with a detection system which allows for the analysis of the phase. By outputting a sinusoidal laser signal, any target that the laser is directed at will reflect the same sinusoidal pattern. By measuring and analysing the reflected signal, and comparing it to that of the phase of the source signal, the relative phase difference can be obtained. The distance between the target and source can then be calculated as a function of the phase difference using the following equation [89]:

$$Distance = \frac{c\Phi}{4\pi f} \quad (2.4)$$

where c is the speed of light in the transmission region, Φ is the phase difference in radians, and f is the laser modulation frequency. While this is an accurate measurement technique, without multiple frequencies being utilized, once the distance to the target and back grows over $c/(2f)$ the distance become ambiguous [90]. This ambiguity is one of the primary drawbacks of using the phase shift method for long distance rangefinding. One solution for overcoming this drawback is to use multiple modulation frequencies, calculating the phase difference for each frequency, before finally finding a distance that satisfies the

multiple phase differences for each frequency [91]. The phase shift method should not be confused with interferometry range finding, which uses phase shifts between the phase of the photon's oscillations. This method is commonly used in handheld devices over the ToF method since it provides a fast and accurate measurement. Complex systems, such as Lock-in Amplifier (LIA), can be implemented using microprocessors [92]. These systems can be used to remove any noise from the environment which may swamp the signal.

A novel approach to circumventing the 2π drawback proposed by Yang et al. is to add a Radio Frequency (RF) modulation to the falling edge of a laser pulse [19]. Briefly, the experimental set up consists of a laser source, beamsplitter, two PIN photodiodes (one for the reference pulse, one for the signal pulse), retroreflector, and measurement electronics. The electronics are responsible for locating the leading edge of the two pulses in order to provide the ToF measurement. The waveform itself was sampled to measure the modulated falling edge of the two signals as well. The phase difference between the reference and signal can then be extracted from the recorded data. The ToF method gives a rough estimate of the distance, solving the ambiguity a pure phase shift method would introduce. Simultaneously, the phase difference still provides the accuracy that is associated with phase shift measurements. This system was used to measure the movement of the retroreflector on a translation stage, with the results showing a marked improvement over using only ToF [19]. It is worth remembering that this system requires compute power to calculate the cross correlation between the reference and signal pulses to calculate the phase difference. As well as this, dispersion caused by the medium will affect the returning pulse modulation frequency. This change would also have to be compensated for in the software, adding to complexity and the compute power required.

Heterodyne detection, where the signal is mixed with a local oscillator, can also be used to improve the signal to noise ratio and the overall accuracy of the system, especially in low light conditions [93], while also reducing noise induced from external illumination

such as solar radiation [94]. The process developed by Lerou, Journet and Bazin, Dupuy, Lescure, and Tap-B teille, Castagnet involves mixing a local oscillator signal with the electrical reference signal of the radio frequency modulation of a continuous laser [95, 90, 93, 96]. The reflected signal from the target is measured using an APD while simultaneously mixing the local oscillator signal electrically to produce a beating signal in the APD output. After passing both the electrical signals from the laser reference and APD through a low pass filter the phase is compared. The intermediate frequency can then be related to the following equation:

$$f_{if} = \frac{2\Delta f}{T_r} \frac{2D}{c} \quad (2.5)$$

where f_{if} is the intermediate frequency, ΔF is the frequencies swept by the VCO, T_r is the time taken for the Voltage Controlled Oscillator (VCO) to do the sweep, D is the distance to the object and c is the speed of light.

2.5.2 Time of Flight Method

The ToF method measures the time that is taken for a photon to leave the source (the start signal) reflect off the target, and return to the detector (the stop signal) [97]. This process can approach the accuracy of the phase shift method and is predominantly used for rangefinding over longer distances, as it overcomes the limitation of phase ambiguity that is found in the phase shift method. In contrast to the phase shift method, the ToF method uses pulses of light, usually with a very short duty cycle. This allows for a high peak power to be used, theoretically increasing the maximum distance before atmospheric attenuation becomes too great, or if a target is less cooperative. To achieve a high accuracy with this process, a very sharp optical rise time is required from the source, and while it is possible to circumvent

this, a fast detector is also ideal. Another issue to consider is the trigger point for the stop signal from the detector. While this may be less of an issue (depending on the application and the resolution required) for a fast rise time detector, this can become a large source of uncertainty for slow detectors. Most commercial ToF devices for rangefinding over a greater distance use NIR and SWIR sources due to the mature technology. These can be purchased as Integrated Circuits (ICs), such as the VL53L0X manufactured by STElectronics, which uses 940 nm laser source and silicon Single Pixel Avalanche Diode (SPAD), or as prebuilt devices, such as the FLIR MLR10K-LX which is able to range up to 16 km using 1535 nm.

The absolute accuracy of most commercial options tops out at cm precision, however inside the laboratory, this accuracy has been pushed to beyond that to the μm [98] and even nm resolution [99]. To achieve nm resolution, optical cross correlation was employed using a femtosecond laser in tandem with a Periodically-Poled Potassium Titanyl Phosphate (PP-KTP) nonlinear crystal. A modelocked femtosecond fibre laser pulse provides the source for the system. This beam is split to create a reference, used later for timing, and a signal pulse, which is directed towards the target for measurement. These two pulses are in orthogonal polarisations. After the signal returns from the scene, the reference and signal are recombined and passed through a PPKTP nonlinear crystal. When temporally overlapped, a pulse is created in the PPKTP crystal. To measure the path length the signal pulse travels, the reference and signal pulse pair travel through the PPKTP twice. These pulses are summed on a balanced detector, and provided the temporal separation between the orthogonal signal and references pulses is correct, generate a bipolar pulse. By monitoring the output of the balanced detector and adjusting the repetition of the frequency of the fibre laser, the researchers were able to measure amplitude modulation of a piezoelectric mirror on the order of 150 nm at a range of 700 m [99].

Moving from high resolution to long distance, it has been reported that a range of 17 km was achieved through the use of multiple signal wavelengths ranging from 630 nm to

975 nm [21]. A group of SPADs, coupled with a Time to Digital Converter (TDC) were used to record the time taken from the signal lasers to travel to the target and return [21]. This system has the benefit of confirming whether the returned signal is true, if for example, only one detector was triggered, this result could be assumed a false trigger caused from the environment. The one downside of this system does appear to be its size; this system has three main parts including a 200 mm diameter telescope, optical routing module and collection electronics. For accurate timing, this system utilises a TDC coupled with a Constant Fraction Discriminator (CFD); both of which are discussed further in Chapter 3. This system appears to allow for a resolution of approximately 30 cm, however it should be noted that the long range measurements were taken with a corner cube as the reflector, rather than off a realistic target. The system also relies on clever arming to reduce the stray counts. Enabling the timing systems for short windows reduces the stray counts significantly by an order of magnitude, generating a higher contrast. This does however require some prior knowledge of the scene to make sure the enabling window is at the correct time. It should also be noted that to keep the system eye-safe, the output power had to be kept low due to the shorter wavelengths used.

3D depth imaging has also been investigated with ranges of up to 10 km being reported [100, 101] and more recently from 45 km [102] to 200 km [103]. These publications used telecommunication wavelengths around 1550 nm, coupled with telescopes for beam expansion and collection, and SPADs for detection. These processes, especially for the longer ranges of 45 km and 200 km, rely heavily on complex algorithms for resolving the image due to the exceptionally low return photon count. For example, in the paper [103], it was reported that the image was created, with on average, less than one photon per pixel. The amount of time required to create such images at these ranges also involved a long acquisition and processing time, upwards of 15 minutes per 320x512 pixel image (rate of 189.7 ms per pixel). While the performance of these systems is impressive, and the long exposures required are

acceptable for static scenes, such as the mountain range imaged in their experiment, this setup is not suitable for fast moving scenes. These systems also rely on cooled SPADs for their high resolution, which adds to the power consumption of the system, making them unsuitable for portable systems.

Interferometry is one solution for obtaining extremely precise resolution measurement. One research group have pushed this further, and have devised a method for potential use for long range distance measurements of up to 30 km [104]. To accomplish this, two frequency combs were employed, with one at a marginally different frequency to the other. One, called the signal, first passed through a semi-transparent mirror before being reflected by a second mirror. This second mirror then reflected the remaining signal. These two reflections were combined with the second frequency comb, known as the local oscillator. By sampling the detector at each local oscillator pulse an image of the signal pulses could be built up, since the local oscillator pulse drifted with time with respect to the signal. The time between these pulses could then be found, which is the ToF.

2.5.3 Infrared Ranging

The use of IR in ranging applications is a relatively new idea, but it is mainly limited to the SWIR due to technological and cost restrictions. Devices like active imaging, ToF rangefinders and cameras, have had extensive use in civil [18, 105], military [106, p. 82], security and defence applications. This technology has only just started entering the consumer market with some examples of usage in cars for autonomous driving [17], high end smartphones for augmented reality applications [107] and games consoles [108], to name but a few. Many of these systems rely on fast FPAs or Single Pixel Detectors (SPDs) to record the timing information precisely, or intensive DSP to produce results. There have been some trials using CO₂ lasers and lead-tin-telluride detectors for ranging [109], where targets

were measured at a range of 5 km with an accuracy of 5 m.

2.6 Range Gated Active Imaging (RGAI)

RGAI offers clear advantages over passive imaging. Not only does it allow for optical depth isolation of elements in the scene, it also overcomes issues with backscattered light, and provides lighting for the scene in dark environments. An example of RGAi can be seen in Figure 2.12. Commonly used in countermeasure and defence settings, RGAi also has the potential to be used for autonomous driving [110], search and rescue [111]. SWIR is a commonly used wavelength for these systems. As mentioned previously, there is an abundance of detectors and sources at the SWIR wavelength range, but it is also invisible to the naked eye, making it ideal for military and defence uses [1, p. 500]. This particular wavelength range is also effective as it has reasonably good atmospheric penetration, as well as minimal scattering from aerosols. There is however a requirement for well defined illuminator pulses and fast gated detectors [112].



Figure 2.12: SWIR passive (a) and SWIR gated imaging system (b) images at a range of 480m. This technology allows for isolating elements of a scene and the improvement in clarity due to reduction in backscattered photons. From [2].

RGAI systems work by emitting a short pulse of laser light towards a target. As the

light is travelling some will be backscattered, as well as being absorbed. This backscattered light can pose significant issues for conventional cameras as all the scattered light will be recorded, obscuring the point of interest of the scene [2]. This is where the gating aspect of the system is employed. Instead of recording the entirety of the scene, the optical sensor will only be active for a short period at a predefined point after the illumination laser is fired. The delay between the laser illumination pulse and the sensor becoming active will define the observed range, while the viewing depth is defined by the time the sensor is enabled for. The amount of time the sensor is active for can be lengthened to include more of the scene, or shortened, to focus in on particular objects. As well as reducing backscatter from the scene, a 3D image can also be created. A 3D scene is achieved by scanning the delay between the illumination pulse and enabling the sensor, and then finally building up the slices [2].

Having short laser pulses and fast rise detectors is a straightforward way of increasing the accuracy of an RGAI system. However, both are not necessary and can increase the computing cost, size and energy draw of the system. Since these systems are commonly used in portable devices, these traits are not desired. Research has been carried out to reduce the effect of this, one research group managed to achieve a depth accuracy of 30 m over a range of 900 m, while only using three exposures [113]. To accomplish this the intensity response of the system needs to be known. This includes how the camera sensor responsiveness varies as it is turned on and off while being illuminated by the laser, since the recorded image is a convolution of the camera and laser. The gate delay of the camera was then shifted so that there was overlap between each exposure. For this technique to work, it is vital that there is overlap between the exposures, as this is how the depth resolution is recovered. In the system described in the paper [113], the intensity response of the imaging system is a trapezoid, with the centre plateau the same width as the rising and falling edges. The three exposures were separated in time such that the rising edge of second pulse occurred at the same time as the plateau of the first pulse. By comparing the intensities of the two

neighbouring exposures, the depth could be extracted.

Hybrid imaging, such as combining active gated-imaging and MWIR-imaging have also been investigated [114]. To accomplish this the use of a $1.5\text{ }\mu\text{m}$ laser source was employed for the illumination source for the active imaging aspect. To complement this, an MCT Electron Injection Avalanche Photodiode (e-APD) FPA, with a resolution of 128×128 pixels was developed that was sensitive to both MWIR radiation and the source $1.5\text{ }\mu\text{m}$ source. This allows for both a passive and active imaging mode. The results presented by Beck et al.[114] show a promising result, resolving features at a range of approximately 9 km. While this system does not rely on MWIR for illumination purposes, it does show that MCT operated in an e-APD fashion is capable of ns operation time. However, one of the main downsides of this system is size and energy consumption, and although it is not mentioned, it is safe to assume that the cost of a system like this would be significant. The MCT detector used in this work is a large area FPA, which are costly and require active cooling. The paper mentions an operating temperature of 77 K, compared to an uncooled detector, this will take a non-zero amount of energy to keep cool.

Pushing the idea further, Matwyschuk has developed a system where multiple wavelengths are used [115]. This particular implementation induces a time difference between the wavelengths generated through the use of a rotating filter wheel coupled with a broadband source. The rotational frequency of the wheel sets the time difference between pulses. The article proposes three main operating modes: non-gated operation, where the camera records everything; gated operation, where the camera is triggered after every wavelength change; and gated imaging where the camera is triggered after all wavelengths have been emitted. The third technique should give the most reliable result, as Matwyschuk mentions that it does not suffer from picking up secondary reflections. By operating their system in this way, Matwyschuk is able to recover velocity information, even if the paths are random. This is possible due to the operator selecting and knowing the order of the filters that generate the

various wavelengths. Since the frequency of the change of wavelength is known, the velocity can be found by measuring the distance travelled between the objects when exposed with the different wavelengths. This system could be converted to an IR system, since detector technologies with wide optical bandwidths exist.

However, there are few reported attempts of pushing RGAI beyond the SWIR. One article from 1976 recorded an attempt at constructing a CO₂ laser based RGAI system [116]. The results from this experiment looked promising considering the technology available at the time: the range of objects, including a truck and some wires, was determined with a gate width of 22.5 m, easily isolating elements of the scene. However, the system itself had a several drawbacks, not least its size. However, modern equipment, such as the QCL, would help significantly in the reduction in the size of the system. The absolute range of the system was not covered in the article. However, Courtenay, Boulter, and Henshall does report testing with a corner cube up to a range of 6.4 km, but no RGAI was reported on at this range [116].

In conclusion, MWIR and LWIR have the potential to offer an improvement in performance compared to shorter wavelength devices where atmospheric transmission is key. However, to maximise the performance due to the sub-par speed of the majority of current generation IR detectors, optical modulators for the IR are required. The development of a variable all-optical ND filter, or shutter, would be beneficial for both laboratory use, as well as improving thermal camera protection and responsivity through gating. This technology could be pushed to allow for long distance rangefinding, as well as active imaging.

Chapter Three

System Operations

This chapter will cover the systems and equipment used in this thesis, including their fundamental operations, and how they are operated. The following sections will cover any notable electronic designs that have been custom-made for the project. The experimental research contained in this thesis has been produced using a combination of lasers and specialised electronics. This equipment includes a Coherent femtosecond laser system, followed by a Optical Parametric Amplifier (OPA); a small diode laser bar and Quantum Cascade Lasers (QCLs); Mercury Cadmium Tellurides (MCTs) detectors and custom electronics.

There are two main experimental setups discussed in this project. The femtosecond system is used when the utmost temporal resolution and energy is required. These qualities of the system are useful for investigating charge carrier dynamics, a key component to the solid state shutter technology that will be discussed in Chapter 4. In this project, the femtosecond system has also been used to establish the maximum performance of the solid state shutter technology, giving a target to achieve with the breadboard system. The OPA integrated into this system enables the possibility of exploring the shutter technology over a greater range of wavelengths, rather than limiting the research to the fixed wavelength QCLs diodes that are used in the breadboard system.

The smaller breadboard system is focussed on turning what is found in the femtosecond system into applications that can be used in the real world. Overall the breadboard set up is a much smaller system, consisting of Mid-Wave Infrared (MWIR) and Long-Wave Infrared (LWIR) QCLs, and solid state Near Infrared (NIR) diode lasers. While this system lacks the temporal accuracy of the femtosecond system, it is still capable of delivering high optical power on the nanosecond scale. This system assesses the feasibility of shrinking the findings of the femtosecond system and finding potential applications for the technology developed. These applications include optical modulators for Infrared (IR), which has been pushed further to a high-speed all optical shutter for LWIR thermal cameras. The breadboard system has also been used to investigate the feasibility of a MWIR and LWIR rangefinder. The MWIR system had a greater focus on electronic signal processing to establish accurate timing, and thus, distance measurements.

3.1 Femtosecond Laser System

The femtosecond laser system is able to deliver watts of average power at 1 kHz in sub-100 fs pulses centred around 800 nm. The high power, short pulse duration source can then be used by the OPA to generate Visible (VIS), Short-Wave Infrared (SWIR) or MWIR light. This system is used when the highest level of temporal accuracy is required in measurements. This accuracy is required for the primary experiments conducted, including investigations into the carrier dynamics of bulk, macro-porous structured and nanoscale structured semiconductors, as well as hybrid materials such as gold impregnated silicon. A popular method for understanding carrier dynamics is the pump-probe experiment. In this experiment, a material is excited with the pump pulse, and the evolution of the excited state of the sample is recorded by the probe pulse, as the time between the pump and probe changes. The arrival time of the two pulses on the surface of the sample is controlled by a mechanical stage

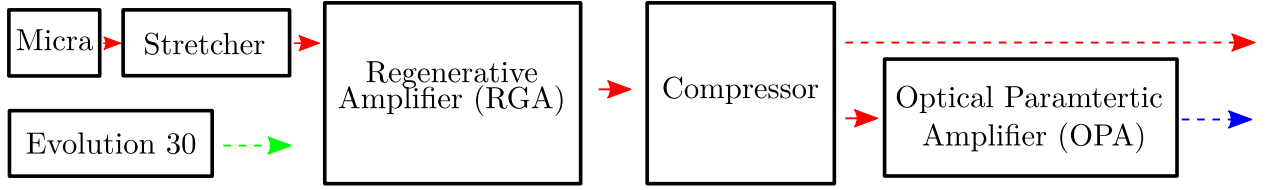


Figure 3.1: Block diagram showing the primary components of the femtosecond system.

which scans the arrival time of one of the pulses with respect to the other. This process exposes multiple stages of excitation: the before, temporal overlap, and later stages. In this work, a retroreflector is mounted to a computer-controlled translational stage which has a resolution on the order of a femtosecond. The signal is recorded using a Lock-in Amplifier (LIA) coupled with a suitable detector, which depends on the wavelength of the probe.

To understand the generation of the laser pulses this system produces, it is easier to split the femtosecond system into four principle stages: the seed laser, produced by a Coherent Micra; the regenerative amplifier, which consists of a Coherent Legend Elite, pumped by a Coherent Evolution-30; the compressor and stretcher, which handles stretching the pulse pre-amplification, and the compression to create sub-100 fs pulses post-amplification; and the OPA, which utilises nonlinear optical processes to generate a variable wavelength output ranging from VIS to MWIR. A block diagram of the primary components can be seen in Figure 3.1

3.1.1 Seed Laser

The seed laser is an 80 MHz, 800 nm centred laser with a bandwidth of approximately 100 nm, produced by a Coherent Micra system. This system is a passively mode-locked laser, which enables a high repetition rate, since active mode-locked lasers rely on external electronics. The saturable absorber in this system is the gain medium itself, a Titanium Sapphire (Ti:Sapphire) crystal. Under the correct conditions, Kerr lensing occurs which locks the

modes. Kerr lensing is achieved when a pulse of significant energy passes through the crystal. The Kerr lensing enables the short intense pulses to be amplified, while any Continuous Wave (CW) is not amplified. The Ti:Sapphire is pumped by a Coherent Verdi 532 nm laser. The 80 MHz signal is generated by the optical path length of the cavity after mode-locking, with a roundtrip of the laser pulse measuring 3.75 m.

3.1.2 Regenerative Amplifier (RGA)

The Regenerative Amplifier (RGA) is the heart of the femtosecond system. The RGA handles the amplification of a stretched seed laser pulse from nanojoules to millijoules, before being sent to the compressor. To generate these intense pulses of energy, another Ti:Sapphire crystal is pumped, although this time with a Coherent Evolution-30 532 nm laser. The Evolution-30 is a Neodymium-doped Yttrium Lithium Fluoride (Nd:YLF), acousto-optically Q-Switched laser, frequency doubled from 1064 nm. Like the Verdi in the Micra system, the Evolution pumps the Ti:Sapphire crystal located in the RGA, this time at a frequency of 1 kHz. As well as the Ti:Sapphire crystal, the RGA cavity consists of four cavity mirrors, two Pockels cells, a quarter wave plate and a polarised output coupler. A single pulse of the seed laser provides the initial pulse for the RGA build up within the amplifier. This seed pulse is constrained within the RGA; each time the pulse does a roundtrip of the cavity the power increases as it passes through the crystal. After a set number of roundtrips, it is released and subsequently compressed to produce the ultrashort pulse. A pair of Pockels cells control the entrance of a single seed pulse and the exit of the amplified pulse. As mentioned in Chapter 2, Pockels cells can modify their birefringence and thus the polarisation of light through the application of an electric field to the electro-optical crystal. The timing of these two Pockels cells is controlled by a Coherent Synchronization & Delay Generator (SDG), which allows for precise timing, relative to the Coherent Micra trigger. After a set number of roundtrips

of the cavity, the exit Pockels cell changes the polarisation of the amplified seed pulse. The timing between the two Pockels cell can be adjusted using the SDG to precisely control the number of roundtrip pulses.

3.1.3 Chirped Pulse Amplification (CPA)

Chirped Pulse Amplification (CPA), a process developed by Strickland and Mourou in 1985 [117], allows for high energy, short pulses to be created. Before this method was developed, there was a limit on how intense a pulse could be. As such, nonlinear effects in the amplifying media could lead to self-focussing, destroying the amplifying medium. To get around this, Strickland and Mourou developed a method that stretches the pulse in the temporal domain by a dispersive medium, such as a grating [117]. In turn making shorter wavelengths travel further. The pulse could then be safely amplified before being compressed in the temporal domain by another dispersive component. With this method, they managed to achieve 2 ps pulses at the mJ level and consequently, CPA is commonly used today in high energy systems, while avoiding damage of the amplifying medium. In the set up used in this work, CPA is achieved by using a pair of diffraction gratings. These dispersive elements are typically called the stretcher and compressor, respectively. An example of this stretching and compression can be seen in Figure 3.2. This process allows the RGA cavity to produce fs, gigawatt energy pulses.

3.1.4 Optical Parametric Amplifier (OPA)

The OPA is an optical device that is able to convert a pump laser to another wavelength of light, through several nonlinear optical stages. In this work, the OPA is used to convert light centred around 800 nm to wavelengths between the VIS to the MWIR range. The

OPA has several distinct sections within it, that are responsible for generating the final output which can be split into four main parts. Firstly, the OPA generates a White Light Continuum (WLC) using a sapphire plate with approximately 20% of the pump power. Secondly, the intensity of the WLC is increased through the pre-amplification stage using a nonlinear crystal coupled with a small fraction of the 800 nm pump. Through parametric amplification, the signal amplitude is increased, and an idler beam is generated, such that the equation $\omega_{idler} = \omega_{pump} - \omega_{signal}$. The signal is then amplified a second time. The generated signal and idler pulse are then used to generate the desired wavelength using the nonlinear processes Difference Frequency Generation (DFG) and Sum Frequency Generation (SFG).

In this system, there are two sources, the signal and idler. The nonlinear processes

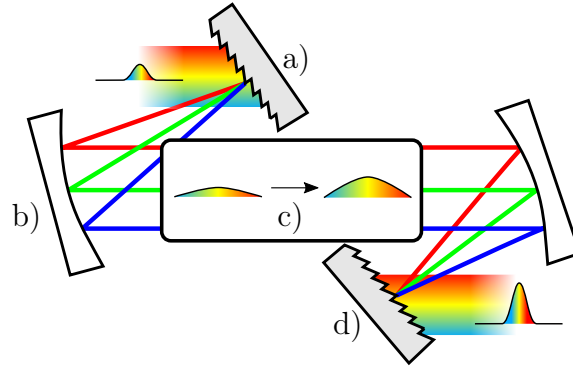


Figure 3.2: Schematic drawing of CPA optical setup. The beam enters the system as a short, low intensity, collimated pulse. The beam is then separated into its constituent wavelengths by a diffraction grating (*a*), otherwise known as the stretcher, before being collimated again at (*b*). At this point, the shorter wavelength light has travelled further than longer wavelengths, spreading out the pulse in time. The resulting pulse is then passed through the amplifier (*c*), increasing its intensity. Finally, the pulse is focussed onto the second diffraction grating, (*d*), the compressor. This compresses the pulse in time, as the longer wavelengths travel further than the shorter ones.

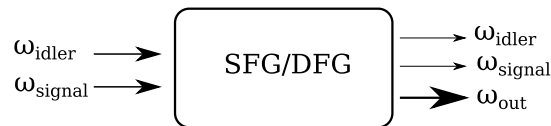


Figure 3.3: Simplified process showing the DFG and SFG processes.

SFG where $\omega_{out} = \omega_{idler} + \omega_{signal}$ and DFG where $\omega_{out} = \omega_{signal} - \omega_{idler}$ occur when light of sufficient intensity falls on a nonlinear crystal, a schematic representation of this can be seen in Figure 3.3. To generate light through SFG and DFG there are a few points that need to be considered. Due to the nature of the pulses involved, the arrival times of the idler and signal beams at the nonlinear crystal need to be overlapped to a high precision. This temporal overlap is achieved using retroreflectors controlled by a computer. Phase matching is another critical component of the nonlinear process, sub-par phase matching can cause low conversion efficiency in the best case, and at worst can lead to no output. To achieve proper phase matching, the angles of the nonlinear crystals are adjusted to find the optimum position. Overall, the OPA allows for the generation of a desired wavelength, ranging from VIS to the MWIR.

3.2 Breadboard System

The breadboard system is an attempt at miniaturising the femtosecond system for use in real world applications. In the case of this work, uses include time of flight rangefinding, active imaging, and a solid state shutter for thermal cameras. The breadboard system consists of three key parts: the source, a QCL; a NIR diode pump laser, for pumping semiconductor optical membranes and windows; and electronics to measure timing signals and control parts of the experiment. Notable electronic parts include: a custom designed and built high speed preamplifier, Constant Fraction Discriminator (CFD) and Time to Digital Converters (TDCs). An overview of the breadboard modulator setup can be seen in Figure 3.4.

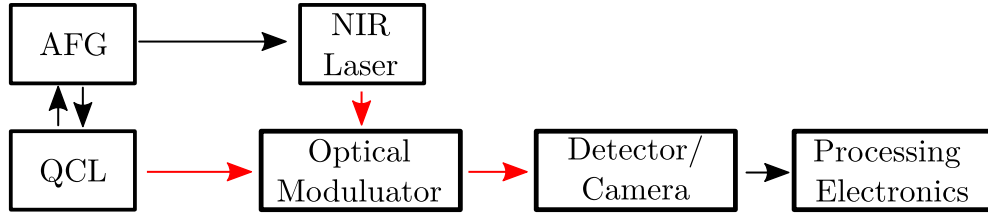


Figure 3.4: Block diagram showing the infrared modulator breadboard setup. The QCL provides the trigger signal to the system, meanwhile the Arbitrary Function Generator (AFG) provides the trigger for the NIR diode optical pump laser, and if required, a gate signal for the QCL for reducing the operating frequency. Red and black lines represent the optical and electrical paths, respectively.

3.2.1 Quantum Cascade Lasers (QCL)

Prior to the development of QCLs, the generation of MWIR and LWIR was limited to lead salt, high quality interband diode lasers, CO and CO₂ lasers, blackbody sources, or generation from the use of nonlinear processes, all of which have serious drawbacks [118, p. 7]. From the book, *Quantum Cascade Lasers* [118], lead salt and diode lasers require cryogenic cooling to operate at these wavelengths. Furthermore, in the case of the diode laser it is limited to the MWIR. While CO and CO₂ lasers are able to deliver high levels of power, they are only able to operate at certain wavelengths. Blackbody sources are generally simple devices, and are able to generate a wide range of wavelengths. However, blackbody sources do not produce coherent light, are generally low power, and are hard or often impossible to modulate at high repetition rates without an external device, such as an optical chopper. DFG allows for highly tuneable wavelength generation, but the system required for production of IR light using DFG is complex [118]. In contrast to systems that use DFG, QCLs are much smaller devices that are able to operate at room temperature. In addition, QCLs can be purchased with a high output power and with a wide bandwidth of operating wavelengths. When compared to our femtosecond system for IR generation, the Hamamatsu QCLs used in this work are a superior candidate for the miniaturisation of the femtosecond system.

Unlike conventional solid state semiconductor diode lasers, which use recombination

between electrons and holes from the conduction and valence bands to produce light, QCLs rely on interband transitions within the conduction band to produce emission [119, 118]. To produce these intersubband transitions, the electrons are confined to certain energy levels by the quantum wells. The band structure that produces the emission can be imagined as an energy staircase consisting of repeating injector and active regions. Electrons are injected at the top, as they travel down the staircase, they either relax to a lower intersubband, or travel through an active region, where photons are emitted. Due to the energy of the electron being confined by the quantum wells, originating from the layer thickness, it is possible to design structures that emit photons at different wavelengths by varying the thickness of the layers. The generation of light originating from layer thickness is different to the operation of standard diode lasers, allowing much more flexibility, as the output wavelength is not limited by the material choice.

To create this quantum well staircase, thin layers of semiconductor are alternated, with the width determining the energy. The first functioning QCL was reported in the article “Quantum Cascade Laser” in 1994 by Faist et al.[119]. The QCL structure was manufactured by growing nanometer thick layers of AlInAs, GaInAs, AlGaInAs, using molecular beam

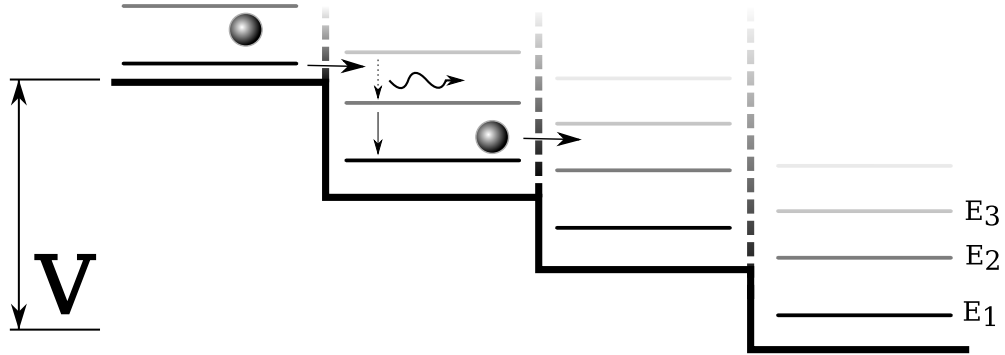


Figure 3.5: Schematic diagram of QCL structure. Dashed lines represent the boundaries of each energy well. The step structure is caused by the applied voltage, V across the structure. Electrons tunnel through the barrier in between energy bands, in this case between E_2 and E_1 before relaxing, producing a photon, as represented by the oscillating line.

epitaxy. Development since then has been rapid, with QCLs available to purchase today in the MWIR and LWIR wavelengths [120, 121, 122], and being pushed to output in the low THz range [123, 124].

3.2.2 Diode Laser

Diode lasers are a suitable choice for the injection of sufficient charge carriers required to induce optical modulation. While the diode laser used in this work lacks the high temporal precision offered by the femtosecond system, it redeems itself in a high average power output, vast choice in package size and design, and at a far lower cost. While there are numerous options for output wavelength available, ranging from Ultra Violet (UV) to SWIR; the primary wavelength for pumping semiconductors in this system is in the NIR centred around 808 nm (like the femtosecond system). However, unlike the femtosecond system, the light is generated by a solid state GaAs-AlGaAs heterostructure [125, p. 196]. When a forward voltage is placed across this structure, a current will flow through generating stimulated emission. Although longer pulses are required to generate a sufficient charge carrier concentration in the modulator (discussed later in Chapter 4), in comparison to the femtosecond system, a diode laser has the advantage when a compact, simple, and efficient system is required.

To power the laser, a driver capable of producing a current source of suitable amplitude and pulse width is required to generate an intense burst of light. The laser driver used is a Direct Energy Instrument PCO-6131, capable of delivering 125 A with a compliance voltage of 20 V. To fire the laser, the PCO-6131 takes a 5 V Transistor-Transistor Logic (TTL) signal. The breadboard system uses a Tektronix AFG to produce this TTL signal. The AFG allows for a more granular control of the timing of the generation and subsequent activation of the modulator. When combined, this system is capable of achieving a peak optical power of up to 80 W with sub- μ s rise times on the leading edge of the optical pulse. This system is far

away from the sub-100 fs pulses generated by the femtosecond system. On the other hand, the breadboard system is able to fit into the size of a shoebox, rather than consuming an entire room, while still providing enough energy to generate a similar number of free charge carriers, discussed in more detail in Chapter 4.

3.3 Electronics

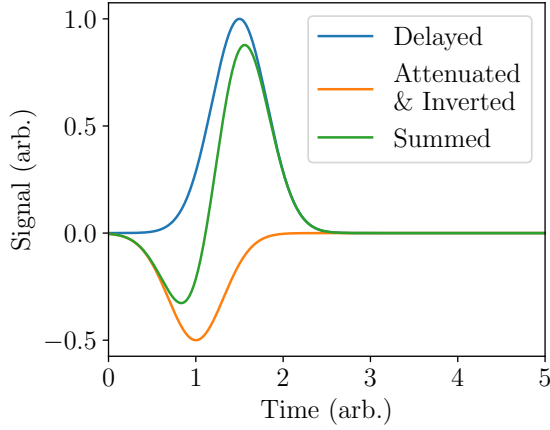
This work does not only focus on optical techniques for rangefinding, but also considers the electronics required to control instruments, process signals and record data. For example, microcontrollers can be used to help automate tasks; a CFD can be used to improve the temporal accuracy of detectors; and TDCs are used for recording arrival times. This section will focus on some of the more notable parts.

3.3.0.1 Constant Fraction Discriminator (CFD)

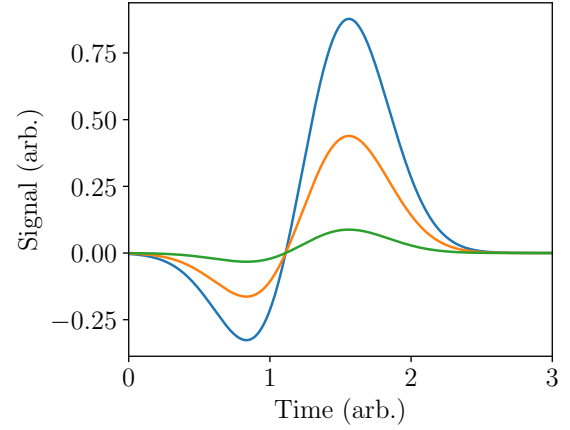
In this project, custom CFDs were designed and made to help improve the temporal resolution of the detectors used for rangefinding. While digital circuits have become commonplace today, they do not always provide the best solution to this problem. Analogue circuits can be designed to perform signal analysis without requiring the signal to be digitised. When precise timing is required, it is not always possible to rely on a rising edge produced by a detector. This is especially true if the detector or source in question does not have a fast rise time. The most obvious issue is hysteresis arising from level triggering of the pulse produced by the detector [126, p. 237]; if no analysis is carried out on the pulse produced by the detector before triggering, the system could trigger at different fractions of the signal, depending on the reflected intensity of the optical signal. This threshold level triggering will reduce the accuracy of the measurement. One solution that would enable threshold level

triggering, which is also mentioned by Baharmast and Kostamovaara [127], could be used to sample the signal using a high speed Analogue to Digital Converter (ADC). This digitised signal could then be followed by Digital Signal Processing (DSP) to identify the peak of the signal before comparing the time difference between generating the pulse and receiving it [127]. This DSP will of course add complexity, cost, power consumption, and additional programming if a ‘smart’ solution is required, for example peak detection. The operating frequency of the ADC used also places a hard-limit on the distance measurement resolution, and how finely it is able to measure the peak, with most ADCs topping out at the GS s^{-1} .

To enable high resolution timing without the need for digitisation and to increase the accuracy of pulsed time of flight systems, a circuit called a CFD can be employed. This circuit is commonly used when a high level of timing precision is required, since it is able to increase the accuracy in two primary ways. The circuit operates on the principle of generating a bipolar pulse, which is passed to a zero-crossing comparator. When the zero crossing comparator sees a zero crossing, it generates a square wave pulse, which can be used to trigger further electronics such as TDCs. To generate the bipolar pulse, the incoming signal from the detector needs to be split. One signal is delayed by a fraction of the rise time of the signal, while the second is attenuated and inverted. These two signals are then mixed to generate the bipolar pulse, a simulation of this process is shown in Figure 3.6. Firstly, it is able to nullify the effect of varying signal amplitudes produced by different intensities of light hitting the detector. Secondly, since the system triggers at the zero crossing point, longer rise time detectors cease to be an issue over a wider dynamic range. This method allows for more sensitive, larger area detectors to be used for precise timing measurements [128, 129]. This is not to say the CFD is the simplest solution. For example, while the dynamic range is increased, time-walk can still be an issue due to Integrated Circuits (ICs) introducing amplitude dependent jitter [130]. In addition, added active components, as well as extra components, can introduce noise into the detected signal, potentially reducing accuracy if



(a) Generation of bipolar pulse. The combination of the delayed, the attenuated and inverted pulses create the summed pulse.



(b) Bipolar pulses created in this fashion all have a zero crossing point at the same time, regardless of initial amplitude.

Figure 3.6: Simulation of bipolar generation for use with CFD.

left unchecked.

3.3.0.2 High Speed Preamplifier

As discussed in the Chapter 2, there are few options for high speed detectors in the MWIR and LWIR. Detectors for this range tend to be slow and responsive, or vice versa [15]. To reach a middle ground, a high speed, high gain preamplifier was designed. The two main classes of preamplifier topologies are voltage amplifiers and transimpedance amplifiers. The type of preamplifier required depends on the photonic sensor used and whether it is biased or not. To achieve this high performance Operational Amplifiers (opamps) are needed which possess a high gain-bandwidth to enable a high gain while maintaining a reasonable rise time. This is not a straightforward task, a high gain, high bandwidth amplifier circuit can become unstable very easily, leading to opamp ringing on the output of the amplifier. The oscillation can be caused by picking up Electromagnetic Interference (EMI) and amplifying frequencies that have a $\frac{\pi}{2}$ phase difference between the output and input in the feedback

loop, essentially causing positive feedback. To avoid these pitfalls, careful circuit design and part selection is essential. There is also usually an element of trial and error involved with high speed analogue circuits once they have been built, which usually involve adjusting the feedback network. Figure 3.7 shows the general topology of a transimpedance amplifier, which was designed as part of this work.

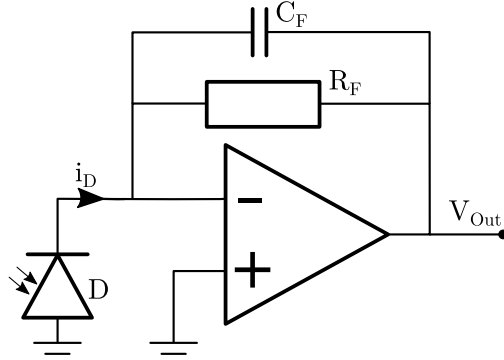


Figure 3.7: Simplified Transimpedance Amplifier (TIA) circuit topology. Gain of circuit goes as $V_{out} = i_D R_F$. Careful selection of capacitor C_F maintains stability of the amplifier.

3.3.1 Time to Digital Converter (TDC)

A TDC is analogous to an electronic stopwatch. TDCs compare the arrival time of two electronic signals, with modern ICs offering resolutions on the scale of tens of ps. Some common designs for TDCs include: use discrete logic gates for measuring the arrival time, such as vernier delay lines [131]; using delay cells, usually NOT gates, in Field Programmable Gate Array (FPGA) for interpolation between clock pulses [132]; or designing custom silicon that use counters [133]. Modern logic gates tend to have a fast propagation time, typically on the order of ps to ns, depending on the type of logic gate and topology. By chaining together multiple identical logic ICs with a known delay time, one can measure the travel time of a pulse to a high precision. This is done by observing how far down the chain a pulse travels before the stop signal arrives.

While it would be possible to make your own TDC with discrete ICs, or by implementing a design on an FPGA, there exist numerous off-the-shelf solutions across numerous price ranges. Off-the-shelf solutions include ICs from manufactures such as Texas Instruments and Maxim Integrated. Buying off-the-shelf reduces the amount of coding, fabrication and calibration required with the DIY solutions, which may significantly reduce the cost, size and time-to-market of a product.

3.3.1.1 TDC7200

One of the TDCs used in this work is a TDC7200 produced by Texas Instruments. From the datasheet [134], this TDC measures the time difference between the start and stop signals by using two internal counters: one a fine counter and the second a coarse counter. In the TDC7200, the fine counter uses a ring resonator topology. The ring resonator is a self-oscillating circuit and consists of an odd number of NOT gates, arranged as seen in Figure 3.8a. This circuit output oscillates between high and low at a rate of $f = 1/n\tau$, where n is the number of elements, and τ is the delay propagation of each individual NOT gate. For this circuit to operate, an odd number of NOT gates are necessary. This output can then be fed into a counter, such as a ripple counter. An example of a 2-bit counter can be seen in Figure 3.8b. The fine counter is only really suitable for short distances. The operating frequency of the fine counter ring oscillator, suggested by the datasheet, is on the order of 20 GHz since the minimum measurable distance is 50 ps. Using this counter for measuring great distances is not a reasonable solution, due to how much storage would be required. To solve this issue, there is a second slower clock source that handles larger distances. The second clock is provided by an external crystal operating at a much slower frequency between 1 MHz to 16 MHz. The TDC7200 uses slower clock source in addition to the fine counter for measuring greater distances, the fine counter handling stop and start triggers in between the slower clock pulses. To communicate with the TDC7200, a Serial Peripheral Interface

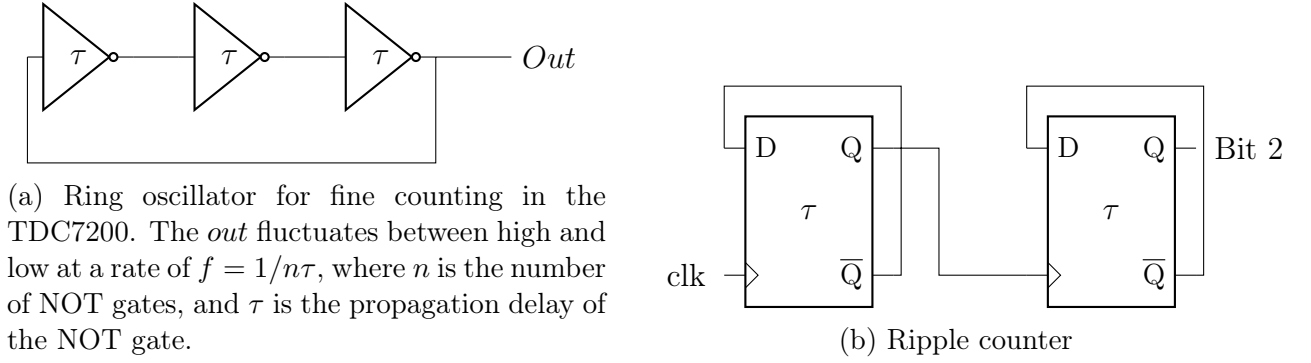


Figure 3.8

(SPI) bus is used. This SPI bus allows for high speed transmission of the measurement for recording and further processing.

3.3.1.2 FAST ComTec P7887

Unlike the TDC7200, the P7887 Fast ComTec TDC is a Peripheral Component Interconnect (PCI) device that requires a computer to operate. While the binwidth is around 5 times greater at 250 ps (from the manual), it is able to collect data at a much higher rate compared to the TDC7200, maxing out at around 10^7 s^{-1} transfers to the computer. From examining the PCI card, the P7887 is driven by a FPGA. There appears to be no dedicated TDC IC included on the board, suggesting that the FPGA handles the timing. The P7887 also has external circuitry allowing for more customisation with regards to how it is triggered, compared to the TDC7200, which is only triggered on a rising or falling 3.3 V TTL pulse.

3.3.2 Microcontrollers

To obtain the maximum performance of the system, it is sometimes preferable to build controlling software and equipment. In the simplest case, this can involve setting multiple parameters on an older piece of equipment that does not have a communication interface,

such as an RS-232 or GPIB. Microcontrollers can also be used as a bridge between ICs and computers. The most notable design that utilise microcontrollers in this work are the laser driver controller for the PCO-6131, and for interfacing with a Texas Instruments TDC7200 IC. The Raspberry Pico is a small but powerful microcontroller; with a high clock speed and numerous IO pins making it suitable for interfacing the TDC7200 to a computer. The details of this will be covered in Chapter 6.

3.4 Experimental Setups

3.4.1 Pump Probe Spectroscopy

Pump probe spectroscopy is an established tool for investigating the ultrafast carrier dynamics of a material [135]. To carry out this experiment, two ultrafast pulses of light are required; the shorter the pulse, the higher the temporal resolution and thus, faster changes in the materials properties can be extracted. One of these pulses is much stronger than the other, usually by a few orders of magnitude. This stronger pulse of light is called the pump and is used to excite charge carriers within the material under test. The intensity of the transmitted or reflected weaker pulse, called the probe, is measured using an acquisition system. In the case of this work, the acquisition system consists of a detector coupled with a LIA. The carrier dynamics can then be investigated by gradually moving one of the pulses, either the pump or the probe, with respect to the other in time. In the femtosecond system, the delay between the pump and probe is achieved through the use of a mechanical optical line. In the most simple form, the transmission and/or reflection can be measured. However, this experiment could be coupled with further optical analysis devices, such as a monochromator, to investigate spectral response.

3.4.2 Breadboard Modulator Setup

A similar technique to pump probe spectroscopy has been implemented in the breadboard setup. However, instead of using a mechanical delay line as seen in the femtosecond system, the diode pump laser uses a separate laser driver, which is independent of the probe. To ensure that there is no frequency drift between the two lasers, the probe laser, a QCL, provides an output from its internal trigger. The trigger signal produced by the QCL is used to trigger an AFG, which in turn drives the NIR pump driver. The AFG is then able to adjust the phase between the pump and probe lasers. This experimental set up was primarily designed to investigate the IR modulator technology discussed in more detail in Chapter 4. Due to its compact size, relative to the femtosecond system, the breadboard modulator setup provides a system for investigating potential applications for the modulator technology outside of the laboratory.

3.4.3 Noise Reduction

Some of the most interesting details lie in the smallest changes of the pump-probe signal. Therefore, it is important to maximise the signal-to-noise ratio of the experiment. In a conventional pump-probe experiment, the pump and probe operate at the same repetition frequency. This is termed single modulation. A result of this is that any noise that occurs at the modulation frequency, which in this case is the pump frequency, is recorded through the LIA. Noise can manifest itself in various places, the most common causes of noise are: line noise from mains appliances, often from unshielded mains powered electronics; high power switching circuitry, this is usually orders of magnitude higher frequency than line noise, and can cause EMI that can be picked up in detectors, or by long BNC cables; high voltage or current switching within the laser system, such as Pockels cells; unstable optical sources causing fluctuations in output power; and even noisy power supplies. The most problematic

are those source of noise that operate at 1 kHz, as there is no way of distinguishing them from the optical signal. The simplest way of increasing the signal-to-noise ratio is to increase the intensity of the optical source as [136, p. 40]:

$$S/N = \frac{I_{ph}}{(2e(I_{ph} + I_d)BF + 4k_BTB/RG^2)^{1/2}} \quad (3.1)$$

where I_{ph} is the current generated by the incident photons, $B = 1/2\pi RC$ where R is the load resistance, and C is the parasitic capacitance of the detector; I_d is the dark current produced by the detector; F is noise introduced by the amplifier; k_B is Boltzmann's constant; and G is the gain of an attached amplifier. However, increasing the optical power is not always a suitable solution, some of the more interesting details, and what may be more useful for applications, can be seen at the lower energy levels. Damage could also occur to the material under investigation if a higher power is used. When the pump probe experiment is being carried out, it is important that minimal power is used for the probe, so as not to introduce any effects of its own to the material. Furthermore, using more power does not improve the situation if the laser source is unstable. Therefore, it is important to find another way to reduce noise in the system. This section will look at two systems, which may help to reduce the noise in the recorded data, and discuss their set up and benefits. The systems are double modulation and pulse sampling, both of which were developed in the laboratory.

3.4.3.1 Double Modulation

The purpose of double modulation is to reduce the noise introduced into the measurements recorded with a LIA [137]. This reduction in noise is achieved by moving the modulation frequency of the signal away from sources of noise. In the femtosecond system the primary

sources of noise originate from shot-to-shot variation between laser pulses, line noise from the mains, noise from instrumentation including the detector and LIA itself, and the high power electrical switching caused by the laser. Noise becomes more pronounced when using the OPA output as the probe. The noise is introduced by the OPA due to it using a fraction of the 800 nm pump beam produced by the Coherent Legend. Any noise present in this pulse is introduced into the output of the OPA when generating VIS, SWIR and MWIR. This added noise is especially problematic as even small changes in the pump intensity used in the OPA can induce significant amplitude variations in its output due to the nonlinear process used to generate the signal.

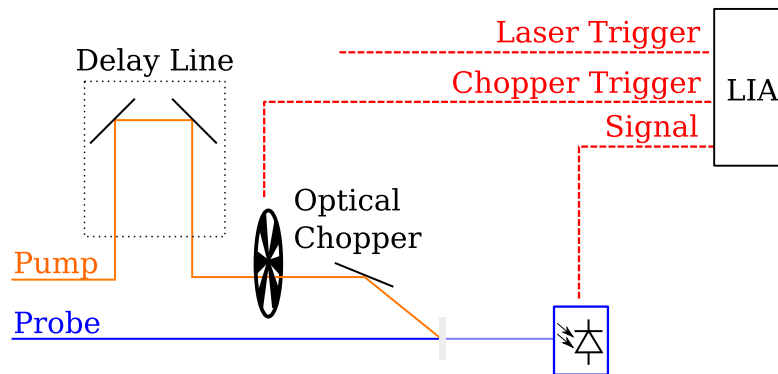


Figure 3.9: Simplified schematic showing double modulation implementation into a pump probe experiment. Dotted box represents the delay line for the pump, while dashed lines represent electrical connections. The laser trigger operates at 1 kHz, and the chopper trigger operates at 500 Hz.

Since the output of the OPA relies on the Legend Amplifier, it is not possible to generate two frequencies within the laser system itself. In order to move the signal away from noise in the frequency domain, the pump and probe pulses require a different operating frequency. Therefore, to enable double modulation, one of the pulses needs to be modulated externally. Owing to the relatively low operating frequency of the laser system (1 kHz), this can be achieved with a mechanical chopper. By using a 50% duty cycle chopper blade and running at 500 Hz, while using the trigger produced by the laser system to avoid frequency drift that could be introduced from separate clocks, it is possible to block every other pulse. It

is vital that the phase of the chopper is set correctly with respect to the laser system, to avoid pump leakage at 1 kHz. The phase of the chopper can be verified by using a detector after the optical chopper to measure the operating frequency. Once set, the LIA needs to be configured to demodulate the signal at 1 kHz and 500 Hz, with both values being recorded to analyse the signal. Using a higher order filter will help reduce the effects of noise situated around the demodulation frequencies, at the expense of settle time, and thus the acquisition speed. A simplified representation of this set up can be seen in Figure 3.9.

Figure 3.10 highlights the resolving power of the double modulation approach; while the signal is still visible in the classic pump probe setup, it could be construed as noise, especially if the change in signal is under 5%. There are a few extra steps to arrive at the double modulated signal. To decrypt the signal, the following equation must be used:

$$V_{Signal}(t) = \pm 2 \frac{V_{500Hz}(t)}{V_{1kHz}(t)} \quad (3.2)$$

where $V_{Signal}(t)$ is the amplitude of the real signal at time t , $V_{500Hz}(t)$ is the amplitude of the signal demodulated at 500 Hz at time t , $V_{1kHz}(t)$ is the amplitude of the signal demodulated at 1 kHz at time t , the factor of 2 is a scaling factor, with the sign determined by the phase of the 500 Hz with respect to the signal. In all of these cases, V is taken as the magnitude of the demodulated signal from the LIA, commonly represented as R .

3.4.3.2 Pulse Sampling

Pulse sampling was attempted in the femtosecond system as part of this work. However, this method never passed the development stage and was dropped as it had numerous reliability issues which made it unsuitable for production use. It should be noted that pulse sampling did prove to be a very effective method of reducing noise in the system, and with future work

could become another powerful tool for catching the smallest changes in signal. This method is based of the work carried out by Werley, Teo, and Nelson, and full details can be found in the article [138]. This method operates by monitoring the difference, pulse-to-pulse, of the probe by calculating a ratio of the transmission. This method forgoes the LIA and replaces it with a National Instruments PCI-6221 Data Acquisition (DAQ) device, pulse stretcher and delay generator. The acquisition system enables the sampling of pulse amplitudes, and is therefore only suitable for larger detector signals, but it is still able to resolve small changes in overall signal amplitude. Sampling the probe signal with and without the material under test when it is optically pumped, and when it is not, enables a ratio of transmission to be established. The use of an additional detector, termed the reference detector, enables the reduction of the shot-to-shot laser noise. This is because any laser noise present on both detectors and any electrical noise picked up should be equal, provided the signal paths and

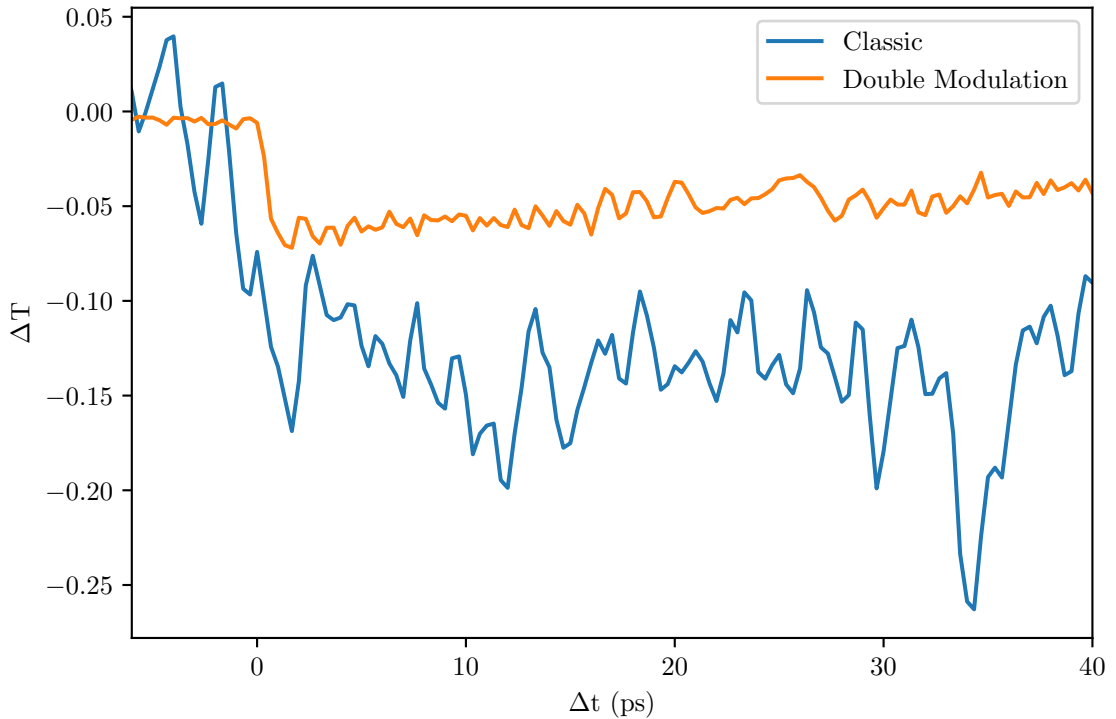


Figure 3.10: Results from a classic pump probe experiment compared to the double modulation implementation of pump probe.

acquisition are similar. The equation for calculating the change in transmission is as follows:

$$\frac{\Delta T}{T_0} = \frac{PD1_u}{PD1_p} \frac{PD2_u}{PD2_p} - 1 \quad (3.3)$$

Where $\Delta T/T_0$ is the change in transmission, $PD1_u$ and $PD1_p$ is the sample detector, unpumped and pumped respectively, $PD2_u$ and $PD2_p$ is the reference detector pumped and unpumped, respectively.

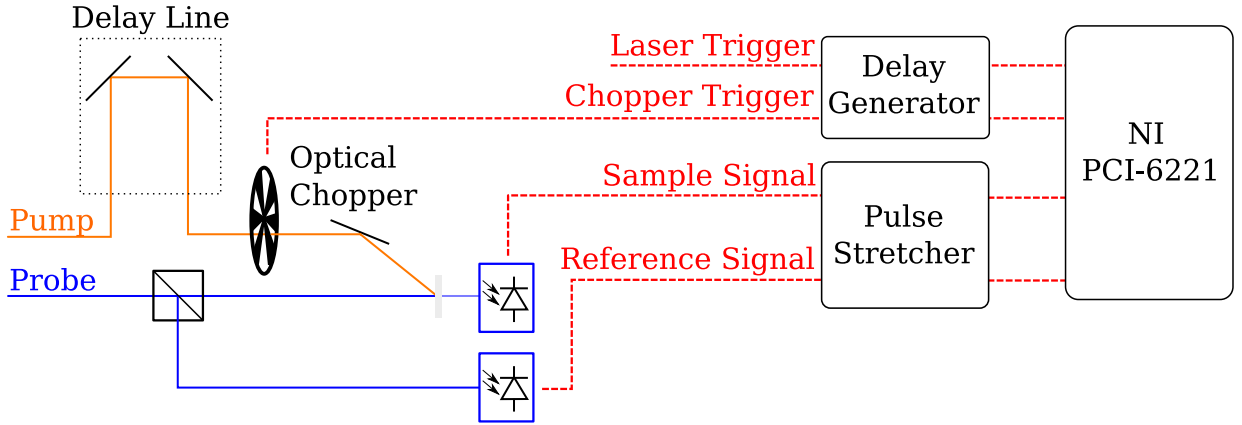


Figure 3.11: Schematic diagram showing the key components of the pulse sampling method incorporated into the pump probe experiment. The pump optical path remains as the double modulation method, however a small fraction of the probe is split and guided to the reference detector so that the power can be monitored and used for noise reduction. The signals from both of the detectors are passed through stretching circuits before being sampled by a computer controlled, National Instruments PCI-6221 DAQ device.

To achieve this operation, like in double modulation, the pump light passes through an optical chopper, operating at a 50% duty cycle relative to the probe, before reaching the sample. The probe light, operating at double the frequency due to the optical chopper, passes through a beam splitter before reaching the sample. The beam splitter passes a fraction of the light to the reference detector, with the majority passing through the sample to be recorded by the sample detector. Both signals from the detectors pass through their own stretching circuit, which is in essence a current preamplifier as shown in Figure 3.7 with

a slow opamp. The need for a stretching circuit reduces the timing precision required for the DAQ sampling time. However, the stretching circuit does have the potential to add noise, and reduce the operating frequency of the experiment. Careful component selection and powering the circuit from a linear Direct Current (DC) source, such as a battery or linear laboratory bench power supply, can help mitigate the risk of added noise.

The acquisition system requires careful timing to achieve accurate results. The laser system produces a 1 kHz signal, and through a frequency divider is used to generate the 500 Hz signal for the optical chopper. This negates any frequency drift that using a separate clock source would introduce. However, the DAQ acquisition card also requires a 500 Hz signal for gating the device, and another, separate 1 kHz signal for triggering the sampling of the two detectors. While the 500 Hz gate pulse only needs to appear prior to the detectors being sampled, the timing of the 1 kHz trigger is important. This signal needs to align with the peak from the stretcher circuit. The phase of this timing pulse with respect to the peak of the stretcher circuit is controlled using a delay function in an AFG. The PCI-6221 DAQ card samples the two detectors when it receives this 1 kHz trigger signal, almost instantaneously (realistically there is a small delay, on the order of μs , between the sampling, but the stretcher circuit helps negate this delay). Figure 3.12 shows the electrical timing of the system.

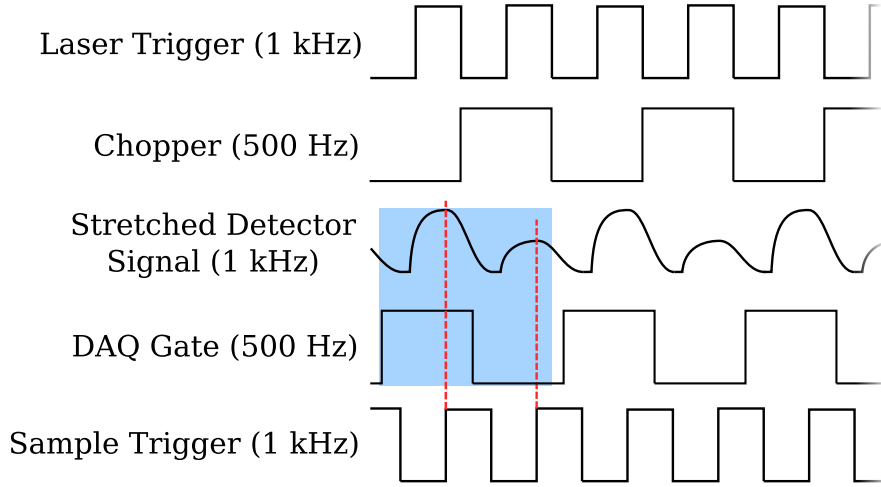


Figure 3.12: All clocks are defined from the laser trigger 1 kHz signal. The highlighted area represents the gating of the PCI6221, and the red dashed lines represent the sampling time. The DAQ gate and sample trigger phase should be adjusted with respect to the laser trigger.

This system allows for the pulse-to-pulse variation of the signal to be characterised and almost entirely removed. While the phase between pump and probe is unchanged, the ratio between pumped and unpumped response should also not change. The results can also be averaged by increasing the number of samples for each delay stage position to help reduce noise. Increasing the number of samples also allows for the correction of laser power drift over time, which is common in our system during long experiments due to environmental temperature changes. The full schematic diagram can be seen in Figure 3.11.

Results of this trial can be seen in Figure 3.13, where a structured silicon sample was optically pumped with NIR light and probed with SWIR light. As can be seen from this figure, the noise level is very low, on the order of 1×10^{-4} , which suggests any signal changes above 0.0001% could be identified.

3.5 Summary

This project uses several different experimental set ups to achieve its goal. Firstly, the operating principles of the femtosecond system were looked at, which covered the generation of ultrafast pulses. Secondly, how these could then be used to generate varying wavelengths from the OPA were identified and discussed. The second system discussed was the bread-board system, which aims to replicate the femtosecond system on a more practical scale for applications relating to Range Gated Active Imaging (RGAI) and Time of Flight (ToF). The key electronics used in the MWIR ToF system were discussed, which included a brief discussion of all parts. Finally, noise reduction in the femtosecond system was discussed, with some results presented showing the improvement seen from implementing the double

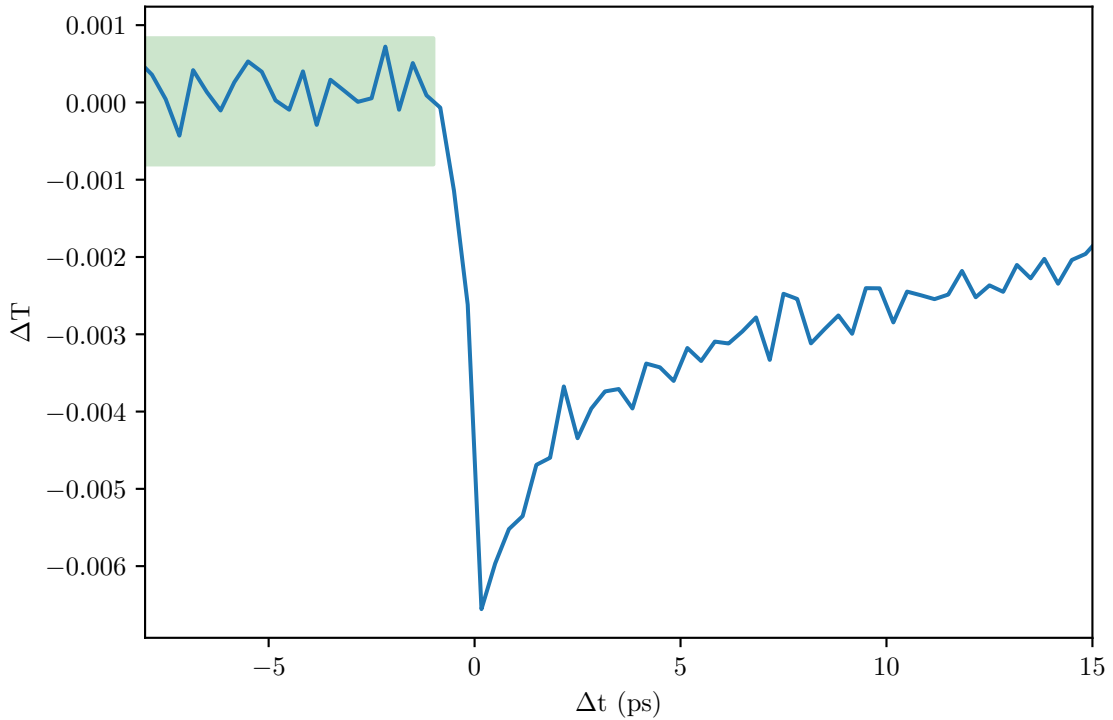


Figure 3.13: Noise reduction when using the pulse sampling method. The standard deviation of the signal before the transmission drop is 3×10^{-4} , suggesting that it would be possible to resolve changes on the order of 10^{-4} in signal variation.

modulation technique.

Chapter Four

Solid State Shutter

One of the objectives of this work is to develop a modulator that could be used with a Infrared (IR) detector or camera. As discussed in previous chapters, there is a real need for high speed, high contrast IR modulators. To achieve high operating speeds and reliability a solid state solution is preferable. As well as modulation depth, operational speed is an important characteristic, and is commonly found in product descriptions of optical modulators. A higher temporal and optical bandwidth allows for the modulator to be used in a greater selection of applications. The modulator in this case consists of a semiconductor optical window that is transmissive to IR under normal conditions. When activated, the window becomes opaque for IR. Activation of the modulator is handled by a Near Infrared (NIR) optical pump. The external NIR optical pump causes excitation of the free carriers within the semiconductor modulator from the valence band to the conduction band, inducing free carrier absorption of IR light. Figure 4.1 shows an simplified example of how the transmission changes with the carrier build-up, and how the modulator returns to its undisturbed state. It should be noted that the time constant for the relaxation of electrons plays an important role in how quickly the solid state shutter returns to normal transmission.

When activated, the apparent opaqueness of the solid state shutter to IR light is

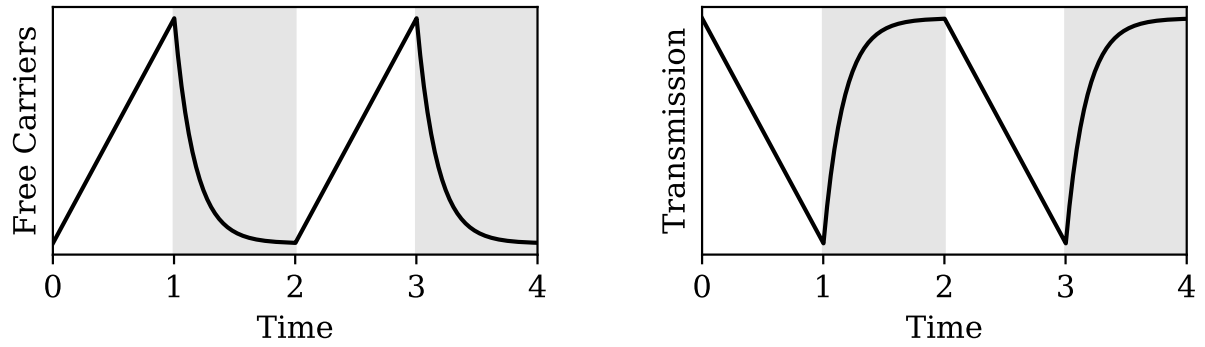


Figure 4.1: Concept of the solid state shutter. Unshaded region represents the activation of the shutter. The grey highlighted region shows the off state, as free carriers recombine. All values are arbitrary in this case.

increased, proportional to the free carrier concentration injected by the pump (in the case of this work, an optical pump is used, however other methods will be covered in the following sections). In comparison to a conventional shutter, the modulator is not a binary state device. Similarly to a Pockels Cell, this modulator has ‘in-between’ states of modulation. This goes from no attenuation beyond the intrinsic absorbance of the modulator, and on, where free carrier absorption occurs and IR light is attenuated. This could lead to interesting use cases, such as an arbitrary function light modulator, and variable Neutral Density (ND) filters for attenuating intense source of radiation. Silicon was chosen for the primary modulator material; as an undoped raw material it already offers high transmittance to IR signals. However, through etching, structures can be created for further performance improvements including transmission and operational bandwidth. This chapter covers operational principles of the solid state shutter, materials that are suitable for the role and the predicted modulation efficiency, and how the theoretical change in transmission is calculated with varying charge carriers.

4.1 Operational Principles

The solid state shutter operates by injecting charge carriers through the use of an external pump source. These charge carriers then cause intraband absorption for Mid-Wave Infrared (MWIR) and Long-Wave Infrared (LWIR) light. Free carriers can be generated through electronic, thermal and optical means [139, 140, 141]. Each process has its own set of advantages and disadvantages, but all have the same response. This section will discuss these potential options for generating free carriers.

For thermal excitation, there exists an empirically derived equation for calculating the intrinsic free carrier concentration n_i [140]:

$$n_i(T) = 5.29 \times 10^{19} \left(\frac{T}{300} \right)^{2.54} \exp(-6726/T) \quad (4.1)$$

Where T is the temperature of the silicon, with other values measured empirically. This relationship can also be derived using: [142, p. 207]:

$$n_i = p_i = 2 \left(\frac{k_B T}{2\pi \hbar^2} \right)^{3/2} (m_e m_h)^{3/4} \exp(-E_g/2k_B T) \quad (4.2)$$

Where p_i is the number of holes, k_B is Boltzmann's constant, \hbar is the reduced Planck's constant, m_e and m_h are the masses of electrons and holes respectively. Both of these models have been plotted in Figure 4.2.

However, this process of generating free carriers is not suitable for high speed modulators, or a thermal camera shutter. As the name suggests, thermal excitation relies on heating of the modulator material to generate the free carriers. A relatively long period of time (compared to electronic and optical excitation) would be required for the heating and

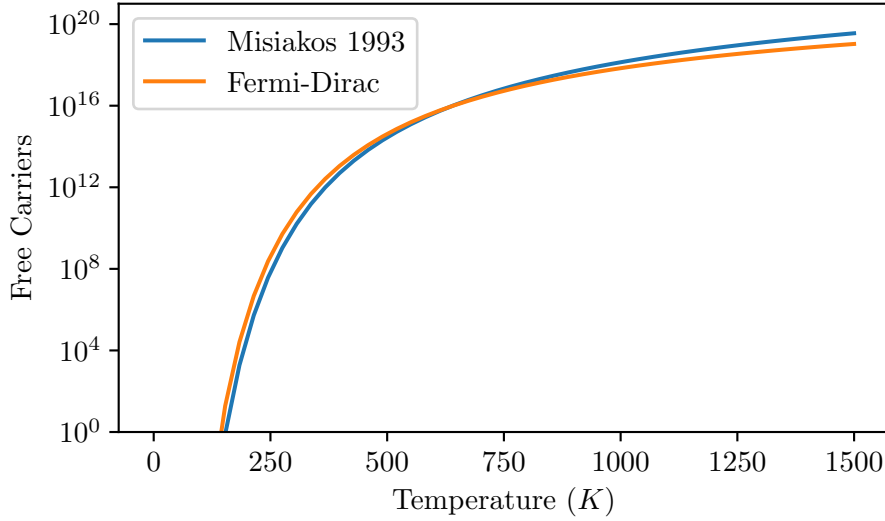


Figure 4.2: Equation 4.1 and 4.2 against temperature. Results valid between 0 K and 350 K for Equation 4.1.

cooling stages to produce sufficient contrast in modulation. This slow process time would limit the operating bandwidth significantly. However, by far the biggest issue with this approach is the additional heat that would be fed into the thermal camera system. This could have side effects such as making it difficult for the Non-Uniform Calibration (NUC) to take place, and adding a sort of colour cast to the image, where heat from the system would bleed into the image of the scene.

Electronic modulation is indeed a possibility. High speed and high current devices are common in numerous electronic devices available today for both the consumer and more niche markets. This includes but is not limited to: switching power supplies, motor drivers and controllers, computer processors, and laser drivers [143, 144]. Due to high demand and rapid development, the miniaturisation of silicon, and more recently, Gallium Nitride (GaN) devices have allowed for small complex circuits operating at high powers to be realised. To generate the required modulation, carriers would have to be injected into the semiconductor modulator electronically. For the purpose of light modulation using an electronic pump, research has been carried out in the Short-Wave Infrared (SWIR) telecommunication wave-

lengths [145, 139], with high modulation bandwidths reported, however there appears to be little to no investigation into longer wavelengths. A potential shortcoming of these electronic modulators would be achieving a homogeneous modulation across a large area. The devices mentioned previously are limited to a small area, due to their use in waveguides for telecommunication purposes. The small active area would make it unsuitable for imaging devices. The difficulties in large area modulation could originate from the local resistance to injected electrons causing inconsistencies between the speed of electrons.

A large area modulator would also have a significant capacitance, which would add a charge and discharge time to the device, impacting the operating bandwidth. This reduced bandwidth, and to an extent, the inconsistencies across the sample, could be addressed by splitting up the large area modulator. Fabricating the modulator as a collection of smaller modulators would enable individually addressable modulation areas. This would reduce the capacitance of the system with the added ability to address each pixel, analogues to a Liquid Crystal Display (LCD) display, as discussed in Chapter 2. Although this is an interesting area to explore it is outside the scope of what is possible with the technology available to us. Nevertheless, it could be an avenue worth investigating in the future.

Optical pumping is the preferred method. With the technology available it is possible to deliver a sharp pulse of energy to fulfil the aim of achieving a fast response, while ensuring a homogenous illumination, which in turn ensures homogenous free carrier generation across the entire modulator surface. To generate free carriers, photons with sufficient energy must be absorbed to excite electrons from the valence to conduction band. When selecting a wavelength of light for optical excitation, the balance between photon energy and penetration depth for that wavelength is critical, especially when a thin semiconductor optical window is used. Since silicon has an indirect bandgap of 1.12 eV and direct bandgap of 3.5 eV, corresponding to a wavelength of approximately 1107 nm and 354 nm respectively, phonon assisted excitation will occur for energies below 3.5 eV[146]. To generate the most free

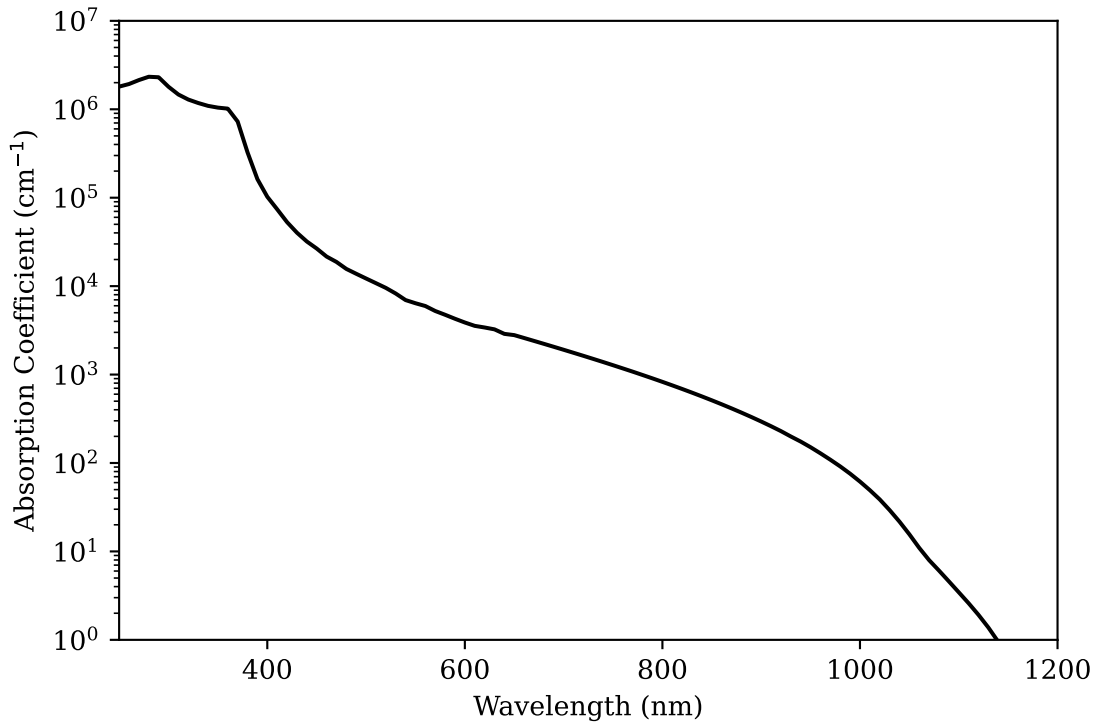


Figure 4.3: Absorption coefficient plotted against incident wavelength. 800 nm proves to be a suitable wavelength for optical pumping due to the high absorption coefficient [147].

carriers, and hence modulation, the number of photons absorbed needs to be maximised without adding excess energy into the semiconductor. Excess energy will reveal itself as heat, and with one of the proposed applications for this technology being thermal cameras, this is not allowable. Increased temperature of the modulator would lead to a reduction in the modulation contrast since the thermal effect reduces the transmissivity of the IR light in the off state, where the modulator should be transparent to IR. Shorter wave NIR is a good candidate for excitation since it is still readily absorbed by silicon, however it does not add too much extra energy to the system.

When light of the correct wavelength, possessing enough energy to excite electrons from the valance band to the conduction band, is shone on a semiconductor, a fraction of that light will be absorbed and generate free carriers. When free carriers are generated, the absorption coefficient of all wavelengths from Visible (VIS) to LWIR is increased [148]. This

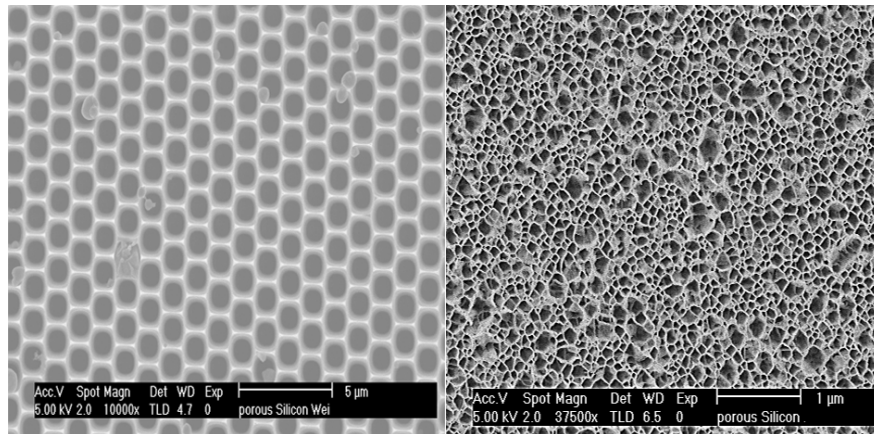


Figure 4.4: Scanning electron microscope images showing a top down view of macro-porous silicon on the left, and nano-porous silicon on the right. Taken from [149].

increased absorption coefficient is caused by free carriers also absorbing incoming light of the shorter wavelengths, which further excites free carriers to higher energy states once in the conduction band [146].

4.2 Suitable Modulator Materials

4.2.1 Optical Silicon Window

Suitable modulator materials should be intrinsically transparent to IR light, with the ability of modifying the optical properties through the free carrier concentration. Silicon is a good choice, not only does it have wideband transmission for IR, provided it is float zone silicon, is readily available and already has an established and mature manufacturing process. Silicon also exhibits strong absorption at 800 nm for optically injecting free carriers, while still allowing approximately 50 μm penetration into the bulk (see Figure 4.7). The silicon windows used in this work are intrinsic silicon optical windows with a thickness of 500 μm . The intrinsic free carrier density is on the order of $1 \times 10^{10} \text{ cm}^{-3}$ at 300 K.

4.2.2 Macro-Porous Silicon

The macro-porous silicon used in this work is a structured photonic membrane. Holes have been etched periodically on the μm scale, with diameters of a similar size. The holes are arranged in a hexagonal layout. These structures were designed to have a higher absorption of the 800 nm pump, while being more transmissive for IR, than that of a standard silicon window. This increased absorption at 800 nm allows for thinner membranes to be used while still absorbing the majority of the pump pulse. Another advantage of the macro-porous silicon over its bulk counterpart is that by adjusting the ratio of silicon to holes, (by changing the hole size, or the spacing between holes) one can modify the effective refractive index of the material. This provides an additional control parameter over the optical response of the material. The effective refractive, ϵ_{eff} index can be estimated using the Maxwell-Garnett mixing equation [135]:

$$\epsilon_{eff} = \epsilon_m + 2p\epsilon_m \frac{\epsilon_p - \epsilon_m}{\epsilon_p + \epsilon_m - p(\epsilon_p - \epsilon_m)} \quad (4.3)$$

where ϵ_m and ϵ_p are the dielectric function of the substrate and holes, respectively, and p is the volume fraction. The structure of macro-porous silicon can be seen in Figure 4.4. In addition to this, photonic bandgaps can be engineered into the material by controlling the structure of the silicon [150]. Although not used in this work, coating the silicon in a thin layer of metal, such as gold, prior to the fabrication of the holes, could introduce plasmonic effects [151].

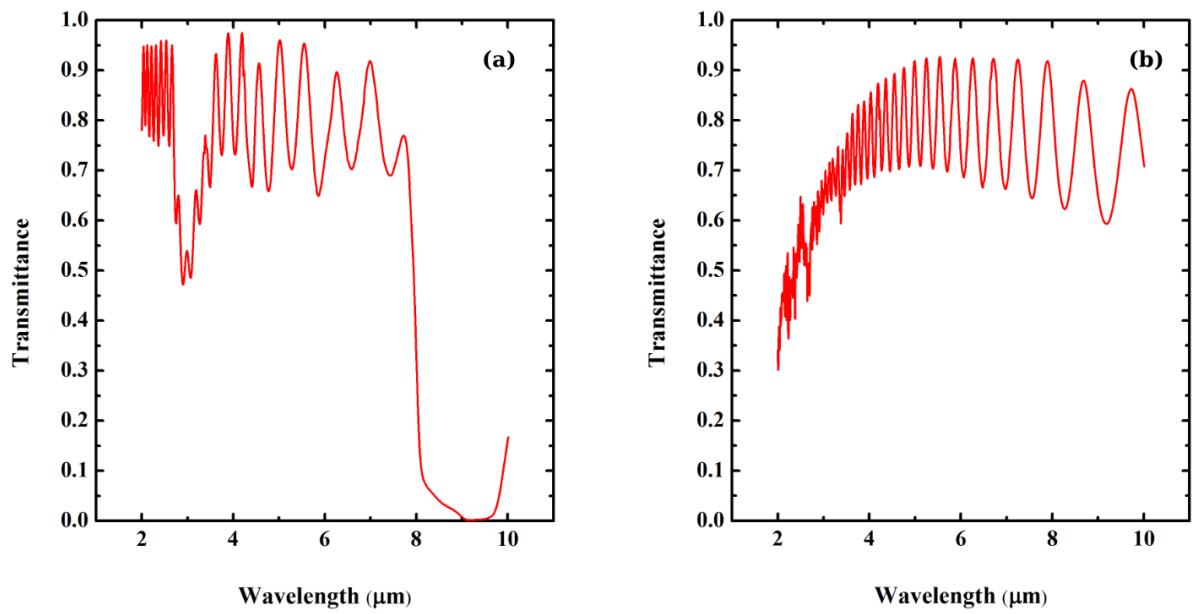


Figure 4.5: Transmission spectrum of nano-porous silicon (shown in (a)) and macro-porous silicon (shown in (b)) in the modulators off state. The transmission spectrum was measured using a Fourier-transform Infrared (FTIR) spectroscope. Interference fringes observed in both samples relate to multiple internal reflections within the porous silicon. Taken from [149].

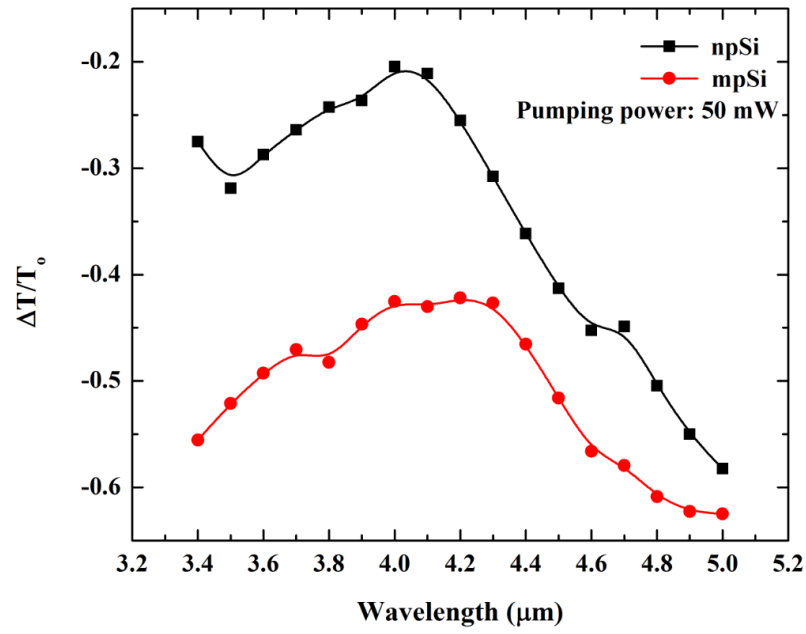


Figure 4.6: Recorded transmission spectrum of MWIR signal after activation of the modulator, obtained using the pump-probe experiment. Macro-porous silicon (mpSi) displays a stronger change in transmission, compared to nano-porous silicon (npSi), around 4 μm . However, both materials tend to approximately 60% attenuation at wavelengths closer to 5 μm . Taken from [149].

4.2.3 Nano-Porous Silicon

Compared to the structured appearance of the macro-porous silicon, nano-porous silicon is a random, sponge like material. Thin silicon skeletal walls are surrounded by air pores. This material has an extremely high surface to volume ratio, which makes it ideal for embedding nanoparticles within the structure. Like macro-porous silicon, this material is created through electro-chemical etching with hydrofluoric acid. By varying the etch current and etch time, the thickness, porosity, and pore size can be adjusted, which further varies the effective refractive index of nano-porous silicon (which can be estimated using Equation 4.3). Due to the large surface area of this material, it is susceptible to surface traps from dangling silicon bonds. These dangling bonds and surface traps increase the recombination rate, making the material ideal for fast optical switching. The structure of nano-porous silicon can be seen in Figure 4.4.

4.2.4 Nano-Porous & Macro-Porous Modulator Spectra

The suitability for a nano-porous silicon and macro-porous silicon based modulator was evaluated in the laboratory's previous work by Zakar et al., and has been included here in Figures 4.6 and 4.5 [149]. Figure 4.5 shows the modulator transmission in its off state. This transmission was measured using a Bruker Fourier-Transform Infrared (FTIR) Hyperion spectroscope. In the modulators off state, shown in Figure 4.5, both the nano-porous silicon (shown in (a)), and the macro-porous silicon (shown in (b)), show generally high transmission, with a dip around $3\mu\text{m}$ for both materials, with it appearing prominently in nano-porous silicon. In addition to the drop at $3\mu\text{m}$, nano-porous silicon exhibits a high attenuation for wavelengths between $8\mu\text{m}$ and $10\mu\text{m}$. The attenuation at $3\mu\text{m}$ is attributed to molecular vibration Si-OH, and the attenuation at $9\mu\text{m}$ caused by molecular vibration Si-O-Si [149].

The transmission for the modulators on state, shown in Figure 4.6, was measured using the femtosecond system using the pump-probe experiment. An 800 nm pump was used, with the wavelength of the probe adjusted using the Optical Parametric Amplifier (OPA). The value for change in transmission for each wavelength generated by the OPA was obtained when the pump and probe were overlapped in time at the zero delay. To compare the modulation efficiency of the two materials, the absolute change in transmittance T , where $T = T_p - T_0$, T_p is the pumped state, and T_0 is the unpumped state, was divided by the unpumped transmission T_0 [149]. From these results, it can be seen that the macro-porous silicon exhibits a higher contrast in modulation at smaller wavelengths. This stronger modulation is attributed to the macro-porous having a lower porosity [149]. As the probe wavelength increases, the modulation of both materials tend to 60%.

4.3 Carrier Dynamics in Silicon

4.3.1 Free Carrier Excitation

To estimate the number of free carriers that can be generated through optical methods a number of parameters need to be decided on, namely the modulator material, excitation wavelength and modulator thickness. For this work, optical pump wavelengths around 800 nm are highly suited to the task; not only is the primary wavelength of the femtosecond system centred around 800 nm, there exist a large selection of high power laser diodes in this wavelength range, as well as having a high absorption coefficient in silicon. While longer wavelengths could be used, as the indirect bandgap of the silicon lies at 1100 nm, 800 nm is the superior choice as the absorption coefficient is significantly smaller beyond 1 μm . The absorption coefficients for silicon can be seen in Figure 4.3. The use of this shorter wave pump allows for much thinner modulators to be used, this ensures a high off state transmis-

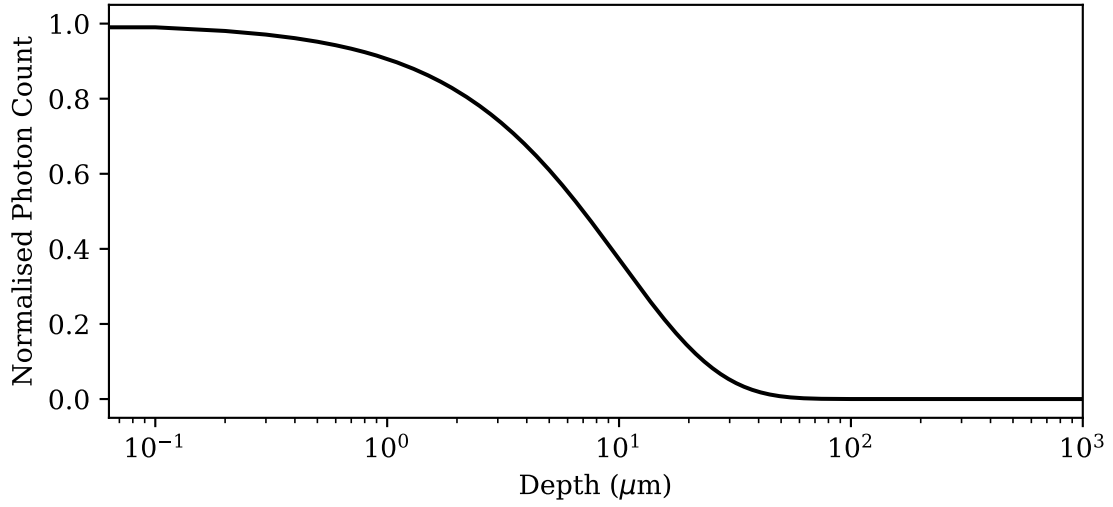


Figure 4.7: Normalised photon absorption as a function of the modulator depth for 800 nm light. Value for absorption coefficient from [147].

sion. To calculate the distribution of generated free carriers at any depth in the modulator the following equation can be used:

$$N_n(\lambda, z) = \alpha F(1 - R) \frac{\lambda}{hc} e^{-\alpha(\lambda)z} \quad (4.4)$$

where N_n is the normalised number of free carriers, α is the absorption coefficient for silicon at 800 nm, F is the laser pulse fluence, R is the fraction of incident light that is reflected, h is Planck's constant, c is the speed of light, and z is the depth into the modulator. To find the number of free carriers generated, assuming all photons absorbed create a electron-hole pair, the number of photons absorbed by the modulator at increasing depth needs to be calculated. This can be integrated to find the total number of free carriers throughout the modulator. However, for calculating the change in transmission of the modulator in the presence of the pump, it is simpler to calculate the free carriers in a thin slice of the modulator. The Transfer Matrix Method (TMM) described in Section 4.5 only applies for homogenous materials. The free carrier concentration in each slice of the

modulator can be calculated using:

$$N(\lambda, z_1, z_2) = N_0 + \alpha F(1 - R) \frac{\lambda}{hc} \int_{z_1}^{z_2} e^{-\alpha z} dz \quad (4.5)$$

where N is the number of free carriers between positions z_1 and z_2 , N_0 is the intrinsic free carrier concentration. Figure 4.7 shows that beyond approximately 50 μm depth, the photon count of the 800 nm optical pump falls off. Thus, only the first 50 μm of depth will contribute to the modulation, with the remainder of the modulator only contributing to the steady state attenuation. On the other hand, using a thicker modulator will help with its thermal stability, allowing for more energy to be absorbed before it bleeds through to the other side and is picked up by the detector.

4.3.2 Free Carrier Decay

Once excited into the conduction band, free carriers in semiconductors have four main ways of relaxing to the valence band. These mechanisms are Auger, Shockley-Read-Hall (SRH), surface, and radiative recombination. Radiative recombination occurs when a hole and electron directly recombine, releasing energy in the form of a photon. If impurities are present in the semiconductor, SRH can occur; SRH recombination is non-radiative, where an electron and hole will recombine at an intermediate energy state (typically a defect state located in the bandgap of the semiconductor). Similar to SRH, Auger recombination is a non-radiative transfer, however it does not require defects for recombination to occur. Instead, the energy released by the recombination is given to a third particle (a hole or electron), moving it to a higher energy state. This excess energy can be given to an electron in the conduction band, or a hole in the valence band. The total lifetime of free carriers can be described using the following equation:

$$\frac{1}{\tau} = \frac{1}{\tau_{nr}} + \frac{1}{\tau_r} \quad (4.6)$$

where τ is the total recombination time constant, τ_{nr} and τ_r represent the non-radiative and radiative time constants, respectively.

With regards to the breadboard system described in Chapter 3, the primary modulator material used is undoped float zone optical grade silicon, so the vast majority of recombination will be due to Auger recombination. The optical pump wavelength used for this system (808 nm) allows for penetration into the bulk of the material, contributions from surface recombination can be ignored since the sample is thick and without a surface structure. Contributions from τ_r are not present due to the indirect bandgap nature of silicon. SRH is also not present as the modulator material used for this setup is undoped silicon.

The Auger recombination rate depends heavily on the temperature of the semiconductor and the number of free carriers. An increase in free carriers, or a decrease in temperature, hastens the recombination rate. The recombination rate will set the operating bandwidth of the modulator, since the turn on time is dictated by the optical pump pulse duration as the excitation is almost instantaneous. The bandwidth can then be estimated, since the free carrier decay in silicon is generally well understood.

The Auger recombination time constant of carriers under high injection conditions, τ_A , can be represented with the following equation [152]:

$$\tau_A = \frac{1}{c_n n_0^2} \quad (4.7)$$

where c_n is the ambipolar Auger coefficient, and n_0 are the majority carrier concentrations. The commonly quoted values for the ambipolar Auger coefficients, c_n and c_p , are

2.8×10^{-31} and 0.99×10^{-31} , respectively[152]. From this equation alone, it can be seen that increasing the number of free carriers, or tuning the Auger coefficients, will result in a faster recombination and therefore increasing the operating speed of the modulator. Surface recombination begins to play a more important role when structured silicon is involved. Materials such as nano-porous and macro-porous silicon, described in Section 4.2, have a significantly higher surface to volume ratio, making the surface recombination lifetime a more significant contribution to the overall lifetime of free carriers.

4.4 Drude Model

The injected free carriers modify the optical response of the modulator through varying its dielectric function. The Drude model can be used to estimate the change of the dielectric function after carrier injection. This model is used to associate the excited state dielectric function with the carrier concentration [153]:

$$\epsilon_{excited} = \epsilon_{int} - \frac{\omega_p^2}{\omega^2 + i\gamma_p\omega} \quad (4.8)$$

where ϵ_{int} is the background permittivity, and the second term, ϵ_D , is known as the Drude term. The ϵ_D term is governed by the frequency of light ω , the scattering rate of the charge carriers in the material γ , typically around 10^{13} s^{-1} to 10^{15} s^{-1} [153, 154] and the plasma frequency ω_p :

$$\omega_p = \sqrt{\frac{Ne^2}{\epsilon_0 m^*}} \quad (4.9)$$

where N is the carrier concentration, e is the charge of an electron, ϵ_0 is the permit-

tivity of free space and m^* is the effective mass of the majority carrier. From Equations 4.8 and 4.9 it can be seen that increasing the free carrier concentration results in an increase in the plasma frequency, thus a decrease in the real component and an increase in the imaginary component of the dielectric function. This in turn will increase the attenuation of the modulator. While the rise time of the optical pump is a key factor in achieving a fast turn on time, the relaxation of the modulator must also be considered. Since the change in transparency depends on the number of excited free carriers, the relaxation of these carriers plays an important role in the maximum achievable bandwidth of the modulator. Selecting a modulator with a fast relaxation time may appear to be a tempting choice, however this introduces another potential issue. A modulator with a fast relaxation time would require a higher peak intensity for the breadboard system, due to the breadboard system relying on carrier accumulation throughout the pulse duration to reach the desired carrier concentration. This is a non issue for the femtosecond system as it is able to deliver high peak powers in femtosecond pulses. However, for the diode bar laser used in the breadboard system that operates on current pulses to generate light, the pulse length and rise time are on the order of microseconds and hundreds of nanoseconds, respectively. Therefore, choosing a modulator that has a recovery time on the order of picoseconds would not work well with a laser diode system that takes hundreds of nanoseconds to deliver the required energy.

4.5 Transmission simulation using the Transfer Matrix Method (TMM)

To gain a better understanding of how the injected free carriers (from the optical pump) influence the optical response of the modulator for IR, a simulation for the breadboard system was built. This was able to estimate the transmission of $10\text{ }\mu\text{m}$ light through the

modulator with increasing 808 nm optical pump powers. As the pump penetrates the sample, its intensity decays exponentially which results in a variation of the refractive index in depth. It is not easy to include this continuous change in a numerical model. Alternatively, by splitting up the modulator into thin slices, an approximation can be made that the refractive index of each slice is constant. The TMM can then be used to describe the propagation of light through each slice of the modulator. This simulation will consider an s polarised electromagnetic wave, travelling in the $+z$ direction. The modulator is semi-infinite in the $x - y$ planes.

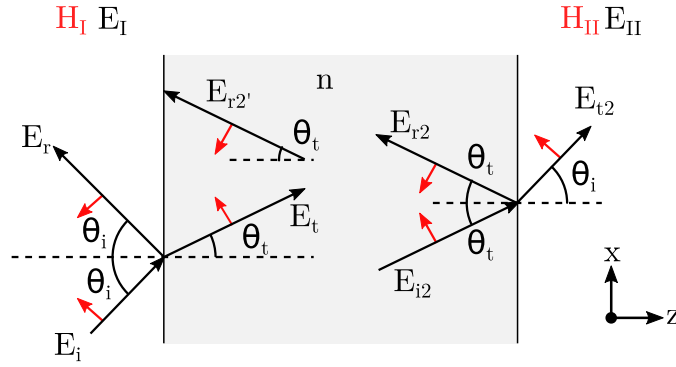


Figure 4.8: Simple TMM set up. A substrate with refractive index n , sandwiched between two semi-infinite mediums of air. E field shown in black solid lines, H field in red.

4.5.1 Refractive Index Calculation

Since the substrate is being sliced up into discrete sections, the refractive index of each slice will need to be calculated. The free carrier concentration in each slice can be calculated using Equation 4.5. The complex effective permittivity, ϵ_r , can be calculated using Equation 4.8. This value for ϵ_r can then be used to calculate the complex refractive index since $\epsilon_r = \epsilon'_r + i\epsilon''_r = (n + ik)^2$, where n is the refractive index, and k is the extinction coefficient.

4.5.2 Transfer Matrix Method Formation

To calculate the transmission of the IR light, the TMM can be used. The TMM is a method that calculates the propagation of electromagnetic waves as it crosses boundaries and travels through mediums. In the simplest case, a medium with refractive index n , sandwiched between two infinite volumes of air will be explained using the TMM, a schematic representation is shown in Figure 4.8. At the first boundary, since the tangential electric field must be continuous across the boundary, the E and H fields can be expressed as

$$\begin{cases} E_I = E_i + E_r = E_t + E_{r'_2} \\ H_I = H_i \cos(\theta_i) - H_r \cos(\theta_i) = H_t \cos(\theta_t) - H_{r'_2} \cos(\theta_t) \end{cases} \quad (4.10)$$

where E_I and H_I are the total field on the left side of the first interface, X_i is the incident field (for E or H), X_r is the reflected field, X_t is the transmitted field, θ_i and θ_t are the angle of incident and transmitted light, respectively, and $X_{r'_2}$ is the reflected field from boundary II at the boundary I. Similarly, at the second boundary, the fields can be described as:

$$\begin{cases} E_{II} = E_{i_2} + E_{r_2} = E_{t_2} \\ H_{II} = H_{i_2} \cos(\theta_t) - H_{r_2} \cos(\theta_t) = H_{t_2} \cos(\theta_i) \end{cases} \quad (4.11)$$

A relationship needs to be derived between E_I and E_{II} , H_I and H_{II} to form the matrices, thus relationships between the fields at each boundaries need to be established. When fields propagate from the first boundary to the second boundary inside the material, the frequency does not change by the phase accumulates:

$$\begin{cases} E_{i_2} = E_t e^{-ikl} \\ E_{r_2} = E_{r'_2} e^{ikl} \end{cases} \quad (4.12)$$

where l is the thickness of a slice, and $k = k_0 n = \frac{\omega n}{c}$, where ω is the angular frequency of light, n is the refractive index of the medium and c is the speed of light in a vacuum. Substituting Equations 4.12 into the electric fields described above in Equations 4.10 and 4.11 gives the following:

$$\begin{cases} E_I = E_t + E_{r'_2} \\ E_{II} = E_{i_2} + E_{r_2} = E_t e^{-ikl} + E_{r'_2} e^{ikl} \end{cases} \quad (4.13)$$

Moving onto the H field, from simplification of the Maxwell equations, it can be said that $ik\vec{E} = i\omega\vec{B}$ and $\vec{B} = \mu_r\mu_0\vec{H}$. From these two equations, we can write $ik\vec{E} = i\mu_r\mu_0\omega\vec{H}$, where $\mu_r = 1$ in non magnetic materials. Rearranging, and using the fact that $c = 1/\sqrt{\epsilon_0\mu_0}$ it can be said that:

$$\vec{H} = n\sqrt{\frac{\epsilon_0}{\mu_0}}\vec{E} = A\vec{E} \quad (4.14)$$

Using this relation, we can rewrite the H fields from Equations 4.10 and 4.11 as

$$\begin{cases} H_I = H_t \cos(\theta_t) - H_{r'_2} \cos(\theta_t) = E_t A \cos(\theta_t) - E_{r'_2} A \cos(\theta_t) \\ H_{II} = H_{i_2} \cos(\theta_t) - H_{r_2} \cos(\theta_t) = E_{i_2} A \cos(\theta_t) - E_{r_2} A \cos(\theta_t) \end{cases} \quad (4.15)$$

So all boundary fields can be related using the X_t and $X_{r'_2}$ forms, the phase accumulation terms need to be inserted into H_{II} . The substitution gives the following set of

equations:

$$\begin{cases} E_I = E_t + E_{r'_2} \\ H_I = AE_t \cos(\theta_t) - AE_{r'_2} \cos(\theta_t) \\ E_{II} = E_t e^{-ikl} + E_{r'_2} e^{ikl} \\ H_{II} = A \cos(\theta_t) E_t e^{-ikl} - A \cos(\theta_t) E_{r'_2} e^{ikl} \end{cases} \quad (4.16)$$

These equations can be re-written in matrix form, starting with the first boundary:

$$\begin{bmatrix} E_1 \\ H_1 \end{bmatrix} = \begin{bmatrix} 1 & 1 \\ A \cos(\theta_t) & -A \cos(\theta_t) \end{bmatrix} \begin{bmatrix} E_t \\ E_{r'_2} \end{bmatrix} = M_1 \begin{bmatrix} E_t \\ E_{r'_2} \end{bmatrix} \quad (4.17)$$

$$\begin{bmatrix} E_2 \\ H_2 \end{bmatrix} = \begin{bmatrix} e^{-ikl} & e^{ikl} \\ A \cos(\theta_t) e^{-ikl} & -A \cos(\theta_t) e^{ikl} \end{bmatrix} \begin{bmatrix} E_t \\ E_{r'_2} \end{bmatrix} = M_2 \begin{bmatrix} E_t \\ E_{r'_2} \end{bmatrix} \quad (4.18)$$

The transfer matrix of the fields E_I and H_I to E_{II} and H_{II} can then be equated:

$$\begin{bmatrix} E_1 \\ H_1 \end{bmatrix} = M_1 M_2^{-1} \begin{bmatrix} E_2 \\ H_2 \end{bmatrix} \quad (4.19)$$

The final transfer matrix M_T , can then be calculated. For simplicity $a = A \cos(\theta_t)$, $b = e^{ikl}$ and $c = e^{-ikl}$:

$$\begin{bmatrix} E_1 \\ H_1 \end{bmatrix} = \frac{1}{2abc} \begin{bmatrix} 1 & 1 \\ a & -a \end{bmatrix} \begin{bmatrix} ab & b \\ ac & -c \end{bmatrix} \begin{bmatrix} E_2 \\ H_2 \end{bmatrix} = \frac{1}{2} \begin{bmatrix} b+c & \frac{b-c}{a} \\ ab-ac & b+c \end{bmatrix} \begin{bmatrix} E_2 \\ H_2 \end{bmatrix} \quad (4.20)$$

$$\begin{bmatrix} E_1 \\ H_1 \end{bmatrix} = \begin{bmatrix} \cos(kl) & i \sin(kl)/A \cos(\theta_t) \\ iA \cos(\theta_t) \sin(kl) & \cos(kl) \end{bmatrix} \begin{bmatrix} E_2 \\ H_2 \end{bmatrix} = M_T \begin{bmatrix} E_2 \\ H_2 \end{bmatrix} \quad (4.21)$$

This matrix, M_T , describes the optical response of one layer of the material. Since the transfer matrix only contains linear operations, one can calculate the transmittance and reflectance of a multilayer material by multiplying the matrix of each layer in sequence.

$$\begin{bmatrix} E_1 \\ H_1 \end{bmatrix} = \prod_{i=1}^N M_i \begin{bmatrix} E_F \\ H_F \end{bmatrix} \quad (4.22)$$

where N is the total number of layers, with each layer having their refractive index n , and angle, θ_t , that form the transfer matrix of that layer.

The transmission of the modulator can now be extracted. To calculate the transmission of light through a material, represented by a matrix, Equation 4.21 should be considered. The left hand side of Equation 4.21 can be represented as:

$$E_I = E_i + E_r = E_0 + rE_0 \quad (4.23)$$

where E_0 is the incident field, and r is the reflection coefficient. Similarly, the right hand side of Equation 4.21 can be written as $E_{II} = tE_0$, where t is the transmission coefficient. To obtain terms for t and r , the H_I and H_{II} must be rewritten in the same way as the E field. This is achieved using the relation in Equation 4.14. However, there are two separate terms as H_I describes the plane wave travelling from air into the substrate, and H_{II} where the wave is travelling from the medium and out of it. These will be referred to as $A_{in} = \sqrt{\frac{\epsilon_0}{\mu_0}} \cos \theta_{in}$ ($n_{air} = 1$) and $A_{out} = n \sqrt{\frac{\epsilon_0}{\mu_0}} \cos(\theta_t)$ (in this case, n is the current refractive

index of the layer of material, this would be recomputed for each subsequent layer). The magnetic strength fields can be re-written as:

$$\begin{cases} H_I = H_i \cos(\theta_i) - H_r \cos(\theta_i) = A_{in}E_0 - rA_{in}E_0 \\ H_{II} = H_{t_2} \cos(\theta_i) = tA_{out}E_0 \end{cases} \quad (4.24)$$

The transfer matrix can then be re-written as:

$$\begin{bmatrix} E_0 + rE_0 \\ A_{in}E_0 - rA_{in}E_0 \end{bmatrix} = \begin{bmatrix} m_{11} & m_{12} \\ m_{21} & m_{22} \end{bmatrix} \begin{bmatrix} tE_0 \\ tE_0A_{out} \end{bmatrix} \quad (4.25)$$

Expanding this matrix can gives the following equations:

$$\begin{cases} E_0 + rE_0 = m_{11}tE_0 + m_{12}tE_0A_{out} \\ A_{in}E_0 - rA_{in}E_0 = m_{21}tE_0 + m_{22}tE_0A_{out} \end{cases} \quad (4.26)$$

Rearranging the second equation and substituting it into the first, the transmission coefficient can be found:

$$t = \frac{2A_{in}}{A_{in}m_{11} + A_{in}A_{out}m_{12} + m_{21} + A_{out}m_{22}} \quad (4.27)$$

This process can be repeated for the reflection coefficient, however for the simulation we are only interested in the transmission. Finally, to find the transmitted intensity through the substrate, the following equation can be used:

$$T = \frac{A_{out}}{A_{in}}|t|^2 \quad (4.28)$$

4.5.3 Simulation Output

The following simulation has been run, following the steps set out above. The pump wavelength was set to 808 nm, with a pulse duration of 10 μ s, and with peak optical powers varying from 0 W to 70 W. The IR signal was set at 10.07 μ m. The sample used is a undoped silicon optical window, with a thickness of 500 μ m, with the slice thickness was set to 1 μ m. The results of this simulation can be seen in Figure 4.9, where the change in transmission with pump fluence, and free carrier generation with pump fluence, can be seen. From the results presented, it can be seen that with the parameters set above, an attenuation of around approximately 50% transmission should be achievable.

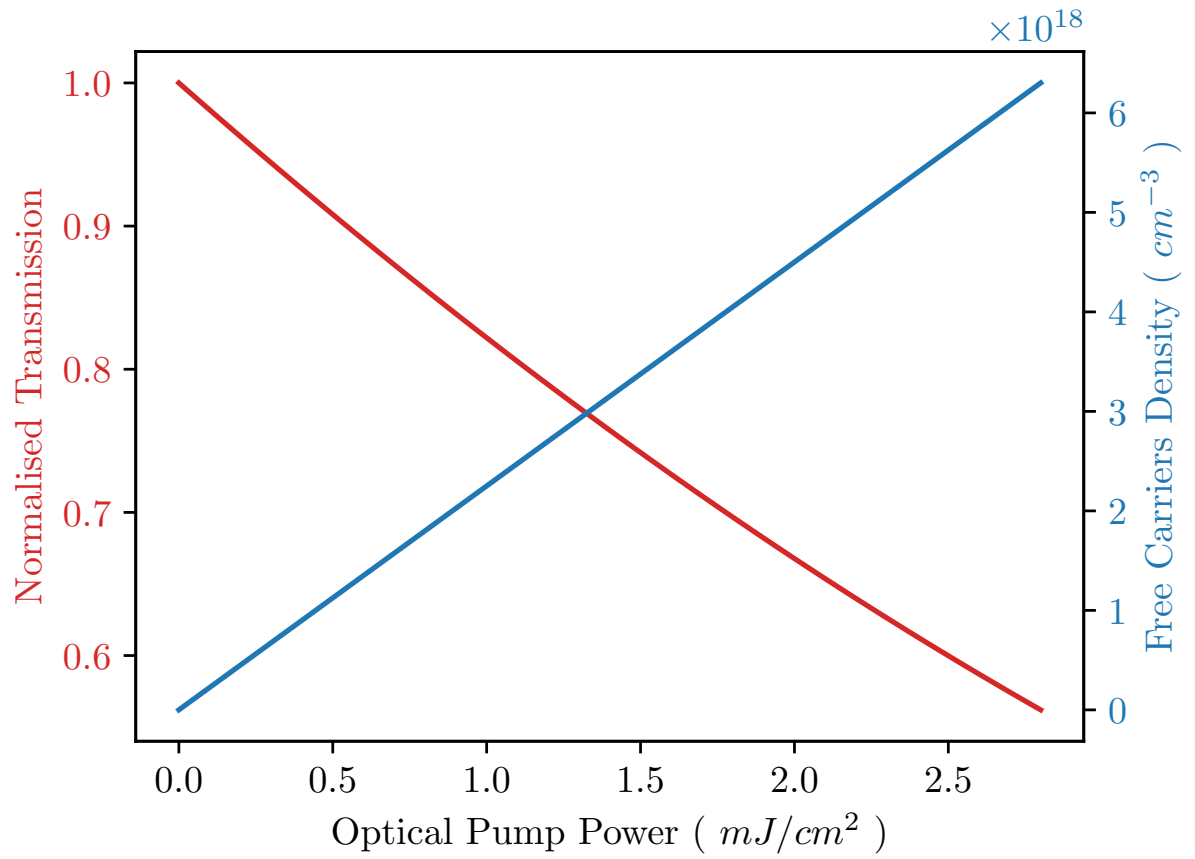


Figure 4.9: Simulation of transmission of a $10\mu m$ probe signal through a $500\mu m$ thick sample as a function of optical pump power, provided by a 800 nm solid state diode.

Chapter Five

All-Optical Shutter

This chapter investigates the feasibility of an all optical shutter for use in thermal imaging, Range Gated Active Imaging (RGAI) and Time of Flight (ToF) applications. Included in this chapter is data and relevant results published in the co-authored paper:

Rihan Wu, Jack Collins, Christopher D. Burgess, Robert A. Lamb, and Andrey Kaplan

Demonstration of time-of-flight technique with all-optical modulation and MCT detection in SWIR/MWIR range

Proc. SPIE 10799, Emerging Imaging and Sensing Technologies for Security and Defence III; and Unmanned Sensors, Systems, and Countermeasures, 1079904 (4 October 2018)

a reformatted conference paper:

Jack Collins, Rihan Wu, Alan Davie, and Andrey Kaplan

All-optical modulator for gated range finding and active imaging in LWIR

Proc. SPIE 11537, Electro-Optical and Infrared Systems: Technology and Applications XVII, 115370L (20 September 2020)

and data and relevant results in the accepted co-authored paper:

Rihan Wu, Elida Nekovic, Jack Collins, Catherine J. Storey, Leigh T. Canham, Miguel Navarro-Cía, and Andrey Kaplan

Taming non-radiative recombination in Si nanocrystals interlinked in a porous network

Physical Chemistry Chemical Physics. 2022 (Accepted)

5.1 All-Optical Modulator for Picosecond Time of Flight in the SWIR and MWIR

The published paper (*All-optical modulator for gated range finding and active imaging in LWIR*) included in Section 5.2, builds on previous collaborative and co-authored work. The paper titled *Demonstration of Time-of-Flight technique with all-optical modulation and MCT detection in SWIR/MWIR range* was published in SPIE Security and Defence 2018 and was written with Wu et al. [155]. What follows is a summary of the key findings in this paper (*Demonstration of Time-of-Flight technique with all-optical modulation and MCT detection in SWIR/MWIR range*) relevant to this thesis.

In the 2018 SPIE paper, we developed an externally optically gated Mercury Cadmium Telluride (MCT) system, improving the temporal resolution of the detector. This external gating was accomplished using the solid state shutter technology discussed previously in Chapter 4, and for which the set up can be seen in Figure 5.1. As mentioned previously, MCT detectors are exceptionally sensitive and proven thermal imaging devices. However, they do have a tendency to have a slow rise time compared to Visible (VIS) detectors of a similar photosensitive area. This sensitivity makes MCT detectors very good at picking out small changes in signal, but less suitable for high speed tasks. One way to improve the temporal resolution of imaging devices is to gate them, either by external methods in the form of a shutter, or internally using electronics. In the case of this paper, we opted for an externally gated optical modulator. In this research, we were able to gate an MCT detector to resolve laser arrival times on the picosecond scale, and with further analysis, could determine of the group velocity dispersion of the probe laser travelling through silica rods.

As discussed in Chapter 4, the all-optical solid state shutter is able to attenuate

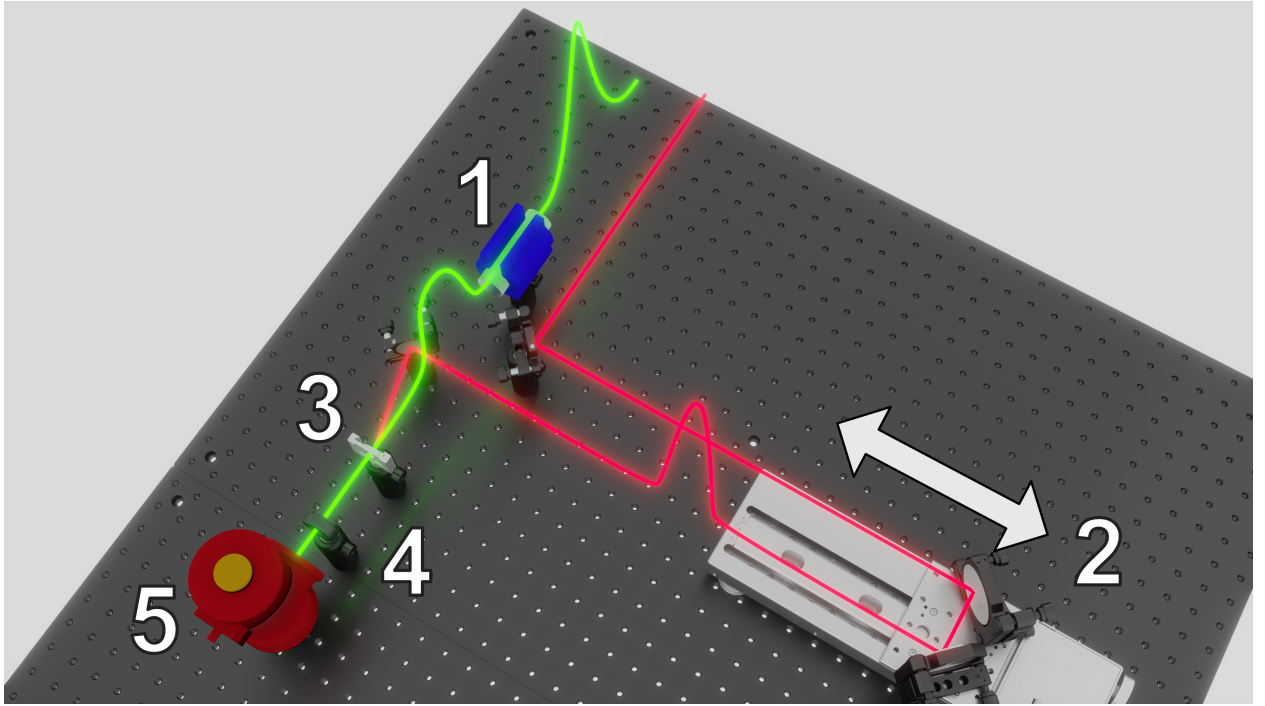


Figure 5.1: Optical set up of the all optical gated shutter for MCTs detectors in the Short-Wave Infrared (SWIR) and Mid-Wave Infrared (MWIR), published in [155]. In this diagram, the probe pulse, in green, travels through the silica rod (1), then passes through the modulator (3) and silicon optical window (4), before being recorded by the MCT detector (5). The pump pulse, represented by the red line, travels along the computer controlled translational stage and retroreflector (2), before being directed onto the surface of the modulator (3). The silicon window (4) absorbs any remnant pump.

wavelengths between the SWIR to the Long-Wave Infrared (LWIR), through intraband absorption. This attenuation occurs when the modulator is activated through the absorption of a Near Infrared (NIR) 800 nm pump. In this experiment, the optical pump and signal were provided by the femtosecond laser system and Optical Parametric Amplifier (OPA), as described in Chapter 3. This experimental set up was operated in a pump-probe configuration, with the pump directed along a variable-length, computer-controlled, optical path, before being focussed onto the modulator surface. The computer-controlled optical path allowed for translational positioning to a resolution of ± 400 nm, with a 200 mm range to scan over. When the optical pump falls on the surface of the modulator, free carriers are generated, causing the absorption of SWIR and MWIR. If the probe arrives at the modulator before the pump in time, the probe passes through the modulator unaffected. When the pump and probe overlap in time, a sudden drop in intensity is observed on the readout of the detector. The scale of this drop in intensity depends on the free carrier concentration generated from the pump; while the rate of the drop is determined by the rise time of the probe pulse, convoluted with the response of the modulator. Further increasing the delay of the probe with respect to the pump shows the recovery of the modulator; modulator materials with a high recombination rate will return to the transmissive state faster.

Depending on the configuration, the probe travels through either just air, 5 cm or 10 cm long silica rods, before passing through the modulator and reaching the detector. The addition of the silica rods increases the optical path for the probe, delaying its arrival time at the modulator. The probe and pump were spatially overlapped on the surface of the modulator while their temporal overlap is controlled by the translational stage. Firstly, a reference time was found by removing the silica rods from the optical path, so the probe was travelling unimpeded. A sudden drop in transmission represents the temporal overlap of the pump and probe on the surface of the modulator, signifying the zero delay. This calibration gives a reference point to compare against the induced delay from the silica

rods. Compared to just air, these silica rods delay the arrival of the probe pulse on the surface of the modulator, necessitating the temporal overlap to be found through scanning the translational stage again. As well as increasing the optical path length, broadening of the probe pulse occurs due to the group velocity dispersion in the silica rods. This broadening of the probe can be seen in the data as shallower gradient in the falling edge.

As the optical pump was scanned through the range, the overlap of the pump and the probe were recorded in time and appear in the data as a drop in signal from the detector (due to the external gating described earlier). Due to the nonlinear process involved in generating the SWIR/MWIR pulses, the probe length is longer in comparison to the pump, on the order of 100 to 200 fs. The further stretching of the probe pulse due to the silica rods can be observed by the shallower gradient found in the change in transmission.

Macro-porous silicon with a thickness of 63 μm , with holes of 1 μm diameter and a separation of 1.5 μm , organised in a hexagonal pattern, was used as the optical modulator material. The activation pulse provided by the femtosecond laser system, generating a change in transmission for the modulator on the femtosecond scale. The ToF of the probe pulse could be deduced from the position of the change in transmission, and the position of the delay stage, using the following equation:

$$ToF = (n(\lambda) - 1) \frac{L}{c} = \frac{D}{c} \quad (5.1)$$

where $n(\lambda)$ is the wavelength-dependent refractive index of the rod, L is the length of silica rod, c is the speed of light in vacuum and D is the extra distance travelled by the probe. Using this method, it was possible to measure the ToF through a 5 and 10 cm silica rod using SWIR and MWIR. The ToF was measured on the ps scale, with the results seen in Figure 5.2. The data presented in Figure 5.2 shows the falling edges for varying wavelengths,

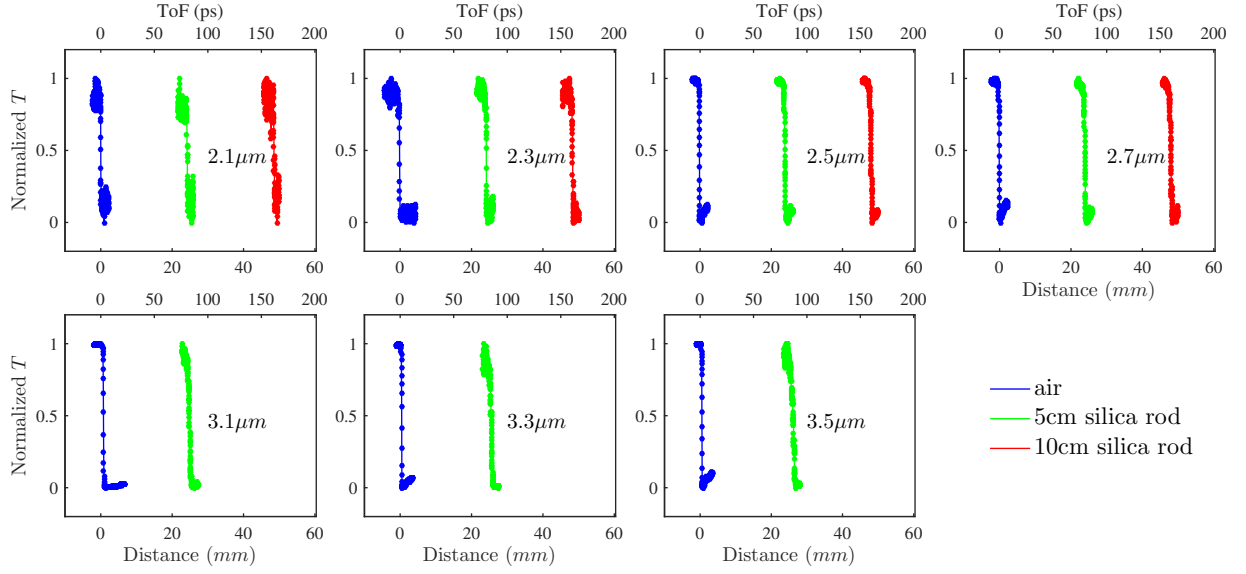


Figure 5.2: ToF results of air and silica rods, published in [155]. Shown above are the varying time of flights for the differing wavelengths while travelling through the silica rods.

after travelling through just air (the zero position), 5 cm of silica, and 10 cm of silica. With this setup it is possible to measure the induced optical delay from the silica rods on the order of ps. It was not possible to measure the ToF for wavelengths greater than $3\mu\text{m}$ in the 10 cm rod due to the higher absorption of the probe in the silica.

The determination of the group velocity dispersion highlights the high temporal accuracy of this system. As the recorded fall in transmission is a convolution of the modulator response and probe pulse shape (which are both known), it is possible to determine the amount of broadening of the probe pulse. The stretch of the probe pulse can be observed in Figure 5.3. The detail observed in the stretching of the probe pulse, through gating the detector, is far beyond what would be achievable with conventional level triggering due to the slow, 400 ns rise time of the detector used.

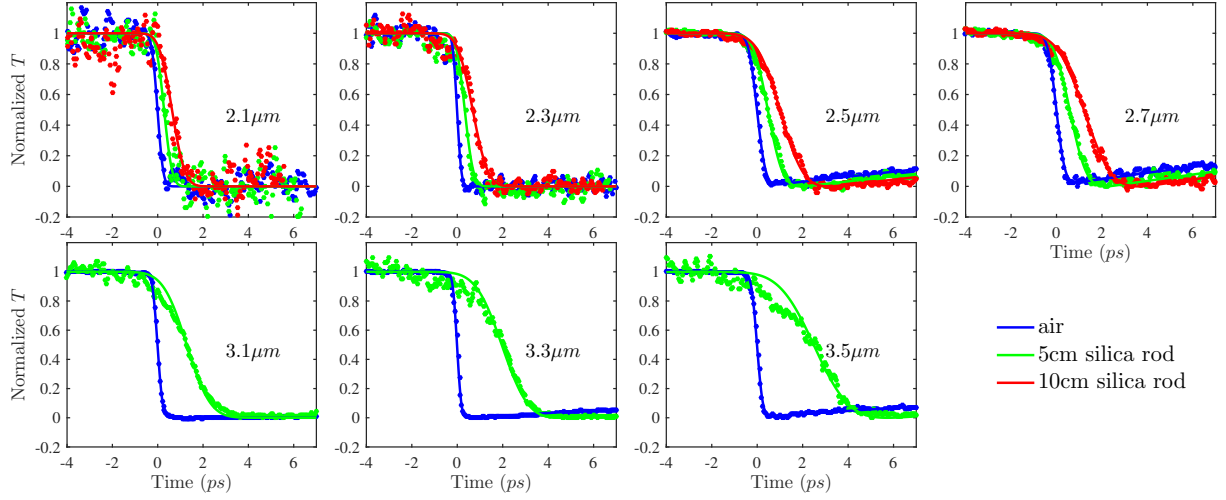


Figure 5.3: Probe pulse broadening induced from passing through the silica rods, published in [155]. Shown above is the stretching of the falling edge of the change in transmission for the differing wavelengths while travelling through the silica rods.

5.2 Compact All-Optical Modulator for Gated Range Finding and Active Imaging in LWIR

The following section includes the reformatted paper, titled *All-optical modulator for gated range finding and active imaging in LWIR*, is published in *SPIE Security and Defence: Proceedings Volume 11537, Electro-Optical and Infrared Systems: Technology and Applications XVII; 115370L (2020)* [156].

Authors: Jack Collins, Rihan Wu, Alan Davie, Andrey Kaplan.

Pushing the concept of the all-optical modulator further, the paper, *All-optical modulator for gated range finding and active imaging in LWIR* included below, aims to make the system described in Section 5.1 more compact and practical while maintaining reasonable performance. The primary components of this compact system are a Hamamatsu 10.07 μm Quantum Cascade Laser (QCL), which is used as the LWIR source; the all-optical modulator, which consists of a Coherent 808 nm diode laser capable of producing a peak optical power of 69 W, and a 500 μm thick intrinsic silicon optical window as the modulator mate-

rial; and the detector, which in the ToF setup was an MCT detector coupled with a Lock-in Amplifier (LIA), and a Thermoteknix MicroCAM3 Vanadium Oxide (VOx) microbolometer thermal camera for RGAI. Firstly, the ToF of a LWIR laser pulse was used to measure the difference between a short optical path and a longer optical path. The difference between these two paths was set at approximately 18 m. The all-optical modulator was used to optically gate the detector. An MCT detector coupled with the LIA was used to record the returning LWIR signal. The arrival time of the pump with respect to the probe at the surface of the modulator was adjusted electronically through the use of an Arbitrary Function Generator (AFG). Like the previous paper, when the pump and probe overlap in time on the surface of the sample, a drop in signal measured by the detector is observed. The minima of the two signals could then be compared to find the arrival times. Secondly, RGAI was implemented using the QCL to illuminate a mask. The image of the mask was focussed onto the modulator, before being recorded by the thermal camera. The gate of the optical modulator was electronically moved in time with respect to the LWIR illuminating pulse, so as to observe the modulation of the LWIR pulse on a thermal camera. The aim of this paper was to assess the feasibility of an active imaging LWIR system for use in RGAI applications and LWIR ToF rangefinder using the all-optical solid state modulator technology.

5.2.1 Theory & Principle of Operation

In this paper, we applied a similar approach as in our previous work where the ToF of a dispersive media was measured by externally gating the detector with an optically controlled modulator[155]. Undoped Silicon was chosen as an active material for the modulation due to its high transmittance to Infrared and ability of tuneable optical properties through carrier injection by a pump laser.

According to the Drude model, the dielectric function of semiconductor has a linear

relationship with the injected carrier concentration, N :

$$\epsilon = \epsilon_{Si} - \frac{Ne^2}{m_e \epsilon_0 (\omega^2 + i\gamma\omega)} \quad (5.2)$$

Where ϵ_{Si} is the intrinsic dielectric function of the bulk silicon, ω is the frequency of the infrared light, m_e and γ are the joint electron-hole plasma optical mass and the scattering rate of the free carriers, respectively. The concentration dependant part of Equation 5.2 can be further separated into the real, $\epsilon_r \sim -\frac{N}{(\omega^2 + \gamma^2)}$, and the imaginary, $\epsilon_i \sim \gamma \frac{N}{\omega^3 + \gamma^2 \omega}$, parts. The scattering rate, γ , of the carriers in the silicon under optical pumping is in the range of 10^{14} s^{-1} ref. [157, 135], which is the same order of magnitude as the frequency of $10 \mu\text{m}$ of the LWIR light ($\omega \approx 2 \times 10^{14} \text{ Hz}$). In this regime, the ratio of the change of the real and imaginary parts is $\frac{\Delta\epsilon_r}{\Delta\epsilon_i} \approx 1$, indicating that they contribute almost equally to the change of optical properties of the silicon window in the modulator.

The transfer matrix method was applied to build a connection between transmitted light intensity and the change of the dielectric function. The transmittance T can be expressed as the following:

$$T = \frac{1}{\sqrt{\epsilon}} \left| \frac{2Y_0}{Y_0 \cos(k) + Y_0^2 \frac{i \sin(k)}{Y_1} + i \sin(k)Y_1 + Y_0 \cos(k)} \right|^2, \quad (5.3)$$

where $Y_0 = \sqrt{\frac{\epsilon_0}{\mu_0}} \cos(\theta_0)$, $Y_1 = \sqrt{\frac{\epsilon_0}{\mu_0}} \sqrt{\epsilon} \cos(\theta)$, $k = k_0 d \cos(\theta)$, θ_0 and θ are the incidence and refracted angles, respectively, d is the thickness of the silicon modulator, ϵ is the dielectric function, other terms have their conventional meanings. By combining Equations 5.2 and Equation 5.3, it can be estimated that a 50% reduction in transmittance can be achieved by injecting $N = 10^{18} \text{ cm}^{-3}$. Further development to calculate the transmittance of semiconducting thin films with nonuniform carrier density distribution can be found else-

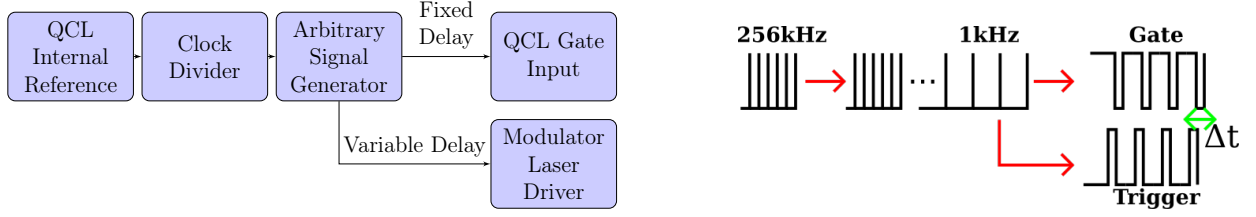
where [158, 159].

There are two routes to reach the desired concentration: apply short intensive optical pump to excite carriers in one pulse or use a long pulse (or multiple of weaker short pulses) to allow carriers to accumulate to a sufficient level before they recombine to the ground state. In our previous works, we exploited the ultrafast femtosecond laser as an optical pump which has a peak intensity of 5 GW cm^{-2} with a pulse length of 100 fs [155, 160]. However, the entire setup is bulky and expensive making it inadequate for various applications. In this work, we reduced the dimensions of the setup by replacing the ultrafast pump laser with a small package diode laser, though it delivers much less intensity in comparison to the femtosecond laser system. To overcome this, the pulse duration of the pump laser, also known as the modulator laser, must be prolonged to allow the excited free carriers to accumulate in time. Since silicon has a relative long recombination time of about $10^{-4} - 10^{-3}$ second [161], we can assume that for a pulse duration shorter than 50 μs , the carrier concentration remains unchanged.

The highest peak intensity of the diode pump laser is $I_{peak} = \sim 69 \text{ W}$. Therefore, we can estimate the required pump pulse duration through $\tau = \frac{NE}{\alpha(1-R)I_{peak}}$ [160], where E is the photon energy $2.46 \times 10^{-19} \text{ J}$, α is the absorption coefficient and R is the reflectance of pump beam. With the known parameter of $\alpha = 8.5 \times 10^2 \text{ cm}^{-1}$, and $R \sim 0.3$, we obtained the appropriate pulse duration of $\sim 6 \mu\text{s}$ to generate $N = 1 \times 10^{18}$ free carriers.

5.2.2 Demonstration Setup

This experiment was setup with two feasibility investigations in mind: is it possible to gate an image of an actively illuminated object and measure distance with the same modulator? For illuminating the scene a Hamamatsu Quantum Cascade Laser (QCL) operating at $10.07 \mu\text{m}$



(a) Flow chart showing electronic timing control and synchronisation of the modulator and signal lasers. The trigger for the modulator laser is derived from the QCL's internal clock so there is no phase drift. To avoid possible heating of the modulator, the frequency was reduced from 256 kHz to 1 kHz. The arbitrary function generator was used to introduce a controlled delay between the modulator and signal laser pulses.

(b) Pulse schematics showing the progression from 256 kHz pulse train provided by internal clock to gating the IR source and triggering the modulator laser at 1 kHz. The modulator laser is triggered on the rising edge of the trigger signal, and can be moved in time independently of the gate signal.

Figure 5.4: Flow chart and pulse schematics of the synchronisation electronics.

at a repetition rate of 256 kHz, which was converted to 1 kHz through electronic control, was used. The beam was steered and focused onto the modulator, while the transmitted intensity was either detected with a Judson Teledyne J12 MCT detector or Thermoteknix MicroCAM3 uncooled thermal camera. The modulator consists of a 500 μm thick silicon optical window, and a 800 nm Coherent diode bar laser operating at 1 kHz with a maximum peak optical power of 69 W. This is focussed to a spot size of 1 mm^2 for the ToF experiment, and 6 mm^2 for the RGAI experiment. The diode laser was driven by a Directed Energy PCO-6131 laser driver.

To ensure there is no temporal drift between the signal and modulation laser, the trigger was taken from the internal clock of the QCL laser driver. This reference signal is then passed through a frequency divider, converting from 256 kHz to 1 kHz, which produced a gate for the signal laser and a trigger for the modulator laser. The absence of the temporal drift was confirmed on an oscilloscope. A flow chart of the driving electronics for this experiment can be seen in Figure 5.4a.

For the ToF investigation, the optical path length for the 10.07 μm signal laser, pro-

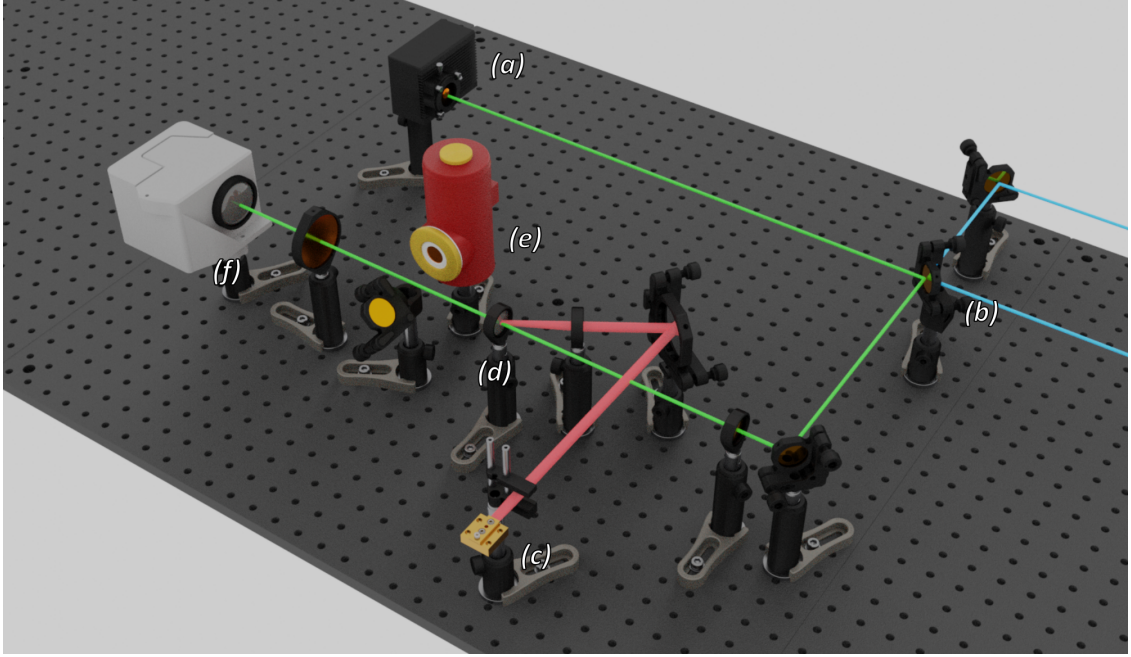


Figure 5.5: ToF and RGAI feasibility demonstrator. The green and blue lines represent the short and long IR optical paths respectively. The red line represents the modulator laser beam. The signal laser is produced by a Hamamatsu QCL (a). The mirror (b) can be flipped down to switch between short and long optical paths. The activation laser for the modulator is provided by the 808 nm diode bar laser (c). The signal is then steered and focussed onto the modulator (d), and then either directed into the MCT (e), or into the uncooled thermal camera (f). For RGAI the mask is added between the final steering mirror and modulator window (d).

viding a train of sub-microsecond pulses, can be changed between two options, with one path being approximately 18 m longer than the other. Care was taken to ensure that the signal beam spot appears at the same position on the modulator surface for both long and short optical paths. An illustration of this setup can be seen in Figure 5.5. The system was calibrated by finding the zero position using the short optical path. The zero position is the instance corresponding to the temporal overlap of the modulator and signal laser pulses. This is represented by the signal minimum after passing through the modulator window, since this is the point of the maximum attenuation. A typical signal trace observed by the oscilloscope can be seen in Figure 5.6. The modulator laser trigger time is adjusted with

respect to the signal laser by the variable delay generator. The signal lasers intensity is recorded by an MCT detector connected to a lock-in amplifier. Once the signal minimum is found, the delay between gating the signal laser and triggering the modulator laser is noted, and the length of the long optical path can be assessed. The length of the optical path was changed and measured again by scanning the delay line and finding a new time for the signal minimum. This can then be converted to a distance by multiplying the difference by the speed of light. The modulator laser pulse length was set to $10\text{ }\mu\text{s}$ with a peak optical power of 69 W , corresponding to an average optical power of 690 mW .

For investigating the feasibility of RGAi only the short optical path was used. The image was recorded by the Thermoteknix camera. This is an uncooled thermal camera which uses a mechanical shutter for periodic non-uniform calibration. To create the image, the signal beam passed through a mask with a silhouette of the Greek letter π (see Figure 5.8), before projection on to the modulator surface. With the signal laser and modulator laser fully overlapped the relationship between modulator laser power and signal transmission can be derived. The temporal response of the system can also be investigated by moving the modulator laser in time with respect to the signal laser and recording the transmission observed on the thermal camera. The images are created by reading the values directly from the sensor of the Thermoteknix camera, before any signal processing is applied to the readings. To achieve a stronger image a pulse train of 5 pulses at a repetition rate of 256 kHz is used for the signal laser. While this affects the overall modulation amount and temporal resolution, it is necessary as the QCL used is not able to deliver enough power over the distance of the optical path in a single pulse to generate a clear image.

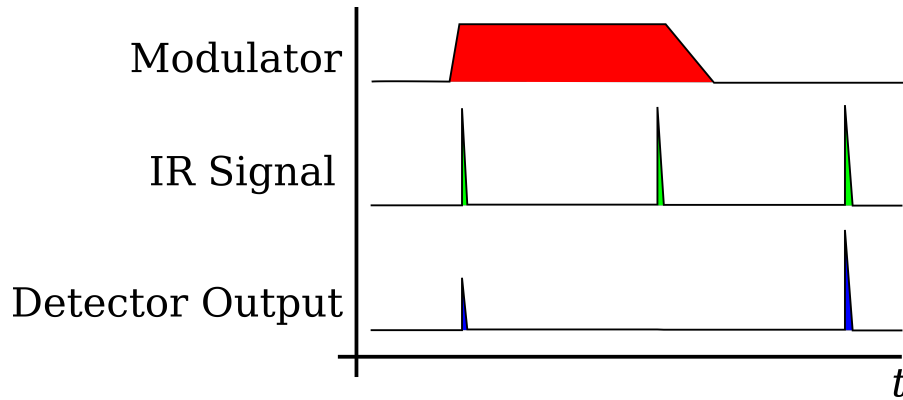


Figure 5.6: Timing diagram showing the effect of the time synchronisation of the modulator activation with respect to the signal laser. The first detected IR pulse in this schematic has not reached maximum attenuation as the carrier concentration has not had sufficient time to buildup. The signal is most attenuated just before the modulator is deactivated. The modulator has a very fast turn off, so the pulses after the modulator pulse are unattenuated.

5.2.3 Results

The results section is split into two subsections. The first covers the use of the modulator for ToF applications with an MCT detector. The second section discusses the results of using a thermal camera with the modulator to record and gate an actively illuminated object.

5.2.3.1 Time-of-Flight Demonstration

The ToF of the signal was compared between two optical paths with an MCT detector used to record the measured change in transmission at $10.07\text{ }\mu\text{m}$ after passing through the modulator. To achieve a high modulation contrast and reduce the stretching on the minima a short modulator pulse of $10\text{ }\mu\text{s}$ at a peak optical power of 69 W was used. This was compared to the short optical path to find the time difference. The ToF data for both paths can be seen in Figure 5.7.

It can be seen that there is a definite minimum position for the short optical path. However, the signal after the long optical path is an order of magnitude weaker once it

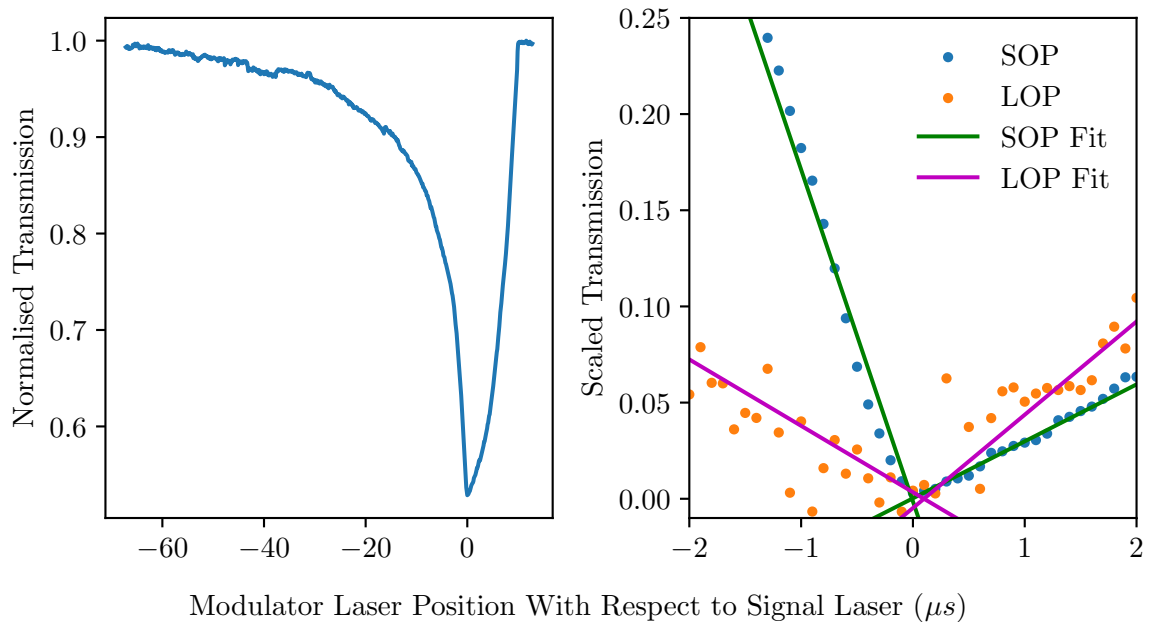


Figure 5.7: Normalised Time-of-flight data shown for the short optical path (SOP) in the left panel, and data for the long (LOP) and short optical paths in the right panel. The signals for the right panel have been normalised between 1 and 0. The intersections of linear fits were used to obtain the minima for both signals. The difference between minima on the abscissa determines the delay time introduced by travel along the longer optical path, corresponding to a distance of 30 m.

reaches the detector, with a significantly lower signal-to-noise ratio. The reduction in signal and increase in noise is mostly due to 12 extra mirrors used for extending the optical path and from divergence of the uncollimated QCL diode. To re-collimate the beam a group of lenses was used to maximise the signal on the detector, however this would have caused variation in the spot size on the modulator surface. The multiple reflections and change of the size causes deterioration of the overlap between the signal and modulator laser spots and worsening of the temporal resolution. The effect of this can be seen in the right pane of Figure 5.7, where the gradients around $0\text{ }\mu\text{s}$ for the short and long paths differ. Nevertheless, from the data seen in Figure 5.7, there is a clear difference observed between the positions of the signals minima. The analysis estimates an extra $(30 \pm 46)\text{ m}$ in path length difference, compared to the actual path length of $(18.0 \pm 0.5)\text{ m}$. This accuracy of the 30 m was calculated using the accuracy of the fit. The majority of the uncertainty originates from the long optical fit. A greater signal to noise ratio would significantly improve the accuracy of this system since the accuracy of the fit of the short optical path is greater by an order of magnitude.

5.2.3.2 Active Image Modulation

Investigation of the possibilities for active image modulation were carried out using the short optical path with the image recorded by an uncooled Thermoteknix MicroCAM3 camera. For this demonstration, a longer pulse was required to illuminate the object due to the low maximum optical output power of the signal laser. To increase the total irradiance, a train of five pulses at a repetition rate of 256 kHz for an illumination time of approximately $20\text{ }\mu\text{s}$ were used. The gating time of the modulator laser was adjusted accordingly to match the illumination time, but using one continuous pulse rather than 5 discrete ones. The peak optical power of the modulation laser was $\sim 67\text{ W}$.

To demonstrate the performance of the modulator for the active imaging a few snap

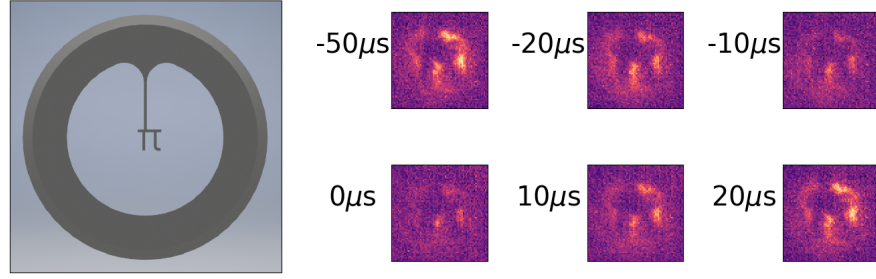


Figure 5.8: A selection of heatmaps of the π -symbol mask imaged by the thermal camera. The times correspond to difference between the modulation (gating) and signal lasers arrivals on the surface of the modulator.

shots were taken at the time instances before, after and at the maximum of the modulation. The data was taken directly from the sensor of the camera before any filtering is applied. To reduce shot noise 3 images were averaged to produce the final output for each gating time. Further processing of the image was carried out to reduce the background. The results can be seen in Figure 5.8 where $0\ \mu\text{s}$ signifies the closest point where the signal arrival and gating are nearly synchronised. A definite reduction in the transmission can be observed on the camera at and around $0\ \mu\text{s}$, with the transmission recovering to normal when the gating lags or is engaged earlier by more than $20\ \mu\text{s}$.

To quantify the observed change in the transmission an illuminated area of the image, rather than the entire image, was chosen. The square highlighted area in Figure 5.9(a) shows the area that was used to calculate the change in transmission. This area was compared to the same area of the unmodulated image. The change in transmission was calculated using equation 5.4,

$$T_{Average} = \sum_{n=1, m=1}^{n=5, m=5} \frac{\frac{Mod_{1,1}}{Unmod_{1,1}} + \frac{Mod_{2,1}}{Unmod_{2,1}} + \frac{Mod_{3,1}}{Unmod_{3,1}} + \dots + \frac{Mod_{n,m}}{Unmod_{n,m}}}{N} \quad (5.4)$$

where Mod and $Unmod$ are pixels values on the modulated and unmodulated images respectively, at pixel co-ordinates n and m , with N being the total number of pixels. The plot in Figure 5.9(b) was generated from this analysis and it shows visually that when the gating corresponds to the arrival the signal laser pulse there is a drastic reduction in transmission at this modulation power. The asymmetric rate of change of the transmission around the zero point is to be expected. The change of transmission is dependent on excited carriers, and the recovery in transmission is related to the relaxation rate of the carriers inside the silicon window. Therefore, for the modulator laser arriving before the signal laser, there may be still excited carriers. However, if a part of the signal laser arrives before the modulator laser then only a fraction of the signal pulse will be modulated.

To further investigate the modulator performance, in particular, to negate a possible effect of the residual heating by the modulator laser, the image was recorded by the thermal camera at multiple modulator states. This can be seen in Figure 5.10, which compares the images taken with the modulator laser disabled or gated following the arrival of the signal laser pulses. Apart from slight changes in the intensity when the modulator laser is active, the image remains mostly unchanged. The areas to take note of can be seen in the top right of the illuminated image and between the legs of π , which can be seen in Figure 5.10(a) and (b). This only occurs when the modulator laser is activated, regardless of its timing with respect to the signal laser. Comparing the images recorded in Figure 5.10(b) and (c), there is virtually no change between the gating activated at 500 μs and 50 μs away from the signal laser, confirming that modulation only occurs when the two pulses are overlapped, or if the modulator laser arrives a short period before the signal laser. This is crucial for imaging in general, as well as timing accuracy for applications such as 3D ToF, a distorted image by residual heating would be of no use.

The modulation contrast of the signal laser should follow the population of the free carriers excited by the modulation diode laser. Hence, varying the power of the modulator

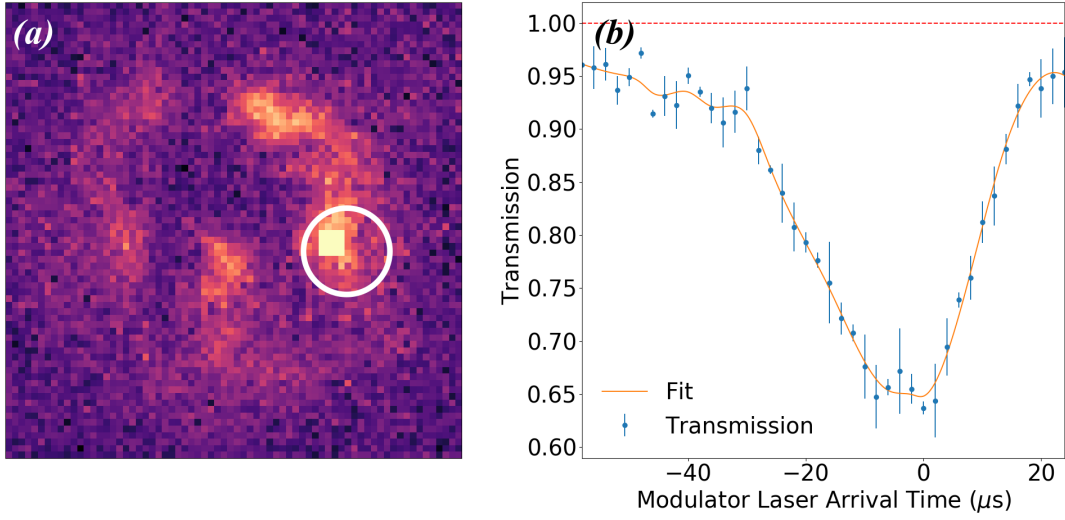


Figure 5.9: Transmission of the modulator as a function of the gating time with respect to the signal arrival time. $0\ \mu\text{s}$ represents the two lasers overlapped in time on the modulator surface. The highlighted square area in (a) shows the group of pixels used to obtain the average value of the signal intensity. Three thermal images were averaged per data point.

laser should vary the intensity of the signal recorded by the camera. To verify this, the modulator laser trigger was synchronised to provide the maximum attenuation of the signal. To vary the modulator power the peak current supplied to the modulator laser diode was varied. The results, presenting the signal intensity transmitted through the modulator as a function of the peak modulator power, can be seen in Figure 5.11. The measured change of the transmission was obtained using Equation 5.4 by comparing the intensity measured by the thermal camera under the maximum modulation of the same area when the modulator laser was gated $500\ \mu\text{s}$ before the signal laser. Due to the experimental setup constraints the modulator laser was used in an S-polarised configuration. Using the modulator laser in a P-polarised orientation would produce a stronger modulation for the same optical power as the absorption would be higher due to fewer reflection losses from the face of the modulator window. Nevertheless, an average change in transmission of approximately 60% was achieved at the highest optical pumping power.

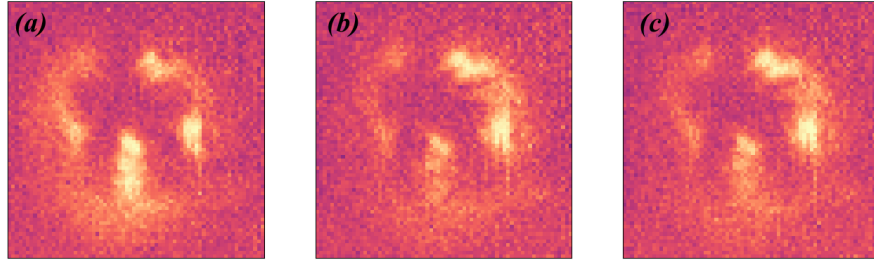


Figure 5.10: The following heatmaps show that there is little to no effect of the modulator laser when the signal laser is not overlapped with the modulator laser; (a) modulator laser disabled, (b) modulator laser occurs 500 μs after the signal laser, (c) modulator laser occurs 58 μs after signal laser. The slight changes can be attributed to thermal lensing effects by the minor increase its temperature.

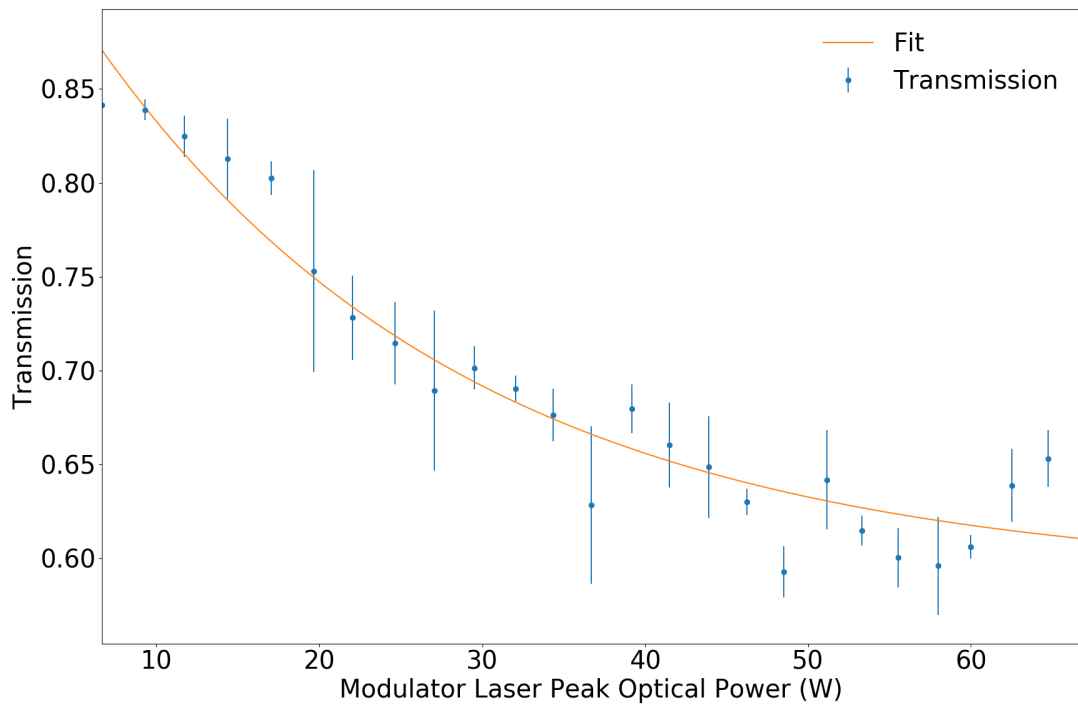


Figure 5.11: Transmission of the modulator as a function of the optical pumping power. Three thermal images were averaged per data point.

5.2.4 Summary of Compact RGAI & ToF System

In summary, we demonstrated that it is possible to gate an uncooled thermal camera as well as an MCT detector and resolve sub- μ s changes. This was done with two demonstrations, firstly we calculated the length of an optical path by comparing the difference in ToF between a short and long optical path. We show that optical path of 18 m difference can be resolved, albeit the resolution requires significant improvement. Secondly, we placed a mask of π in the beam path and scanned the modulator gate to demonstrate the ability of the modulator to be used for active imaging. Overall, we demonstrated the ability to measure the arrival time of the signal laser on an uncooled thermal camera with resolution approaching a few μ s, with a relatively compact system. We believe the all-optical modulator can be used in the applications such as rangefinding and RGAI in the LWIR. With further development and use of a stronger IR source the potential for a LWIR ToF/RGAI device comes one step closer to the reality.

5.3 Porous Silicon Based Modulator

Using structured silicon, such as porous silicon, allows for the tuning of the operating bandwidth of the modulator by adjusting the structure parameters. By carefully tuning pore size as well as the amount of oxidation of a porous silicon's structure, the recombination time, and activation energy can be tuned. In the accepted paper, *Taming non-radiative recombination in Si nanocrystal interlinked in a porous network*, it was found that the surface passivation determined the recombination mechanism, while a porosity increase would hasten the recombination rate due to spatial confinement. Hydrogenated samples would exhibit a slower recombination rate, compared to an oxidised sample of the same porosity, shown in Figure 5.13.

To determine the optical response of the nano-porous modulator, the pump (800 nm) probe (2.5 μm) experiment was used, as discussed in Chapter 3. The power was fixed for each sample to only generate a free carrier concentration of $N \approx 7 \times 10^{19} \text{ cm}^{-3}$ for each sample so the recombination rate could be compared between them. The nano-porous silicon used had a thickness of 120 μm , with porosities varying from 66% to 88%. The samples were oxidised in an oven set to 600 $^{\circ}\text{C}$. To measure the structural properties of the nano-porous silicon, the Brunauer-Emmett-Teller method was used. These oxidised nano-porous membranes could then be re-hydrogenated after oxidation in a hydrofluoric dip with a 10% concentration for 30 seconds, which from the results seen in Figure 5.12. This process returns the nano-porous silicon to its pre-oxidised state. The process of re-hydrogenating reduces the abundance of oxide bonds (see Figure 5.12), which are one of the causes for increased recombination rate. In addition, Figure 5.13 shows the carrier density for hydrogenated and oxidised porous silicon as a function of time after excitation by the pump pulse.

The results of this paper highlight the ability to adapt the recombination rate in nano-porous silicon samples. By harnessing this knowledge and technology, highly customisable modulators could be fabricated by tuning the amount of oxidation and porosity, allowing for the perfect high speed Infrared (IR) modulator to be created.

(Figure 5.12 and 5.13 appear *Rihan Wu, Elida Nekovic, Jack Collins, Catherine J. Storey, Leigh T. Canham, Miguel Navarro-Cía, and Andrey Kaplan* **Taming non-radiative recombination in Si nanocrystals interlinked in a porous network** Physical Chemistry Chemical Physics. 2022 (Accepted))

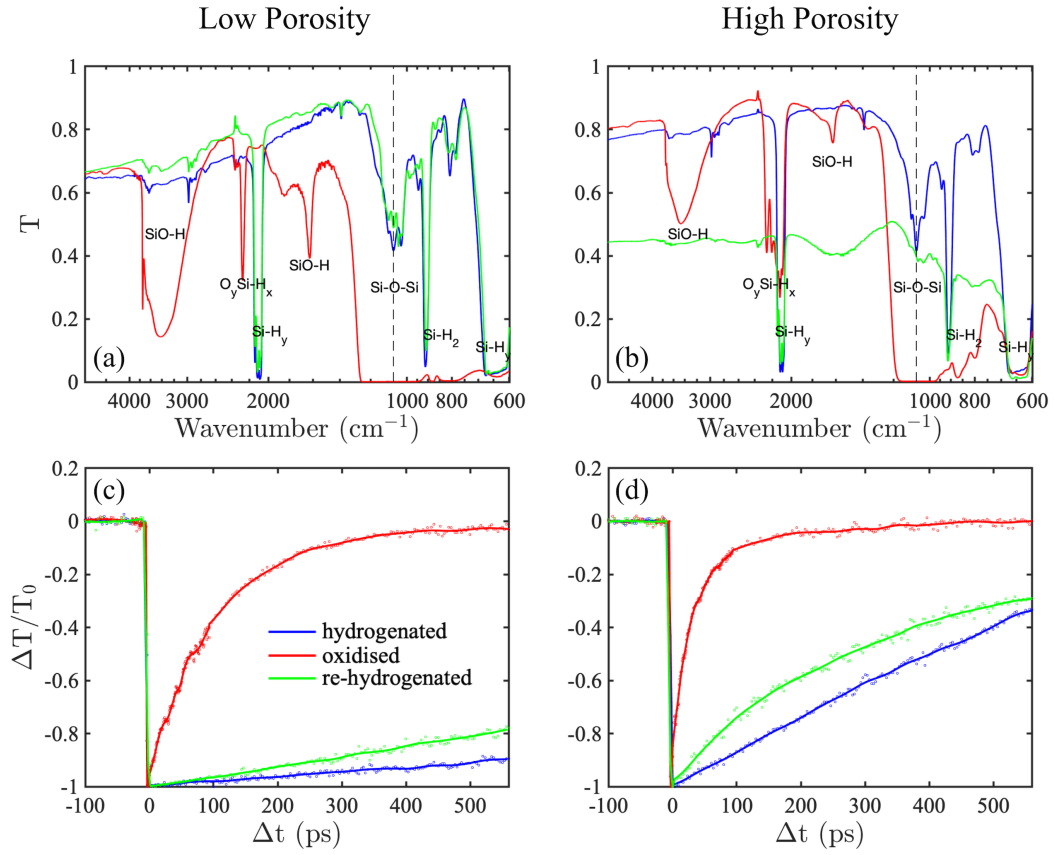


Figure 5.12: Fourier Transform Infrared (FTIR) spectrums (a-b) and pump-probe results (c-d) for low (a,c) and high porosity (b,d) samples. Higher porosity samples show a faster recombination, while across the board, hydrogenated samples show slower recombination. It is speculated that collapsing pores after re-hydrogenating the nano-porous silicon may have caused the difference between the hydrogenated and re-hydrogenated silicon for the FTIR spectrum and pump-probe results.

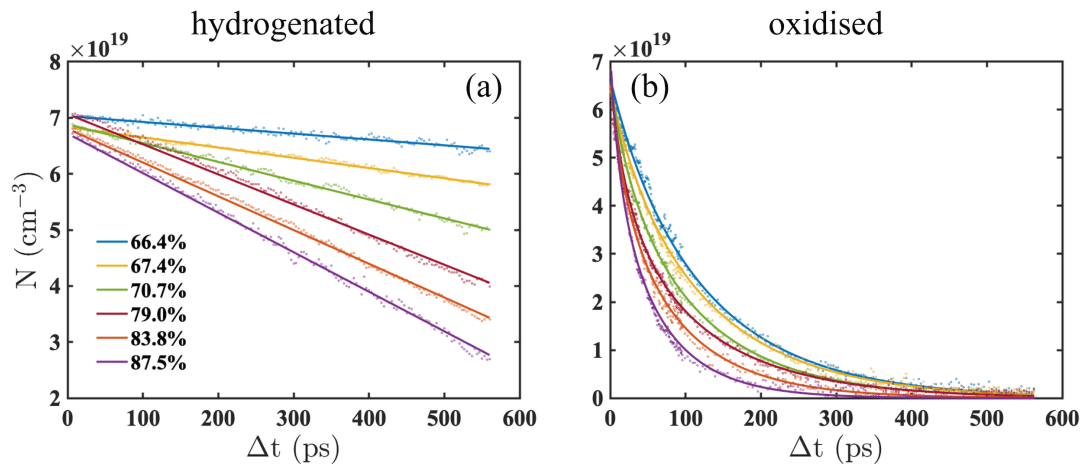


Figure 5.13: Recombination rate of hydrogenated and oxidised samples at varying porosities. Oxidised samples exhibit a much faster recombination rate, returning to normal levels of carriers significantly sooner than hydrogenated samples.

Chapter Six

MWIR Time of Flight

6.1 Introduction

While the optical filter technology discussed in previous sections has an obvious home in Mid-Wave Infrared (MWIR) and Long-Wave Infrared (LWIR) cameras, another potential application for MWIR is for use in time of flight range finders and cameras. Currently, there exist no known MWIR optical rangefinder on the market, so a custom solution, with accompanying electronics, has been designed and built. Optical Time of Flight (ToF) rangefinding is the process of measuring a distance by timing the round trip of light. The most basic setup would involve a time piece, photon source and detector. The distance can then be obtained by measuring the time between emitting a pulse of light and detecting the backscattered light. While ToF is a reasonably well established area in defence, it has only recently started to emerge in the consumer space. The majority of these devices utilise Near Infrared (NIR) and Short-Wave Infrared (SWIR) as the illumination source, predominately due to the abundance of fast source and detector technology which is a requirement for precise and fine measurements. However, there are some drawbacks to using these wavelengths of light. Shorter wavelengths of light, relative to MWIR and LWIR, will suffer from atmospheric scat-

tering, as described in Chapter 2. This issue could be overcome with the use of a stronger light source, however this would introduce further drawbacks. Increasing optical power will reduce suitability for many applications due to the increased size, power consumption, and risk to eyes. This is especially dangerous at NIR, since the eye has a reduced blink reflex at this wavelength and is still able to focus this wavelength of light onto the retina. The longer wavelengths of MWIR and LWIR should offer a much greater ranging distance with similar pulse energies, but with the reduction of the risk to eyes. By using MWIR or LWIR would enable the use of stronger lasers, theoretically increasing the ability to measure greater distances.

However, the optical design and implementation is only half the story; the signal processing and timing circuitry needs careful consideration to reach its full potential. In the most basic laser ToF rangefinding system, the primary components required are a laser source, detector and measurement device (such as an oscilloscope). This equipment can then be used to measure the difference between the emission of the pulse of light from the laser, to the arrival time of the reflected signal. Relying on a rising edge to generate a reliable stop signal for a Time to Digital Converter (TDC) would likely lead to inaccurate timings, especially if the rise time of the source or detector is slow. Further issues are encountered when signals of different amplitudes are produced by the detection circuitry. Without sampling the wave and maintaining a set fraction trigger point, timing inaccuracies due to amplitude walk can be introduced. With a set threshold voltage, signals of lesser amplitudes will appear to occur later than ones with greater amplitudes, provided the rise time remains the same. Varying amplitude can be caused by atmospheric scintillation, detection noise, source variation, and targets of varying reflectivities. Therefore, depending on an oscilloscope alone is not reliable, nor the fastest way of measuring the timing delay between the signal and reflected signal.

This chapter will investigate the feasibility of a MWIR rangefinding device. Initially,

the optical setup will be discussed, then the focus will be turned to the signal processing electronics and timing devices. The design of these will be covered, and the efficacy investigated. This MWIR rangefinder will then be compared to a Visible (VIS) rangefinding device. Circuit diagrams of the high speed preamplifier, CFDv4, CFDv6, and TDC circuit can be seen in Appendix A.1, A.2, A.3 and A.4, respectively.

6.2 Optical system design

To evaluate the performance of the MWIR rangefinder, a benchmark VIS rangefinder system was built. This benchmarking system would establish a baseline for the MWIR system, and verify the accuracy of the TDC. A general schematic diagram of the experimental setup can be seen in Figure 6.1. This benchmark system used a 633 nm laser diode as the source, coupled with a SNEG-250-20-N laser driver produced by Ikeos Research. This laser driver is able to produce 800 ps width pulses. To detect the signal, a Thorlabs Si detector was used with a rise time of 1 ns. A computer-controlled translation stage was used to adjust the path length to test the resolution. The translation stage, a VT-80, offers a maximum resolution of 200 nm, with a repeatability of ± 400 nm when travelling in one direction. This corresponds to a temporal change of 13 fs, far beyond the capability of the TDC used.

In the MWIR investigation, the VIS laser was replaced for a Quantum Cascade Laser (QCL) Distributed Feedback (DFB) source produced by Hamamatsu emitting at 4.48 μm . To drive this laser, a Hamamatsu C11635 is used which is able to generate a 10 ns optical pulse. A lens was fitted to the front of the driver to aid collimation of the beam. This MWIR investigation used both an Mercury Cadmium Telluride (MCT) and a InAsSb detector in two separate sub-experiments. The InAsSb detector was fitted to the translational stage itself, whereas the investigation using the MCT was at a fixed position only. The detectors

used were a photoconductive model J15 MCT produced by Teldyne Judson, coupled with a Teldyne Judson PA-101 pre-amplifier, and a InAsSb P13243-011MA detector produced by Hamamatsu. The MCT detector has a rise time on the order of 400 ns, whereas the Hamamatsu photodiode has a rise time on the order of 15 ns. However, the InAsSb is not as sensitive as the MCT. Therefore, a germanium lens is used to increase the collection power of the system.

6.3 Electrical System

While the optical system may seem straightforward, the electrical system is more complex. The electrical signal path can be seen in Figure 6.1. There are three key elements that require consideration for the MWIR rangefinder: the detector and preamplifier for detection, the analogue circuitry required for the Constant Fraction Discriminator (CFD), and the digital control for the TDC. Each of these elements will be discussed in turn in the sections below.

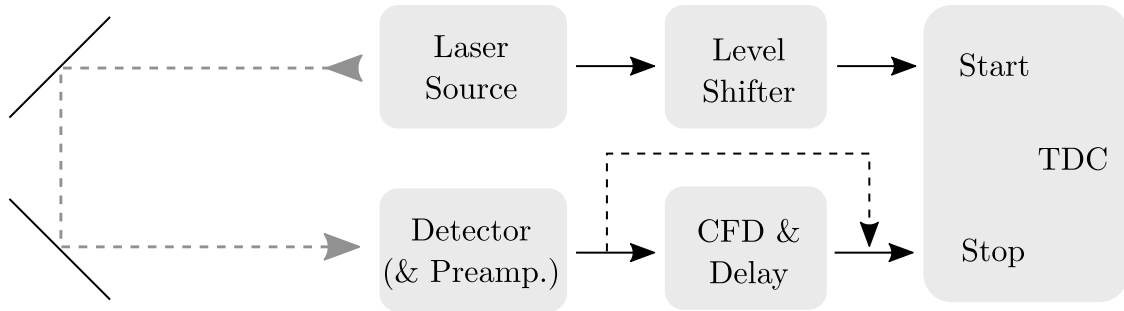


Figure 6.1: Schematic of optical and electrical setup for the MWIR rangefinder. The optical signal is provided by a laser diode, and is directed along a variable optical path (633 nm and 4.48 μm InAsSb) or fixed optical path (4.48 μm MCT), represented by the grey dashed line. The electrical signal path is represented by the black solid line. When benchmarking the system, the *CFD & Delay* was omitted, represented by the black dashed line, as the rise time of the visible photodiode is on the nanosecond scale. The start signal is provided by the laser driver, and is first put through a level converter to ensure compatibility with the TDC. The TDC will measure the time between the start and stop signals.

6.3.1 High Gain-Bandwidth Preamplifier

Starting with detection, this work uses two detector technologies in this setup. The MCT detector used in this research is provided with a preamplifier by the manufacturer (Teldyne Judson). On the other hand, the InAsSb photodiode used does not come with a matched preamplifier. Compared to the MCT, the InAsSb photodiode is much less sensitive, resulting in the need for preamplification. Hamamatsu offer a compatible amplifier for the InAsSb detector, however it is a general purpose amplifier that would result in the fast rise time of the InAsSb photodiode being lost due to the slow rise time of this preamplifier. In brief, any benefit of using this photodiode is lost as the response will be stretched by the preamplifier available from Hamamatsu. Consequently, a high speed preamplifier must be designed and built to maintain a fast rise time.

Achieving a high gain while maintaining a wide bandwidth is not a straightforward task. At the heart of an preamplifier lies at least one Operational Amplifier (opamp). These Integrated Circuits (ICs) are responsible for providing the gain. The InAsSb detector used in this work will be operated in photocurrent mode, and as a result a Transimpedance Amplifier (TIA) is required. The topology of a TIA can be seen in Figure 3.7, and its gain can be set using by the feedback resistor, $V_{out} = R_F I_{photo}$, where R_F is the feedback resistance and I_{photo} is the current produced by the photodiode. In comparison to the MCT detectors used in this work, which has a responsivity of $1 \times 10^3 \text{ V W}^{-1}$, the InAsSb detector chosen produces 1 mA W^{-1} . Therefore, to produce signal comparable to that of the MCT, the photodiode needs a gain of approximately 10^6 V/A .

When designing a high speed amplifier, one of the key opamp parameters is the gain-bandwidth product. This value sets the maximum gain achievable at a certain bandwidth before the 3 dB rolloff. The opamp selected for this work is the OPA657 produced by Texas Instruments. The OPA657 offers a 1.6 GHz gain-bandwidth product, but this is still not

enough to achieve the high gain required while maintaining the fast rise time. Fortunately, it is possible to cascade amplifiers in series to achieve a higher gain, without impacting the bandwidth as significantly as using a single opamp with the same gain. The resulting gain of a cascaded amplifier circuit is the gain of each amplifier multiplied together. This effect can be seen in high gain amplifier circuits, which often offer separate outputs for each stage. The ability of accessing earlier amplification stages increases flexibility, this feature is found in the PA-101 preamplifier used with the MCT. In the circuit designed for the InAsSb preamplifier, two OPA657s have been used to achieve a high gain without significantly impacting the maximum bandwidth. The first stage offers a gain of 10,000, while the second offers a gain of 1000, giving a combined gain of 10^7 V/A.

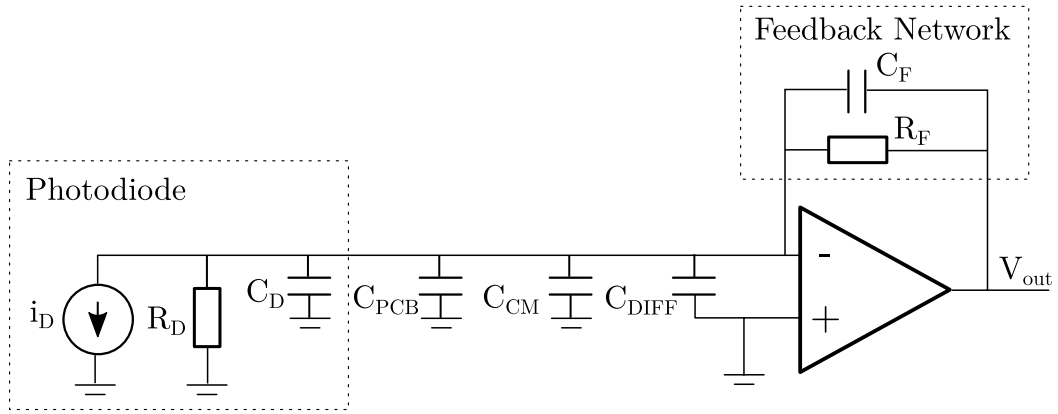


Figure 6.2: TIA with included stray capacitances: capacitance due to circuit board layout and soldering C_{PCB} ; the common mode, C_{CM} , and differential mode, C_{DIFF} stray capacitances; and C_D , the diode capacitance. The photodiode has been separated into its constituent components.

Starting with the TIA portion of the preamplifier, a design process needs to be followed to make sure the circuit operates smoothly without instability issues, which will lead to ringing and oscillation on the output. The document, SBOA268A found at [162], was used as a resource to design the TIA discussed below. Since the preamplifier uses two cascaded opamps to achieve the high gain, the TIA gain was set to 10000. While an ideal TIA would only consist of a current source, in this case a photodiode, an opamp and a feedback resistor. However, photodiodes have an intrinsic capacitance and resistance, and opamps have

capacitances on the input. Not only this, the layout and construction of the Printed Circuit Board (PCB) can also introduce stray capacitances. If these parasitic stray capacitances go unchecked, they can generate instability. This is because the capacitances introduce a lag to the response of the amplifier, which leads to positive feedback and oscillations. A more complete schematic of a TIA, with parasitic capacitances, can be seen in Figure 6.2. The instability identified here will be discussed later, as initially the theoretical bandwidth of the TIA needs to be calculated using the following equation:

$$f_{-3dB} = \sqrt{\frac{GBWP}{2\pi R_F C_D}} \quad (6.1)$$

where f_{-3dB} is the -20 dB/decade roll off, $GBWP$ is the gain-bandwidth product, R_F is the feedback resistance. The C_D are the combination of stray capacitances from: the diode, the PCB and opamp inputs capacitances. When applied to this set up, the C_D term is calculated as follows: the diode capacitance is 0.7 pF, the capacitances for the differential and common-mode inputs for the opamp are 0.7 pF and 4.5 pF, respectively. An estimate of the PCB capacitance gives a total C_D of approximately 6 pF. Using Equation 6.1 and the value for C_D calculated previously, results in a f_{-3dB} point at 65.1 MHz.

To compensate for the induced instability identified above, from the diodes parasitic capacitance, a feedback capacitor, C_F , can be added in parallel with the feedback resistor, R_F . While C_F tames the instability, it simultaneously imposes an f_{-3dB} bandwidth cutoff of its own, reducing the bandwidth of the TIA if not chosen carefully. To calculate a suitable value which does not affect the previously calculated bandwidth, the following equation is used:

$$C_F \leq \frac{1}{2\pi R_F f_{-3dB}} \quad (6.2)$$

Where f_{-3dB} was the previously calculated bandwidth of 65.1 MHz, which gives a value of 0.2 pF for C_F . While this value for C_F allows the TIA to achieve a bandwidth of 65.1 MHz that was set initially, it is not realistic to use such a small value. Consequently, C_F will be switched out for 1 pF to still maintain a high bandwidth. The stability of the circuit can be verified using the following equation:

$$GBWP > \frac{C_F + C_D}{2\pi R_F C_F^2} \quad (6.3)$$

which gives a value of 111,000, less than the $GBWP$ of the OPA657. The theoretical rise time of the amplifier can then be calculated using the following equation [163, p. 49], with the new f_{-3dB} point at 16 MHz due to $C_F = 1$ pF:

$$t_r = \frac{0.35}{f_{-3dB}} \quad (6.4)$$

For the values selected, a rise time of 22 ns is achieved. This is of course, entirely theoretical, and does not account for capacitances introduced from soldering and the circuit board layout, to name a few. After building the board these values were adjusted, especially for the feedback network.

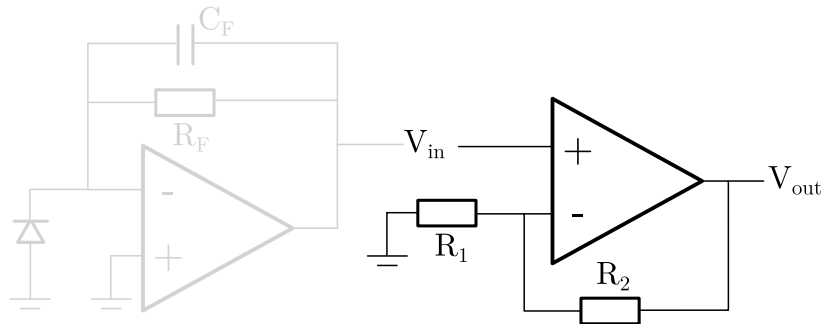
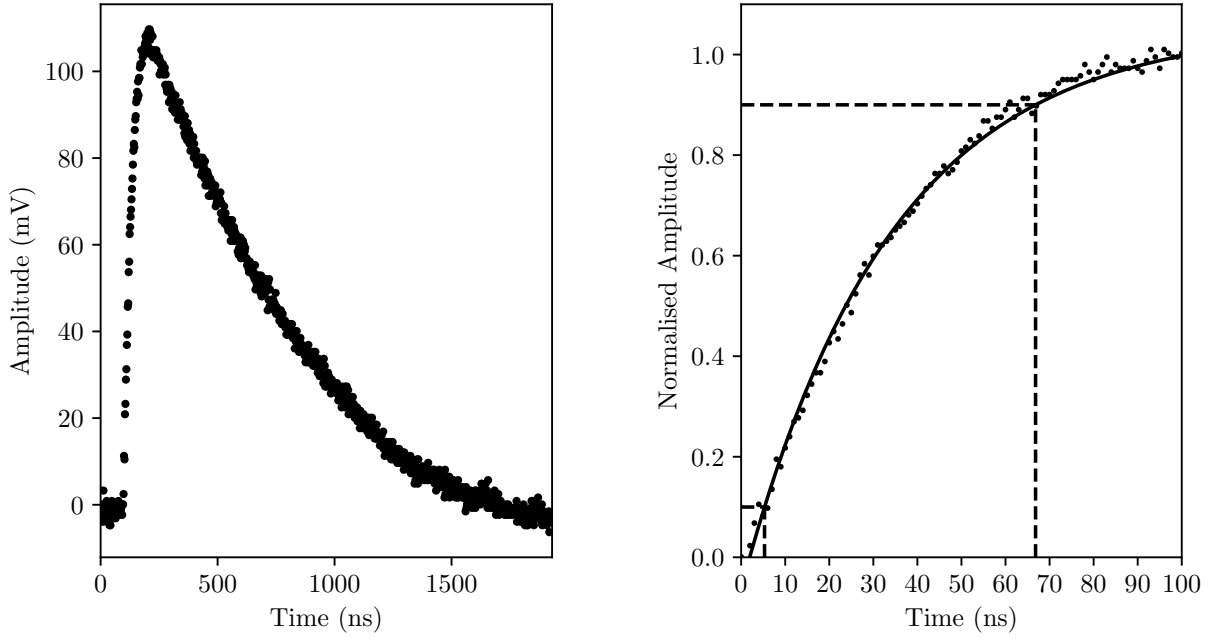


Figure 6.3: Wide bandwidth non-inverting amplifier with a gain set by $V_{out} = V_{in}(1 + R_2/R_1)$. The greyed out section shows the simplified TIA schematic, the first stage of the preamplifier circuit.

The second stage of the preamplifier is a wide band voltage amplifier. This second amplifier takes the output of the TIA and amplifies it further to ensure a wide bandwidth operation. The second OPA675 is in a non-inverting configuration, as can be seen in Figure 6.3. The values chosen for R_1 and R_2 are $1\text{ k}\Omega$ and $1\text{ M}\Omega$, respectively. These resistor values give a gain of 1000, while maintaining a bandwidth of 160 MHz, as calculated from $GBWP = \text{Gain} \times \text{Bandwidth}$. This combination of gain and gain-bandwidth product leads to a rise time of 2 ns, however, this rise time is limited by the rise time of the TIA. The resulting performance of the preamplifier can be seen in Figure 6.4. Figure 6.4a shows the overall response of the preamp, with Figure 6.4b focussing on the rise time. From Figure 6.4b it can be seen that the rise time is on the order of 60 ns, far from the predicted rise time of 22 ns. The rise to of 60 ns was calculated by fitting an exponential curve to the points and then calculating the time difference between 10% and 90% of the signal amplitude. A possible explanation for this increased rise time would be parasitic capacitance in the feedback network which was not included in the original calculations from the circuit board layout. While this rise time is approximately three times worse than the predicted performance, it still offers a faster response than that of the MCT used in this work.

6.3.2 Constant Fraction Discriminator

Following the preamplifier is the CFD, which is designed to improve the temporal accuracy of the system. Since the two detectors used have significantly different rise times, two separate CFDs with their corresponding delay lines were developed. As discussed in Chapter 3, the CFD is a circuit that is able to output a trigger on reception of a detector signal to high temporal accuracy, while avoiding the uncertainty introduced from amplitude walk. Like the high speed preamplifier mentioned above, a CFD had to be designed and created. In total, there were six revisions of this board, with versions four (CFDv4) and six (CFDv6)



(a) Response of the high speed, two stage, InAsSb preamplifier, with an approximate gain of 10^7 V/A.

(b) Rising edge of preamplifier output with an exponential fit. Dashed lines represent 10% and 90% of the signal.

Figure 6.4: Preamplifier response with the InAsSb photodiode. Rise time calculated to be 63 ns using the exponential fit.

being the most successful. The CFD can be split up into sub-circuits: the arming, delaying, attenuation and mixing, and zero crossing subcircuits. Each of these will be discussed in turn. Firstly, the input signal is tested against a threshold, this arms the output of the CFD. Arming the CFD lessens the chance of outputting a trigger pulse due to noise. The signal is then split along two separate paths, one delayed by a pulse length, and the other is inverted and attenuated. Following this, they are then mixed back together. Finally, the signal is fed into a comparator, which looks for the zero crossing point. When a zero crossing point is detected, and the CFD has been armed, a trigger pulse is outputted from the system. A schematic of the CFD can be seen in Figure 6.5.

To complement Figure 6.5, key points of the CFDv6 circuit were measured, this can be seen in Figure 6.6. Each plot in Figure 6.6 shows a distinct point in the circuit, and

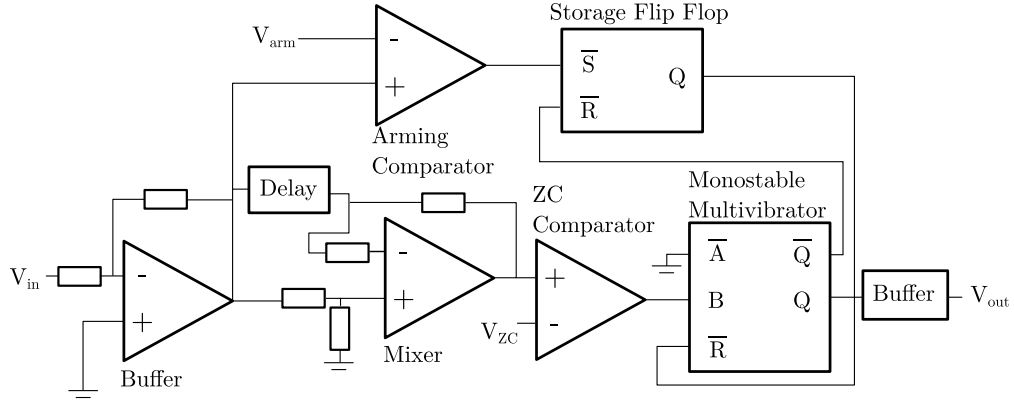


Figure 6.5: Schematic highlighting primary components of the CFDv6 circuit. An input signal, V_{in} is first inverted, before then being split into three paths. Detail of the signal path is covered in text. V_{arm} is the arming threshold voltage, V_{zc} is the zero crossing voltage.

what the signal looks like with a given input. These steps will be discussed in detail in the following paragraphs.

6.3.2.1 Input Buffer

The input buffer stage handles the signal separation and suitable 50Ω termination for the preamplifier. In earlier designs, BUF602s were used which are suitable for high bandwidth applications and unity gain. However, these buffers were later switched out for OPA657s to allow for additional gain to be applied while simultaneously inverting the signal.

6.3.2.2 CFD Arming

The arming of the system is handled by a comparator (see Figure 6.5). Under normal conditions, the IC holds its output high. When a strong enough pulse enters the system, the output of the IC drops to 0V. The threshold for the comparator going low is set by V_{arm} . Since the pulse may only be momentarily strong enough to trigger the comparator, this signal must be stored. To store the armed status, the flip-flop IC can be used. This records the status of the comparator, passing on the status to the monostable vibrator. A truth table

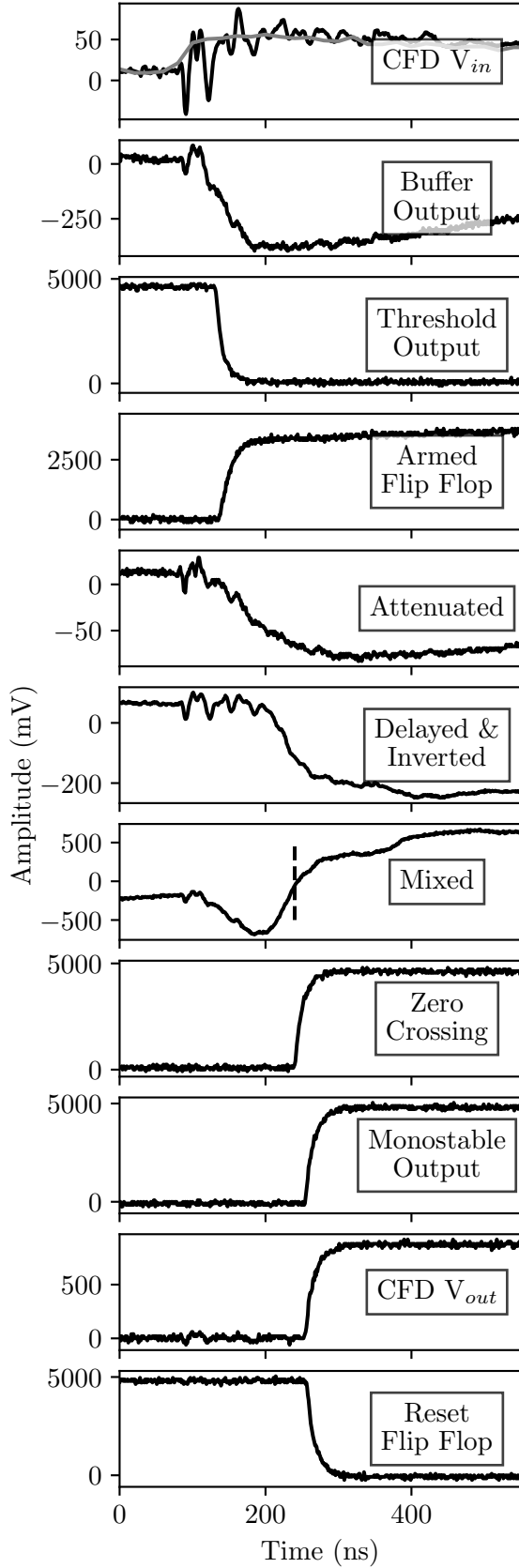


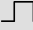

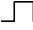

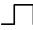
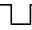
Figure 6.6: Progression of the signal throughout the CFD. Firstly a signal is supplied to the CFD ($CFD V_{in}$), the grey line is to guide the eye. This signal is buffered, inverted and amplified (Buffer Output). This is then split into three paths, the arming comparator outputs a low signal when a strong input is detected (Threshold Output), which is then stored in the storage flip flop, which outputs a high signal (Armed Flip Flop), which enables the output of the CFD. The attenuated, and the delayed and inverted pulses are mixed by a second OPA657 configured in a differential amplifier configuration, applying a small level of gain to generate the amplitude difference between the two signal. The zero crossing is then found in the mixed signal, represented by the dashed line. When the zero crossing (ZC) point is detected, the (ZC) comparator output goes high, triggering the output of the monostable vibrator. To buffer the signal, another comparator is used ($CFD V_{out}$). Finally the system is reset by the inverted out of the monostable vibrator, which resets the flip flop.

of the operation of the flip-flop (74LS279) and monostable multivibrator (74HC123) used can be seen in Table 6.1. The role of the monostable multivibrator will be discussed below. Without storing the signal, the arming comparator may return to its untriggered state before the zero crossing comparator is triggered. Storage of the armed signal is required for finding the zero crossing point.

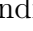

The threshold voltage is set by a variable potentiometer, so it can be adjusted dependent on the signal. In earlier designs this was a single turn 10 k Ω trimmer, however this was later substituted out for a ten-turn potentiometer for higher accuracy. Although not implemented in these designs, a second monostable multivibrator could be used to reset the flip-flop after a set period. This second monostable multivibrator would reset the system if no zero crossing was detected after a set period, disarming the system. This disarming method would reduce the chance of outputting a trigger due to noise. Due to the long rise time of the MCT detector, in CFDv4, the arming pulse was delayed before enabling the output monostable vibrator. This delay was implemented because of the long signal delay required to generate the bipolar pulse for finding the zero crossing point. This delayed arming of the output monostable multivibrator reduces the likelihood of the CFD outputting before the zero crossing point due to noise. The delay for the output monostable vibrator was induced by monostable multivibrator positioned after the arming comparator. The RC constant for this delaying monostable multivibrator was set to match that of the delay between arming and the zero crossing point.

6.3.2.3 Delay Line

To generate a bipolar pulse required for the zero crossing detection, a delay must be introduced to the signal through the means of a transmission line. If a fast silicon detector was used, this would be a simpler task and a circuit designer could use a longer track on the

			\overline{A}	B	\overline{R}	Q	\overline{Q}
			H	X	H	L	H
			X	L	H	L	H
\overline{S}	\overline{R}	Q	L	\uparrow	H		
H	H	Q_0	\downarrow	H	H		
L	H	H	X	X	L	L	H
H	L	L	X	L	H		
L	L	H					

(a)
(b)

Table 6.1: Truth tables for \overline{S} - \overline{R} flip flops (a) and monostable vibrator (b). In both cases, Q and \overline{Q} represent the outputs, while all other terms are inputs. H and L represent high and low signal inputs respectively. A Q_0 output maintains the previous output state, while  and  represent high and low pulses. X represents an indifference to the pin polarity. \uparrow and \downarrow represent rising and falling edges, respectively. The CFD circuit outputs a trigger when the conditions highlighted are achieved.

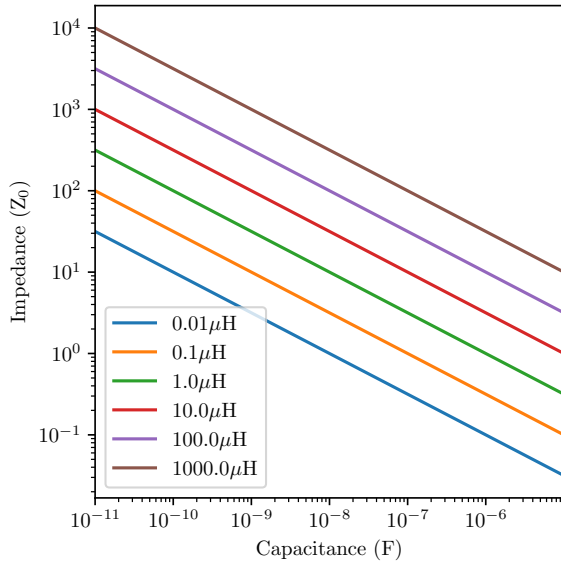
PCB to delay the signal. Unfortunately, this is not possible with the detectors used in this work, given that a longer delay, on the order of 70 ns is required for the InAsSb detector, and around 400 ns for the MCT. The most reliable way of generating a sizeable delay is using a custom designed transmission delay line. Usually, transmission lines are designed to reduce the propagation time, impedance, and attenuation of an electrical signal to maximise power delivery at the fastest rates. The reduction in transmission delay is achieved by minimising the capacitance and inductance of the transmission line. The attenuation is minimised by using low resistance materials, while the reduction of the impedance is achieved by balancing the ratio of inductance to capacitance. The delay induced from the transmission line can be made longer by increasing the inductance and capacitance of the signal path. While this could be done by using a very long PCB track or BNC cable, it is not a practical solution. To achieve a delay of 70 ns, a BNC cable of approximately 21 m is needed. Therefore, discrete capacitors and inductors are required. The impedance and delay time of a signal path can

be calculated using the following Equations 6.5 and 6.6 [126, p. 1126]:

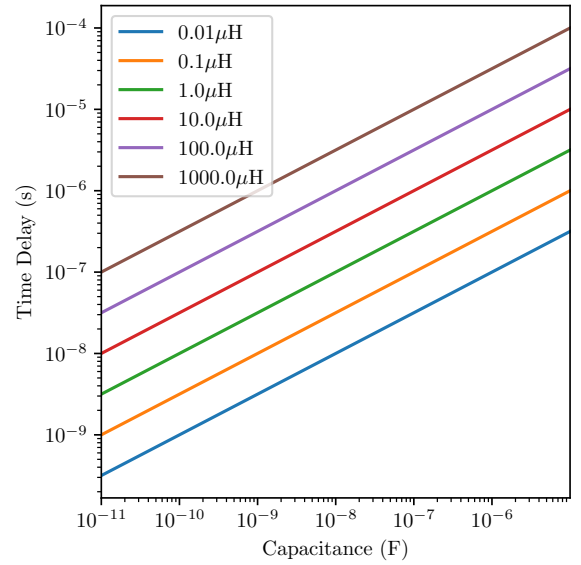
$$Z_0 = \sqrt{L/C} \quad (6.5)$$

$$t_p = N\sqrt{LC} \quad (6.6)$$

where Z_0 is the path impedance, L and C are the inductance and capacitance per unit length, respectively. t_p is the delay induced by the path, and N is the number of transmission line elements. Plots showing how the capacitance affects delay and impedance with varying inductances are shown in Figure 6.7. A schematic representation of a transmission line with source and sink can be seen in Figure 6.8.



(a) Capacitance against impedance for various inductance values. Plotted from Equation 6.5



(b) Capacitance against delay time for various inductance values. Plotted from Equation 6.6.

Figure 6.7: Dependence of capacitance and inductance on delay and impedance of a signal path.

The final values of the inductor and capacitor for the InAsSb detector delay, after

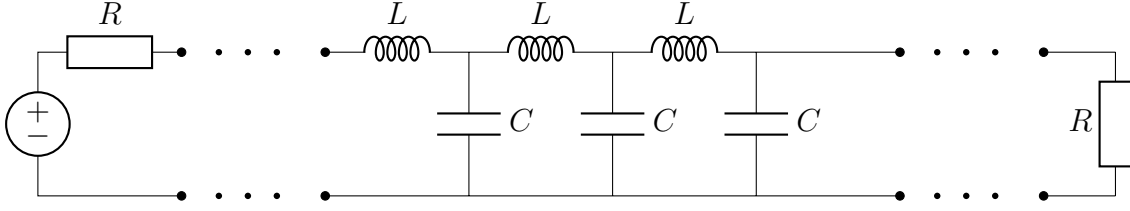
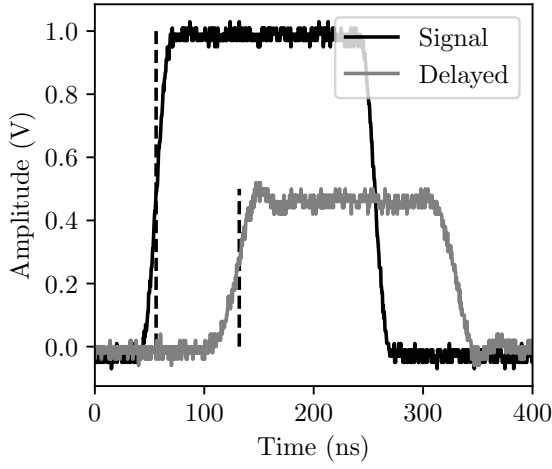


Figure 6.8: Transmission line circuit, designed to achieve the maximum power transmission, and avoid reflection. The source and sink resistance R should be matched to the transmission line impedance. A unit of the transmission line is an inductor followed by a capacitor.

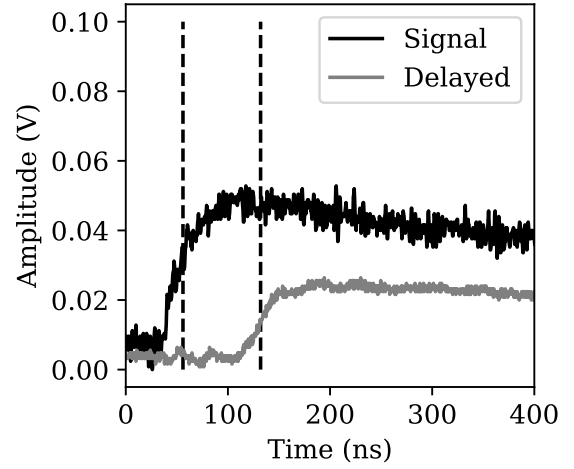
tuning to achieve the best result, were 0.47 μH and 180 pf, respectively. There were seven of these units in total, which should produce a delay of 73.58 ns when calculated using Equation 6.6. To verify that the circuit matched the requirements, a step function (produced by an Arbitrary Function Generator (AFG)) with a rise time of 18 ns was applied. The results have been plotted in Figure 6.9a. From this plot it can be seen that the rise time is not as fast as the applied wave, and that there is a small amount of ringing visible. This ringing is mostly likely due to an impedance mismatch. However, when the high speed InAsSb detector is used as the signal source, the ringing disappears and the delayed signal more closely matches that of the applied wave (Figure 6.9). That said, the attenuation of the pulse is strong, and is reduced to 45% of its original value.

6.3.2.4 Bipolar Pulse Generation

To mix the delayed wave with the original signal, an opamp is used in a differential amplifier topology. Using an active mixer over a passive one allows for amplification to be applied and handles the inversion of the delayed signal. The OPA657 was used for this due to its high bandwidth and familiarity. The undelayed signal comes straight from the buffer opamp and is fed into the non-inverting input. There is no need to invert this signal as the buffer handles this. The delayed signal is fed into the inverting input to generate a positive pulse. An amplification of 3.9 was applied to the delayed wave to compensate for the attenuation of



(a) Delay induced to a step pulse provided by an AFG.



(b) Delay board used with the high speed InAsSb detector.

Figure 6.9: Delay induced by the delay board. Dashed lines cross the signal at 50% of amplitude of the pulse and are spaced 76 ns apart. Attenuation of the pulse can be attributed to the Direct Current (DC) resistance of the inductors.

the delay circuit and to provide the ratio between delayed and inverted signals required for the operation of the CFD. The output of this mixer can be seen in Figure 6.6 and simulated in Figure 6.10. After mixing, the signal is compared against V_{ZC} , which is set below 0 V by a few mV. The zero crossing comparator will transition from low to high during the negative cycle of the bipolar pulse, before transitioning high after the zero crossing point. The rising edge will trigger the monostable vibrator as shown by the highlighted row in Table 6.1, where R will be high if the system is armed.

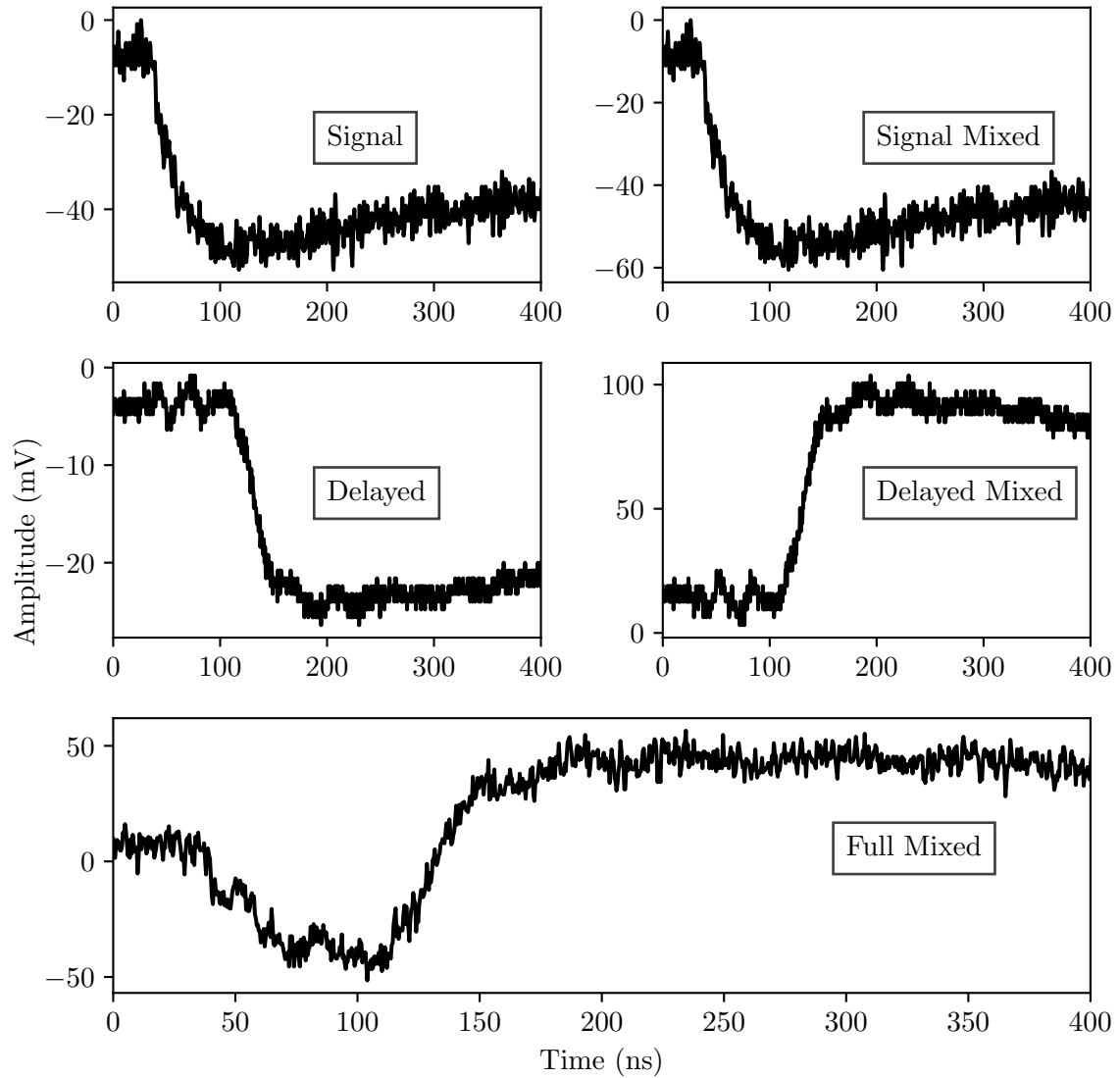


Figure 6.10: Simulation showing how the delayed signal is mixed with the signal from the buffer. The top and middle right waveforms have been calculated from the theoretical gain applied by the mixer opamp, with the bottom waveform being summed from the two mixed signals.

6.3.2.5 CFD Output

Since the monostable vibrator is unable to provide enough current to drive a $50\ \Omega$ terminated device, a line driver buffer is used. In this case, a LT1719 comparator is used with a 1 V

amplitude. The pulse width of the output of the CFD, V_{out} , is set by an RC constant connected to the monostable multivibrator.

6.3.3 Timing

The final signal processing step in this chain is recording the time difference between the start, produced by the internal trigger of the QCL, and the output of the CFD. To accomplish this, a TDC is used. As mentioned in Chapter 3, TDCs are the most reliable way to measure ToF operating in a pulsed mode. TDCs can be implemented relatively easily with minimal components and without the need for powerful computing demands that Digital Signal Processing (DSP) would require. Two TDCs were used in this work, one a Peripheral Component Interconnect (PCI) based TDC, and the second an IC based TDC, both of which have been discussed in Chapter 3. Since this rangefinder could be used in a portable device, a standalone portable TDC board was developed, as well as the system being tested on a PC based TDC.

While the PC based TDC is a plug-and-play solution, the IC based TDC7200 requires external circuitry to function correctly. Most importantly, this TDC includes a Microcontroller Unit (MCU) to interface between the it and a PC. The MCU tasked with this is the Raspberry Pico. The Raspberry Pico was chosen over the more common Arduino ATMEGA 328 based devices as it offers a larger selection of IO, a faster internal clock speed, and can be programmed in C. Most importantly, the higher clock speed should give an improved data transfer rate between the TDC7200 across the Serial Peripheral Interface (SPI) bus, and for processing the data. However, the speed between the PC and MCU will be limited by the serial interface. The inputs of the TDC7200 require 3.3 V Transistor-Transistor Logic (TTL) signals, but the signal produced by the QCL reference produces a 1 V pulse into $50\ \Omega$. To interface the QCL and CFD with the TDC, an LT1719 comparator is used. Not only does

this handle the voltage level conversion, but this comparator triggering allows for different start signals, CFDs, or detectors, to be used.

6.4 Results and Discussion

The following section discusses testing stages and presents the results of the TDC, VIS system and MWIR system.

6.4.1 TDC7200 Testing

To ensure that the accuracy of the homemade TDC circuit is within specifications it was tested against a two channel AFG. One channel drives the start, the other drives the stop of the TDC. The delay between these two channels was varied across a wide range of values, spanning from tens of nanoseconds to microseconds. The results that can be seen in Figure 6.11 were calculated by taking away the delay set on the AFG from the measured time difference by the TDC to show the deviation from the set delay. These results show that the median deviation measured by the TDC system is generally between 200 ps to 400 ps longer than it should be, corresponding to a distance of 6 cm to 12 cm. Between 100 ns and 500 ns the spread of the data increases, with a greater spread of outliers. The TDC7200 has two measurement modes, one for time differences below 500 ns, and one for values greater than 500 ns. The two measurement modes are due to the external clock counting with a coarse counter for greater time differences. One of the causes for the median drop in temporal deviation seen in Figure 6.11 between 100 ns to 500 ns could be due to a cumulative error in the fine counter period, before switching to the coarse counter.

The majority of the data points in mode 1, and for the data taken in mode 2 suggests

the system adds an extra 200 ps to 400 ps to the measured time. The most likely source of this induced delay could be due to a path length difference between the start and stop signals between the AFG and TDC. The stop signal on the TDC PCB used is approximately an inch longer than that of the start signal. In FR4 PCBs for an outer trace, the propagation time is 140 ns/inch to 180 ns/inch [164, p. 6]. Another source of the deviation could be caused by impedance mismatches between the AFG and TDC PCB.

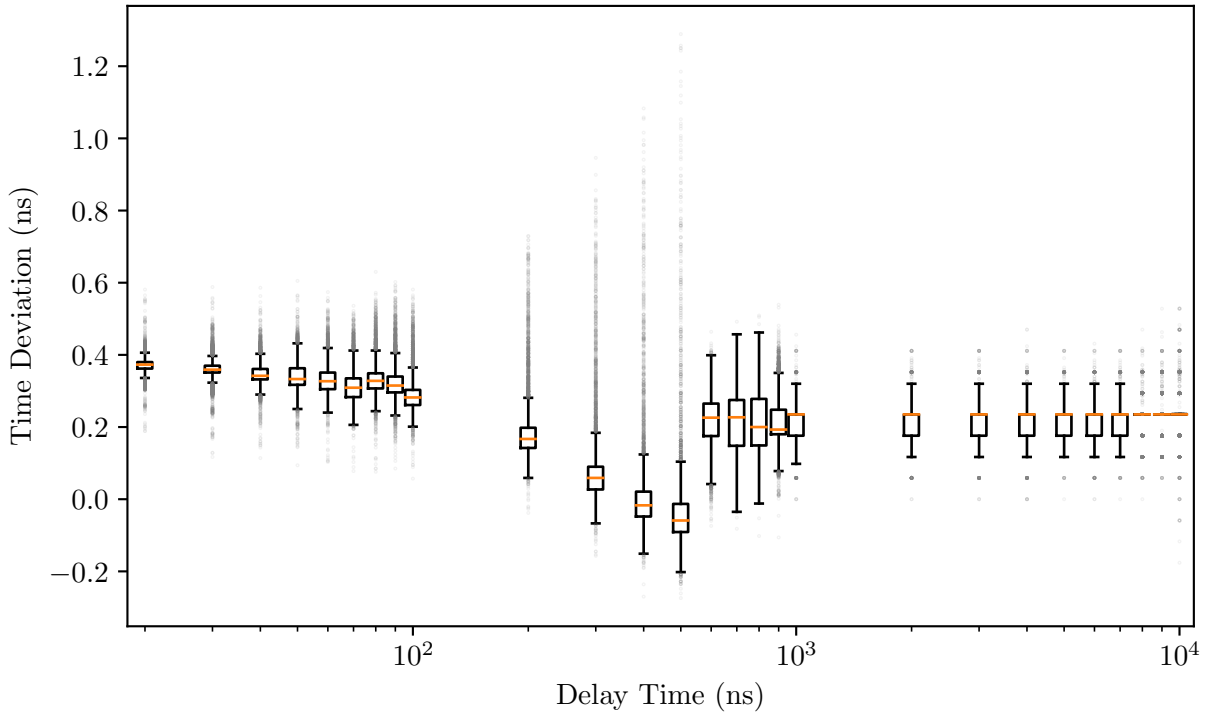


Figure 6.11: Boxplot showing the measured deviation for different stop-start delays produced by a two channel AFG. The boxes contain the 25th to 75th quartile, and the whiskers containing the $1.5 * IQR$, where IQR is the interquartile range. Outliers are shown in light grey, and the median shown in orange. The AFG produced two trigger signals separated by a set delay, 9999 samples were collected for each delay interval. In general, the stop signal arrives approximately 0.2 ns to 0.4 ns later than it should, settling at around 0.2 ns after 500 ns where mode 2 is enabled on the TDC (used for measuring times greater than 500 ns where the coarse counter is enabled). This added 0.2 ns could be induced from a differential in PCB track lengths.

6.4.2 633 nm Benchmarking

For the benchmarking system, the 633 nm diode laser was used with TDC7200 (see Figure 6.1). For interfacing the detector to the TDC7200, an LT1719 comparator with V_{thres} set at half the amplitude of the detector signal was used. The CFD was not used in this case, as the detector has a ns rise time. The results from this benchmark can be seen in Figure 6.12. It can be seen that there is a definite drift away from the theoretical distance that should have been measured as the optical path length increases. This drift is illustrated in Figure 6.13a. There are two potential causes for this: firstly, the translational stage may not be parallel to direction of the beam, secondly, the 633 nm source has a high divergence in both the slow and fast axes. Even though the 633 nm laser was collimated there was a reduction in the signal output as the path length increased. This reduction in signal would lead to the comparator, and thus, the TDC triggering at a higher fraction of the detectors signal. This would give the effect of light travelling further (an exaggerated example of this can be seen in Figure 6.15b). However, in the worst case, the TDC is only triggering 60 ps later than it should. Figure 6.13b shows the number of samples against the relative error. This data was taken with the translational stage at a fixed position. From this data, and from the accuracy shown in the previous section, it can be seen that the system is capable of cm resolution.

6.5 MWIR Rangefinder Testing

With the 633 nm benchmark establishing a baseline to reach, the CFD electronics and high speed MWIR preamplifier could be integrated into the setup (see Figure 6.1). A $4.48\mu\text{m}$ QCL was used to test the accuracy of the CFD. As the accuracy of the TDC has already been established, this test focusses on the preamplifier and CFD in use. Two experimental set ups are used to test the accuracy of this system: the performance of the InAsSb detector

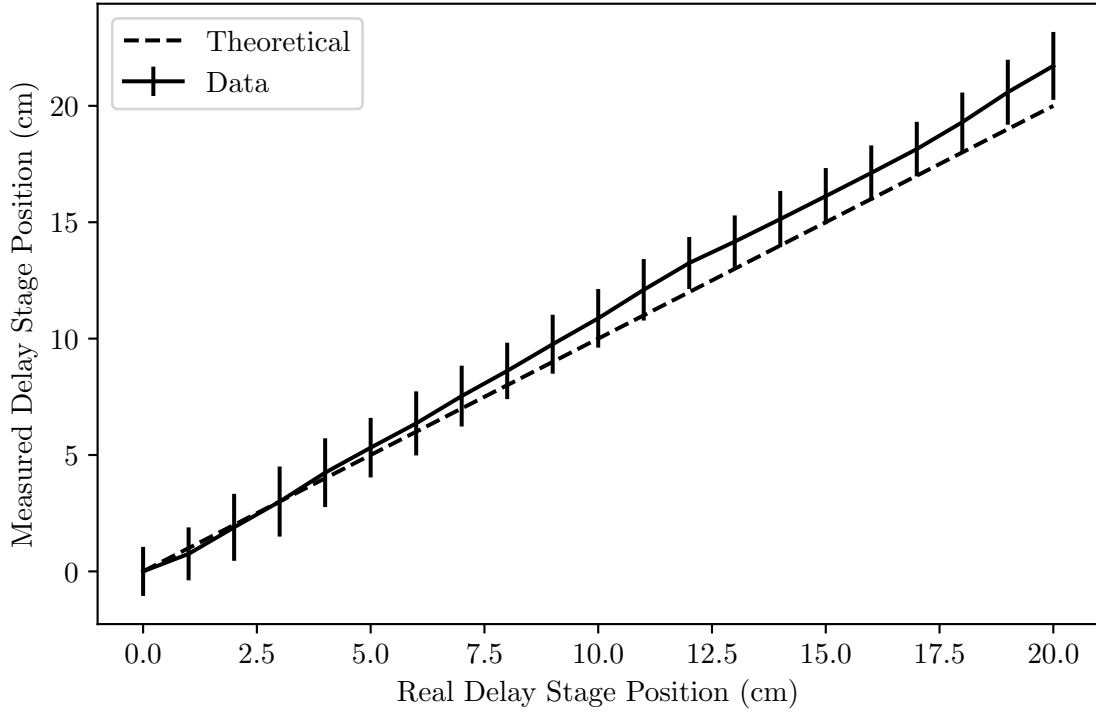
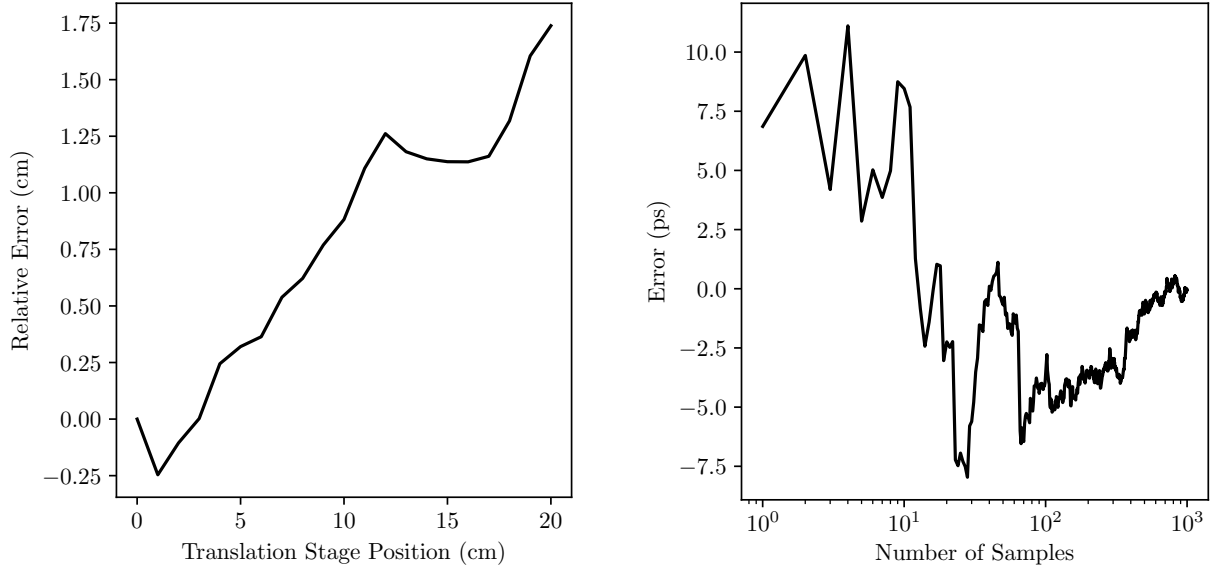


Figure 6.12: Comparison of the real added path length, shown by the theoretical line (1:1 ratio) against the measured path length by the 633 nm benchmarking system.

with CFDv6, and the MCT with CFDv4. The InAsSb detector was fitted to a VT-80 translational stage, whereas the MCT was used in a static configuration. In particular the accuracy, potential issues and possible causes will be presented. As well as investigating the absolute resolution, the bipolar pulse used for zero crossing will be observed at varying amplitudes and the results presented. Finally, future improvements will be discussed, both to the benchmarking setup and the circuitry.

For each detector technology, the stop of the TDC was triggered using both threshold level triggering and by using the CFDs. By testing both of these source for the stop signal a conclusion can be drawn on the efficacy of the CFD. To ensure that no other components affected the measurements being taken, the InAsSb detector was fitted to the translation stage, with the source directly opposite. A reference ToF was measured for the translational stage at its zero position, corresponding to the shortest optical path. The translational



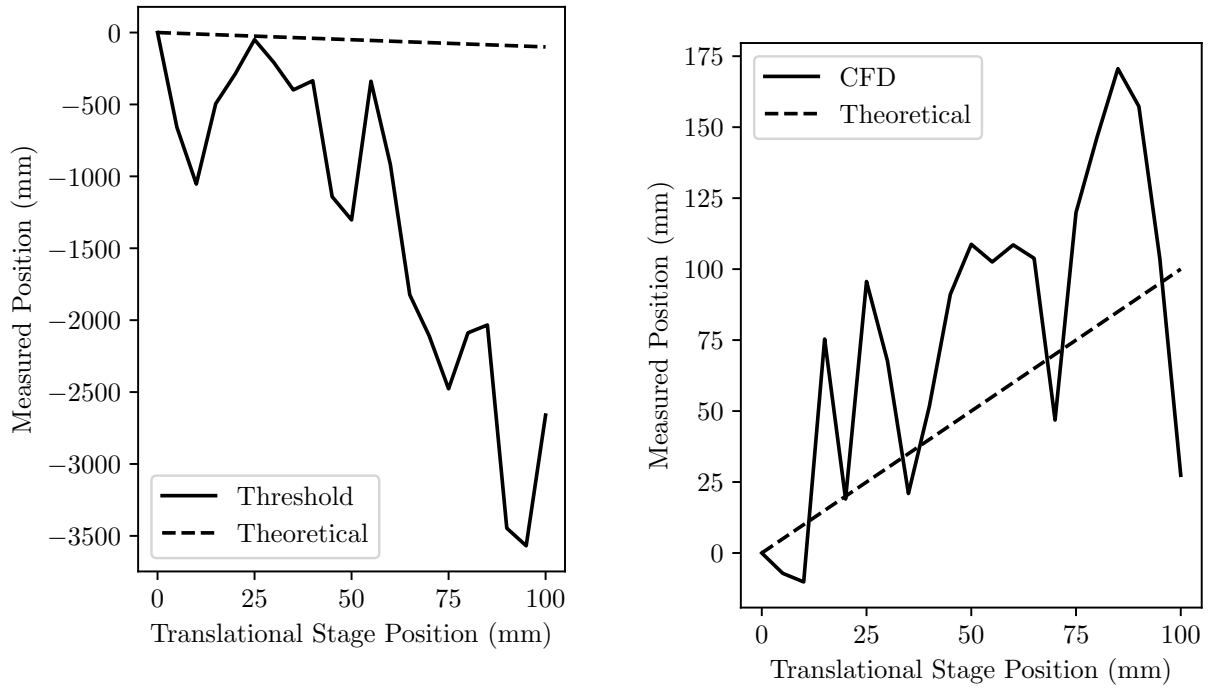
(a) Relative error of each translational stage position of the 633 nm benchmarking system. Error increases due to reduced amplitude seen at the detector.

(b) Sample count against temporal error measured at a single translational stage point for the 633 nm system. The system stabilises after 1000 samples.

Figure 6.13: Positional and temporal error for the 633 nm benchmarking system.

stage was then moved in 1 cm increments, with each position recording the new ToF. The measured ToF could then be compared to the translational stage position. Every effort was made to collimate the QCL to make sure that the signal amplitude did not vary significantly throughout the translational stage range. This process was repeated with CFDv6 for the InAsSb detector, and CFDv4 for the MCT detector, and without, using threshold level triggering only to investigate the efficacy of the CFD in question. The results of both the level triggering only (see Figure 6.14a) and CFD (see Figure 6.14b) can be seen in Figure 6.14 for the InAsSb detector.

To obtain the data shown in Figure 6.14a for threshold triggering, the stop comparator of the TDC7200 was set to half of the full amplitude of the wave. This data suggests that the focus of the laser was towards the back of the stage. However, this was not clear on an oscilloscope, leading to an increasing amplitude as the optical path length was increased.

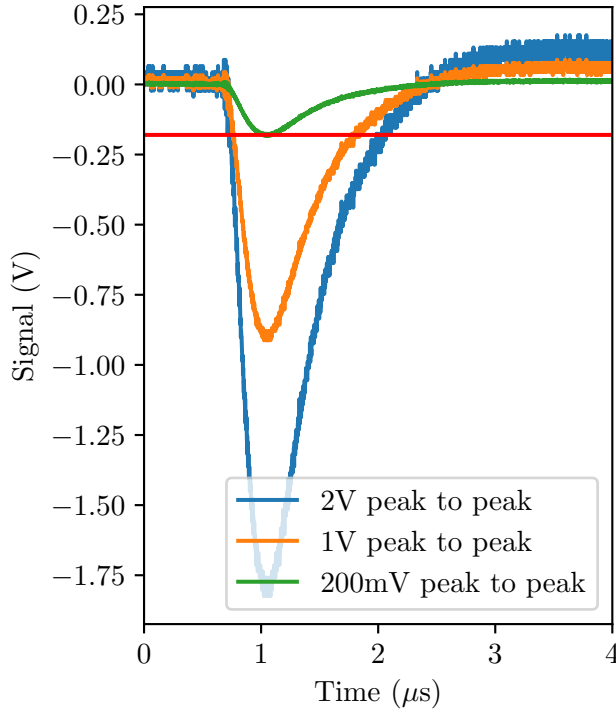


(a) Plot of added path length against the measured position for threshold level triggering. The negative distance measured is due to the amplitude of the wave growing as the optical path length increases due to an uncollimated beam. Theoretical line shows a 1:1 ratio between x and y axis.

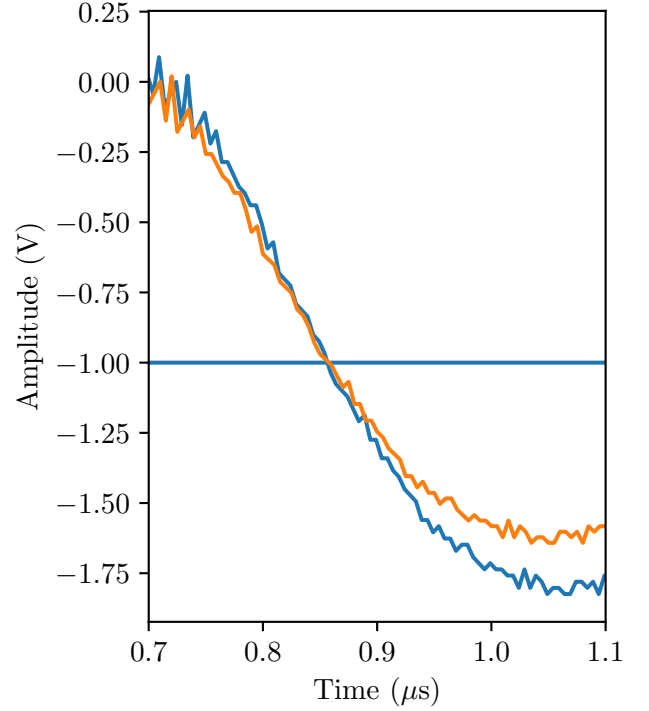
(b) Plot of added path length against the measured position. While not as precise as the 633 nm benchmark, it does show a significant improvement over the MWIR threshold triggering shown opposite. Theoretical line shows a 1:1 ratio between x and y axis.

Figure 6.14: Positional and temporal error for the MWIR rangefinder for threshold level triggering and the CFD system. A total of 9999 samples were taken and averaged for each translational stage position.

Thus, the system will trigger at a higher fraction of the signal as the optical path length increases. Essentially, the system is triggered earlier, due to the increase in amplitude of the signal outgrowing the change in time. This growing signal has the effect of making it appear that the optical path length is shortening, as signified by the negative position movement. An example of this effect can be seen in Figure 6.15b, where there is a difference of 10% in amplitude. The greater amplitude had to be delayed in time by approximately 14 ns to overlap at the same trigger point of -1 V, otherwise it would appear to trigger at an earlier time, even though they both appear at the same time as seen in Figure 6.15a.



(a) Effect of amplitude walk. Real data taken from an MCT, and scaled to show different heights. Without DSP, to trigger at all amplitudes the threshold has been set to 180 mV, corresponding to a trigger time of 1.024 μ s for the smallest signal. This will cause the 1 V and 2 V to trigger at 761 ns and 725 ns, respectively.



(b) Effect of amplitude walk. Two waves of different amplitudes moved in time by 14 ns to overlap at a threshold voltage set at 1 V.

Figure 6.15: Positional and temporal error for the CFD benchmarking system.

From the results shown in Figure 6.14b, it can be seen that the use of the CFDv6 with the InAsSb detector, while not perfect, shows a clear trend that fluctuates around the theoretical measurement distance. At each translational stage position, 9999 points were taken, and the standard deviation of each translational stage position was calculated as can be seen in Figure 6.16. From these results, it can be seen that even though the standard deviation is similar, there is a systematic error introduced by the threshold level triggering that is impossible to correct for without sampling the entire waveform. These results also show that threshold level triggering is more susceptible to noise; such as atmospheric effects and

scintillation, electronic noise or source amplitude variations. However, due to the entangled nature of the noise it is difficult to isolate it to one single issue. While it may be possible to reduce the impact of electrical noise induced from sources such as the thermal noise in the ICs used, or shot noise from the detector, through averaging, atmospheric effects can be more random. While the performance of the MWIR system while using the CFD does not match that produced by the 633 nm system, it is far better than that of level triggering method (see in Figure 6.14a).

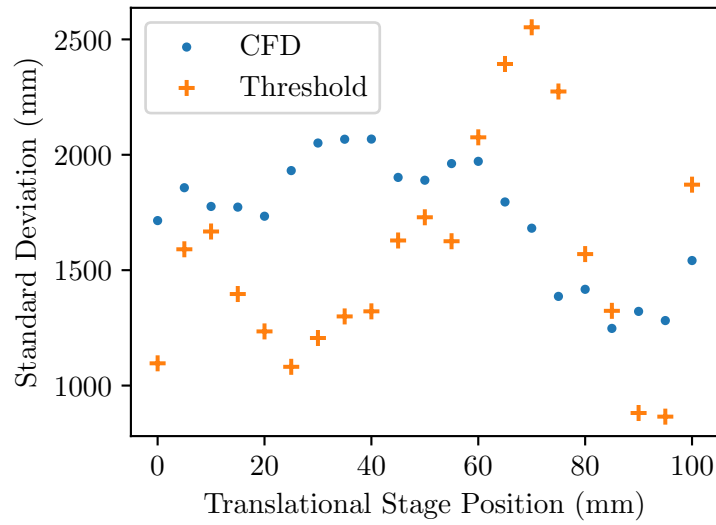


Figure 6.16: Standard deviation of each position after 9999 samples for threshold level triggering shown in orange, and the CFD system, shown in blue. Both methods have a similar standard deviation, although threshold level triggering is more erratic.

Due to the weight and construction of the MCT detector, it was not possible to mount it on the translational stage. Instead, the accuracy of this setup was assessed by fixing the distance between the detector and source, and comparing the level triggering against CFDv4. The P7887 and TDC7200 were used as the TDC to compare the timing precision between the two devices. The results from this can be seen in Figure 6.17. For testing the TDC without the CFD, the P7887 was set to trigger at half the peak-to-peak amplitude. These histograms show a clear advantage in using the CFD over level triggering, even in a stationary environment, with an order of magnitude reduction shown in the spread of data.

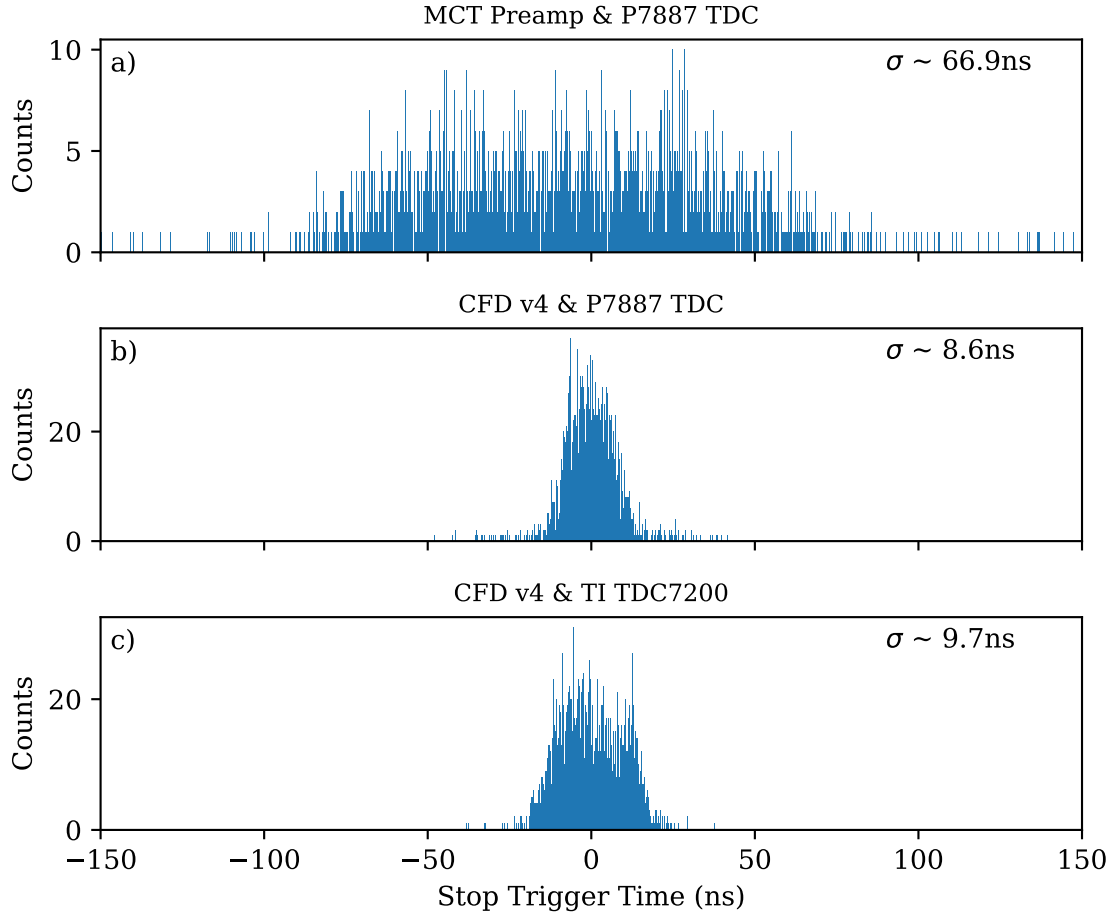


Figure 6.17: Histograms showing the distribution of stop times for two different TDCs and signal conditioning. 2000 counts have been plotted, with the standard deviation for each histogram shown in the corner.

To examine the generated bipolar pulse as varying amplitudes, the detector position was fixed, and the focus of the source adjusted (see Figure 6.18). Eight samples were captured and averaged for each waveform to avoid baseline amplitude variations. The inset of Figure 6.18 shows an enlarged view around the zero crossing point. While the points do not cross through zero (most likely due to a small offset voltage at one of the opamp inputs), nearly all cross within 5 ns over an order of magnitude change. This stretched zero crossing point appears to be one of the main contributors to limiting resolution of the system, as 5 ns corresponds to approximately 1500 mm, as seen in Figure 6.18. Reducing the range of zero crossing points would aid in increasing the accuracy of the system.

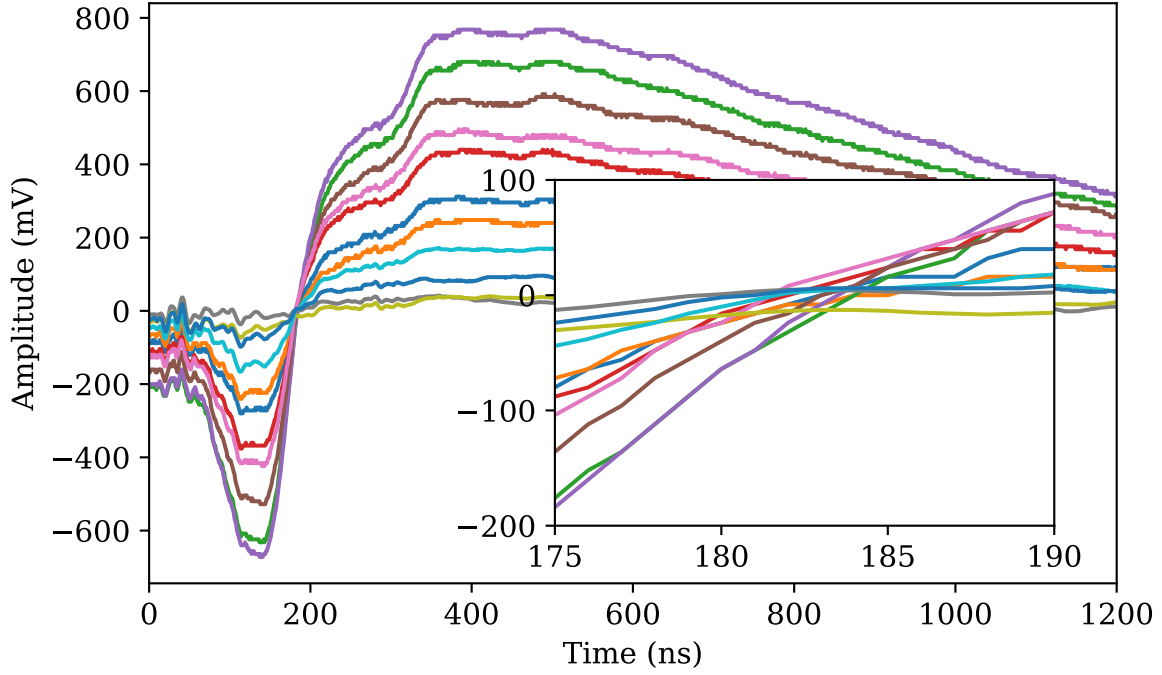


Figure 6.18: Range of amplitudes of signal input into CFDv6, measured after the mixing opamp. Inset shows the zero crossing in point in detail. All waveforms cross within 5 ns. Each waveform is an average of eight samples. Input amplitude to the CFD varied between 2 mV peak-to-peak to 55 mV peak-to-peak.

6.6 Summary and Outlook

Currently, there is no known product on the market that offers long distance rangefinding using the MWIR. As there is no solution available today for a MWIR rangefinder, a custom design was implemented. This section covered the theory of operation of the circuitry involved in rangefinding, the implementation, testing and results of using MWIR as a replacement for NIR and SWIR sources for rangefinding. To accomplish this, a system needed to be designed to accommodate the slower detector technology, due to limitations of the technology currently available. To accommodate the slower rise time of MCT detectors, a CFD was built, which not only allows for precise temporal accuracy with varying amplitude waves, but also provides reliable triggering for slower detectors. Exploring other detector

technologies led to the usage of InAsSb detector technology. The detector used in this work was a P13243-011MA produced by Hamamatsu. These low cost MWIR detectors have a fast rise time with a reasonable D^* rating. However, to achieve the same output as the MCT detectors used in our laboratory a preamplifier needed to be constructed that had a gain of 10^6 V/A without affecting the rise time significantly.

To verify the accuracy of the MWIR rangefinder, and to help identify sources of errors, the system was benchmarked with a high speed picosecond 633 nm laser diode, coupled with a ns rise time detector. A retroreflector fitted to a computer-controlled translational stage allowed for precise control of the optical path length so a benchmark could be established. It was found that with this VIS setup, a resolution on the cm scale is achievable.

The MWIR setup was then thoroughly tested. Both an MCT and the high speed, InAsSb detector were tested with their respective CFDs, which were also compared against straightforward level triggering. It was found that the CFDs played a significant role in increasing the temporal accuracy of both detector technologies by at least an order of magnitude. While the accuracy did not quite match that of the VIS system, it can be seen from the results that MWIR does offer potential for use in rangefinding.

Future investigations into this work should look into longer range field tests. Longer range field tests were attempted as part of this work, but unfortunately the source was not strong enough. The accuracy could be further improved by reducing noise, and losses within the preamplifier, CFD, and TDC circuits. The overall performance may have been impacted due to the prototype, and in some cases handmade, nature of the fabrication of some of the PCBs, impedance mismatches, ground loops, and non-ideal signal paths. Careful control of the signal impedances was not possible due to the handmade nature of the PCBs. Commercial manufacturing of the PCBs could reduce ringing and losses seen in the CFD and delay line especially. This reduction in losses would also have the added benefit of requiring

less amplification stages. Splitting elements onto separate circuit boards helps significantly with prototyping, however this can introduce ground loop issues. Future development could see these individual circuits moved onto a single PCB, overcoming the issue outlined above. Finally, while the high-speed preamplifier was functional, the rise time could be further improved. Again, this may have been due to the fabrication style of the circuit, as fast prototyping was required due to time constraints. To conclude, MWIR has proven to be a viable and exciting option for MWIR rangefinding; it achieves performance close to that of a visible system, while theoretically offering greater ranging distance due to the longer wavelength used.

Chapter Seven

Conclusion

In conclusion, this thesis covers the development of Infrared (IR) technologies for applications in rangefinding and thermal cameras. To begin with, a case was put forward for the potential benefits of using Mid-Wave Infrared (MWIR) and Long-Wave Infrared (LWIR) over short wavelength for rangefinding and long range applications, such as Optical Wireless Communication (OWC). From assessing the primary causes for atmospheric absorption and scattering, it can be seen that longer wavelengths offer a definite benefit over shorter wavelengths in the Visible (VIS) to Short-Wave Infrared (SWIR). The benefits and potential applications of using thermal imaging over conventional VIS imaging was also investigated. This review of previous studies highlighted the importance of considering other types of imaging such as IR in camera applications.

The current state of detector technology, sources and modulators for the IR were then assessed and compared to their visible counterparts. This identified the primary area that required attention for improvements for enabling high speed operation for thermal cameras and rangefinding. It was found that the component most at fault for slow operation of longer wave IR lies with the detector, and by extension, modulators. The focus was then turned onto assessing the state of long distance rangefinding, due to the potential benefits of using

IR. It was found that, for the most part, research does not push beyond the SWIR. While there have been some examples of extremely long distance rangefinding using Near Infrared (NIR) and SWIR, the acquisition time made them only suitable for static targets. This is primarily due to the high absorption in the atmosphere, significantly reducing the number of photons returning from the scene.

In Chapter 3, the systems used in this work were then discussed. Starting with the femtosecond system, the primary components were introduced, and their operation explained. The primary use for the femtosecond system in this work is examining changes in the modulator on a scale of femtoseconds. It was also used to assess the maximum performance obtainable from the modulator, which was later discussed in Chapter 5. The breadboard system was then introduced. This smaller system aims to capture the functionality of the femtosecond system in a compact, manageable, and cheaper system. Of course, it is not possible to shrink such a system without trade-offs, these were discussed in detail, with the primary drawback being a reduced temporal resolution. However, this was later found in Chapter 5 to be of high enough performance to offer a real improvement over mechanical options. This project relies on electrical signal processing, as well as optical methods, for rangefinding. A collection of the circuits built for this project were introduced, including a high-speed amplifier for an InAsSb detector, a Constant Fraction Discriminator (CFD), and Time to Digital Converter (TDC) circuit. The chapter concluded with a discussion on the importance of noise reduction. The idea of double modulation and pulse sampling were introduced, and an explanation of their implementation. Results presented showing the improvement in noise, with changes in transmission and reflection on the order of 0.5% being detectable with the double modulation technique.

Chapter 4 covered the operating principles of the solid state shutter that is used for gating a detector of Focal Plane Array (FPA). Since the transmission of IR through the optical modulator is inversely proportional to the excited free carrier concentration, and the

attenuation caused by intraband absorption, various methods were described for generation of the free carriers. High operational speed and modulation contrast are required, therefore the mechanisms for excitation and recombination were investigated. To predict the possible modulation achievable with the breadboard system, a simulation was devised. The NIR optical pump penetration into the sample was calculated. The photon count along the depth of the optical modulator could then be used to calculate the free carrier concentration. Combining the free carrier concentration with the Drude model gives an estimation for the complex refractive index change, induced by the excess free carriers modifying the plasma frequency. The effect of the refractive index gradient on IR light could then be calculated using the Transfer Matrix Method (TMM). Later, in Chapter 5, this simulation was used as a model for fitting to results.

The focus of Chapter 5 was the implementation of the solid state shutter in applications relating to Time of Flight (ToF) and Range Gated Active Imaging (RGAI). Initially, the shutter technology was used to externally gate a sensitive but slow Mercury Cadmium Telluride (MCT) detector in the femtosecond system. This experimental setup was able to determine the extra optical path length travelled by the probe after inserting silica rods into its path. Using the pump probe technique, extra path length of the probe could be measured by using the all-optical modulator to gate the MCT detector. The modulator was activated by the femtosecond pump pulse, ensuring a swift turn on time. Without the optical modulator, the detector has a rise time on the order of 400 ns, limiting the temporal resolution of the entire system. However, through the process of gating the detector with the modulator, the arrival time of the probe after travelling through air only, a 5 cm, and a 10 cm silica rod could be measured on the order of picoseconds. By examining the falling edge of the change in transmission of the modulator after travelling through air and a silica rod, the Group Velocity Dispersion (GVD) of the probe through the silica rods could be determined, highlighting the increase in temporal resolution achieved through gating the detector.

This method of improving temporal accuracy was then integrated into the breadboard system. As well as ToF, the idea of LWIR RGAI was explored. The system consisted of a $10.07\text{ }\mu\text{m}$ Quantum Cascade Laser (QCL) source, a NIR 80 W diode laser was used as the optical pump, and an intrinsic silicon optical window was used as the modulator. A trigger was provided from the QCL's internal oscillator to an Arbitrary Function Generator (AFG), which provided the trigger for the optical pump diode. This triggering systems ensured a stable operating frequency between the two lasers, while also allowing for the phase between the two lasers to be adjusted, simulating the mechanical optical delay line in the femtosecond system. It was found that a uncooled microbolometer FPA could be externally gated with the all-optical shutter, achieving microsecond resolution. With a single pixel MCT detector, coupled with a Lock-in Amplifier (LIA), it was possible to achieve sub-microsecond resolution while measuring an 18 m optical path using the LWIR QCL as a source.

Moving away from the all-optical modulator, Chapter 6 focusses on an electronic signal processing route for determining the ToF. A $4.48\text{ }\mu\text{m}$ QCL was used as the source, while an MCT and InAsSb were used to detect the signal. Three circuits were designed, and custom made. These circuits included a high-speed preamplifier for the InAsSb photodiode; a CFD and accompanying delay board for increasing the temporal resolution; and a portable TDC for recording the ToF between the QCL trigger and the detector signal. To match the output of the MCT with its respective amplifier, the InAsSb detector needed to have a gain of at least 10^6 , while maintaining a sub-100 ns rise time. The final design and circuit offered a gain of 10^7 , with a rise time of approximately 70 ns. Two separate CFDs and delay boards were designed for the MCT and InAsSb detectors due to their varying electrical outputs. A detailed walkthrough of these devices were provided, showing how the signal progresses through the CFD. Finally, a TDC circuit was built to complement and improve on a PC based TDC, offering a more portable solution for field testing.

These circuits were able to offer at the very least, an order of magnitude improve-

ment on the temporal resolution of these detectors without the electrical processing. The TDC was found to have picosecond resolution in the 633 nm benchmark set up, allowing for centimetre resolution. The 633 nm source and detector were then replaced with their MWIR counterparts, including their matched CFDs. Looking at a histogram of the results obtained from the MCT, the standard deviation of the distribution reduced from 67 ns when level threshold triggering was employed, to under 10 ns with the use of a CFD. The InAsSb detector was then fitted to a translational stage. By incrementing the position of the stage and recording a value at each point, the resolution of the detector and CFD could be assessed. It was found that with enough averaging, amplitude walk could be corrected for by using the CFD, and the increase in optical path length could be observed. This was repeated without the CFD, where simple level triggering was employed. Due to amplitude walk, the optical path length was not observable, and was lost in the effect of amplitude walk.

The performance of both the solid state shutter and the MWIR rangefinder, has not been fully exploited. Starting with the all-optical shutter, efficiency of the system is a key area that could be improved on. Firstly, limiting the heat added to the system through optical pumping will improve the contrast of the modulation, and clarity of the final image. An increase in modulation efficiency will also reduce the optical pump power required. This reduction in pump power will increase the possibility of the technology being used in small portable devices. Modulation efficiency could be improved through the use of composite nanostructured materials or engineered plasmonic structures, such as gold clusters embedded in nano porous silicon membranes [165, 166].

A field test of the MWIR rangefinder will go a long way in proving its potential utility in long distance rangefinding. One of the primary sources originates from the CFDs. Since the CFDs are active devices, they are able to introduce and amplify any surrounding Electromagnetic Interference (EMI), or introduce noise of their own from noise in their power supply rails, for example. Moving all sub-circuits onto a single Printed Circuit Board (PCB)

would improve circuit integrity, as well as reducing the possibility of ground loops forming between separate PCBs. Finally, refabricating the InAsSb preamplifier on machine made PCB, rather than hand etched PCB, would allow for careful control of the track layout and size. This would reduce stray capacitances which should improve both the response and the signal to noise ratio.

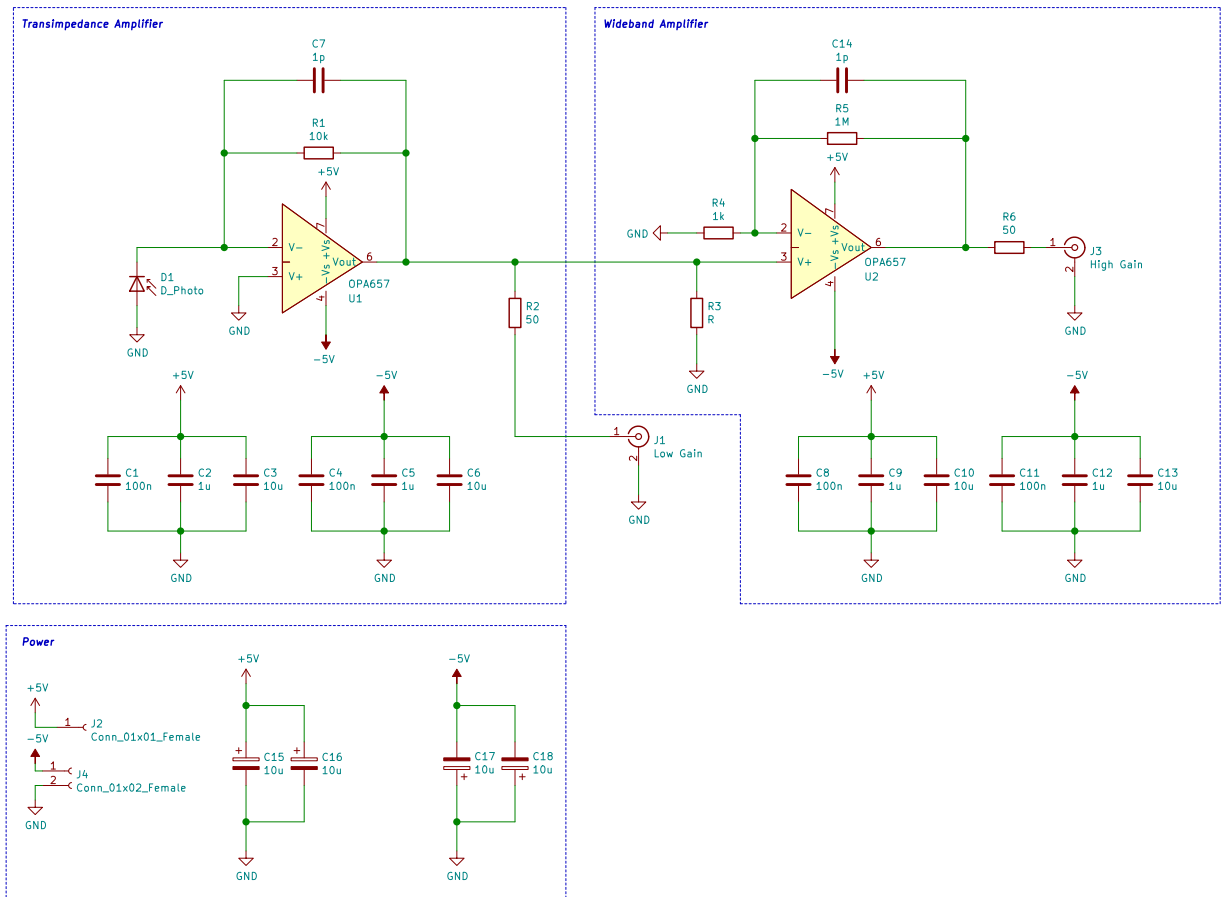
Appendix One

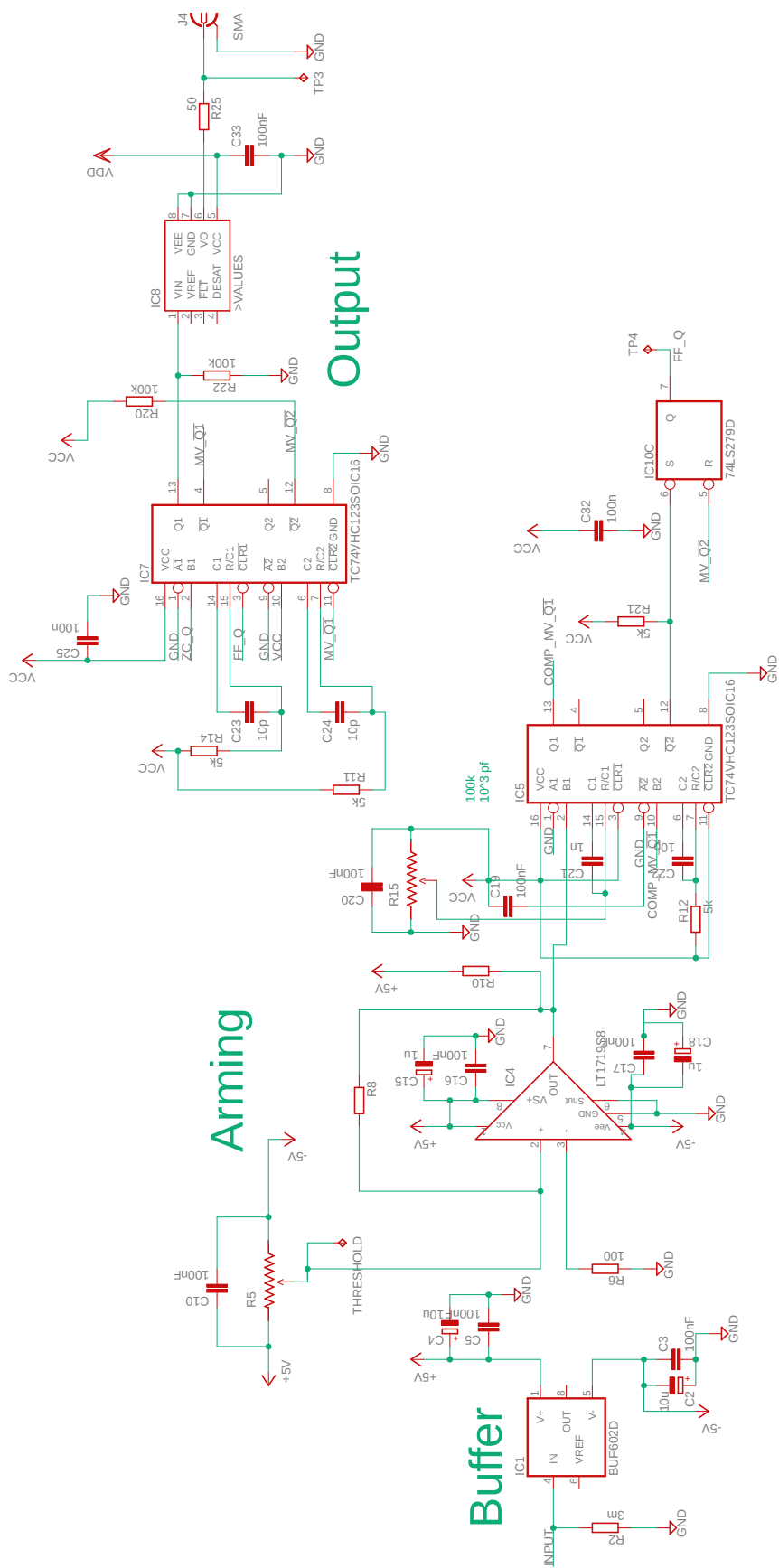
Electrical Schematics

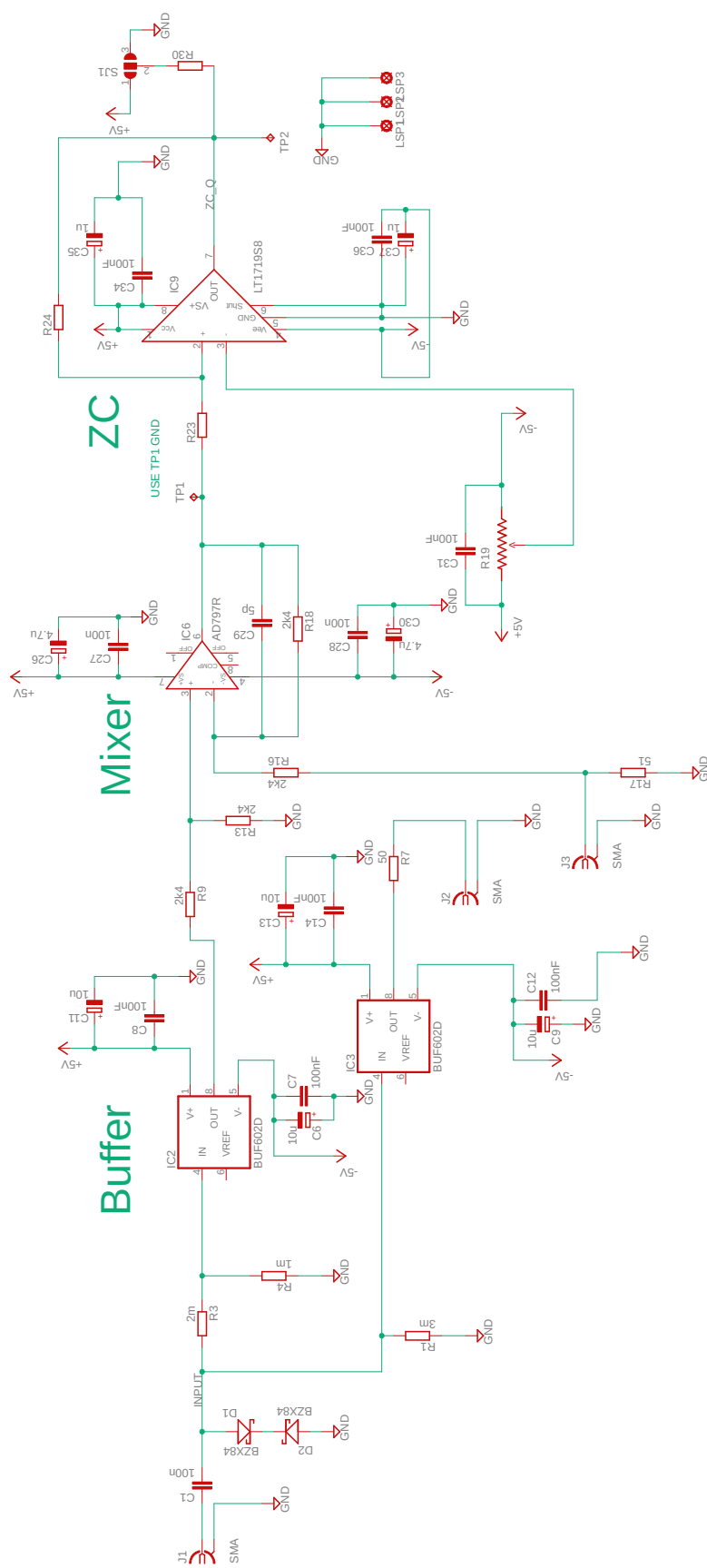
A.1 High Speed Preamplifier v2

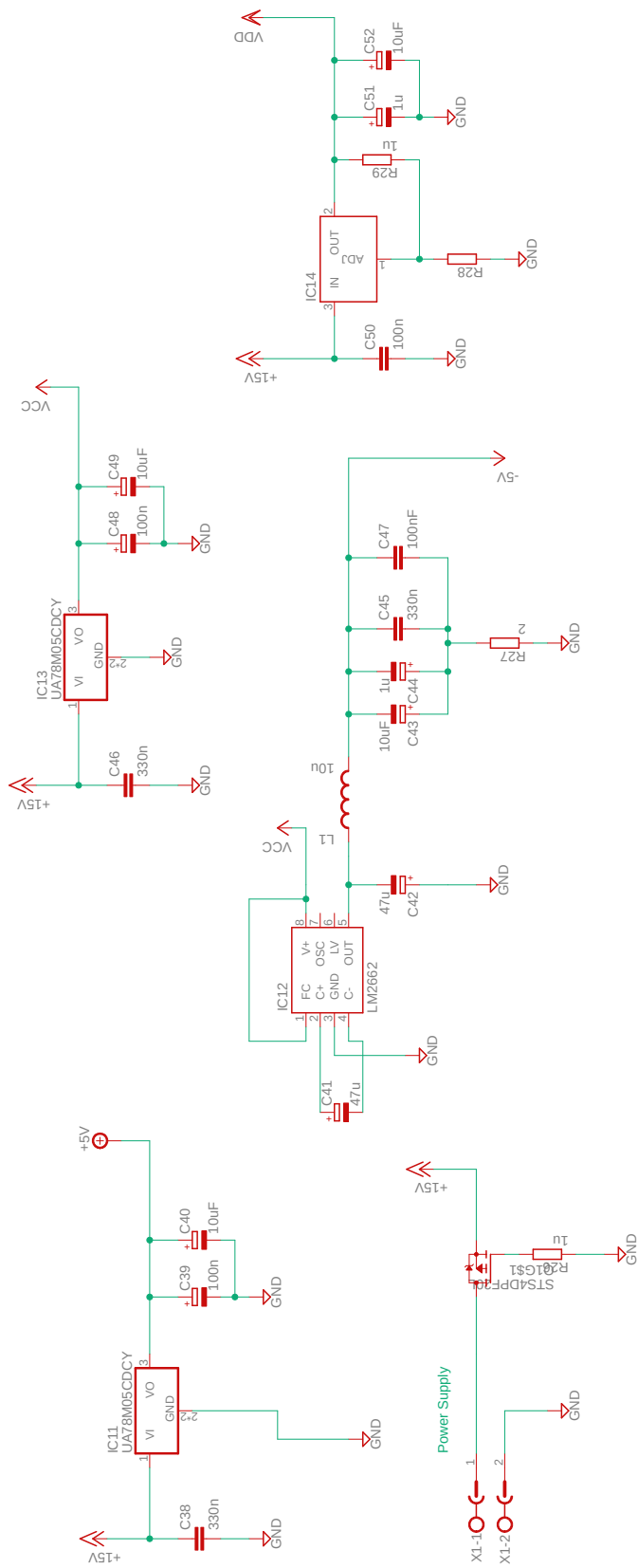
A.2 CFDv4

High Speed Amplifier v2



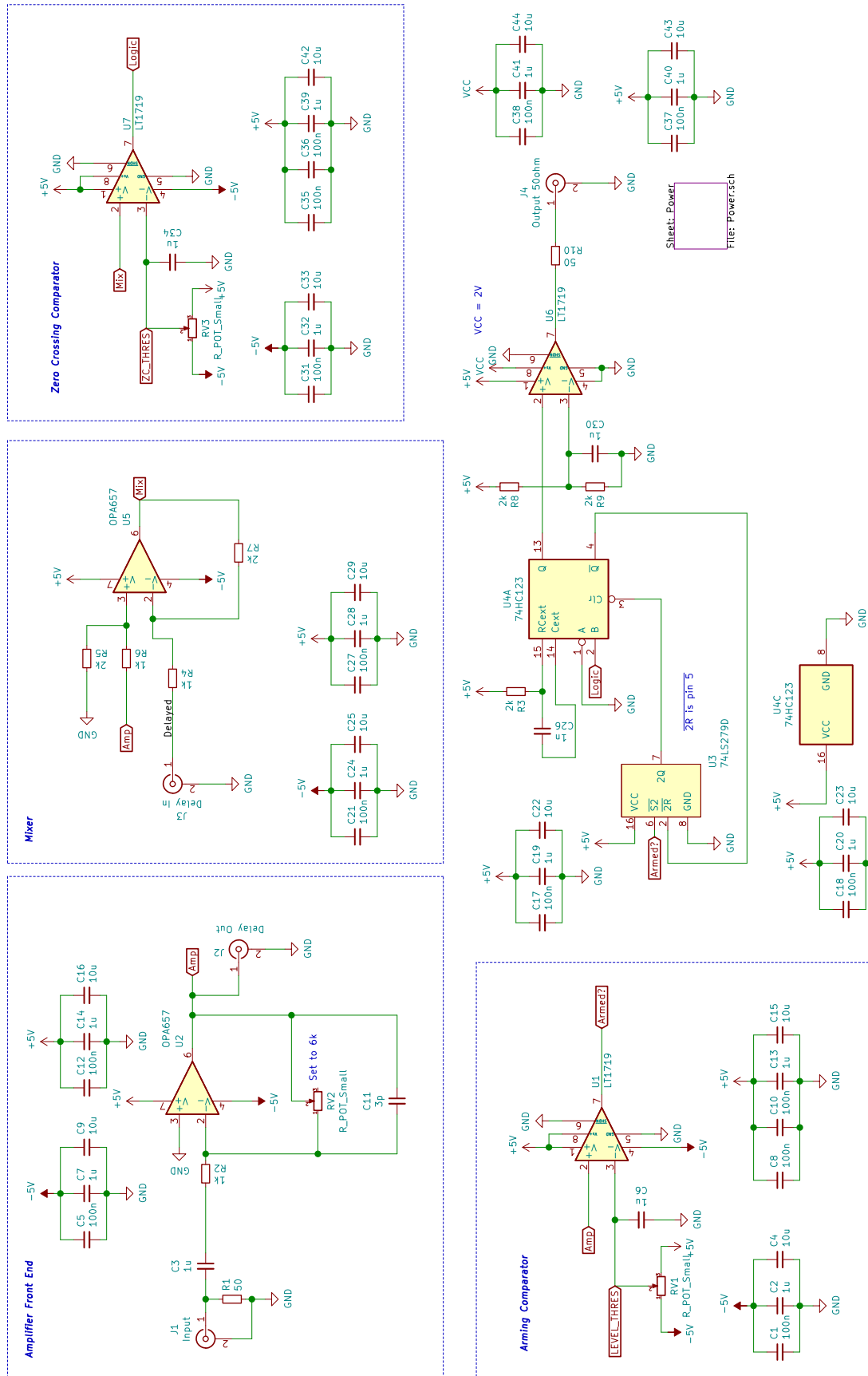




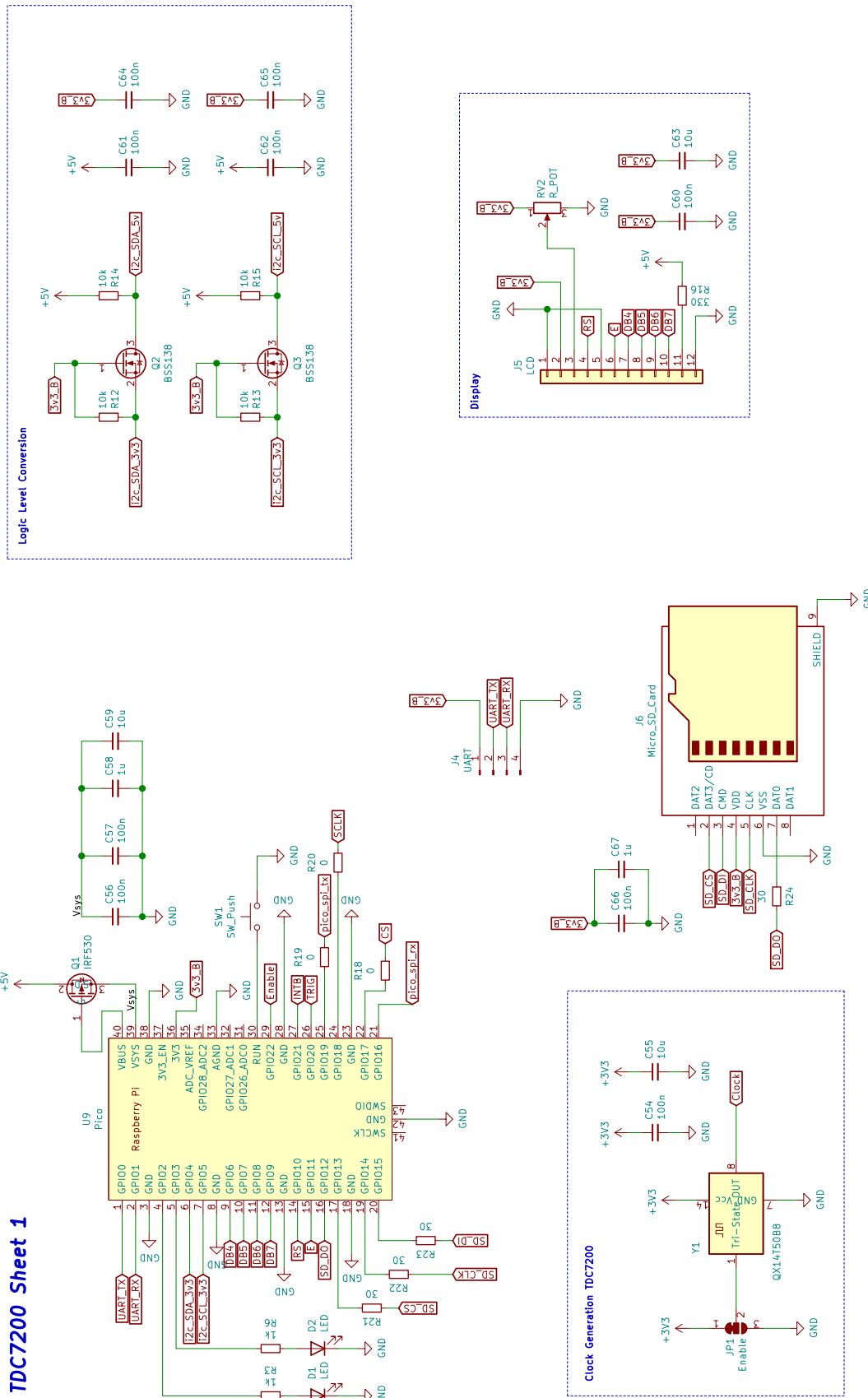


A.3 CFDv6

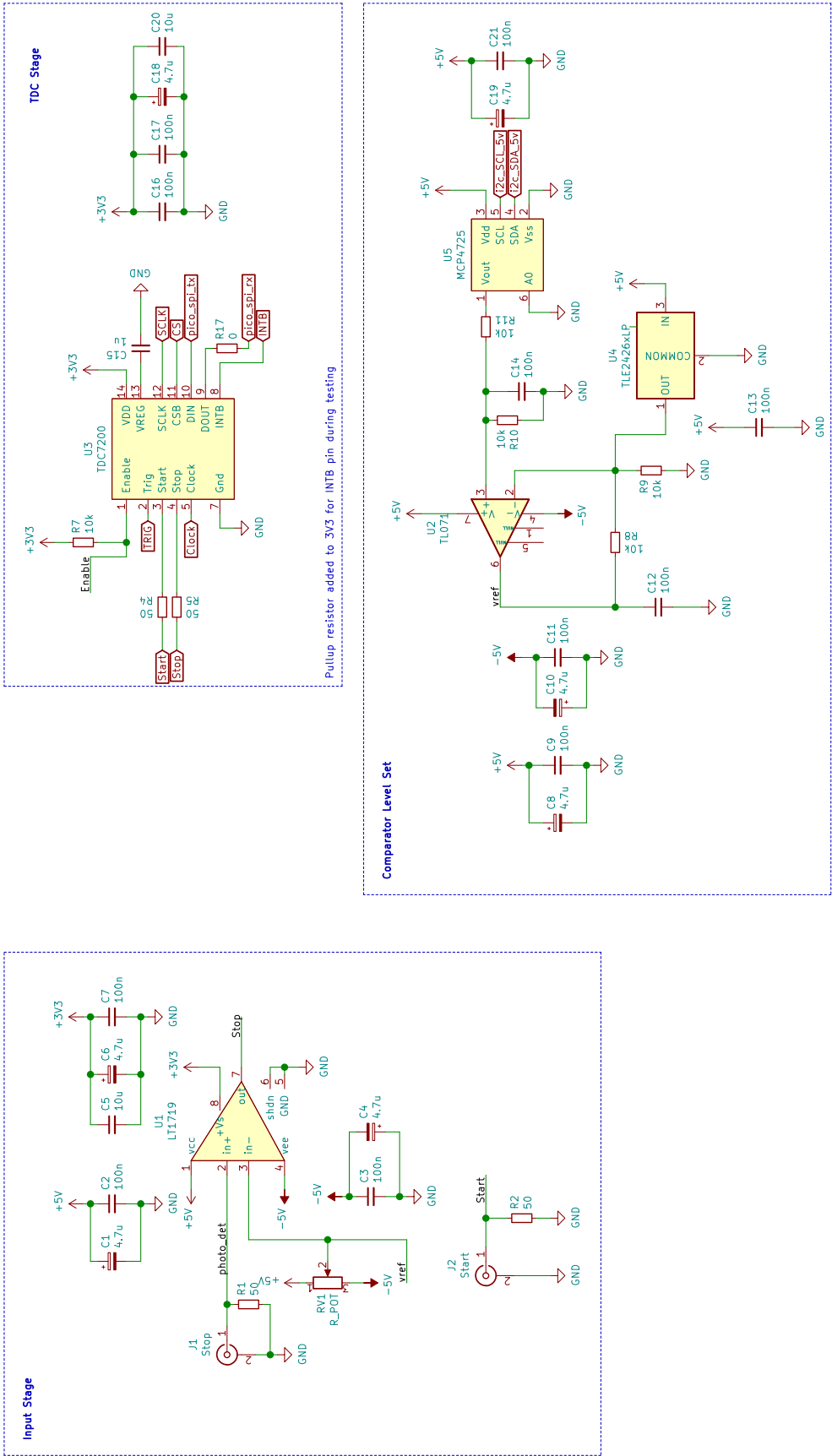
CFDv6



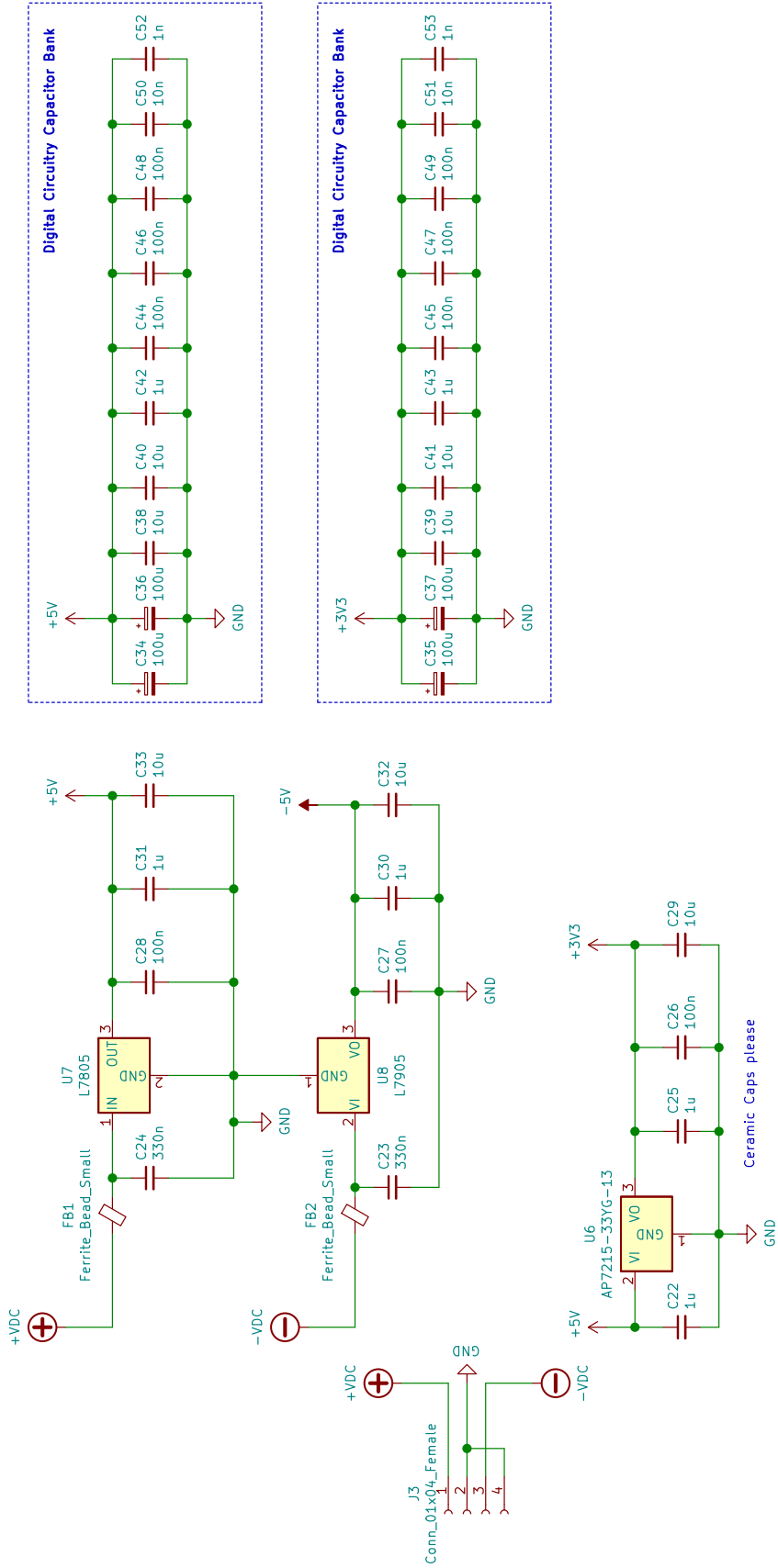
A.4 TDC7200



TDC7200 Sheet 2



TDC7200 Sheet 3



References

- [1] Michael Vollmer and Klaus-Peter Möllman. *Infrared thermal imaging : fundamentals, research and applications / by Michael Vollmer and Klaus-Peter Mollmann*. Weinheim: Wiley-VCH, 2010, pp. 53–55. ISBN: 9783527407170.
- [2] Benjamin Göhler and Peter Lutzmann. “Review on short-wavelength infrared laser gated-viewing at Fraunhofer IOSB”. In: *Optical Engineering* 56.3 (2016), p. 031203. ISSN: 0091-3286. DOI: [10.1117/1.oe.56.3.031203](https://doi.org/10.1117/1.oe.56.3.031203).
- [3] Zhuomin M. Zhang, Benjamin K. Tsai, and Graham Machin. *Radiometric temperature measurements*. eng. Experimental methods in the physical sciences 43. Amsterdam Boston: Academic Press, 2010. ISBN: 978-0-12-375091-4.
- [4] K. Elliott Cramer, Patricia A. Howell, and Hazari I. Syed. “Quantitative thermal imaging of aircraft structures”. In: ed. by Sharon A. Semanovich. Orlando, FL, Mar. 1995, pp. 226–232. DOI: [10.1117/12.204859](https://doi.org/10.1117/12.204859).
- [5] Jong-Hwan Kim and Brian Y. Lattimer. “Real-time probabilistic classification of fire and smoke using thermal imagery for intelligent firefighting robot”. en. In: *Fire Safety Journal* 72 (Feb. 2015), pp. 40–49. ISSN: 03797112. DOI: [10.1016/j.firesaf.2015.02.007](https://doi.org/10.1016/j.firesaf.2015.02.007).
- [6] Rossano Albatici, Arnaldo M. Tonelli, and Michela Chiogna. “A comprehensive experimental approach for the validation of quantitative infrared thermography in the

- evaluation of building thermal transmittance”. en. In: *Applied Energy* 141 (Mar. 2015), pp. 218–228. ISSN: 03062619. DOI: [10.1016/j.apenergy.2014.12.035](https://doi.org/10.1016/j.apenergy.2014.12.035).
- [7] A.A. Gowen et al. “Applications of thermal imaging in food quality and safety assessment”. en. In: *Trends in Food Science & Technology* 21.4 (Apr. 2010), pp. 190–200. ISSN: 09242244. DOI: [10.1016/j.tifs.2009.12.002](https://doi.org/10.1016/j.tifs.2009.12.002).
- [8] Fatih Erden et al. “VOC gas leak detection using Pyro-electric Infrared sensors”. In: *2010 IEEE International Conference on Acoustics, Speech and Signal Processing*. 2010 IEEE International Conference on Acoustics, Speech and Signal Processing, ICASSP 2010. Dallas, TX: IEEE, Mar. 2010, pp. 1682–1685. ISBN: 978-1-4244-4295-9. DOI: [10.1109/ICASSP.2010.5495500](https://doi.org/10.1109/ICASSP.2010.5495500).
- [9] Kun Liang et al. “Nonuniformity correction based on focal plane array temperature in uncooled long-wave infrared cameras without a shutter”. en. In: *Applied Optics* 56.4 (Feb. 2017), p. 884. ISSN: 0003-6935, 1539-4522. DOI: [10.1364/AO.56.000884](https://doi.org/10.1364/AO.56.000884).
- [10] Chia-Kai Liang, Li-Wen Chang, and H.H. Chen. “Analysis and Compensation of Rolling Shutter Effect”. In: *IEEE Transactions on Image Processing* 17.8 (Aug. 2008), pp. 1323–1330. ISSN: 1057-7149, 1941-0042. DOI: [10.1109/TIP.2008.925384](https://doi.org/10.1109/TIP.2008.925384).
- [11] J. S. Accetta and David L. Shumaker, eds. *The Infrared and electro-optical systems handbook*. Vol. 7. Ann Arbor, Mich. : Bellingham, Wash: Infrared Information Analysis Center ; SPIE Optical Engineering Press, 1993. ISBN: 978-0-8194-1072-6.
- [12] Baoliang Wang and Jennifer List. “Basic optical properties of the photoelastic modulator: Part I. Useful aperture and acceptance angle”. In: *Optics & Photonics 2005*. Ed. by Joseph A. Shaw and J. Scott Tyo. San Diego, California, USA, Aug. 18, 2005, p. 58881I. DOI: [10.1117/12.617904](https://doi.org/10.1117/12.617904).

-
- [13] M. M. de Lima et al. “Compact Mach-Zehnder acousto-optic modulator”. In: *Applied Physics Letters* 89.12 (Sept. 18, 2006), p. 121104. ISSN: 0003-6951, 1077-3118. DOI: [10.1063/1.2354411](https://doi.org/10.1063/1.2354411).
- [14] Yuxia Zhang et al. “Broadband atomic-layer MoS₂ optical modulators for ultrafast pulse generations in the visible range”. en. In: *Optics Letters* 42.3 (Feb. 2017), p. 547. ISSN: 0146-9592, 1539-4794. DOI: [10.1364/OL.42.000547](https://doi.org/10.1364/OL.42.000547).
- [15] Teldyne Judson Technologies. *Photoconductive Mercury Cadmium Telluride Detectors*.
- [16] I. C. Gardner. “The Coincidence Type Self-Contained Range Finder”. en. In: *Journal of the Optical Society of America* 5.5 (Sept. 1921), p. 420. ISSN: 0030-3941. DOI: [10.1364/JOSA.5.000420](https://doi.org/10.1364/JOSA.5.000420).
- [17] You Li and Javier Ibanez-Guzman. “Lidar for Autonomous Driving: The Principles, Challenges, and Trends for Automotive Lidar and Perception Systems”. In: *IEEE Signal Processing Magazine* 37.4 (July 2020), pp. 50–61. ISSN: 1053-5888, 1558-0792. DOI: [10.1109/MSP.2020.2973615](https://doi.org/10.1109/MSP.2020.2973615).
- [18] Bettina Petzold, Peter Reiss, and Wolfgang Stössel. “Laser scanning—surveying and mapping agencies are using a new technique for the derivation of digital terrain models”. In: *ISPRS Journal of Photogrammetry and Remote Sensing* 54.2 (July 1999), pp. 95–104. ISSN: 09242716. DOI: [10.1016/S0924-2716\(99\)00005-2](https://doi.org/10.1016/S0924-2716(99)00005-2).
- [19] Hongzhi Yang et al. “A novel hybrid TOF/phase-shift method for absolute distance measurement using a falling-edge RF-modulated pulsed laser”. In: *Optics & Laser Technology* 114 (June 2019), pp. 60–65. ISSN: 00303992. DOI: [10.1016/j.optlastec.2019.01.029](https://doi.org/10.1016/j.optlastec.2019.01.029).

-
- [20] Bruce H. Walker. *Optical engineering fundamentals*. 2nd ed. Tutorial texts series v. TT82. OCLC: ocn268547513. Bellingham, Wash: SPIE Press, 2008. 277 pp. ISBN: 978-0-8194-7540-4.
- [21] Gerald S. Buller et al. “Multiple wavelength time-of-flight sensor based on time-correlated single-photon counting”. In: *Review of Scientific Instruments* 76.8 (Aug. 2005), p. 083112. ISSN: 0034-6748, 1089-7623. DOI: [10.1063/1.2001672](https://doi.org/10.1063/1.2001672).
- [22] H. Horvath. “Atmospheric light absorption—A review”. en. In: *Atmospheric Environment. Part A. General Topics* 27.3 (Feb. 1993), pp. 293–317. ISSN: 09601686. DOI: [10.1016/0960-1686\(93\)90104-7](https://doi.org/10.1016/0960-1686(93)90104-7).
- [23] T.S. Kubo and T.J. Kane. “Diode-pumped lasers at five eye-safe wavelengths”. In: *IEEE Journal of Quantum Electronics* 28.4 (Apr. 1992), pp. 1033–1040. ISSN: 00189197. DOI: [10.1109/3.135225](https://doi.org/10.1109/3.135225).
- [24] Cheng Gong et al. “Short-wave infrared, medium-wave infrared, and long-wave infrared imaging study for optical readout microcantilever array infrared sensing system”. In: *Optical Engineering* 52.2 (Feb. 5, 2013), p. 026403. ISSN: 0091-3286. DOI: [10.1117/1.OE.52.2.026403](https://doi.org/10.1117/1.OE.52.2.026403).
- [25] Helmut Budzier et al. *Thermal infrared sensors: theory, optimisation and practice*. 1. ed. Chichester: Wiley, 2011. 302 pp. ISBN: 978-0-470-97690-6 978-0-470-97691-3 978-0-470-97675-3 978-0-470-87192-8.
- [26] J.W. Strutt. “XV. On the light from the sky, its polarization and colour”. In: *The London, Edinburgh, and Dublin Philosophical Magazine and Journal of Science* 41.271 (Feb. 1871), pp. 107–120. ISSN: 1941-5982, 1941-5990. DOI: [10.1080/14786447108640452](https://doi.org/10.1080/14786447108640452).
- [27] John H. Seinfeld and Spyros N. Pandis. *Atmospheric chemistry and physics: from air pollution to climate change*. New York: Wiley, 1998. 1326 pp. ISBN: 978-0-471-17815-6 978-0-471-17816-3.

-
- [28] R. T. H. Collis and E. E. Uthe. “Mie scattering techniques for air pollution measurement with lasers”. In: *Opto-electronics* 4.2 (May 1972), pp. 87–99. ISSN: 0306-8919, 1572-817X. DOI: [10.1007/BF01421174](https://doi.org/10.1007/BF01421174).
- [29] Hao Zhang et al. “Development and performance detection of higher precision optical sensor for coal dust concentration measurement based on Mie scattering theory”. In: *Optics and Lasers in Engineering* 144 (Sept. 2021), p. 106642. ISSN: 01438166. DOI: [10.1016/j.optlaseng.2021.106642](https://doi.org/10.1016/j.optlaseng.2021.106642).
- [30] Haim Manor and Shlomi Arnon. “Performance of an optical wireless communication system as a function of wavelength”. In: *Applied Optics* 42.21 (July 20, 2003), p. 4285. ISSN: 0003-6935, 1539-4522. DOI: [10.1364/AO.42.004285](https://doi.org/10.1364/AO.42.004285).
- [31] M. Taslakov, V. Simeonov, and H. van den Bergh. “Line-of-sight data transmission system based on mid IR quantum cascade laser”. In: *Lasers and Applications in Science and Engineering*. Ed. by Steve Mecherle. San Jose, CA, Feb. 7, 2008, 68770F. DOI: [10.1117/12.763731](https://doi.org/10.1117/12.763731).
- [32] Martin Laurenzis and Frank Christnacher. “Laser gated viewing at ISL for vision through smoke, active polarimetry, and 3D imaging in NIR and SWIR wavelength bands”. In: *Advanced Optical Technologies* 2.5 (Jan. 1, 2013). ISSN: 2192-8584, 2192-8576. DOI: [10.1515/aot-2013-0040](https://doi.org/10.1515/aot-2013-0040).
- [33] Scott Prahl. *miepython*. Version: 2.2.3 <https://github.com/scottprahl/miepython>.
- [34] H. C. van de Hulst. *Light scattering by small particles*. New York: Dover Publications, 1981. 470 pp. ISBN: 978-0-486-64228-4.
- [35] Mikhail N. Polyanskiy. *Refractive index database*. <https://refractiveindex.info>. Accessed on 2022-03-14.

-
- [36] George M. Hale and Marvin R. Querry. “Optical Constants of Water in the 200-nm to 200- μ m Wavelength Region”. In: *Applied Optics* 12.3 (Mar. 1, 1973), p. 555. ISSN: 0003-6935, 1539-4522. DOI: [10.1364/AO.12.000555](https://doi.org/10.1364/AO.12.000555).
- [37] Jane Hodgkinson and Ralph P Tatam. “Optical gas sensing: a review”. In: *Measurement Science and Technology* 24.1 (Jan. 1, 2013), p. 012004. ISSN: 0957-0233, 1361-6501. DOI: [10.1088/0957-0233/24/1/012004](https://doi.org/10.1088/0957-0233/24/1/012004).
- [38] Lazhar Kassa-Baghdouche and Eric Cassan. “Mid-infrared gas sensor based on high-Q/V point-defect photonic crystal nanocavities”. In: *Optical and Quantum Electronics* 52.5 (May 2020), p. 260. ISSN: 0306-8919, 1572-817X. DOI: [10.1007/s11082-020-02366-w](https://doi.org/10.1007/s11082-020-02366-w).
- [39] Christian Ranacher et al. “Mid-infrared absorption gas sensing using a silicon strip waveguide”. In: *Sensors and Actuators A: Physical* 277 (July 2018), pp. 117–123. ISSN: 09244247. DOI: [10.1016/j.sna.2018.05.013](https://doi.org/10.1016/j.sna.2018.05.013).
- [40] Robert Bogue. “Detecting gases with light: a review of optical gas sensor technologies”. In: *Sensor Review* 35.2 (Mar. 16, 2015), pp. 133–140. ISSN: 0260-2288. DOI: [10.1108/SR-09-2014-696](https://doi.org/10.1108/SR-09-2014-696).
- [41] R.V. Kochanov et al. “HITRAN Application Programming Interface (HAPI): A comprehensive approach to working with spectroscopic data”. In: *Journal of Quantitative Spectroscopy and Radiative Transfer* 177 (July 2016), pp. 15–30. ISSN: 00224073. DOI: [10.1016/j.jqsrt.2016.03.005](https://doi.org/10.1016/j.jqsrt.2016.03.005).
- [42] Fredrick G. Smith. *The Infrared and electro-optical systems handbook*. Vol. 2. Ann Arbor, Mich. : Bellingham, Wash: Infrared Information Analysis Center ; SPIE Optical Engineering Press, 1993. 8 pp. ISBN: 978-0-8194-1072-6.
- [43] Steve D. Lord. *ATRAN NASA Technical Memorandum 103957*. 1992.

-
- [44] R. Häussler et al. “Large real-time holographic 3D displays: enabling components and results”. In: *Applied Optics* 56.13 (May 1, 2017), F45. ISSN: 0003-6935, 1539-4522. DOI: [10.1364/AO.56.000F45](https://doi.org/10.1364/AO.56.000F45).
- [45] Elchanan Bruckheimer et al. “Computer-generated real-time digital holography: first time use in clinical medical imaging”. In: *European Heart Journal – Cardiovascular Imaging* 17.8 (Aug. 2016), pp. 845–849. ISSN: 2047-2404, 2047-2412. DOI: [10.1093/ehjci/jew087](https://doi.org/10.1093/ehjci/jew087).
- [46] Paul C Mogensen and Jesper Glückstad. “A phase-based optical encryption system with polarisation encoding”. en. In: *Optics Communications* 173.1-6 (Jan. 2000), pp. 177–183. ISSN: 00304018. DOI: [10.1016/S0030-4018\(99\)00633-1](https://doi.org/10.1016/S0030-4018(99)00633-1).
- [47] Cedric Lam et al. “Fiber optic communication technologies: What’s needed for data-center network operations”. In: *IEEE Communications Magazine* 48.7 (July 2010), pp. 32–39. ISSN: 0163-6804. DOI: [10.1109/MCOM.2010.5496876](https://doi.org/10.1109/MCOM.2010.5496876).
- [48] Fuan Liu et al. “An α -BaTeMo₂O₉ Acousto-Optical Q-Switch for All-Fiber Lasers”. In: *IEEE Photonics Technology Letters* 33.9 (May 2021), pp. 445–448. ISSN: 1041-1135, 1941-0174. DOI: [10.1109/LPT.2021.3064231](https://doi.org/10.1109/LPT.2021.3064231).
- [49] F. Poletti et al. “Towards high-capacity fibre-optic communications at the speed of light in vacuum”. In: *Nature Photonics* 7.4 (Apr. 2013), pp. 279–284. ISSN: 1749-4885, 1749-4893. DOI: [10.1038/nphoton.2013.45](https://doi.org/10.1038/nphoton.2013.45).
- [50] Mingbo He et al. “High-performance hybrid silicon and lithium niobate Mach–Zehnder modulators for 100 Gbit s⁻¹ and beyond”. In: *Nature Photonics* 13.5 (May 2019), pp. 359–364. ISSN: 1749-4885, 1749-4893. DOI: [10.1038/s41566-019-0378-6](https://doi.org/10.1038/s41566-019-0378-6).
- [51] J. E. Murray and W. H. Lowdermilk. “ND : YAG regenerative amplifier”. In: *Journal of Applied Physics* 51.7 (July 1980), pp. 3548–3556. ISSN: 0021-8979, 1089-7550. DOI: [10.1063/1.328194](https://doi.org/10.1063/1.328194).

-
- [52] S. Dong et al. “Fast $\lambda/4$ and $\lambda/2$ voltage Pockels cell driver for an internally seeded and cavity dumped regenerative laser amplifier”. In: *Review of Scientific Instruments* 57.4 (Apr. 1986), pp. 539–543. ISSN: 0034-6748, 1089-7623. DOI: [10.1063/1.1138924](https://doi.org/10.1063/1.1138924).
- [53] Jin Tao et al. “Mass-Manufactured Beam-Steering Metasurfaces for High-Speed Full-Duplex Optical Wireless-Broadcasting Communications”. In: *Advanced Materials* (Dec. 28, 2021), p. 2106080. ISSN: 0935-9648, 1521-4095. DOI: [10.1002/adma.202106080](https://doi.org/10.1002/adma.202106080).
- [54] K. Suzuki et al. “High-speed bi-directional polarisation division multiplexed optical transmission in ultra low-loss (1.3 dB/km) polarisation-maintaining photonic crystal fibre”. In: *Electronics Letters* 37.23 (2001), p. 1399. ISSN: 00135194. DOI: [10.1049/el:20010964](https://doi.org/10.1049/el:20010964).
- [55] F. T. Wenthen and L. R. Snowman. “High Speed Light Choppers”. en. In: *Applied Optics* 12.4 (Apr. 1973), p. 822. ISSN: 0003-6935, 1539-4522. DOI: [10.1364/AO.12.000822](https://doi.org/10.1364/AO.12.000822).
- [56] Matthew P. Edgar, Graham M. Gibson, and Miles J. Padgett. “Principles and prospects for single-pixel imaging”. In: *Nature Photonics* 13.1 (Jan. 2019), pp. 13–20. ISSN: 1749-4885, 1749-4893. DOI: [10.1038/s41566-018-0300-7](https://doi.org/10.1038/s41566-018-0300-7).
- [57] Mahmut Sami Yazici et al. “Integration of MEMS IR detectors with MIR waveguides for sensing applications”. In: *Optics Express* 28.8 (Apr. 13, 2020), p. 11524. ISSN: 1094-4087. DOI: [10.1364/OE.381279](https://doi.org/10.1364/OE.381279).
- [58] Mark A Richardson and John A Coath. “Infrared optical modulators for missile testing”. en. In: *Optics & Laser Technology* 30.2 (Mar. 1998), pp. 137–140. ISSN: 0030-3992. DOI: [10.1016/S0030-3992\(98\)00035-8](https://doi.org/10.1016/S0030-3992(98)00035-8).
- [59] Mohammad Ali Khalighi and Murat Uysal. “Survey on Free Space Optical Communication: A Communication Theory Perspective”. In: *IEEE Communications Surveys*

- IEEE Transactions on Microwave Theory and Techniques* 62.4 (2014), pp. 2231–2258. ISSN: 1553-877X, 2373-745X. DOI: [10.1109/COMST.2014.2329501](https://doi.org/10.1109/COMST.2014.2329501).
- [60] W.S. Rabinovich et al. “Infrared data link using a multiple quantum well modulating retro-reflector on a small rotary-wing UAV”. In: *2000 IEEE Aerospace Conference. Proceedings (Cat. No.00TH8484)*. Vol. 3. Big Sky, MT, USA: IEEE, 2000, pp. 93–100. ISBN: 978-0-7803-5846-1. DOI: [10.1109/AERO.2000.879837](https://doi.org/10.1109/AERO.2000.879837).
- [61] A Graf et al. “Review of micromachined thermopiles for infrared detection”. In: *Measurement Science and Technology* 18.7 (July 1, 2007), R59–R75. ISSN: 0957-0233, 1361-6501. DOI: [10.1088/0957-0233/18/7/R01](https://doi.org/10.1088/0957-0233/18/7/R01).
- [62] A. Hossain and M.H. Rashid. “Pyroelectric detectors and their applications”. In: *IEEE Transactions on Industry Applications* 27.5 (Oct. 1991), pp. 824–829. ISSN: 00939994. DOI: [10.1109/28.90335](https://doi.org/10.1109/28.90335).
- [63] R. W. Whatmore. “Pyroelectric devices and materials”. In: *Reports on Progress in Physics* 49.12 (Dec. 1986). Publisher: IOP Publishing, pp. 1335–1386. DOI: [10.1088/0034-4885/49/12/002](https://doi.org/10.1088/0034-4885/49/12/002).
- [64] Xiaochao Tan et al. “Non-dispersive infrared multi-gas sensing via nanoantenna integrated narrowband detectors”. In: *Nature Communications* 11.1 (Dec. 2020), p. 5245. ISSN: 2041-1723. DOI: [10.1038/s41467-020-19085-1](https://doi.org/10.1038/s41467-020-19085-1).
- [65] Samuel Pierpont Langley. *The "bolometer"*. The Society, 1881.
- [66] Per Ericsson et al. “Toward 17 μm pitch heterogeneously integrated Si/SiGe quantum well bolometer focal plane arrays”. In: *SPIE Defense, Security, and Sensing*. Ed. by Bjørn F. Andresen, Gabor F. Fulop, and Paul R. Norton. Orlando, Florida, United States, May 13, 2011, p. 801216. DOI: [10.1117/12.883827](https://doi.org/10.1117/12.883827).

-
- [67] Hyung-Kew Lee et al. “A high fill-factor infrared bolometer using micromachined multilevel electrothermal structures”. In: *IEEE Transactions on Electron Devices* 46.7 (July 1999), pp. 1489–1491. ISSN: 00189383. DOI: [10.1109/16.772496](https://doi.org/10.1109/16.772496).
- [68] M. Safy and A. Hafz Zaky. “Design of a high fill-factor micromachined bolometer for thermal imaging applications”. In: *2010 5th International Microsystems Packaging Assembly and Circuits Technology Conference*. 2010 5th International Microsystems, Packaging, Assembly and Circuits Technology Conference (IMPACT). Taipei, Taiwan: IEEE, Oct. 2010, pp. 1–4. ISBN: 978-1-4244-9783-6. DOI: [10.1109/IMPACT.2010.5699494](https://doi.org/10.1109/IMPACT.2010.5699494).
- [69] M. Tarasov et al. “Carbon nanotube based bolometer”. In: *JETP Letters* 84.5 (Nov. 2006), pp. 267–270. ISSN: 0021-3640, 1090-6487. DOI: [10.1134/S0021364006170085](https://doi.org/10.1134/S0021364006170085).
- [70] Gustavo Vera-Reveles et al. “High-Sensitivity Bolometers from Self-Oriented Single-Walled Carbon Nanotube Composites”. In: *ACS Applied Materials & Interfaces* 3.8 (Aug. 24, 2011), pp. 3200–3204. ISSN: 1944-8244, 1944-8252. DOI: [10.1021/am2007036](https://doi.org/10.1021/am2007036).
- [71] Andrew Blaikie, David Miller, and Benjamín J. Alemán. “A fast and sensitive room-temperature graphene nanomechanical bolometer”. In: *Nature Communications* 10.1 (Dec. 2019), p. 4726. ISSN: 2041-1723. DOI: [10.1038/s41467-019-12562-2](https://doi.org/10.1038/s41467-019-12562-2).
- [72] Dmitri K. Efetov et al. “Fast thermal relaxation in cavity-coupled graphene bolometers with a Johnson noise read-out”. In: *Nature Nanotechnology* 13.9 (Sept. 2018), pp. 797–801. ISSN: 1748-3387, 1748-3395. DOI: [10.1038/s41565-018-0169-0](https://doi.org/10.1038/s41565-018-0169-0).
- [73] Ronald G. Driggers. *Introduction to infrared and electro-optical systems / Ronald G. Driggers, Melvin H. Friedman, Jonathan Nichols*. eng. Second edition. 2012. ISBN: 978-1-60807-101-2.
- [74] G. Finger et al. “Development of HgCdTe large format MBE arrays and noise-free high speed MOVPE EAPD arrays for ground based NIR astronomy”. In: *International*

- Conference on Space Optics — ICSO 2014*. International Conference on Space Optics 2014. Ed. by Bruno Cugny, Zoran Sodnik, and Nikos Karafolas. Tenerife, Canary Islands, Spain: SPIE, Nov. 17, 2017, p. 210. ISBN: 978-1-5106-1615-8 978-1-5106-1616-5. DOI: [10.1117/12.2304270](https://doi.org/10.1117/12.2304270).
- [75] Ian Baker et al. “Developments in MOVPE HgCdTe arrays for passive and active infrared imaging”. In: SPIE Security + Defence. Ed. by Gary W. Kamerman et al. Edinburgh, United Kingdom, Nov. 19, 2012, 85421A. DOI: [10.1117/12.981850](https://doi.org/10.1117/12.981850).
- [76] Xiaoli Sun et al. “HgCdTe avalanche photodiode detectors for airborne and spaceborne lidar at infrared wavelengths”. In: *Optics Express* 25.14 (July 10, 2017), p. 16589. ISSN: 1094-4087. DOI: [10.1364/OE.25.016589](https://doi.org/10.1364/OE.25.016589).
- [77] J. Rothman, G. Lasfargues, and J. Abergel. “HgCdTe APDs for free space optical communications”. In: SPIE Security + Defence. Ed. by Edward M. Carapezza et al. Toulouse, France, Oct. 29, 2015, 96470N. DOI: [10.1117/12.2197171](https://doi.org/10.1117/12.2197171).
- [78] Anand Singh, Vanya Srivastav, and Ravinder Pal. “HgCdTe avalanche photodiodes: A review”. In: *Optics & Laser Technology* 43.7 (Oct. 2011), pp. 1358–1370. ISSN: 00303992. DOI: [10.1016/j.optlastec.2011.03.009](https://doi.org/10.1016/j.optlastec.2011.03.009).
- [79] B. F. Levine et al. “New 10 μm infrared detector using intersubband absorption in resonant tunneling GaAlAs superlattices”. In: *Applied Physics Letters* 50.16 (Apr. 20, 1987), pp. 1092–1094. ISSN: 0003-6951, 1077-3118. DOI: [10.1063/1.97928](https://doi.org/10.1063/1.97928).
- [80] L. Gendron et al. “Quantum cascade photodetector”. In: *Applied Physics Letters* 85.14 (Oct. 4, 2004), pp. 2824–2826. ISSN: 0003-6951, 1077-3118. DOI: [10.1063/1.1781731](https://doi.org/10.1063/1.1781731).
- [81] Tatsuo Dougakiuchi et al. “High photoresponse in room temperature quantum cascade detector based on coupled quantum well design”. In: *Applied Physics Letters* 109.26 (Dec. 26, 2016), p. 261107. ISSN: 0003-6951, 1077-3118. DOI: [10.1063/1.4973582](https://doi.org/10.1063/1.4973582).
- [82] Hamamatsu. *Quantum Cascade Photodetector P16309-01 (February 2022)*. Feb. 2022.

-
- [83] Hamamatsu. *InAsSb photovoltaic detectors*. 2020.
- [84] Nik Rajic and Neil Street. “A performance comparison between cooled and uncooled infrared detectors for thermoelastic stress analysis”. en. In: *Quantitative InfraRed Thermography Journal* 11.2 (July 2014), pp. 207–221. ISSN: 1768-6733, 2116-7176. DOI: [10.1080/17686733.2014.962835](https://doi.org/10.1080/17686733.2014.962835).
- [85] Amir Averbuch, Gabi Liron, and Ben Zion Bobrovsky. “Scene based non-uniformity correction in thermal images using Kalman filter”. en. In: *Image and Vision Computing* 25.6 (June 2007), pp. 833–851. ISSN: 02628856. DOI: [10.1016/j.imavis.2006.05.019](https://doi.org/10.1016/j.imavis.2006.05.019).
- [86] Yanpeng Cao and Christel-Loic Tisse. “Single-image-based solution for optics temperature-dependent nonuniformity correction in an uncooled long-wave infrared camera”. en. In: *Optics Letters* 39.3 (Feb. 2014), p. 646. ISSN: 0146-9592, 1539-4794. DOI: [10.1364/OL.39.000646](https://doi.org/10.1364/OL.39.000646).
- [87] Chengwei Liu et al. “FPN estimation based nonuniformity correction for infrared imaging system”. en. In: *Infrared Physics & Technology* 96 (Jan. 2019), pp. 22–29. ISSN: 13504495. DOI: [10.1016/j.infrared.2018.09.025](https://doi.org/10.1016/j.infrared.2018.09.025).
- [88] Robert Olbrycht, Boguslaw Wiecek, and Tomasz Swiatczak. “Shutterless method for gain nonuniformity correction of microbolometer detectors”. In: *2009 MIXDES-16th International Conference Mixed Design of Integrated Circuits Systems*. 2009, pp. 378–380.
- [89] B. Journet, G. Bazin, and F. Bras. “Conception of an adaptative laser range finder based on phase shift measurement”. In: *Proceedings of the 1996 IEEE IECON. 22nd International Conference on Industrial Electronics, Control, and Instrumentation*. Vol. 2. Taipei, Taiwan: IEEE, 1996, pp. 784–789. ISBN: 978-0-7803-2775-7. DOI: [10.1109/IECON.1996.565977](https://doi.org/10.1109/IECON.1996.565977).

-
- [90] B. Journet and G. Bazin. “A low-cost laser range finder based on an FMCW-like method”. In: *IEEE Transactions on Instrumentation and Measurement* 49.4 (Aug. 2000), pp. 840–843. ISSN: 00189456. DOI: [10.1109/19.863935](https://doi.org/10.1109/19.863935).
- [91] Sungui Hwang, Junhwan Jang, and Kyihwan Park. “Solving 2pi ambiguity problem of a laser scanner based on phase-shift measurement method or long distances measurement”. In: *2012 12th International Conference on Control, Automation and Systems*. 2012, pp. 1250–1252.
- [92] Lars E. Bengtsson. “A microcontroller-based lock-in amplifier for sub-milliohm resistance measurements”. en. In: *Review of Scientific Instruments* 83.7 (July 2012), p. 075103. ISSN: 0034-6748, 1089-7623. DOI: [10.1063/1.4731683](https://doi.org/10.1063/1.4731683).
- [93] David Dupuy, Marc Lescure, and H l ne Tap-B teille. “Analysis of an avalanche photodiode used as an optoelectronic mixer for a frequency modulated continuous wave laser range finder”. In: *Journal of Optics A: Pure and Applied Optics* 4.6 (Nov. 1, 2002), S332–S336. ISSN: 1464-4258. DOI: [10.1088/1464-4258/4/6/377](https://doi.org/10.1088/1464-4258/4/6/377).
- [94] Aude Martin et al. “Photonic Integrated Circuit-Based FMCW Coherent LiDAR”. In: *Journal of Lightwave Technology* 36.19 (Oct. 2018), pp. 4640–4645. ISSN: 0733-8724, 1558-2213. DOI: [10.1109/JLT.2018.2840223](https://doi.org/10.1109/JLT.2018.2840223).
- [95] R. J.L. Lerou. “A cw CO2 laser rangefinder using heterodyne detection and on-off amplitude modulation”. In: *Optics and Laser Technology* 15.3 (1983), pp. 153–159. ISSN: 00303992. DOI: [10.1016/0030-3992\(83\)90063-4](https://doi.org/10.1016/0030-3992(83)90063-4).
- [96] D. Castagnet. “Avalanche-photodiode-based heterodyne optical head of a phase-shift laser range finder”. In: *Optical Engineering* 45.4 (Apr. 1, 2006), p. 043003. ISSN: 0091-3286. DOI: [10.1117/1.2190229](https://doi.org/10.1117/1.2190229).
- [97] Jan Nissinen, Ilkka Nissinen, and Juha Kostamovaara. “Integrated Receiver Including Both Receiver Channel and TDC for a Pulsed Time-of-Flight Laser Rangefinder

- With cm-Level Accuracy”. In: *IEEE Journal of Solid-State Circuits* 44.5 (May 2009), pp. 1486–1497. ISSN: 0018-9200. DOI: [10.1109/JSSC.2009.2017006](https://doi.org/10.1109/JSSC.2009.2017006).
- [98] Alessandro Pesatori et al. “High-Resolution Mode-Locked Laser Rangefinder With Harmonic Downconversion”. In: *IEEE Transactions on Instrumentation and Measurement* 61.5 (May 2012), pp. 1536–1542. ISSN: 0018-9456, 1557-9662. DOI: [10.1109/TIM.2012.2183437](https://doi.org/10.1109/TIM.2012.2183437).
- [99] Joohyung Lee et al. “Time-of-flight measurement with femtosecond light pulses”. In: *Nature Photonics* 4.10 (Oct. 2010), pp. 716–720. ISSN: 1749-4885, 1749-4893. DOI: [10.1038/nphoton.2010.175](https://doi.org/10.1038/nphoton.2010.175).
- [100] Aongus McCarthy et al. “Kilometer-range, high resolution depth imaging via 1560 nm wavelength single-photon detection”. In: *Optics Express* 21.7 (2013). ISBN: 9781479905942, pp. 8904–8915. ISSN: 1094-4087. DOI: [10.1364/OE.21.008904](https://doi.org/10.1364/OE.21.008904).
- [101] Agata M. Pawlikowska et al. “Single-photon three-dimensional imaging at up to 10 kilometers range”. In: *Optics Express* 25.10 (May 15, 2017). Publisher: The Optical Society, p. 11919. DOI: [10.1364/oe.25.011919](https://doi.org/10.1364/oe.25.011919).
- [102] Zheng-Ping Li et al. “Single-photon computational 3D imaging at 45 km”. In: *Photonics Research* 8.9 (Sept. 1, 2020), p. 1532. ISSN: 2327-9125. DOI: [10.1364/PRJ.390091](https://doi.org/10.1364/PRJ.390091).
- [103] Zheng-Ping Li et al. “Single-photon imaging over 200 km”. In: *Optica* 8.3 (Mar. 20, 2021), p. 344. ISSN: 2334-2536. DOI: [10.1364/OPTICA.408657](https://doi.org/10.1364/OPTICA.408657).
- [104] I. Coddington et al. “Rapid and precise absolute distance measurements at long range”. In: *Nature Photonics* 3.6 (June 2009), pp. 351–356. ISSN: 1749-4885, 1749-4893. DOI: [10.1038/nphoton.2009.94](https://doi.org/10.1038/nphoton.2009.94).
- [105] A. Brook, E. Ben-Dor, and R. Richter. “Fusion of hyperspectral images and LiDAR data for civil engineering structure monitoring”. In: *2010 2nd Workshop on Hyperspectral Image and Signal Processing: Evolution in Remote Sensing*. 2010 2nd Workshop

- on Hyperspectral Image and Signal Processing: Evolution in Remote Sensing (WHISPERS). Reykjavik, Iceland: IEEE, June 2010, pp. 1–5. ISBN: 978-1-4244-8906-0. DOI: [10.1109/WHISPERS.2010.5594872](https://doi.org/10.1109/WHISPERS.2010.5594872).
- [106] J. S. Accetta and David L. Shumaker, eds. *The Infrared and electro-optical systems handbook*. Vol. 6. Ann Arbor, Mich. : Bellingham, Wash: Infrared Information Analysis Center ; SPIE Optical Engineering Press, 1993. ISBN: 978-0-8194-1072-6.
- [107] Yuan Tian et al. “Handling occlusions in augmented reality based on 3D reconstruction method”. In: *Neurocomputing* 156 (May 2015), pp. 96–104. ISSN: 09252312. DOI: [10.1016/j.neucom.2014.12.081](https://doi.org/10.1016/j.neucom.2014.12.081).
- [108] John Sell and Patrick O’Connor. “The Xbox One System on a Chip and Kinect Sensor”. In: *IEEE Micro* 34.2 (Mar. 2014), pp. 44–53. ISSN: 0272-1732. DOI: [10.1109/MM.2014.9](https://doi.org/10.1109/MM.2014.9).
- [109] M. J. Taylor et al. “Pulsed CO₂ TEA laser rangefinder”. In: *Applied Optics* 17.6 (Mar. 1978), p. 885. ISSN: 0003-6935. DOI: [10.1364/AO.17.000885](https://doi.org/10.1364/AO.17.000885).
- [110] Ofer David, Norman S. Kopeika, and Boaz Weizer. “Range gated active night vision system for automobiles”. In: *Applied Optics* 45.28 (Oct. 1, 2006), p. 7248. ISSN: 0003-6935, 1539-4522. DOI: [10.1364/AO.45.007248](https://doi.org/10.1364/AO.45.007248).
- [111] Deni Bonnier and Vincent Larochelle. “Range-gated active-imaging system for search-and-rescue and surveillance operations”. In: *Aerospace/Defense Sensing and Controls*. Ed. by Bjorn F. Andresen and Marija S. Scholl. Orlando, FL, June 27, 1996, p. 134. DOI: [10.1117/12.243458](https://doi.org/10.1117/12.243458).
- [112] Frank Christnacher et al. “Influence of gating and of the gate shape on the penetration capacity of range-gated active imaging in scattering environments”. In: *Optics Express* 23.26 (Dec. 28, 2015), p. 32897. ISSN: 1094-4087. DOI: [10.1364/OE.23.032897](https://doi.org/10.1364/OE.23.032897).

-
- [113] Martin Laurenzis, Frank Christnacher, and David Monnin. “Long-range three-dimensional active imaging with superresolution depth mapping”. In: *Optics Letters* 32.21 (Nov. 1, 2007), p. 3146. ISSN: 0146-9592, 1539-4794. DOI: [10.1364/OL.32.003146](https://doi.org/10.1364/OL.32.003146).
- [114] Jeff Beck et al. “Gated IR Imaging with 128×128 HgCdTe Electron Avalanche Photodiode FPA”. In: *Journal of Electronic Materials* 37.9 (Sept. 1, 2008), pp. 1334–1343. ISSN: 1543-186X. DOI: [10.1007/s11664-008-0433-4](https://doi.org/10.1007/s11664-008-0433-4).
- [115] Alexis Matwyschuk. “Multiple-wavelength range-gated active imaging in superimposed style for moving object tracking”. In: *Applied Optics* 56.27 (Sept. 20, 2017), p. 7766. ISSN: 1559-128X, 2155-3165. DOI: [10.1364/AO.56.007766](https://doi.org/10.1364/AO.56.007766).
- [116] T.H. Courtenay, J.F. Boulter, and H. Henshall. “Active imaging with a TEA-CO₂-laser”. In: *Infrared Physics* 16.1 (Jan. 1976), pp. 95–102. ISSN: 00200891. DOI: [10.1016/0020-0891\(76\)90017-8](https://doi.org/10.1016/0020-0891(76)90017-8).
- [117] Donna Strickland and Gerard Mourou. “Compression of amplified chirped optical pulses”. In: *Optics Communications* 56.3 (Dec. 1985), pp. 219–221. ISSN: 00304018. DOI: [10.1016/0030-4018\(85\)90120-8](https://doi.org/10.1016/0030-4018(85)90120-8).
- [118] Jérôme Faist. *Quantum Cascade Lasers*. First edition. OCLC: ocn835962241. Oxford, United Kingdom: Oxford University Press, 2013. 306 pp. ISBN: 978-0-19-852824-1.
- [119] Jerome Faist et al. “Quantum Cascade Laser”. In: *Science* 264.5158 (Apr. 22, 1994), pp. 553–556. ISSN: 0036-8075, 1095-9203. DOI: [10.1126/science.264.5158.553](https://doi.org/10.1126/science.264.5158.553).
- [120] *Quantum cascade lasers (QCLs)*. Hamamatsu. URL: <https://www.hamamatsu.com/jp/en/product/lasers/semiconductor-lasers/qcls.html>.
- [121] *Quantum and Interband Cascade Lasers (QCLs and ICLs), 3 - 11 μ m*. Thorlabs. URL: https://www.thorlabs.com/newgrouppage9.cfm?objectgroup_ID=6932.
- [122] *Alpine Lasers*. Alpine Lasers. URL: <https://www.alpeslasers.ch/>.

-
- [123] Yongquan Zeng, Bo Qiang, and Qi Jie Wang. “Photonic Engineering Technology for the Development of Terahertz Quantum Cascade Lasers”. In: *Advanced Optical Materials* 8.3 (Feb. 2020), p. 1900573. ISSN: 2195-1071, 2195-1071. DOI: [10.1002/adom.201900573](https://doi.org/10.1002/adom.201900573).
- [124] Boyu Wen and Dayan Ban. “High-temperature terahertz quantum cascade lasers”. In: *Progress in Quantum Electronics* 80 (Nov. 2021), p. 100363. ISSN: 00796727. DOI: [10.1016/j.pquantelec.2021.100363](https://doi.org/10.1016/j.pquantelec.2021.100363).
- [125] W. W. Chow and S. W. Koch. *Semiconductor-laser fundamentals: physics of the gain materials*. Berlin ; New York: Springer, 1999. 245 pp. ISBN: 978-3-540-64166-7.
- [126] Paul Horowitz. *The art of electronics*. Third edition. New York, NY: Cambridge University Press, 2015. 1192 pp. ISBN: 978-0-521-80926-9.
- [127] Aram Baharmast and Juha Kostamovaara. “High-speed wide dynamic range linear mode time-of-flight receiver based on zero-crossing timing detection”. In: *Optical Engineering* 59.10 (Oct. 14, 2020). ISSN: 0091-3286. DOI: [10.1117/1.OE.59.10.104102](https://doi.org/10.1117/1.OE.59.10.104102).
- [128] Ari Kilpelä et al. “Timing discriminator for pulsed time-of-flight laser rangefinding measurements”. In: *Review of Scientific Instruments* 69.5 (1998). Publisher: American Institute of Physics Inc., pp. 1978–1984. ISSN: 00346748. DOI: [10.1063/1.1148884](https://doi.org/10.1063/1.1148884).
- [129] M. Tanaka et al. “Development of a monolithic constant fraction discriminator”. In: *IEEE Transactions on Nuclear Science* 39.5 (Oct. 1992), pp. 1321–1325. ISSN: 0018-9499, 1558-1578. DOI: [10.1109/23.173199](https://doi.org/10.1109/23.173199).
- [130] Hansang Lim. “Constant Fraction Discriminator Involving Automatic Gain Control to Reduce Time Walk”. In: *IEEE Transactions on Nuclear Science* 61.4 (Aug. 2014), pp. 2351–2356. ISSN: 0018-9499, 1558-1578. DOI: [10.1109/TNS.2014.2339362](https://doi.org/10.1109/TNS.2014.2339362).

-
- [131] P. Dudek, S. Szczepanski, and J.V. Hatfield. “A high-resolution CMOS time-to-digital converter utilizing a Vernier delay line”. In: *IEEE Journal of Solid-State Circuits* 35.2 (Feb. 2000), pp. 240–247. ISSN: 0018-9200, 1558-173X. DOI: [10.1109/4.823449](https://doi.org/10.1109/4.823449).
- [132] Jian Song, Qi An, and Shubin Liu. “A high-resolution time-to-digital converter implemented in field-programmable-gate-arrays”. In: *IEEE Transactions on Nuclear Science* 53.1 (Feb. 2006), pp. 236–241. ISSN: 0018-9499. DOI: [10.1109/TNS.2006.869820](https://doi.org/10.1109/TNS.2006.869820).
- [133] J.-P. Jansson, A. Mantyniemi, and J. Kostamovaara. “A CMOS Time-to-Digital Converter With Better Than 10 ps Single-Shot Precision”. In: *IEEE Journal of Solid-State Circuits* 41.6 (June 2006), pp. 1286–1296. ISSN: 0018-9200. DOI: [10.1109/JSSC.2006.874281](https://doi.org/10.1109/JSSC.2006.874281).
- [134] *TDC7200 Time-to-Digital Converter for Time-of-Flight Applications in LIDAR, Magnetostrictive and Flow Meters*. SNAS647D. Rev. D. Texas Instruments. Mar. 2016.
- [135] Ammar Zakar et al. “Carrier dynamics and surface vibration-assisted Auger recombination in porous silicon”. In: *Physical Review B* 97 (2018), p. 155203. DOI: [10.1103/PhysRevB.97.155203](https://doi.org/10.1103/PhysRevB.97.155203).
- [136] Silvano Donati. *Photodetectors: devices, circuits, and applications*. Upper Saddle River, NJ: Prentice Hall PTR, 2000. 423 pp. ISBN: 978-0-13-020337-3.
- [137] S. V. Frolov and Z. V. Vardeny. “Double-modulation electro-optic sampling for pump-and-probe ultrafast correlation measurements”. en. In: *Review of Scientific Instruments* 69.3 (Mar. 1998), pp. 1257–1260. ISSN: 0034-6748, 1089-7623. DOI: [10.1063/1.1148792](https://doi.org/10.1063/1.1148792).
- [138] Christopher A. Werley, Stephanie M. Teo, and Keith A. Nelson. “Pulsed laser noise analysis and pump-probe signal detection with a data acquisition card”. In: *Review of Scientific Instruments* 82.12 (Dec. 2011), p. 123108. ISSN: 0034-6748, 1089-7623. DOI: [10.1063/1.3669783](https://doi.org/10.1063/1.3669783).

-
- [139] J. Fujikata et al. “High performance PIN Ge photodetector and Si optical modulator with MOS junction for photonics-electronics convergence system”. In: *2013 18th Asia and South Pacific Design Automation Conference (ASP-DAC)*. 2013 18th Asia and South Pacific Design Automation Conference (ASP-DAC 2013). Yokohama: IEEE, Jan. 2013, pp. 655–656. ISBN: 978-1-4673-3030-5 978-1-4673-3029-9 978-1-4673-3028-2. DOI: [10.1109/ASPDAC.2013.6509674](https://doi.org/10.1109/ASPDAC.2013.6509674).
- [140] Konstantinos Misiakos and Dimitris Tsamakis. “Accurate measurements of the silicon intrinsic carrier density from 78 to 340 K”. In: *Journal of Applied Physics* 74.5 (Sept. 1993), pp. 3293–3297. ISSN: 0021-8979, 1089-7550. DOI: [10.1063/1.354551](https://doi.org/10.1063/1.354551).
- [141] S. M. (Solomon Meerovich) Ryvkin. *Photoelectric effects in semiconductors*. New York: Consultants Bureau, 1964.
- [142] Charles Kittel. *Introduction to solid state physics*. 8th ed. Hoboken, NJ: Wiley, 2005. 680 pp. ISBN: 978-0-471-41526-8.
- [143] Jeremy Witzens. “High-Speed Silicon Photonics Modulators”. In: *Proceedings of the IEEE* 106.12 (Dec. 2018), pp. 2158–2182. ISSN: 0018-9219, 1558-2256. DOI: [10.1109/JPROC.2018.2877636](https://doi.org/10.1109/JPROC.2018.2877636).
- [144] Wolfgang Heinrich et al. “GaN pushing the limits of high-speed switching”. In: *2018 22nd International Microwave and Radar Conference (MIKON)*. 2018 22nd International Microwave and Radar Conference (MIKON). Poznan, Poland: IEEE, May 2018, pp. 73–76. ISBN: 978-83-949421-1-3. DOI: [10.23919/MIKON.2018.8405339](https://doi.org/10.23919/MIKON.2018.8405339).
- [145] G. T. Reed et al. “Silicon optical modulators”. In: *Nature Photonics* 4.8 (Aug. 2010), pp. 518–526. ISSN: 1749-4885, 1749-4893. DOI: [10.1038/nphoton.2010.179](https://doi.org/10.1038/nphoton.2010.179).
- [146] B. G. Yacobi. *Semiconductor materials: an introduction to basic principles*. Microdevices. New York: Kluwer Academic/Plenum Publishers, 2003. 228 pp. ISBN: 978-0-306-47361-6.

-
- [147] Carsten Schinke et al. “Uncertainty analysis for the coefficient of band-to-band absorption of crystalline silicon”. In: *AIP Advances* 5.6 (June 2015), p. 067168. ISSN: 2158-3226. DOI: [10.1063/1.4923379](https://doi.org/10.1063/1.4923379).
- [148] D.K. Schroder, R.N. Thomas, and J.C. Swartz. “Free Carrier Absorption in Silicon”. In: *IEEE Journal of Solid-State Circuits* 13.1 (Feb. 1978), pp. 180–187. ISSN: 0018-9200. DOI: [10.1109/JSSC.1978.1051012](https://doi.org/10.1109/JSSC.1978.1051012).
- [149] Ammar Zakar et al. “MWIR optical modulation using structured silicon membranes”. In: SPIE Security + Defence. Ed. by Keith L. Lewis and Richard C. Hollins. Edinburgh, United Kingdom, Oct. 25, 2016, p. 999203. DOI: [10.1117/12.2242287](https://doi.org/10.1117/12.2242287).
- [150] U. Grüning et al. “Macroporous silicon with a complete two-dimensional photonic band gap centered at 5 μm ”. en. In: *Applied Physics Letters* 68.6 (Feb. 1996), pp. 747–749. ISSN: 0003-6951, 1077-3118. DOI: [10.1063/1.116729](https://doi.org/10.1063/1.116729).
- [151] T. W. Ebbesen et al. “Extraordinary optical transmission through sub-wavelength hole arrays”. en. In: *Nature* 391.6668 (Feb. 1998), pp. 667–669. ISSN: 0028-0836, 1476-4687. DOI: [10.1038/35570](https://doi.org/10.1038/35570).
- [152] Mark J. Kerr and Andres Cuevas. “General parameterization of Auger recombination in crystalline silicon”. In: *Journal of Applied Physics* 91.4 (Feb. 15, 2002), pp. 2473–2480. ISSN: 0021-8979, 1089-7550. DOI: [10.1063/1.1432476](https://doi.org/10.1063/1.1432476).
- [153] K. Sokolowski-Tinten and D. von der Linde. “Generation of dense electron-hole plasmas in silicon”. In: *Physical Review B* 61.4 (Jan. 15, 2000), pp. 2643–2650. ISSN: 0163-1829, 1095-3795. DOI: [10.1103/PhysRevB.61.2643](https://doi.org/10.1103/PhysRevB.61.2643).
- [154] O. D. Restrepo, K. Varga, and S. T. Pantelides. “First-principles calculations of electron mobilities in silicon: Phonon and Coulomb scattering”. In: *Applied Physics Letters* 94.21 (May 25, 2009), p. 212103. ISSN: 0003-6951, 1077-3118. DOI: [10.1063/1.3147189](https://doi.org/10.1063/1.3147189).

-
- [155] Rihan Wu et al. “Demonstration of time-of-flight technique with all-optical modulation and MCT detection in SWIR/MWIR range”. In: *Emerging Imaging and Sensing Technologies for Security and Defence III; and Unmanned Sensors, Systems, and Countermeasures*. Ed. by Gerald S. Buller et al. Vol. 10799. International Society for Optics and Photonics. SPIE, 2018, pp. 10–17. DOI: [10.1117/12.2500326](https://doi.org/10.1117/12.2500326).
- [156] Jack Collins et al. “All-optical modulator for gated range finding and active imaging in LWIR”. In: *Electro-Optical and Infrared Systems: Technology and Applications XVII*. Electro-optical and Infrared Systems: Technology and Applications XVII. Ed. by Duncan L. Hickman and Helge Bürsing. Online Only, United Kingdom: SPIE, Sept. 20, 2020, p. 20. ISBN: 978-1-5106-3887-7 978-1-5106-3888-4. DOI: [10.1117/12.2574006](https://doi.org/10.1117/12.2574006).
- [157] Rihan Wu et al. “All-optical modulation and ultrafast switching in MWIR with sub-wavelength structured silicon”. In: *Applied Sciences (Switzerland)* 9.9 (2019). ISSN: 20763417. DOI: [10.3390/app9091808](https://doi.org/10.3390/app9091808).
- [158] Wei He et al. “Reconstructing charge-carrier dynamics in porous silicon membranes from time-resolved interferometric measurements”. In: *Scientific Reports* 8.1 (2018), p. 17172. DOI: [10.1038/s41598-018-35210-z](https://doi.org/10.1038/s41598-018-35210-z).
- [159] Sung Jin Park et al. “All-optical modulation in Mid-Wavelength Infrared using porous Si membranes”. In: *Scientific Reports* 6.1 (2016), p. 30211. DOI: [10.1038/srep30211](https://doi.org/10.1038/srep30211).
- [160] A. Zakar et al. “MWIR optical modulation using structured silicon membranes”. In: *Emerging Imaging and Sensing Technologies*. Ed. by Keith L. Lewis and Richard C. Hollins. Vol. 9992. International Society for Optics and Photonics. SPIE, 2016, pp. 1–7. DOI: [10.1117/12.2242287](https://doi.org/10.1117/12.2242287).
- [161] Jan Schmidt, Mark Kerr, and Pietro P. Altermatt. “Coulomb-enhanced Auger recombination in crystalline silicon at intermediate and high injection densities”. In: *Journal of Applied Physics* 88.3 (2000), pp. 1494–1497. DOI: [10.1063/1.373878](https://doi.org/10.1063/1.373878). eprint: <https://doi.org/10.1063/1.373878>.

- [162] Tim Green, Pete Semig, and Collin Wells, eds. *Analog Engineer's Circuit Cookbook: Amplifiers*. Second Edition - SLYY137. Texas Instruments Incorporated, 2019.
- [163] D. I. Crecraft and Stephen Gergely. *Analog electronics: circuits, systems and signal processing*. eng. Oxford: Butterworth-Heinemann, 2007. ISBN: 978-0-7506-5095-3.
- [164] Howard W. Johnson and Martin Graham. *High-speed digital design: a handbook of black magic*. Englewood Cliffs, N.J: Prentice Hall, 1993. ISBN: 978-0-13-395724-2.
- [165] Rihan Wu et al. "Localized Plasmon Field Effect of Gold Clusters Embedded in Nanoporous Silicon". In: *Advanced Optical Materials* 9.9 (May 2021), p. 2002119. ISSN: 2195-1071, 2195-1071. DOI: [10.1002/adom.202002119](https://doi.org/10.1002/adom.202002119).
- [166] Weishuai Chen et al. "Surface Dual Composite Nanostructure for Improving Visible Light Absorption in Thin Silicon Films". In: *IEEE Photonics Journal* 14.4 (Aug. 2022), pp. 1–7. ISSN: 1943-0655, 1943-0647. DOI: [10.1109/JPHOT.2022.3192278](https://doi.org/10.1109/JPHOT.2022.3192278).